COATING OF CATALYST SUPPORTS: LINKS BETWEEN SLURRY CHARACTERISTICS, COATING PROCESS AND FINAL COATING QUALITY

by

STEPHEN ADEMOLA ADEGBITE

A thesis submitted to
University of Birmingham
for the degree of
DOCTOR OF PHILOSOPHY

School of Chemical Engineering
University of Birmingham
June 2010

ABSTRACT

Tightening legislation for vehicles across the world has caused the use of monolith catalysts in automotive emission control to become ubiquitous. Control of the adherence and homogeneity of the platinum group metal (PGM) coating onto the monolith block, to maximise catalytic performance for a minimum PGM loading, is therefore paramount. In this study, an automatic film application is used for coating γ–alumina slurries onto Fecralloy®, an integral component of metallic monolith catalysts, to achieve the desired coating properties.

Upon coating of the Fecralloy® coupons, the samples preoxidised for 10 h gave the best performance in terms of coating loading (7.94 mass %) and adherence (< 10 mass % loss) based on ultrasonic vibration test. These conditions produced the optimal surface topography, typified by conspicuous and randomly-oriented α–alumina whiskers which promote coating adherence. The optimal coating loading and adherence were achieved at a pH of 4 and solids concentrations not exceeding 40 wt%.

A newly devised technique using the electromechanical testing system showed that finest particle coatings of 40 wt% solids concentration produced the best coating adherence. At solids concentration of 45 wt% the coating adherence was poor and insensitive to the blends of different particle size distributions.

Dedicated to "Mama Wa" — my sweet grandmother

"A good head and a good heart are always a formidable combination. But when you add to that a literate tongue or pen, then you have something very special."
— Nelson Mandela

ACKNOWLEDGEMENTS

I sincerely thank the Engineering and Physical Sciences Research Council (EPSRC) and Johnson Matthey Plc for their financial support. A huge debt of gratitude is due to the Schools of Chemical Engineering and Metallurgy & Materials for providing me with all the necessary equipment for this research.

I would like to give special thanks to my supervisors — Professor Mostafa Barigou, Dr Mark Simmons, Dr Alison Wagland and Professor Hugh Stitt — for their invaluable advice, professionalism and patience. I am grateful to Dr Richard Greenwood, Professor Stuart Blackburn, Dr Rachel Bridson, Mr John Wedderburn, Mr Alan Saywell, Professor Zhibing Zhang, Mrs Lynn Draper and Mr Jason Mahoney for offering me adequate assistance.

I owe Dr Regina Santos and my pioneer tutor, Dr Bushra Al-Duri, a huge gratitude for writing brilliant references for me, without which I probably would not have been admitted to this course. I acknowledge the friendliness of my fellow students, who have made the experience a lot interesting.

I am highly indebted to my parents — Mr and Mrs Jonathan Adegbite — for their overwhelming support, and likewise my siblings: Dr Adewunmi Ojo, Dr Afolabi Adegbite and Miss Temitope Adegbite.

CONTENTS

LIST OF FIGURES

LIST OF TABLES

NOMENCLATURE

Upper case symbols

$\equiv S_{acid} - OH$	γ–alumina hydrated site with acidic character
$\equiv S_{basic} - OH$	γ–alumina hydrated site with basic character
H^+, OH^-	potential determining ions
F	Faraday constant (96,484 C mol^{-1})
K	adsorption equilibrium constant
S_{al}	surface area of γ–alumina ($m^2\ kg^{-1}$)
C, $C_{adsorbed}$	concentration of active species (mol m^{-3})
C_{bulk}	bulk concentration of element (wt %)
C_b	initial concentration of element (wt %)
D_S	diffusion coefficient for the support ($m^2\ s^{-1}$)
V_L	liquid volume (l)
P	power consumed (W)
V(1), V(2)	total interaction energy (V)
V_A	van der Waals attraction (V)
$V_R(1)$, $V_R(2)$	electrostatic repulsion (V)
SN, SN_M	number of stress events (–)
SE, SE_i, SE_j, $\overline{SE}$	stress energy (J)
SE_{GM}	stress energy of grinding media (J)
N_C	number of media contacts (–)
P_S	probability that a particle is caught and sufficiently stressed at a media contact (–)
N_P	number of particles in the mill tank (–)
N	shaft speed (rpm)
Po	power number (–)
D	shaft diameter (m)
$SF_{M,j}$	frequency of the stress events of interval j (s^{-1})
$E_{m,p}$, $E_{m,M}$	specific energy (J kg^{-1})
Re	Reynolds number and the Froude
Fr	Froude number
C_{EE}, C_{EC}	constants
R_a, R_q, R_t, R_{max}	2D roughness parameters (μm)
S_a, S_q, S_t, S_{max}	3D roughness parameters (μm)

S_n	stress on coating due to compression (MPa)
S_p	stress on coating due to tension (MPa)
F_p	force on coating due to tension (kN)
A	contact area (mm^2)

Lower case symbols

m_{al}	mass of γ–alumina (kg)
m_{solute}	mass number of constituent element (g)
m_{alloy}	average molar mass of Fecralloy® (g)
m_u	mass of foil before coating (kg)
m_c	mass of foil after coating (kg)
m_a	mass of foil undergoing ultrasonic vibration (kg)
k_p	parabolic rate constant ($m^2 s^{-1}$)
x	distance from the support surface (m)
t	preoxidation time (h)
w	second half-width (m)
$\Delta\overline{m}$	specific mass gain (mg cm^{-2})
a , b , c , d	constants
n, z	constants
$d_{0.1}$, $d_{0.5}$, $d_{0.9}$	particle diameter based on volume distribution (µm)
d_{al}	diameter of γ-alumina particles (µm)
d_l	particle diameter for large polystyrene spheres (µm)
d_s	particle diameter for small polystyrene spheres (µm)
t_m	milling time (s)
c_{al}	γ–alumina solids concentration (wt%)
d_{GM}	diameter of grinding media (µm)
v_t	circumferential speed of the shaft (m s^{-1})
v_E	energy transfer factor (–)
$c_{L,i}$	loss factor (–)
g	acceleration due to gravity (ms^{-2})
n	flow behaviour index (–)
k	consistency index (unit depends on n value)
c_v	γ–alumina solids concentration (vol. %)
c_{water}	concentration of liquid medium (vol. %)
$c_{v\max}$	maximum solids packing (vol. %)

k_{ET}	kinetic energy of particles (J)
v_{al}	particle velocity (m s^{-1})
w_{adh}	work of adhesion (kJ m^{-2})
h_{crit}	displacement at stabilisation stress (mm)
h_{break}	displacement at breaking point (mm)
f	constant

Greek symbols

γ, δ, θ, α	alumina phases
σ_{al}	net surface charge of γ–alumina (C cm^{-2})
Γ_{H^+}, Γ_{OH^-}	surface concentration of ions (mol cm^{-2})
ζ	zeta potential (mV)
Γ, Γ_{max}	adsorption density (mol m^{-2})
ϕ	Pilling-Bedworth ratio of oxide formed (–)
ε	porosity of the bulk of the media (–)
ρ_{al}	density of γ–alumina particles (kg m^{-3})
ρ_{GM}	density of grinding media (kg m^{-3})
ρ_{slurry}	slurry density (kg m^{-3})
ρ_{water}	density of liquid medium (kg m^{-3})
φ_{GM}	media load (%)
μ_{slurry}	slurry dynamic viscosity (Pa s)
μ	slurry apparent viscosity (Pa s)
$[\mu]$	intrinsic viscosity (Pa s)
$\dot{\gamma}$	shear rate (s^{-1})
τ	shear stress (Pa)
μ_r	relative viscosity of slurry (–)
μ^o	apparent viscosity of pure water (Pa s)

Abbreviations

PGMs	platinum group metals
CO	carbon monoxide
NO	oxides of nitrogen
HCs	hydrocarbons
JM	Johnson Matthey
ECT	emission control technologies
UN	United Nations
SN	number of stress events
SE	stress energy
LPI	laser profiling interferometry
IR	infra red
NMR	nuclear magnetic resonance
PGAA	prompt-gamma activation analysis
SAXS	small-angle X-ray scattering
pzc	point of zero charge
iep	isoelectric point
AlOOH	boehmite
RPA	revised physical adsorption
Fe	iron
Cr	chromium
Al	aluminium
Y	yttrium
Si	silicon
La	lanthanum
SEM	scanning electron microscopy
XRD	X-ray diffraction
erfc	complementary error function
FIB	focussed ion beam
psds	particle size distributions
ESA	electrokinetic sonic amplitude
UKAEA	United Kingdom Atomic Energy Authority
ETS	Electromechanical testing system

1

INTRODUCTION

1.1 BACKGROUND TO EMISSION CONTROL CATALYSTS

From 1940 to 1950s air quality problems were experienced in some urban cities in the USA because of the increasing numbers of cars (Haagen-Smit and Fox, 1954; Haagen-Smit et al., 1953). The first major applications of monolith catalysts (Figure 1.1) during this period were for automotive emission control and for the decolourisation of nitric acid tail gas.

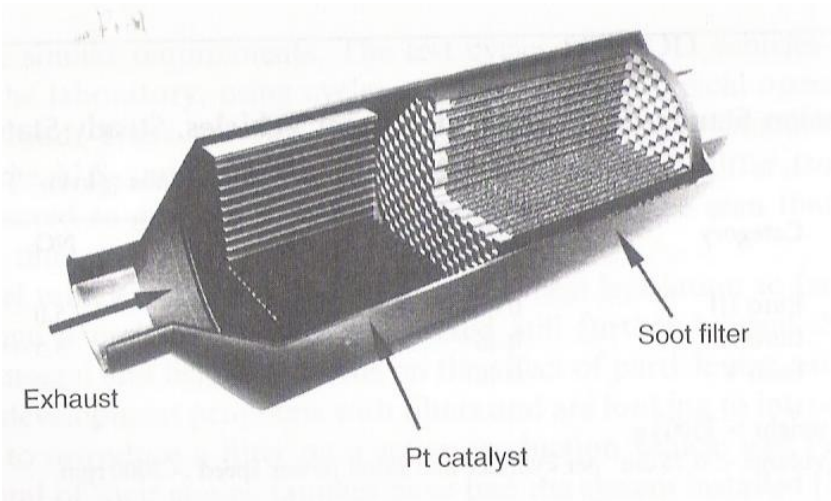

Figure 1.1. Schematic diagram of the motor vehicle catalyst used for emission control (Cybulski and Moulijn, 2006).

In the late 1960s researchers in the USA began to develop more interests in monoliths in their quest for effective afterburner catalysts because of their characteristic low pressure drop. This led to the development and industrial production of monolith catalysts of increased longevity which would meet the requirements of the 1970 Clean Air Act (Nievergeld, 1998; Cybulski and Moulijn, 1994). The emergence of the first cars equipped with monolith catalysts began in 1975. Today there are several hundred millions of monolith catalysts fitted in motor vehicles worldwide (Twigg, 2007).

Throughout the last three decades the advancements in emission control technology have been propelled by stringent legislation (Figure 1.2). One major success worth noting is that since 1975 emission levels from exhaust systems of passenger cars have fallen by more than 90% (relative to the 1960s), with future targets aimed at zero emissions (Twigg, 2006; Acres and Harrison, 2004).

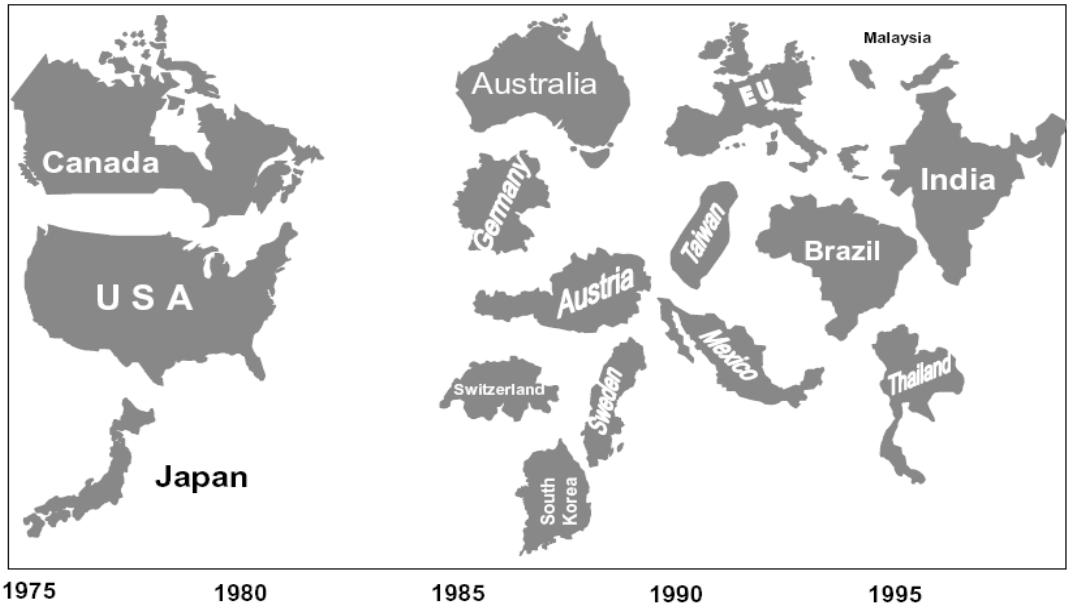

Figure 1.2. Introduction of emission control legislation across the world (Acres and Harrison, 2004).

From 1977 the USA government allowed states, such as California, where there were pressing air quality problems, to legislate lower emission limits than the rest of the USA. These emission limits decreased steadily in subsequent years, especially from 1993 onwards, as tighter legislations were introduced (Cybulski and Moulijn, 2006).

Europe originally lagged behind the USA with automotive catalyst fitting not required until 1993, and is now catching up according to the recent trends in legislation (Collins and Twigg, 2007). Today all countries in the world that legislate for emissions have adopted either the USA (i.e. Federal Test Procedure) or the European (i.e. Motor Vehicle Emissions Group) regulation test except for Japan, which has its own test. For instance, China and India use the European test, while South America uses the USA test (Cybulski and Moulijn, 2006).

The industrial sponsor of this project, Johnson Matthey (JM) Plc, is a global leader in the production of novel catalysts for emission control in both automotive and industrial applications. The Emission Control Technologies (ECT), a business division of JM that specialises in this area, has manufacturing sites in 4 continents: Europe (e.g. UK and Germany); Asia (e.g. China and India); America (e.g. USA and Mexico) and Africa (e.g. South Africa).

The fact that JM has supplied one-third of all automotive catalysts ever made highlights its unique role as a major player in the catalyst industry (Acres and Harrison, 2004). To this end, JM spent the sum of £ 87.6 million on research and development in 2008/2009 (Johnson Matthey Annual Report & Accounts, 2009).

Going by the progressive trend in the population of industrialised developing countries, notably China and India, there will be increased demand for transportation (both personal and goods) in the future (Onozaki, 2009). In parallel to this, the United Nations (UN) have consistently been pursuing the need for reducing global emissions (Pachauri et al., 2007). These factors, coupled with the stringent emission limits, will invariably increase the competition in the catalyst industry for the development of modern technologies to enhance automotive catalytic functions (Collins and Twigg, 2007; Onishi, 2007; Jobson, 2004).

1.2 POLLUTANTS AND AUTOMOTIVE COMBUSTION PROCESSES

The exhaust gas stream consists of 3 major pollutants: carbon monoxide (CO), oxides of nitrogen (NO) and hydrocarbons (HCs). This stream is converted inside the exhaust pipe, which houses the catalyst, into environmentally less harmful products as shown by these equations (Acres and Harrison, 2004):

$$2CO + O_2 \longrightarrow 2CO_2 \quad (1.1)$$

$$2CO + 2NO \longrightarrow 2CO_2 + N_2 \quad (1.2)$$

$$2HC + 5O_2 \longrightarrow 4CO_2 + 2H_2O \quad (1.3)$$

The monolith catalyst remains inactive until it is warmed up to a certain temperature. During this period carbonaceous matter is deposited on the active sites of the catalyst, causing a decrease in its activity. The deposit is quickly burned off by combustion processes after the right temperature for activity has been reached. The warm-up period lasts for a few minutes and depends on the thermal capacity of the catalyst. Up to 75 % of pollutants are emitted during this period. The lower the thermal capacity of the catalyst, the shorter the warm-up period, and this leads to an overall reduction in emissions (Cybulski and Moulijn, 2006).

1.3 CATALYST MANUFACTURE FROM MONOLITHS

Monolith catalysts are manufactured in industry by coating γ–alumina slurries – the carrier of the platinum group metals (PGMs) – onto structured catalyst supports. These catalysts are essentially used in environmental applications but also in chemical and construction processes (Williams, 2001). They can be metal-based or ceramic-based depending on the type of monoliths they are made from (Figure 1.3).

Monoliths are honeycomb materials that act as catalyst supports (i.e. substrates) upon which coating slurries are deposited. They have channels which are straight and parallel. They are of two types: metallic monoliths, made from Fecralloy®; and ceramic monoliths, mostly made from cordierite (Avila et al., 2005).

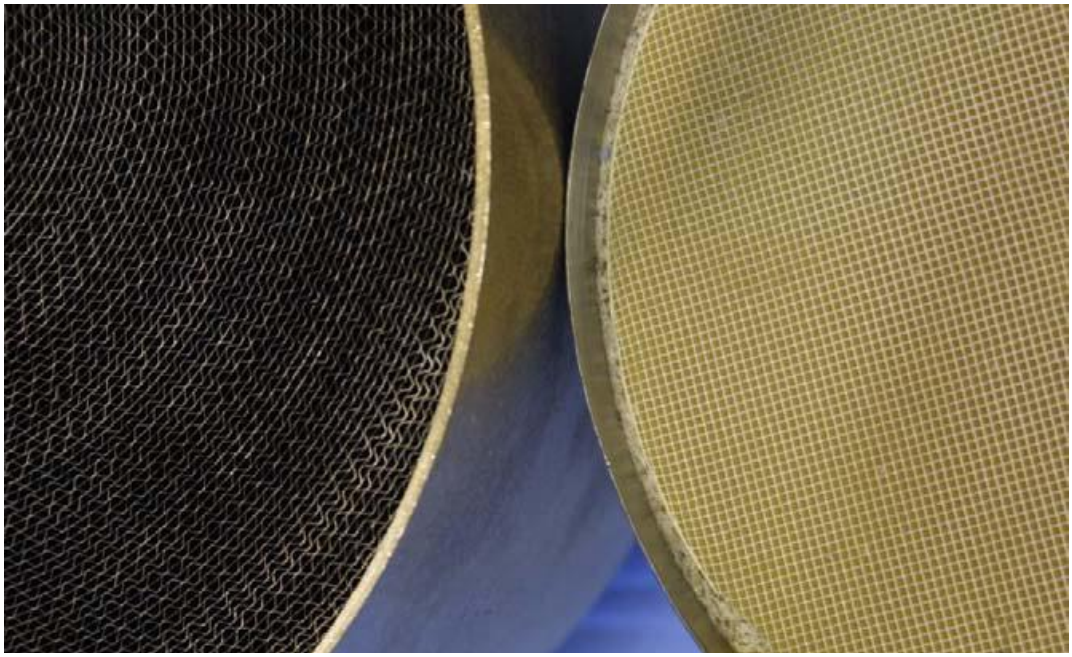

Figure 1.3. Examples of metal-based catalyst (left) and ceramic-based cordierite catalyst (right) (Twigg, 2006).

Due to their high geometric surface area, low-pressure drop, thinner walls and ease of production when compared to conventional fixed bed and slurry reactors, monoliths have also been developed as novel catalytic reactors in heterogeneous liquid phase and multiphase gas-liquid systems (Edvinsson et al., 1995).

Both metal-based and ceramic-based monolith catalysts have their advantages and disadvantages, and the preferred choice depends on the end application (Cybulski and Moulijn, 2006; Avila et al., 2005). Monolith catalysts with thin walls have low thermal capacity, which make them advantageous at reducing warm-up period (Bruck, 2002). Metal monoliths have significantly thinner walls compared to ceramic monoliths, and this enables the former to have a much shortened warm-up period which leads to increased catalytic efficiency (Sun et al., 2007; Fei et al., 2003).

On the other hand, ceramic monoliths are relatively cheap and have large pores which absorb the slurry, and this improves the coating adherence. The thermal expansion of the coating is also similar to ceramic monoliths compared to metal (Williams, 2001). These problems can however be tackled by proper slurry formulation, and the use of metal monoliths which are based on an appropriate alloy, such as Fecralloy®, that is specially processed to form an adherent and stable alumina surface layer (Jia et al., 2007; Cybulski and Moulijn, 2006; Burgos et al., 2003). Fecralloy® is therefore chosen in this study as the catalyst support onto which the coating slurry is deposited.

1.4 DESIGN OF METAL MONOLITHS FROM FECRALLOY®

Fecralloy® represents the metal strip from which most metal monoliths are made. Metal monoliths can be formed into different design structures, the most common of which is based on rolling alternate corrugated and flat strips of metal foil (Figure 1.4). This is achieved by crimping a metal strip on a pair of rollers having teeth of a pre-specified profile, often sinusoidal or triangular, and combining the crimped sheet with a flat sheet of similar width to avoid intermeshing. Multiple parallel channels are generated in-between the corrugated strip as both sheets are rolled around a spindle until a desired diameter is reached (Cybulski and Moulijn, 2006; Avila et al., 2005).

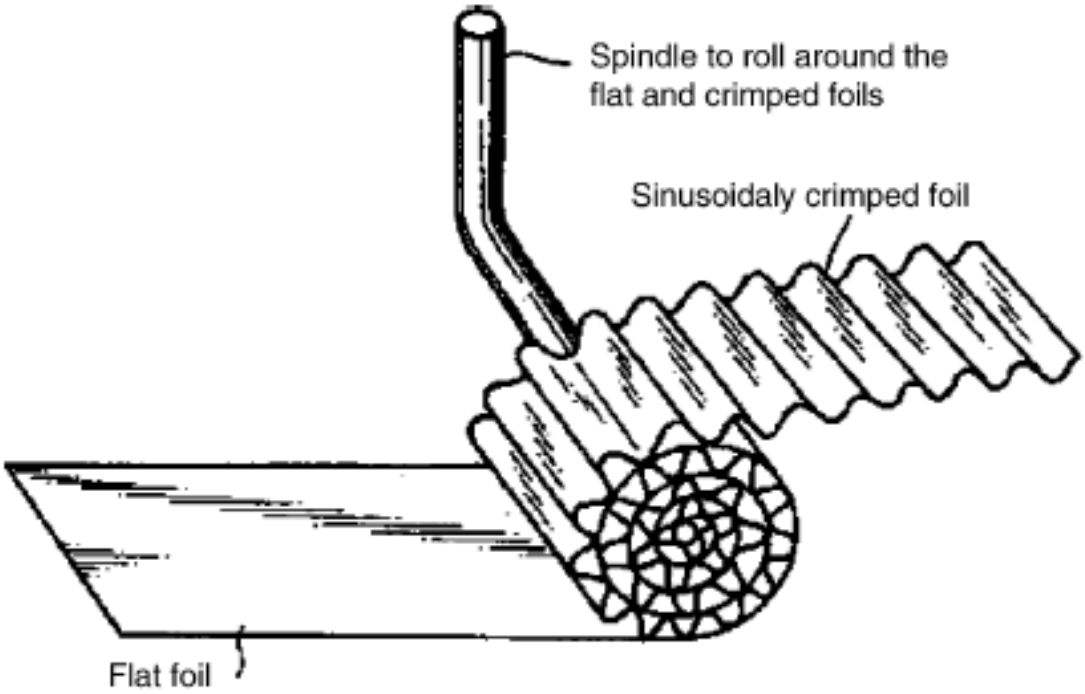

Figure 1.4. Fabrication of metal monoliths by rolling around a spindle alternate flat and crimped foils (Sakurai et al., 1998).

This is followed by fabrication, i.e., the welding of the outermost strip to the one underneath. To achieve variation in the number of cells per unit area, the pitch and width of the profile on the crimping rolls are carefully altered. The thinnest metal strip possible is mostly used for making metal monolith catalysts, and this is backed by key scientific principles, such as (Cybulski and Moulijn, 2006):

(a) **Weight**: For a fixed density of channels per unit cross-sectional area, the weight of a unit is directly proportional to the thickness of a metal strip. Therefore, a lightweight strip of fixed density will have a small thickness.

(b) **Pressure drop**: A thin metal strip will increase the open area, and give a lower pressure drop. A low pressure drop is advantageous for combustion reactions in an automotive exhaust system

(c) **Catalyst performance**: The ability of a catalyst to **"**light-off**"** is a way of determining catalyst performance. Light-off is the temperature that governs conversion efficiency. It is the temperature at the catalyst surface and not the temperature of the inlet gas. The possibility of substantial heat drain from the surface into the monolith catalyst may inhibit light-off.

The variants of the flat and crimped strip concept have been developed over the years with a view to improving the monolith catalyst efficiency to meet stringent emission legislation. Illustrated in Figure 1.5 are three of these variant structures – **"**SM**"**, **"**LS**"** and **"**TS**"** – which have been reported (Bruck et al., 1995; Held et al., 1994). The SM and LS structures provide the possibility of the whole of the catalytic surface being used, even if flow distribution at the catalyst front face is not uniform, because their designs allow flow between the channels. In the TS structure however, flow is restricted within a specified channel, but micro-corrugation at 90^{o} to the flow direction cause turbulence and thereby reduce the thickness of the stagnant layer through which reactants have to diffuse.

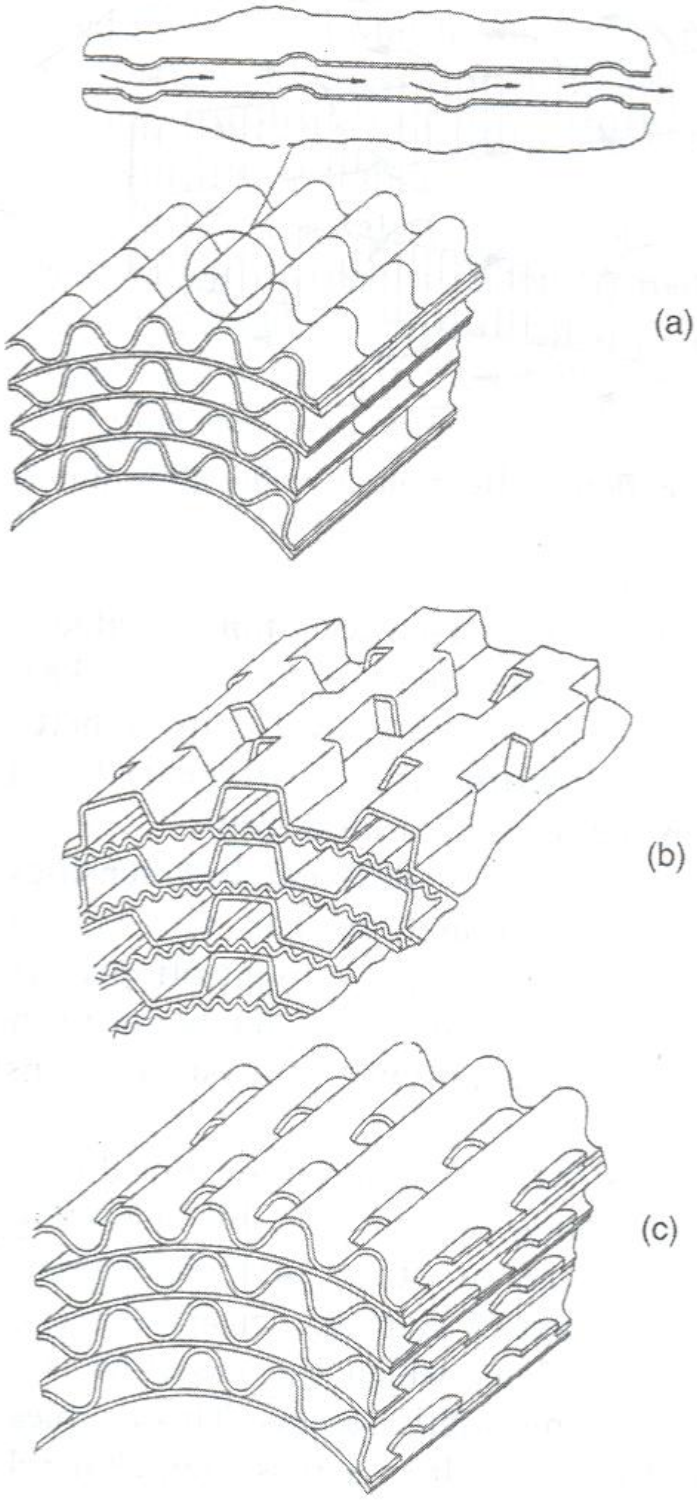

Figure 1.5. Structural features of metal monoliths designed to enhance turbulence: (a) TS structure in which corrugated layers have microcorrugation at 90^{o} to the flow direction; (b) SM structure in which channel flow is split into multiple flow paths and (c) LS structure in which interconnecting flow paths are achieved with partial countercorrugation of the corrugated layer (Drawings: courtesy of Emitec).

1.5 PREPARATION PATH FOR COATINGS

The preparation path for coatings showing the process units and key parameters is given in Figure 1.6.

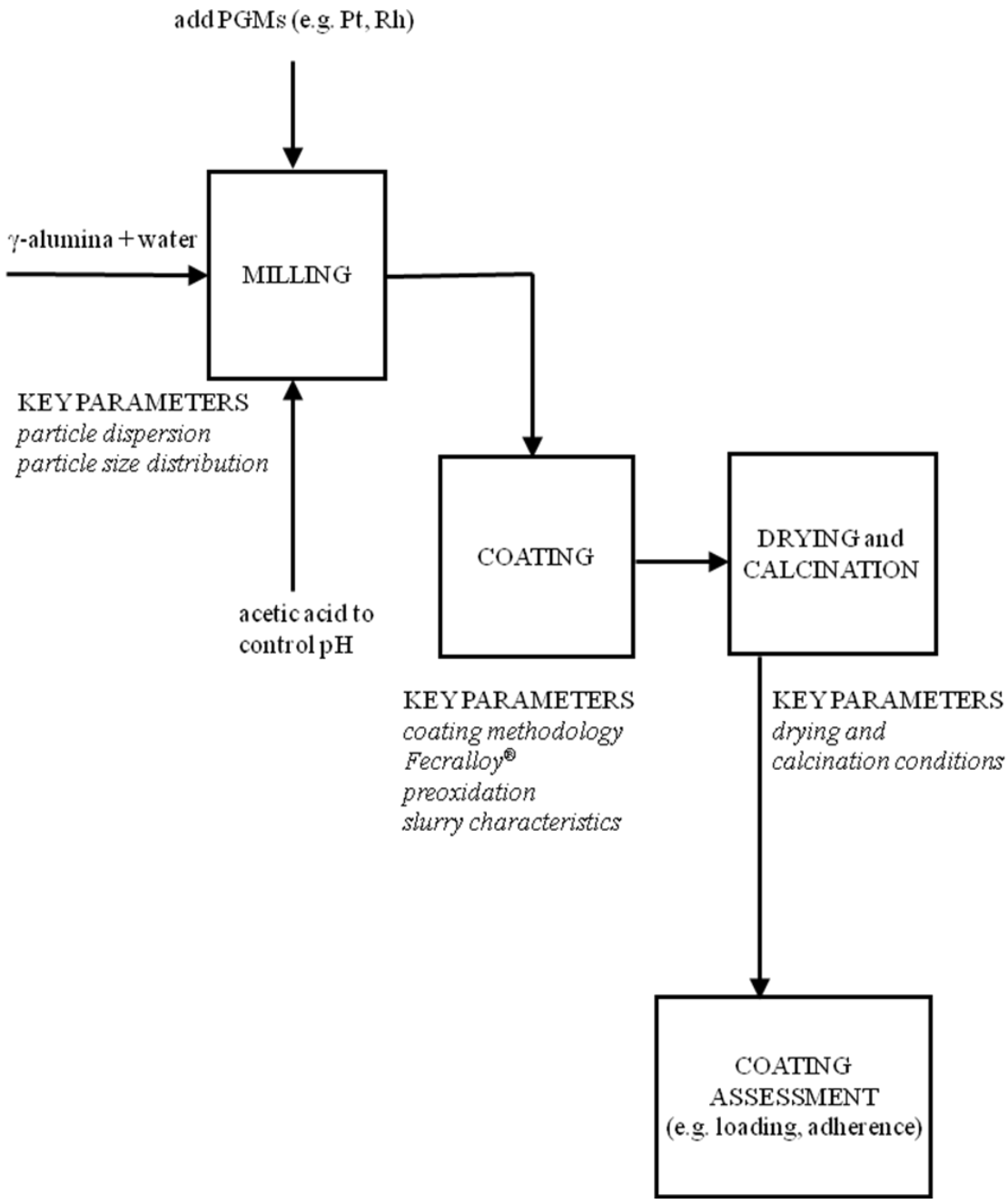

Figure 1.6. Preparation path for coatings (Avila et al., 2005; Nijhuis et al., 2001).

The coating slurry is an aqueous suspension which consists of the following components: PGMs (e.g. Pt, Pd, Rh), γ-alumina particles and a dispersant. The dispersant can be in the form of an acid (e.g. acetic acid). Due to the high cost of the PGMs, most of the previous studies on the preparation of coatings have been based on slurries containing γ–alumina particles without the PGMs (e.g. Jia et al., 2007; Xu and Koelling, 2005; Agrafiotis and Tsetsekou, 2000). The slurry is milled and then deposited onto the monolith by a coating method to generate a substrate/washcoat composite, which is subsequently dried and calcined leading to a well adhered coating (Jia et al., 2007).

A description of the process units carried out, and the current knowledge gaps are presented below:

(a) **Milling**: The coating slurry containing γ–alumina is adjusted to a suitable pH which produces the best particle dispersion, and is then comminuted in a mill until the required particle size distribution (psd) is achieved. The types of mill that have been used for this purpose include the stirred bead mill (e.g. Fadhel and Frances, 2001), ball mill (e.g. Yang and Sigmund, 2003) and the jet mill (e.g. Omura et al., 2005). As shown in Figure 1.6, the γ–alumina particles must be adequately dispersed in the slurry by pH control to prevent aggregation inside the mill tank. The pH at which the particles are well dispersed was found to be 3.8 – 4.5 (Agrafiotis and Tsetsekou, 2000). Of the various mill types mentioned, it is only the stirred bead mill that had been studied in detail in terms of the mechanism of particle fragmentation, which is governed by basic

communition concepts (Kwade, 2004; Kwade, 2003; Kwade and Schwedes, 2002; Becker et al., 2001; Fadhel and Frances, 2001). However, the effects of slurry characteristics (e.g. solids concentration) and the grinding media diameter on the psds of ground γ–alumina particles have not been properly investigated. The understanding of what influences the psds of ground γ–alumina particles is useful for the preparation of slurries of the desired specifications (Kwade, 1999; Kwade et al., 1996).

(b) **Coating**: There are two industrial methods of coating slurry onto Fecralloy® substrates. The first method involves coating the Fecralloy® already formed into a monolith by pouring the slurry through or by sucking the slurry into the monolith channels. The second method involves coating the Fecralloy® before the monolith is constructed by dipping in the slurry (dip-coating), painting or spraying (Benkreira, 2007; Cybulski and Moulijn, 2006).

A literature survey has shown that the main method of coating Fecralloy® in the laboratory is by dip-coating (Jia et al., 2007; Zhao et al., 2003; Fei et al., 2003; Valentini et al., 2001), though other methods have been used, such as electrophoretic deposition (Sun et al., 2007), chemical vapour deposition (Janickle et al., 2000), physical vapour deposition which can be cathodic sputtering, electron-beam evaporation or pulsed laser deposition (Kestenbaum et al., 2002). Each of these coating methods has its advantages and disadvantages, and the method to be chosen in a given application depends on the required coating properties (Meille, 2006). The common disadvantage of dip-coating is the inconsistency in the coating quality as evidenced from the wide

variation in the coating loadings (Jia et al., 2007). There is therefore a need to develop a more consistent laboratory-scale method of coating Fecralloy® to produce the desired coating properties. In this thesis, an automatic film applicator equipped with wire-wound bars is chosen as the coating instrument because it had been designed to ensure consistency and reproducibility of coatings (Sheen Instruments Manual, 2006).

Apart from the coating method, the preoxidation conditions of Fecralloy® prior to coating have been shown to be crucial to producing well adhered coatings (Jia et al., 2007; Zhou et al., 2007; Cybulski and Moulijn, 2006; Avila et al., 2005). Fecralloy® preoxidation involves thermal treatment under oxidising conditions at temperatures in the range of 900 – 1200 ^{o}C for 5 – 30 h (Jia et al., 2007; Pragnell et al., 2005; Fei et al., 2003). The assessment of Fecralloy® surface microstructure produced by preoxidation have been based on scanning electron microscopy (SEM) and X-ray diffraction (XRD) (Shen et al. 2006; Badini and Laurella, 2001), without any consideration of the surface roughness and topography profile.

The slurry characteristics (i.e. pH, rheology, solids concentration and psds) have been shown to be influential to the coatings deposited onto Fecralloy®. The pioneering study in this area was by Jia et al. (2007) and they concluded that the optimal coating properties in terms of loading and adherence could be achieved by using a slurry at pH of 4 – 6, solids concentration up to 35 wt% and particle diameter $d_{0.9}$ of less than 10 μm. Considering the importance of monolith catalysts, there are currently several knowledge gaps which need to be filled, such as investigating the coating properties at a wider pH margin and how coating properties are influenced by mixing slurries of different psds.

(c) **Drying and calcination**: The coatings are dried at a temperature above 100 ^{o}C for 1 – 2 h and calcined at 350 – 700 ^{o}C for 1 – 3 h to prevent cracks and ensure good coating adherence (Cybulski and Moulijn, 2006). The presence of extensive cracks is detrimental to the coating integrity because the coatings would have low mechanical resistance, leading to peeling off under rigorous conditions (Zhou et al., 2007). The drying and calcination conditions reported in the literature have been narrowed to temperatures and durations only, and there has not been clarity in terms of the profiles used, and how this influences coating properties (e.g. Jia et al., 2007; Zhou et al., 2007; Fei et al., 2003; Zhao et al., 2003; Badini and Laurella, 2001).

(d) **Coating assessment**

(i) *Coating loading*: The amount of the coating on the Fecralloy® is referred to as the coating loading. The revised physical adsorption (RPA) model in Equation (1.4) was proposed (Spieker and Regalbuto, 2001; Agashe and Regalbuto, 1997) and further simplified (Hao et al., 2003). It shows that the concentration of the γ–alumina particles is proportional to the adsorption of the PGMs [based on $(PtCl_6)^{2-}$] used for catalytic functions. It is therefore paramount to have sufficient γ–alumina loading on the Fecralloy® surface, while not comprising on the coating adherence (Cybulski and Moulijn, 2006).

$$C_{adsorbed} = \frac{m_{al} S_{al}}{V_L} \Gamma_{\max} \left(\frac{KC}{1 + KC} \right) \qquad (1.4)$$

where

$C_{adsorbed}$ = concentration of active species adsorbed for catalytic functions

Γ_{max} = maximum adsorption density (mol m^{-2})

K = adsorption equilibrium constant

C = concentration of the active species remaining at equilibrium (mol m^{-3})

m_{al} = mass of γ–alumina (kg)

S_{al} = surface area of γ–alumina (m^2 kg^{-1})

V_L = liquid volume (m^3)

The conventional technique for determining the coating loading is by the measuring the mass increase of the Fecralloy® caused by the dried and calcined coatings (Zhou et al., 2007).

(ii) *Coating adherence*: Well adhered coatings are firmly attached onto the Fecralloy® and they will not fall off easily when subjected to operational stresses in the exhaust system (Cybulski and Moulijn, 2006). The assessment of coating adherence has mainly been based on the mass loss from ultrasonic vibration (Zhao et al., 2003; Valentini et al., 2001). This test involves the soaking of coatings in petroleum ether, and then treating them in an ultrasonic vibrator for 5 – 60 min. The petroleum ether, being a non-polar solvent which contains mostly pentane, acts by weakening the attractive bonds in the coatings (Housecroft and Constable, 2002). The treated sample is dried afterwards and the mass loss is evaluated.

Thermal shock had been used by Zhao et al. (2003) and Jia et al. (2007) for assessing coating adherence. Germani et al. (2007) and Roth et al. (1987) have used drop test and

a scratch tester respectively. There is urgent need to devise new methods for measuring the coating adherence because none of the conventional methods is physically derived.

(iii) *Coating thickness and homogeneity*: It is somewhat difficult to define a typical thickness of the coating layer as this certainly differs from one catalyst manufacturer to another, depending on the coating methods used, and the application of the finished catalyst. However, the coating is usually as thick as the metal substrate, i.e. 40 – 50 μm (Cybulski and Moulijn, 2006).

The coating thickness and homogeneity have usually been assessed by SEM, through which images of the side and surface of the coatings are provided (Jia et al., 2007; Zhou et al., 2007; Giani et al., 2006; Wu et al., 2005; Fei et al., 2003). Fei et al (2003) have, in addition, used a focussed ion beam (FIB) technique for assessing the coating thickness. Meille (2005) and Roth et al. (1987) have assessed coating thickness using a micrometer and a profilometer respectively.

The technique for assessing coating thickness and homogeneity should have a high degree of accuracy and resolution, and SEM clearly outperformed other techniques in these areas judging by its predominant use.

1.6 THE NEED FOR RESEARCH

The number of the previous studies aimed at determining how the coating properties are influenced by the slurry characteristics and the coating process is not commensurate with the wide range of applications of monolith catalysts. In addition there is hardly one of these studies which was thorough and capable of closing the knowledge gaps existing in the process units outlined in section 1.5.

It is extremely important to produce well adhered, homogeneous and reproducible coatings for long-lasting productivity and to achieve this, all the process units as well as the key parameters need to be properly studied. The knowledge of how particles are adequately dispersed and how to obtain optimal substrate microstructure upon which to coat is invaluable for obtaining the desired coating properties.

At present there is no well-documented approach of assessing substrate surface topography as well as how the parameters of the coating process affect the coating properties. The underlying factors which govern coating loading and adherence are not clear-cut.

The influence of the particle size distributions (especially those obtained from slurry mixtures) on coating properties have not been extensively studied. Furthermore, the conventional techniques of measuring coating adherence are crude, and there is therefore a need to devise new techniques which are not only quantitative but also physically derived.

This study is intended to make contributions in bridging the knowledge gaps adumbrated in the last 2 paragraphs, and thereby contributing to the effort of reducing emissions. The understanding of what needs to be done to achieve the desired coating properties is also crucial in minimising the inherent lag between the **"**number of studies**"** and the **"**value of monolith catalysts**"**.

1.7 AIMS OF RESEARCH

This project involves the optimisation of the coating of catalyst supports (based on Fecralloy®) used in motor vehicles for emission control. At the heart of achieving this is obtaining a scientific understanding of the coating of Fecralloy® by determination of the relationship between the slurry properties and the coating process to the final coating quality.

The project aims are the following:

a) to derive an optimal Fecralloy® surface microstructure for coating;
b) the development of protocols for a model coating process using wire wound bars under controlled conditions using an automatic film applicator;
c) to determine the effects of slurry properties (pH, solids loading, particle size distributions, rheology) upon coating homogeneity and adherence onto Fecralloy® substrates and
d) to develop a scientific approach to quantify the adherence of the applied coating.

1.8 STRUCTURE OF THESIS

The thesis consists of 8 Chapters. The roles of monolith catalysts in emission control applications, the preparation path for coatings as well as the aims of research have been outlined in Chapter 1.

Chapter 2 provides the necessary background information on the literature of slurry coating on Fecralloy®. The items discussed include the scope, findings and limitations of previous studies.

Chapter 3 describes the various stages of slurry preparation which consist of particle stabilisation and the fragmentation behaviour in the bead mill. The analysis in this Chapter relates the particle comminution in the mill to the number of stress events (SN), stress energy (SE) and the specific energy ($E_{m,p}$). The various strategies for achieving the aims of this research are also presented.

Chapter 4 investigates slurry rheology, which controls the flow behaviour, by focussing on the shear flow and the parametric characterisation. The parameters studied are pH, solids concentration, particle size distribution and temperature.

The influence of preoxidation of Fecralloy® efficacy as a catalyst support is considered in Chapter 5. In this pioneering study, a laser profiling interferometer was used for measuring Fecralloy® surface roughness. The coating was applied onto Fecralloy® using an automatic film applicator designed for this purpose. Some aspects of this study

were published in the conference proceedings of the 8th World Congress of Chemical Engineering (2009) as outlined below:

Adegbite, S. A., Barigou, M., Simmons, M. J. H., Wagland, A. and Stitt, E. H., 2009, Influence of preoxidation on Fecralloy® efficacy as a catalyst support, 8th World Congress of Chemical Engineering, Montréal, Canada, 1-6.

Chapter 6 explains the derivation of an optimal coating methodology using an automatic film applicator, and the effects of the slurry characteristics (i.e. pH, solids concentration) on the coating properties.

The use of an electromechanical testing system for measuring the adherence of coatings of various particle size distributions is described in Chapter 7. This technique of assessing coatings relies on fundamental scientific principles.

In Chapter 8 all the results are summarised and concluding remarks are presented.

The main findings of this research have been presented at the JM annual conferences held at Nottingham (2007 & 2008) and Loughborough (2009).

2

LITERATURE REVIEW

This chapter begins with a detailed description of the critical factors in the preparation path which can influence the coating quality as well as the various tests for assessing the coating quality. The main agenda of this chapter is provided in the background literature review of slurry coating on Fecralloy® with reference to these critical factors. This review considers the scope, findings and limitations of the previous studies. The knowledge gained is useful in the design of experiments which are discussed in subsequent chapters.

2.1 INTRODUCTION

The quality of a slurry coating is determined by all its performance-determining properties, such as loading, adherence, thickness and homogeneity. A coating of sufficient loading and thickness will have more than enough active sites of the PGMs for catalytic performance (Spieker and Regalbuto, 2001; Agashe and Regalbuto, 1997).

However, excessive coating loading and thickness due to an ineffectual coating technique may result in heterogeneity of the applied coating, and can also impinge on the coating adherence (Cybulski and Moulijn, 2006). In addition to this, when the rheology and the particle size distributions (psds) of the coating slurry are not properly optimised, the end result can be poor coating adherence, which results in the untimely loss of PGMs and catalytic inefficiency (Agrafiotis et al., 2000).

A detailed preparation path for coatings (Figure 2.1) shows the critical factors at each process unit which can influence the coating quality. These factors can be measured and controlled by various techniques which are discussed in this Chapter. A series of tests have been developed for assessing the coating properties, but there is a need to devise new techniques especially for coating adherence, as current tests have not been developed on a scientific basis, and only produce relative data.

This Chapter describes previous work (their scope, findings and limitations) on how the critical factors influence the coating properties, and opens up the knowledge gaps

existing at present. This is followed by a review of conventional techniques for assessing coating properties.

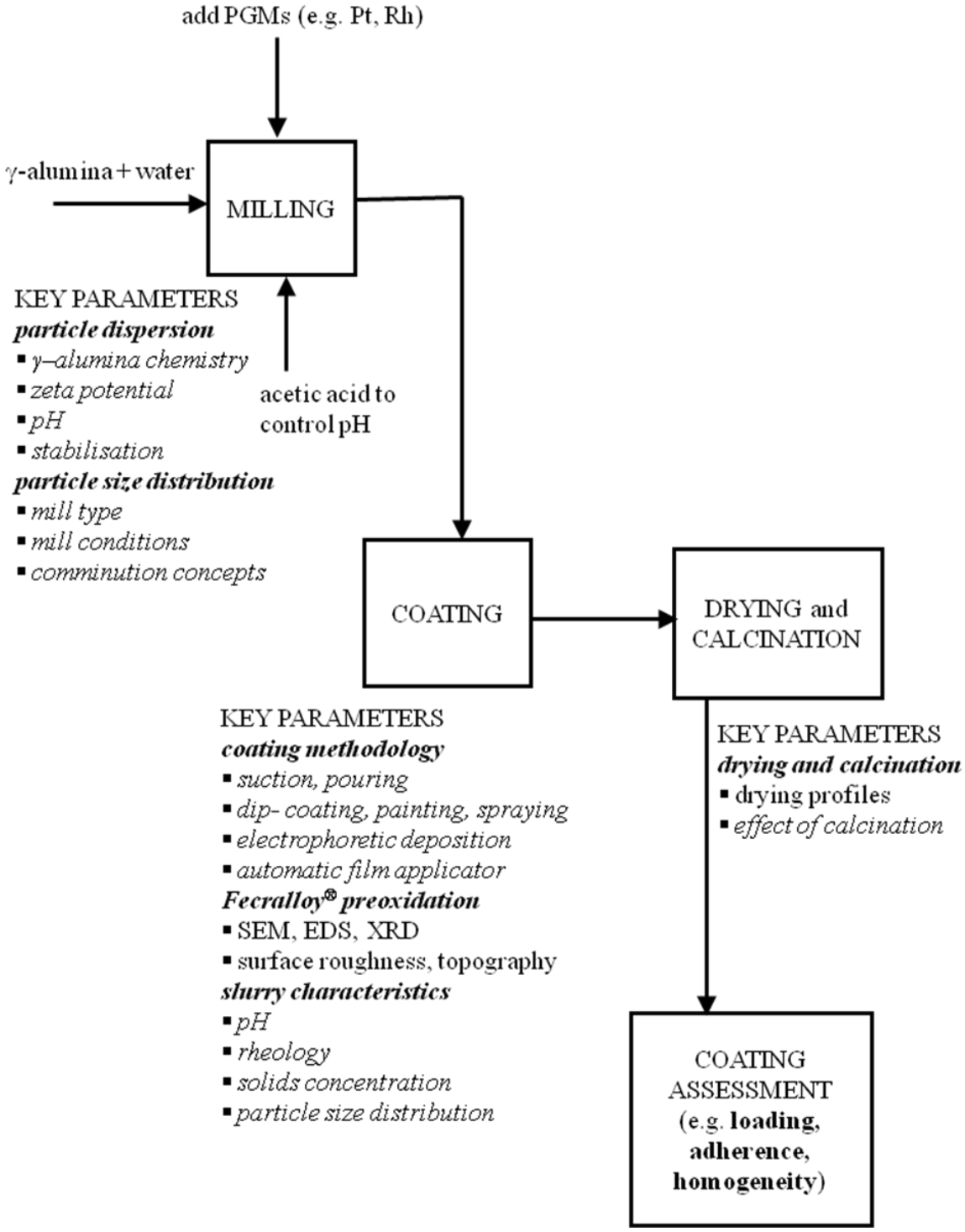

Figure 2.1. A detailed preparation path for coatings (Avila et al., 2005; Nijhuis et al., 2001; Valentini et al., 2001; Schwarz et al., 1995).

2.2 FACTORS WHICH INFLUENCE COATING QUALITY

According to Figure 2.1, the critical factors which can influence coating quality are the following: (a) particle dispersion; (b) particle size distribution; (c) coating methodology, (d) Fecralloy® preoxidation; (e) coating assessment; (f) slurry characteristics and (g) drying and calcination.

2.2.1 Particle dispersion

The γ–alumina particles should be properly dispersed in the slurry before milling, and this is enabled by its unique chemistry (i.e. structure and properties).

(a) *Structure*: The γ–alumina structure has been studied over the last few decades by techniques, such as IR spectroscopy (Morterra and Magnacca, 1996), NMR spectroscopy (Pecharroman et al., 1999) and recently by prompt-gamma activation analysis (PGAA) (Paglia et al., 2004a; Paglia et al., 2004b). The structure of γ–alumina (Figure 2.2) is traditionally considered as a cubic defect spinel type (Lippens and Steggerda, 1970; Wyckoff, 1968). The defective nature is obtained from the presence of only trivalent Al cations in the spinel-like structure. The oxygen lattice is built up by a cubic close-packed stacking of oxygen layers and the Al atoms occupy the octahedral and tetrahedral sites (Trueba and Trasatti, 2005).

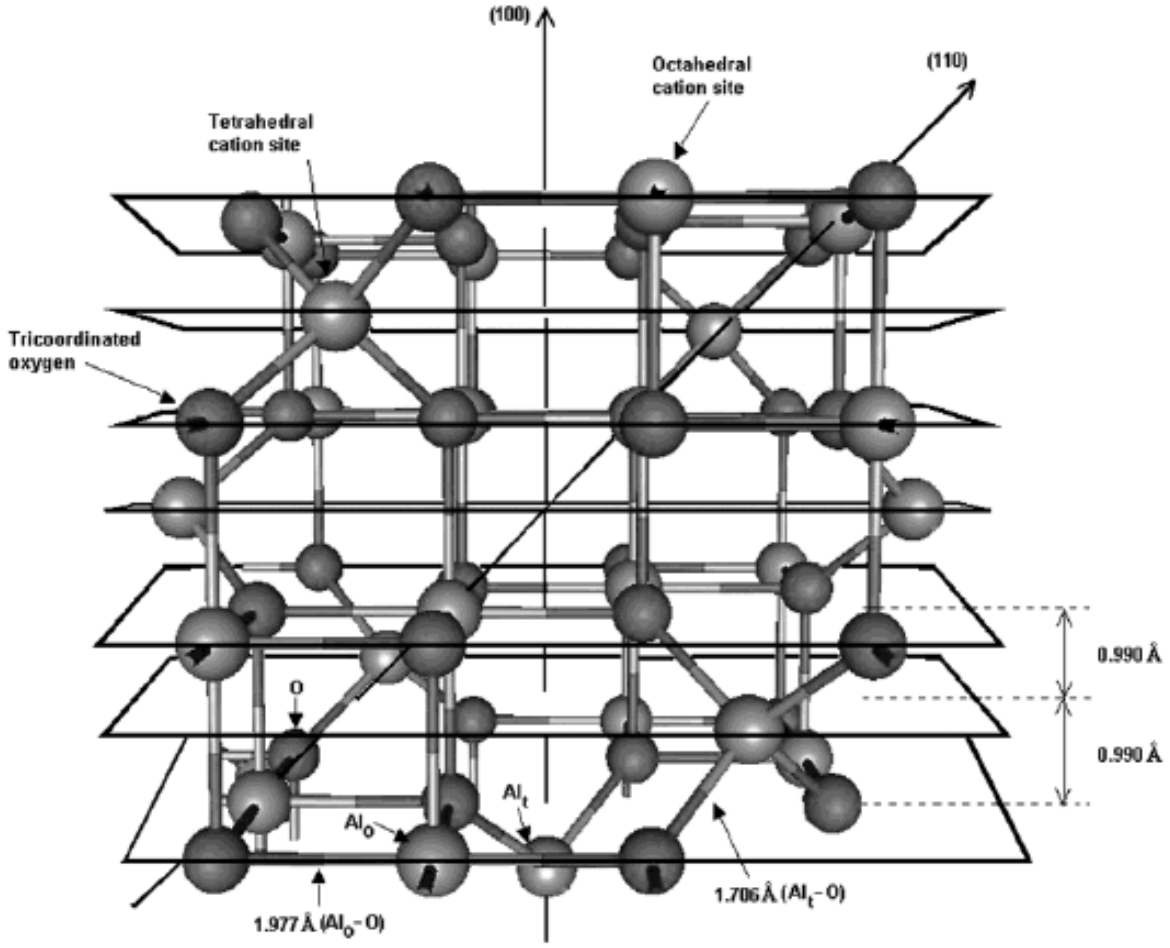

Figure 2.2. γ–Alumina spinel-type unit cell (Ionescu et al., 2002).

(b) *Physical properties*: Of the various forms of alumina known, γ–alumina has an enviable record of having a wide area of applications as a catalyst support material in the automotive and petroleum industries (Wefers, 1990). This is because of its rich blend of properties: high surface area, high porosity and high hydrothermal stability (Morterra and Magnacca, 1996). At room temperature γ–alumina exists as an odourless white powder having a bulk density of 800 kg m^{-3}. When coarse particles of boehmite are thermally dehydrated at a temperature above 400 – 450 ^{o}C, the surface area and pore volume of the γ–alumina particles produced are usually less than 250 m^2 g^{-1} and 0.50 cm^3 g^{-1} respectively (Trueba and Trasatti, 2005). To improve its textural properties,

several methods of alumina synthesis that use traditional techniques of preparative chemistry have been developed, such as precipitation and hydrolysis (Macedo et al., 2004; Deng et al., 2002; Gonzalez-Pena et al., 2001; Tikhov et al., 1999).

(c) *Acid-base properties*: γ–Alumina particles, like most solid oxides, develop pH-dependent surface charges when present in an aqueous solution, as illustrated by the general equilibria given by (Brown et al., 1999; Schwarz et al., 1995; Brunelle, 1978):

$$\equiv S - OH_2^+ \Leftrightarrow \equiv S_{basic} - OH \ + H^+ \qquad (2.1)$$

$$\equiv S_{acid} - OH \ + \ OH^- \Leftrightarrow \equiv S - O^- + H_2O \qquad (2.2)$$

where $\equiv S_{acid} - OH$ and $\equiv S_{basic} - OH$ represent hydrated sites at γ–alumina surface with acidic and basic characters respectively.

The ability of γ–alumina to adsorp cations (e.g. silica-alumina) or anions (e.g. magnesia) or both cations and anions (e.g. zirconia) in an aqueous solution depending on the concentrations of the available acid and basic sites is the reason why γ–alumina is referred to as amphoteric – a characteristic behaviour that is central to its use as a catalyst support material. When present in an aqueous solution, the acid and basic sites behave exactly as acid and basic substances. They therefore respond reversibly to pH change with concurrent variation of the total surface charge, with H^+ and OH^- ions usually designated as potential determining ions in the absence of specific adsorption (Trueba and Trasatti, 2005). The net surface charge of γ–alumina, σ_{al} , measured in C cm^{-2}, is defined according to (Koopal, 1996; Daghetti et al., 1983):

$$\sigma_{al} = F\left(\Gamma_{H^+} - \Gamma_{OH^-}\right) \qquad (2.3)$$

where

Γ_{H^+} and Γ_{OH^-} (both measured in mol cm^{-2}) are the surface concentrations of positively and negatively charged groups respectively; F is the Faraday constant (96,484 C mol^{-1}).

The point of zero charge pzc is the pH at which σ_{al} = 0, (i.e. where $\Gamma_{H^+} = \Gamma_{OH^-}$). The pzc is usually determined by potentiometric titration as this can be directly translated into proton-adsorption isotherms (La Parola et al., 2003; Bandosz et al., 1998).

Another important parameter which characterises γ–alumina/solution interfaces is the isoelectric point, iep – the pH at which the zeta potential (ζ) of particles is zero. The zeta potential is related only to the presence of free charges in the diffuse layer in solution and can be determined by electrokinetic experiments, such as electroacoustics (Greenwood and Kendall, 2000) and electrophoresis (Brunelle, 1978).

The measurement of zeta potential by an Acoustosizer is based on electroacoustics (first reported by Debye, 1933). This is the application of alternating electric field which generates a sound wave through the slurry. The zeta potential is determined from the magnitude and phase of the sound wave. This technique allows for the simultaneous measurement of both the zeta potential as well as the electrokinetic sonic amplitude (ESA) diameter of γ–alumina particles as a function of pH (Greenwood, 2003; Hunter, 1998).

Alternatively, the zeta potential can be determined by a Zetamaster which is based on electrophoresis, first discovered by Reuss in 1808 (Voyutsky, 1978). This is the application of electric field through the slurry leading to the motion of charged particles. The particles with a positive charge go to the cathode and the negatively charged to the anode (Housecroft and Constable, 2002; Shaw, 1992).

The iep and the pH at with the γ–alumina particles are adequately dispersed (i.e. $\zeta > |30|$ mV) have been found in the literature to be 7.7 – 7.9 and 3.8 – 4.5 respectively (Agrafiotis and Tsetsekou, 2000; Davies and Binner, 2000; Nowack et al., 1996; Tijburg et al., 1991). To improve the milling throughput, there should be adequate dispersion of the γ–alumina particles at the maximum solids concentration possible (Anklekar et al., 1998). For γ-alumina particles dispersed in these kinds of slurries – where the pH is adjusted by acidic or alkaline solutions – the dispersion mechanism is electrostatic. This is because stabilisation hinges on the dominant effect of the electrostatic repulsion of particles (Anklekar et al., 1998; Shaw, 1992). A schematic representation of the electrostatic dispersion mechanism is given in Figure. 2.3.

The interplay between the electrostatic and van der Waals forces in Figure 2.3 resulting in the total interaction energy curves is a demonstration of an electrostatic stabilisation. The total interaction energy V(1) is obtained by the summation of an attractive van der Waals curve V_A and the electrostatic repulsion curve $V_R(1)$, and likewise V(2) is obtained from V_A and $V_R(2)$. The slurry at $V_R(1)$ will experience more stabilisation (i.e. have pH further away from the iep) than the slurry of $V_R(2)$ because $V_R(1) > V_R(2)$ (Shaw, 1992). At a certain distance the attractive van der Waals forces begin to have

greater effect, making it easier for particle aggregation. This is applicable to very highly concentrated slurries (Hill and Carrington, 2006).

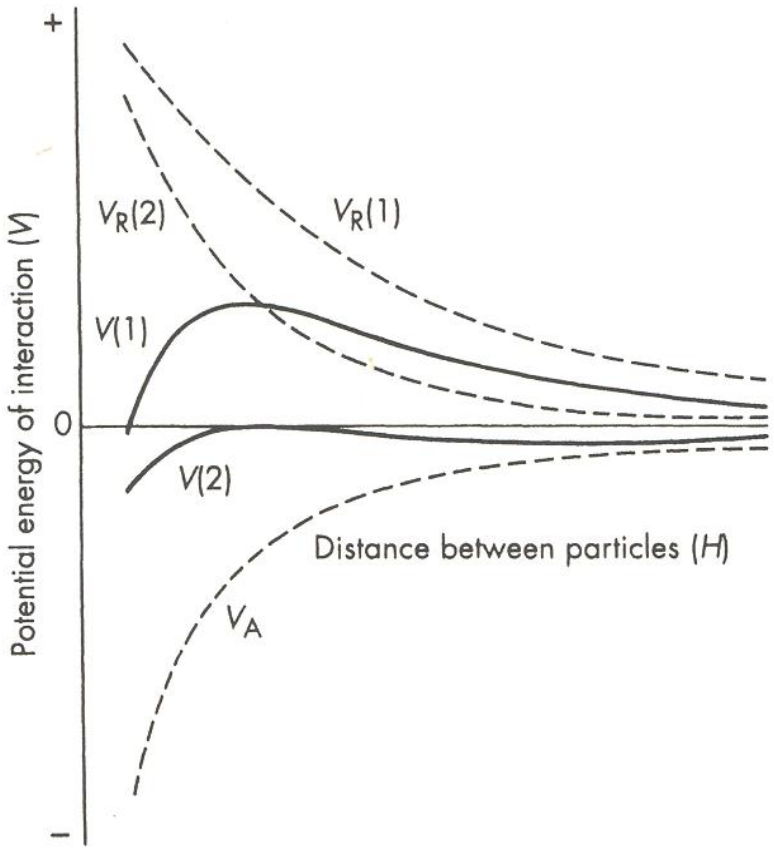

Figure 2.3. Electrostatic dispersion mechanism of γ–alumina particles in a slurry dispersed with acid or alkaline solution (Shaw, 1992).

2.2.2 Particle size distribution

Some studies (e.g. Germani et al., 2007; Jia et al., 2007) have found that the finer particles produced by the milling of γ–alumina particles have good coating adherence. Therefore, the milling process should be targeted at producing γ–alumina particles of the desired particle size distributions (psds). The milling of γ–alumina slurries to obtain

these distributions have been done using different mill types: stirred bead mill (e.g. Fadhel and Frances, 2001), ball mill (e.g. Yang and Sigmund, 2003) and the jet mill (e.g. Omura et al., 2005). The particles are mixed and fragmented by the mechanical agitation produced inside these mills by the moving shafts and the grinding media. Stirred bead mills are increasingly used in many applications (e.g. pharmaceuticals, coatings, paints) for microgrinding, dispersion and disintegration of particles in the liquid phase (Fadhel and Frances, 2001). Due to their increasing demand for producing fine and ultra-fine particles making them advantageous compared to other mills, stirred bead mills have been the subject of a growing number of scientific studies (Kwade, 1999).

2.2.2.1 Basic comminution concepts

The γ–alumina fragmentation inside a stirred bead mill can only be properly described in the context of basic comminution concepts. The comminution process in a stirred bead mill is determined by two factors (Kwade and Schwedes, 2002; Kwade, 1999):

(a) how often each feed particle (and fragments arising from the feed particle) is stressed and

(b) how high is the stress energy (or intensity) at each stress event

In reality the feed particles and the resulting fragments are not stressed at equal intervals with the same stress energy, but generally at unequal intervals with different stress energies because the movement of the grinding media and particles are statistical.

Therefore, only frequency distributions can suitably describe the number of stress events and the stress energy. Since there have not been any distributions developed to this effect, it is, in practice, sufficient to use characteristic parameters to describe the averages of the number of stress events and the stress energy (Kwade, 2004).

(a) Number of stress events (SN): in a batch grinding process (such as the bead mill used in this study) the average number of stress events on each product particle is determined by (Kwade, 1999; Kwade et al., 1996):

(i) N_C – the number of media contacts (–);

(ii) P_S – the probability that a particle is caught and sufficiently stressed at a media contact (–) and

(iii) N_P – the number of particles in the mill tank (–)

$$SN = \frac{N_C P_S}{N_P} \tag{2.4}$$

$$SN \propto \frac{\varphi_{GM}(1-\varepsilon)}{\left[1-\varphi_{GM}(1-\varepsilon)\right]} \frac{Nt_m}{d_{GM}^2} \frac{\rho_{al}}{\rho_{slurry} c_{al}} \tag{2.5}$$

where

SN = number of stress events (–)

ε = porosity of the bulk of the media (–)

ρ_{al} = density of γ–alumina particles (kg m^{-3})

t_m = milling time (s)

ρ_{slurry} = slurry density (kg m^{-3})

c_{al} = γ–alumina solids concentration (wt%)

N = shaft speed (rpm)

d_{GM} = diameter of grinding media (μm)

φ_{GM} = media load (%)

It is somewhat ironic that, considering the frequent use of the phrase ‘‘stress event’’, there is no wording of what a stress event actually means in the literature. According to the Oxford English Dictionary, stress is defined as the **“**pressure exerted on a material object**”**, while an event is a **“**special set of circumstances**”**. Therefore a stress event in this case can be defined as any circumstance in which pressure is exerted on the γ–alumina particles by the grinding media inside the mill. Similarly, other words (such as strain, constriction and squeezing) can be used interchangeably for the pressure or tension exerted on the γ–alumina particles.

(b) Stress energy (SE): to describe the stress energy in the bead mill, the following assumptions are made (Kwade and Schwedes, 2002):

(i) only single particles are stressed intensively between the grinding media;

(ii) the diameter of the rotating shaft is constant and

(iii) the tangential velocity of the grinding media is proportional to the circumferential speed of the shaft

Therefore, the stress energy is given by this expression:

$$SE \propto SE_{GM} = d_{GM}^3 \rho_{GM} v_t^2 \qquad (2.6)$$

where

SE = stress energy (J)

SE_{GM} = stress energy of grinding media (J)

v_t = circumferential speed of the shaft (m s^{-1})

ρ_{GM} = density of grinding media

(c) Specific energy ($E_{m,p}$) *and the transfer factor* (v_E): due to the various forms of energy dissipation, it is known that only a small fraction of the energy consumed by the mill is used by the grinding media in the comminution of product particles. Figure 2.4 shows the different ways by which energy is lost in a stirred bead mill (Kwade, 2003).

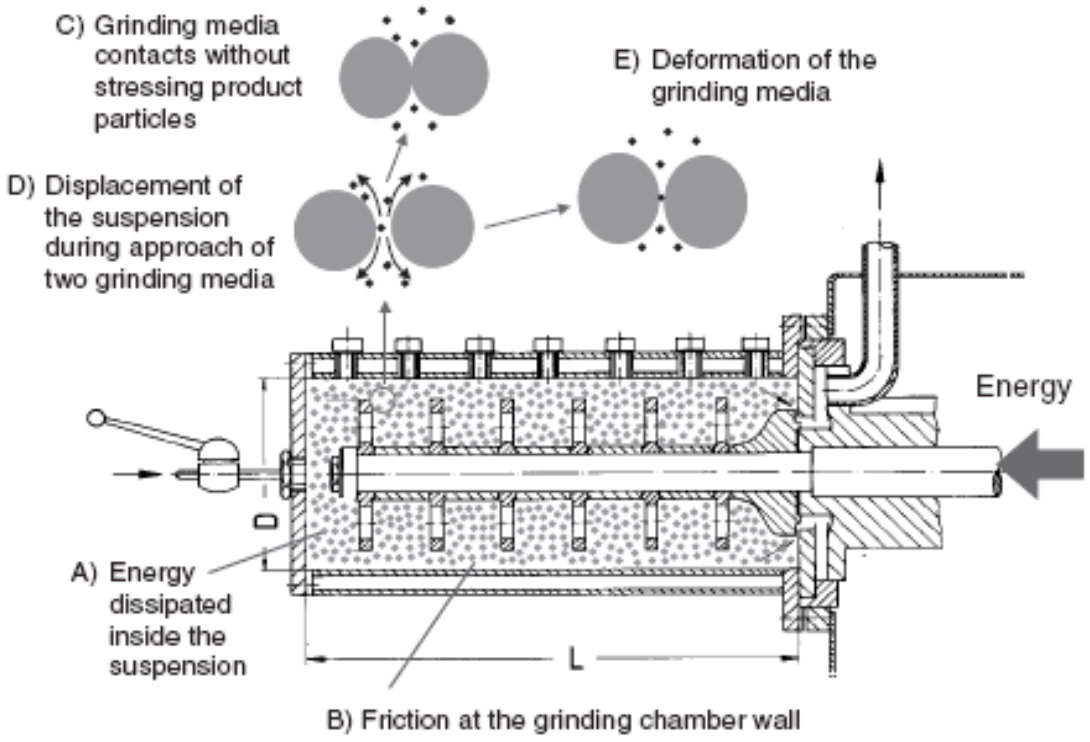

Figure 2.4. Energy loss in a stirred bead mill (Kwade, 2003).

The specific energy supplied to the grinding media in the comminution of product particles $E_{m,p}$ (J kg^{-1}) is therefore given by this relationship (Kwade, 2004):

$$E_{m,p} = \frac{\sum_{i=1}^{SN_M} SE_i}{m_{al}} = \frac{\sum_{j=1}^{n} SE_j . \Delta SF_{M.j}}{m_{al}} . t_m \quad (2.7)$$

$$E_{m,p} = \frac{SN_M . \overline{SE}}{m_{al}} = v_E E_{m,M} \quad (2.8)$$

where

SE_i = stress energy at stress event i (J)

SN_M = total number of stress events (–)

SE_j = average stress energy of interval j (J)

$SF_{M,j}$ = frequency of the stress events of interval j (s^{-1})

$\overline{SE}$ = mean stress energy (J)

$E_{m,M}$ = total specific energy consumption by the mill (J kg^{-1})

m_{al} = mass of γ–alumina particles (kg)

v_E = energy transfer factor (–)

The energy transfer factor v_E in Equation (2.8) can be defined by the loss factors $c_{L,i}$ represented in Figure 2.4 as follows (Kwade, 2003):

$$v_E = \sum_{i=A}^{E} \left(1 - c_{L,i}\right) \quad (2.9)$$

where

$c_{L,A}$ = percentage of the kinetic energy transferred to the milled product stream (–)

$c_{L,B}$ = part of the kinetic energy of the grinding media lost due to friction at the grinding chamber wall (–)

$c_{L,C}$ = part of the kinetic energy of the grinding media consumed to displace slurry during approach of two grinding media (–)

$c_{L,D}$ = kinetic energy of the grinding media lost due to media contacts without stressing product particles (–)

$c_{L,E}$ = part of the kinetic energy consumed by the deformation of the grinding media at a stress event (–)

$E_{m,p}$ is also given by (Fadhel and Frances, 2001):

$$E_{m,p} = \frac{v_E N^3 \rho_{slurry} \rho_{al} D^5 t_m Po}{m_{al}} \tag{2.10}$$

where

Po = power number (–)

D = shaft diameter (m)

For a fixed shaft geometry, Po is defined by this expression (Perry et al., 1997):

$$Po = f(\mathrm{Re}, Fr) \tag{2.11}$$

where

Re and Fr are the shaft Reynolds number and the Froude number respectively, which are given by (Perry et al., 1997):

$$\mathrm{Re} = \frac{ND^2 \rho_{slurry}}{\mu_{slurry}} \tag{2.12}$$

$$Fr = \frac{N^2 D}{g} \tag{2.13}$$

where

μ_{slurry} = dynamic viscosity of slurry (Pa s)

g = acceleration due to gravity (m s^{-2})

Power number Po is also given by (Perry et al., 1997):

$$Po = \frac{P}{\rho_{slurry} N^3 D^5} \tag{2.14}$$

where

P is the power consumed (W)

However, the effects of slurry solids concentration and milling time on the psds of ground γ–alumina particles have not been properly investigated in the literature. Even more so there is no clarity as to how the use of grinding media of different diameters influences the psds of ground particles. A good understanding of how these parameters influence the psds of ground particles is useful for the preparation of slurries of the desired specifications at the minimum energy input (Kwade, 1999; Anklekar et al., 1998; Kwade et al., 1996).

2.2.2.2 *Particle sizing by laser diffraction*

There are different properties (such as volume, surface area) which can be measured from a given particle depending on which measuring technique is being used (Figure 2.5). This means that one technique will produce a different measurement from another technique that measures an alternative dimension. However, for comparison between

techniques the generally accepted standard is by making reference to a hypothetical spherical particle (Rawle, 2002).

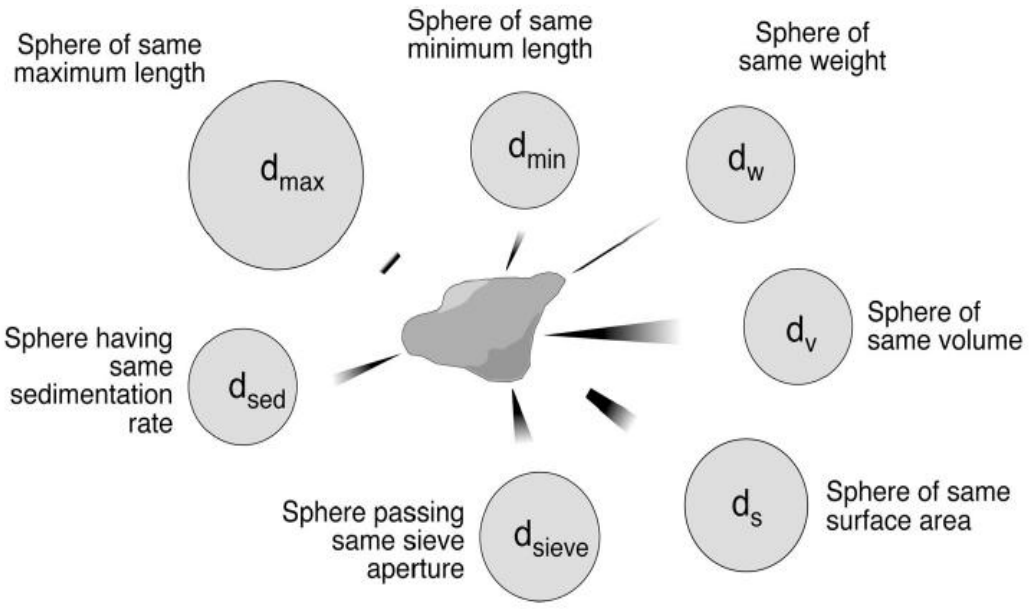

Figure 2.5. Different size measurements of the same particle (Rawle, 2002).

Particle sizing by laser diffraction measures the dimension of a sphere of same volume (d_v) as the particle being measured. A volume distribution is then generated which is equivalent to a weight distribution at constant density. This is the preferred distribution for chemical engineers in the coating industry because it indicates where most of the mass of material is located in terms of particle diameter (Rawle, 2003). Particle sizing by laser diffraction is non-destructive and flexible. This technique also provides a rapid data acquisition, high reproducibility (±0.5 %) as well as a wide measuring range (0.02 – 2000 µm) (Rawle, 2002). Therefore, laser diffraction is chosen as the technique for particle sizing in this study. The underlying principle of laser diffraction is based on the fact that particles passing through a laser beam scatter light at an angle that is directly

related to their size. The large particles scatter light at narrow angles with high intensity, whereas the small particles scatter at wider angles but with low intensity (Figure 2.6) (Kippax, 2005).

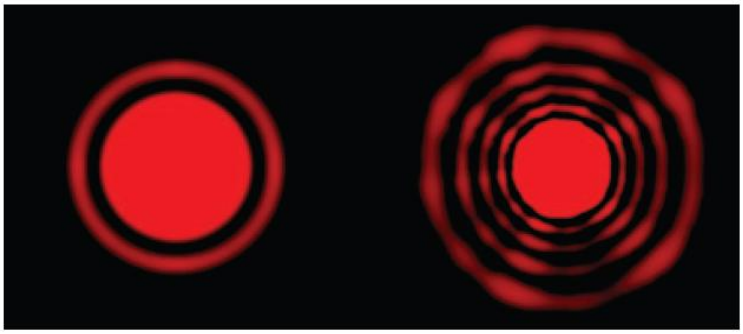

Figure 2.6. Light scattering patterns observed for different particles (the angular range and the intensity changes relate directly to the particle size) (Kippax, 2005).

2.2.3 Coating methodology

At present there are two industrial methods for coating Fecralloy® substrates. The first involves coating the Fecralloy®, which is already formed into a monolith, by pouring the slurry through or by suction (i.e. sucking the slurry into the monolith channels). This is followed by the removal of the excess slurry by gravitational draining or by applying pressure to clear the channels of all but requisite coating thickness. The composite is dried (normally above 100 ^{o}C) and calcined at 350 – 700 ^{o}C for good adherence of the coating within itself and to the monolith (Cybulski and Moulijn, 2006).

The second method involves coating the Fecralloy® before the monolith is constructed. In this method, the coating is applied onto the Fecralloy® by dip-coating, painting or spraying. This process may be repeated several times to achieve the required coating thickness. After completion of the coating process, the monoliths can be formed in the conventional way (Cybulski and Moulijn, 2006). One of the arguments against coating application before the construction of the monolith is that the presence of the coating makes welding or brazing difficult (Määthänen and Lylykangas, 1990).

For experimental studies in the laboratory, the coating of Fecralloy®, usually in the form of coupons or slabs, is mostly done using one of the application techniques of the second method, with dip-coating being the most preferred (Jia et al., 2007; Meille et al., 2005; Zhao et al., 2003; Fei et al., 2003; Schimpf et al., 2002; Valentini et al., 2001). Though not as commonly used as dip-coating, the spraying of coatings on Fecralloy® has also been chosen as the laboratory method in some studies (Meille et al., 2005; Sidwell et al., 2003; Wu et al., 2001). Other methods have also been used in the laboratory, such as electrophoretic deposition (Sun et al., 2007), chemical vapour deposition (Janickle et al., 2000), physical vapour deposition which can be cathodic sputtering, electron-beam evaporation or pulsed laser deposition (Kestenbaum et al., 2002; Roth et al., 1987). Each of these coating methods has its advantages and disadvantages, and the method to be chosen in a given application depends on the required coating properties (Meille, 2006).

The process of dip-coating involves immersing the Fecralloy® into the slurry for 15 – 20 s and withdrawing at a velocity of 3 – 12 cm/min. This is followed by drying and

calcination (Jia et al., 2007; Fei et al., 2003; Zhao et al., 2003; Schimpf et al., 2002; Wu et al., 2001). A spray of the slurry particles is applied in the case of spraying. This may be repeated until the desired coating thickness is achieved (Schuessler et al., 2003). The slurry viscosity used for dip-coating differs from that used for spraying as the shear rate is many times larger during spraying than immersing (Meille, 2006).

Wu et al. (2001) used both dip-coating and spraying methods to apply slurries on Fecralloy® mesh, though two different slurries were used for comparison. A slurry containing γ–alumina suspended in poly-vinyl alcohol and water was sprayed, while a slurry containing γ–alumina suspended in boehmite sol was dip-coated. They found that both methods achieved the same coating thickness, but the sprayed coating was more adhered than that of the dip-coated one. Fei et al. (2003) studied the coating properties of dip-coated Fecralloy® rods using γ–alumina slurries produced from two different sol gel routes. The effects of a number of the coating process parameters, such as withdrawal speed (3 – 12 cm/min) and soaking time (30 s and 5 min), were investigated. Their results showed no effects of the withdrawal speed and the soaking time on the coating thickness.

The common disadvantage of dip-coating and spraying is the inconsistency in the coating quality as evidenced from the wide variation in the coating loadings (Jia et al., 2007; Wu et al., 2001). There is therefore a need to develop a more consistent laboratory-scale method of coating Fecralloy® to produce the desired coating properties. In this study, the γ–alumina slurry is coated onto the Fecralloy® at a controlled shear rate using an automatic film applicator equipped with wire-wound bars. The film

applicator is chosen as the coating instrument because it had been designed to ensure consistency and reproducibility of coatings (Sheen Instruments Manual, 2006). The film applicator is a versatile bench top instrument which has been used not only in coating industries, but also in paint, ink and paper industries (Braaten et al., 1998).

2.2.4 Fecralloy® preoxidation

Fecralloy® is the integral component of metal catalysts. It is an alloy of iron (Fe), chromium (Cr), aluminium (Al) as well as other elements (such as yttrium) in minute quantities. The use of Fecralloy® as catalyst supports was pioneered by JM and the United Kingdom Atomic Energy Authority (UKAEA), in collaboration with Resistalloy who developed the technology for producing thin strip (Pratt and Cairns, 1977). The usual way of preparing the Fecralloy® surface to ensure its compatibility and adherence to γ–alumina coatings is by thermal treatment under oxidising conditions. This process is known as preoxidation during which an adherent oxide layer is formed on the Fecralloy® surface (Perez et al., 2001; Richardson et al., 2000). It provides enrichment of the Fecralloy® surface with aluminium, therefore prolonging the product component life by the protection of the base support against high temperature oxidation (Nicholls and Quadakkers, 2002).

When preoxidised at temperatures between 300 – 400 ^{o}C, the Fecralloy® surface oxide is rich in chromium. However at temperatures exceeding 800 ^{o}C an alumina-rich surface is formed which is the prerequisite for high temperature oxidation resistance. The

alumina oxide is formed by oxidation of bulk aluminium which migrates to the surface (U.S Atomic Energy Commission Report, 1966). If the oxide layer is broken, it self-heals next time the Fecralloy® is exposed to high temperature (Cybulski and Moulijn, 2006).

Only a few previous studies on the effects of preoxidation on Fecralloy® efficacy as a catalyst support exist. Most of these (such as Wloch et al., 2006; Pragnell et al., 2005; Wu et al., 2005; Fei et al., 2003) have used Fecralloy® preoxidation conditions in the range of 900 – 1200 ^{o}C for between 5 – 30 h, without any predetermination of the optimal conditions suitable for their applications. It was found that some γ–alumina, Fe and Cr were contained on the Fecralloy® surface irrespective of the preoxidation conditions chosen (Badini and Laurella, 2001; Tien and Pettit, 1972). The optimal preoxidation conditions depend on the percentage of constituents elements in the Fecralloy®, and likewise on the method of coating slurry onto the Fecralloy® (Chapman, 1982).

The techniques reported in the literature for assessing Fecralloy® surface microstructure after preoxidation have been based on using scanning electron microscopy (SEM) and X-ray diffraction (XRD) (e.g. Jia et al., 2007; Zhou et al., 2007; Shen et al., 2006; Zhao et al., 2003; Badini and Laurella, 2001; Tien and Pettit, 1972). It is rather surprising that none of these techniques have considered the Fecralloy® surface roughness based on the awareness that coatings adhere onto rough surfaces.

Zhou et al. (2007) found the optimal preoxidation conditions of Fecralloy® (Fe = 74 wt%, Cr = 20 wt% and Al = 6 wt%) to be at 900 ^{o}C for 10 h when γ–alumina slurry of 25.3 wt % solids concentration was dip-coated. Jia et al. (2007) and Zhao et al. (2003) however in their studies both found the optimal preoxidation conditions to be at 950 ^{o}C for 10 h when slurry of 35 wt% solids concentration was dip-coated. The composition of Fecralloy® used in the study by Jia et al. (2007) was Fe (70 wt%), Cr (25 wt%) and Al (5 wt%), though the Fecralloy® composition used by Zhao et al. (2003) was not specified.

The transport processes in the growing of oxide layer on Fecralloy® surface have been attributed to the presence of small amounts of reactive elements in its composition (Pint et al., 1995; Stott et al., 1995). These reactive elements can be yttrium (Y), silicon (Si) or Lanthanum (La), and are present in less than 0.5 wt% composition. Another study concluded that the presence of yttrium can prevent defective voids and wrinkling in Fecralloy® microstructure during preoxidation (Tolpygo, 1999). It was shown that the reactive elements are concentrated in the grain boundaries of the alumina layers formed on Fecralloy® surface during preoxidation. This positioning enables them to act as glue between grains, thus reducing the oxygen permeability and increasing the layer stability and adherence (Fukuda et al., 2002). It is well documented by the European Commission SMILER project which aimed at extending the lifetime of Fecralloy® across the operating temperature range that prolonged preoxidation at 800 – 950 ^{o}C for up to 2000 h would lead to complete chemical failure (Tatlock et al., 2005). This represents the consequence of concurrent depletion of the constituent elements (essentially Al, Cr and Fe) in the base Fecralloy®, and this will continue until the total

consumption of the whole structure (Bennett et al., 2005). The depletion profile of constituent elements across the support thickness was derived (Cowen, 1974) and later modified (Evans et al., 1999) as given in the following:

$$C_{bulk} = C_b - \frac{100 m_{solute}}{m_{alloy}} \frac{1}{2\phi} \left(\frac{\pi k_p}{D_S} \right)^{1/2} \times \sum_{n=0}^{\infty} \left[erfc\left(\frac{2nw + x}{2(D_S t)^{1/2}} \right) + erfc\left(\frac{2(n+1)w - x}{2(D_S t)^{1/2}} \right) \right] \quad (2.15)$$

where

erfc denotes the complementary error function

C_{bulk} = bulk concentration of constituent element (wt %)

C_b = initial concentration of constituent element (wt %)

m_{solute} = mass number of constituent element (g)

m_{alloy} = average molar mass of the support (g)

ϕ = Pilling-Bedworth ratio of oxide formed (-)

k_p = parabolic rate constant ($m^2 s^{-1}$)

D_S = diffusion coefficient for the support ($m^2 s^{-1}$)

x = distance from the support surface (m)

t = preoxidation time (s)

w = second half-width (m)

A more recent hyperbolic model given in Equation (2.16) provides a simple description of the preoxidation profile in terms of the specific mass gain and time (Pragnell et al., 2005). This explains why the hyperbolic model in Equation (2.16) is well received and preferable to Equation (2.15), which is somewhat cumbersome. The hyperbolic model

was developed from experimental studies of preoxidation of Fecralloy® carried out at temperatures of 900 and 925 ^{o}C for 0 – 70 h.

$$\Delta\overline{m} = \frac{at}{b+t} + \frac{ct}{d+t} \qquad (2.16)$$

where

a, b, c and d are constants

$\Delta\overline{m}$ = specific mass gain (mg cm^{-2})

t = preoxidation time (h)

2.2.5 Slurry characteristics

The slurry characteristics (e.g. pH, rheology, solids concentration) are very important to producing coatings of the desired quality (Germani et al., 2007; Jia et al., 2007; Cybulski and Moulijn, 2006; Zhao et al., 2003). Over the past few decades, the studies of the rheology of γ–alumina slurries have involved both steady shear and oscillatory rheology. The shear rheology deals with the deformation behaviour of a material that is subjected to shear stress. Oscillatory rheology, however, provides information about the viscoelasticity of the material, i.e. its viscous and elastic properties (Binner and McDermott, 2006; Barnes et al., 1989). The oscillatory rheology is mostly applicable to slurries of high solids concentration (50 – 85 wt %) as their solid-like and liquid-like characteristics can simply be determined from the viscoelasticity measurements (e.g. Binner and Santacruz, 2006). This explains why the shear rheology is apposite to γ–alumina slurries used for coating metallic substrates which are generally prepared between 15 – 45 wt% (Germani et al., 2007; Jia et al., 2007; Dressler et al., 2006).

There have been some recent studies on the rheology of γ–alumina slurries (e.g. Binner and McDermott, 2006; Palmqvist et al., 2006; Cristiani et al., 2005; Xu and Koelling, 2005; Vishista and Gnanam, 2004; Yang and Sigmund, 2003; Yang and Sigmund, 2002; Valentini et al., 2001; Agrafiotis et al., 2000; Agrafiotis and Tsetsekou, 2000; Davies and Binner, 2000; Anklekar et al., 1998; Blachou et al., 1992)

Palmqvist et al. (2006), Vishista et al. (2004) and Anklekar et al. (1998) described the rheological behaviour of γ–alumina slurries of solids concentration between 5 – 51 wt% as shear thinning. The dispersants used in these studies were ammonium citrate, ammonium polymethacrylate, polyaminobenzoic acid, ammonium tartarate, lignosulphonate and polyethylene amine.

The dependence on pH of the viscosity of slurries of concentrations of 8 – 44 wt% has been investigated (Shi and Zhang, 2000). The pH range investigated was notably 3 – 6 and these slurries were dispersed with hydrochloric acid and ammonia. Their results showed that the minimum viscosity was achieved at pH values within 3 – 4 after which the slurry viscosity increased.

Binner and McDermott (2006) and Agrafoitis and Tsetsekou (2000) went further to study the effects of solids concentration of 30 – 51 wt% on the slurry viscosity. Their slurries were dispersed by hydrochloric acid, ammonium polymethacrylate and ammonium polyacrylate. They found that the slurry viscosity increased with solids concentration in a consistent pattern. The Kreiger-Dougherty equation is commonly used to describe this increase in slurry viscosity (Barnes et al., 1989):

$$\mu = \mu^{o}\left(1-\frac{c_v}{c_{v\max}}\right)^{-[\mu]c_{v\max}} \tag{2.17}$$

where

μ = slurry viscosity (Pa s)

μ^{o} = viscosity of pure water (Pa s)

c_v = γ–alumina solids concentration (vol. %)

$c_{v\max}$ = maximum solids packing (vol. %)

$[\mu]$ = intrinsic viscosity which depends on the shape of the γ–alumina particles (Pa s)

The product $[\mu]c_{v\max}$ is often given as 2 for close packed particles such as γ–alumina

According to Hill and Carrington (2006), $c_{v\max}$ is defined as the highest volume of solid particles that can be added to a fluid. This simply means that the slurry behaves like a rigid solid when its solids concentration exceeds the maximum solids packing.

Furthermore, the increase in slurry viscosity with solids concentration has also been modelled (Starov et al., 2002) by Equation (2.18) and by the modified Eilers and Chong equations in Equations (2.20) & (2.21) (Edirisinghe et al., 1992).

$$\mu_r = \frac{\mu}{\mu^{o}} = \frac{1}{(1-c_v)^{f}} \tag{2.18}$$

and

$$c_v = \frac{c_{al}\rho_{water}c_{water}}{\rho_{al}(1-c_{al})} \tag{2.19}$$

where

μ_r = relative viscosity of slurry (–)

c_{water} = concentration of liquid medium (vol. %)

ρ_{al} = density of γ–alumina particles (kg m^{-3})

ρ_{water} = density of liquid medium (kg m^{-3})

f is a constant

$$\frac{1}{\mu_r^{0.5}-1} = \frac{1}{C_{EE}}\frac{1}{c_v} - \frac{1}{C_{EE}c_{v\max}} \tag{2.20}$$

$$\frac{1}{\mu_r^{0.5}-1} = \frac{c_{v\max}}{C_{EC}}\frac{1}{c_v} - \frac{1}{C_{EC}} \tag{2.21}$$

where

C_{EE} and C_{EC} are constants

2.2.5.1 Assessment of coatings

Upon coating Fecralloy® with γ–alumina slurries, there have been various techniques used for assessing the coating properties, such as coating loading, adherence, thickness and homogeneity.

(a) Coating loading

The concentration of the coating layer on the Fecralloy® is referred to as the coating loading. The conventional technique for determining the coating loading is by measuring the mass of the Fecralloy® before and after the coating process (i.e. after drying and calcination) using a mass balance, and then calculating the percentage mass gain (Zhou et al., 2007).

(b) Coating adherence

The coating adherence refers to how strongly attached the washcoat is to the Fecralloy®. The assessment of coating adherence has mainly been based on the mass loss from ultrasonic vibration (Zhao et al., 2003; Valentini et al., 2001). This test involves the soaking of coatings in petroleum ether, and then treating them in an ultrasonic vibrator for 5 – 60 min. The petroleum ether, being a non-polar compound, acts by weakening the attractive bonds in the coatings (Housecroft and Constable, 2002). The treated sample is dried afterwards and the mass loss is evaluated.

Thermal shock has also been used by Zhao et al. (2003) and Jia et al. (2007) for assessing coating adherence. This test involves heating the coatings at 950 – 1050 ^{o}C for 20 – 60 min, and then tempering them in water at room temperature. This procedure is repeated several times and the mass loss is measured afterwards. The setback for assessing coating adherence by ultrasonic vibration and thermal shock is that both methods are not physically derived. In addition the methods require considerable amount of time before the adherence measurements are taken, and this may be detrimental for business.

Germani et al. (2007) used a drop test for assessing coating adherence. In this test the coatings were dropped several times on a hard surface from a fixed height (e.g. 50 cm) and the mass loss was then measured. This method is flawed by the inconsistencies which may arise in the coating adherence obtained at the fixed height.

For measuring the adherence of sputtered γ–alumina coatings on metallic substrates, Roth et al. (1987) have used a scratch tester, where a diamond point of defined curvature is drawn across the sample with an increasing normal load. The critical load is reached at the instant when the coating begins to strip from the substrate. This point is determined by observing the acoustic emission and by inspection with a microscope. Unlike γ–alumina coatings which can be up to 50 μm, this method is suited for coatings of minimal thickness of around 1 – 6 μm.

There is an urgent need to devise new methods for measuring the coating adherence because none of the conventional methods is physically derived. A physically derived method means that the measured coating variables are based on fundamental scientific quantities (e.g. stress, displacement). As there are mechanical and thermal stresses inside the exhaust system of automobiles, these quantities properly describe the coating adherence, and they should therefore be reflected in the new methods (Cybulski and Moulijn, 2006).

(c) Coating thickness and homogeneity

The coating homogeneity refers to how the washcoat is uniformly dispersed across the Fecralloy® surface. The coating thickness and homogeneity have been assessed by the SEM, through which images of the side and surface of the coatings are provided (Jia et al., 2007; Giani et al., 2006; Fei et al., 2003). The underlying principle of SEM is based on the collisions of electron beam with the specimen, thereby resulting into the emission of reflective rays, which are measured and counted (Smith, 2002).

Fei et al (2003) have, in addition, used a focussed ion beam (FIB) technique for assessing the coating thickness. Meille (2005) and Roth et al. (1987) have assessed coating thickness using a micrometer and a profilometer respectively.

The technique for assessing coating thickness and homogeneity should have high degree of accuracy and resolution, and the SEM clearly outperformed other techniques in these areas judging by its predominant use.

2.2.5.2 Findings from coating assessment

A sizeable number of studies have been done in recent years on the effects of slurry characteristics on the coating properties (e.g. Fornasiero et al., 2008; Germani et al., 2007; Jia et al., 2007; Zhou et al., 2007; Giani et al., 2006; Shen et al., 2006; Wu et al., 2005; Fei et al., 2003; Zhao et al., 2003; Reymond, 2001). The slurry characteristics studied include slurry sol type and concentration (Zhou et al., 2007; Fei et al., 2003), slurry solids concentration, pH and psds (Fornasiero et al., 2008; Jia et al., 2007; Zhou et al., 2007) and the addition of ceria-zirconia solution (Jia et al., 2007; Shen et al., 2006) and PGMs (Fornasiero et al., 2008; Giani et al., 2006; Reymond, 2001). The coating method used in these studies was dip-coating except for Giani et al. (2006) who used suction.

Fei et al. (2003) studied the coatings on dip-coated Fecralloy® rods using γ–alumina slurries produced from two different sol gel routes: aqueous-based colloidal sol and

alcohol-based polymeric sol. The rectangular Fecralloy® rods (10 x 5 x 0.7 mm) used for this study had the following chemical composition: Fe (68.8 wt%); Cr (22 wt%); Al (7 wt%); Y (0.15 wt%) and Mo (2 wt%). These rods were preoxidised in air at 982 ^{o}C for 30 h prior to coating deposition to form α–alumina oxide layers. The effect of sol concentration on the coating properties was investigated. The sol concentration had significant effect on the coating thickness, and they concluded that the sol concentration must be carefully controlled to prevent cracks and spallation during drying and calcination. They also found that the alcohol-based polymeric sol was better suited for coating Fecralloy® than the aqueous-based colloidal sol because the alcohol had better homogeneity, lower surface tension and higher evaporation rate. Zhou et al. (2007) moved further by using a boehmite sol to improve the adherence between the γ–alumina coatings and the Fecralloy® coupons. These coupons (40 x 25 x 0.05 mm) used for this study were composed of Fe (74.0 wt%), Cr (20.2 wt%), Al (5.75 wt%) and Hf (0.04 wt%) and they were preoxidised at 900 ^{o}C for 10 h. They found that the optimal sol layer loading at 2.0 – 6.6 wt%.

Jia et al. (2007) in their pioneering study investigated the effects of γ–alumina slurry characteristics on the coatings deposited onto Fecralloy® [thickness of 50 μm; and composition of Fe (70 wt%), Cr (25 wt%) and Al (5 wt%)]. The γ–alumina particles were dispersed in acetic acid, and the slurry characteristics were the following: pH (3 – 6.5), psds ($d_{0.9}$ of 1.68 – 33.39 μm) and solids concentration (15 – 45 wt%). They concluded that the optimal coating properties in terms of loading and adherence could be achieved by using slurry at pH of 4 – 6, solids concentration of 35 wt% and particle diameter $d_{0.9}$ of less than 10 μm. These findings are comparable to those of Zhou et al.

(2007) who found the optimal solids concentration to be below 25.3 wt% when boehmite sol (2.0 – 6.6 wt%) was used as intermediary layer.

Further to the work by Jia et al. (2007), the effect of slurry psds on γ–alumina coatings was buttressed in the study by Germani et al. (2007) in which stainless steel platelets (grade 316Ti and dimensions: 50 x 50 x 1 mm) were used as substrates. The particle diameter $d_{0.5}$ of the slurries used were 3 and 28 µm respectively, and their solids concentrations were 26 – 50 wt%. They also concluded that the slurry of smaller particle diameter of 3 µm produced better adherence onto the platelets. Shen et al. (2006) and Jia et al. (2007) showed that the coating adherence on the Fecralloy® could be improved by the addition of $Ce_{0.68}Zr_{0.32}O_2$ solid solution into the slurry as the latter enhances thermal stability by inhibiting the transformation of γ–alumina to other phases.

Giani et al. (2006) deposited an active washcoat of Pd/ γ–Al_2O_3 onto Fecralloy® [Fe (73 wt%), Cr (20 wt%), Al (5 wt%) and Y (2 wt%)] metal foams. After preoxidising the foams at 900 ^oC for 10 h, the Fecralloy® foams were coating by suction by percolating the slurry through at velocity of 1.5 cm/min using a vacuum pump. This was followed by the wet impregnation of the washcoated foams in $Pd(NO_3)_2$ diluted solution. They found that though double loading was achieved by coating twice, the coating adherence was compromised as a result. In addition the coating technique impregnated up to 80 wt% of the palladium initially into the foams, and this increased their activity and mass transfer performance measured from CO oxidation.

Fornasiero et al. (2008) also studied the coating of γ–alumina slurries onto Fecralloy® rods [thickness of 22 μm and composition: Fe (70 wt%), Cr (25 wt%) and Al (5 wt%)]. The rods were preoxidised at 950 ^{o}C prior to slurry coating, and the PGMs (i.e. Pt and Pd) were finally deposited on the washcoat by ionic exchange. They showed that the PGMs were highly dispersed and produced good oxidation catalysts for CO, HCs and particulates. The presence of ceria-zirconia mixed oxides in the slurry was found to be beneficial to the metal dispersion and oxidation activity, and the bimetallic Pt/ Pd onto $Ce_{0.6}Zr_{0.4}O_2$–Al_2O_3 coating was an optimised combination in terms of activity and thermal stability. The previous studies on the effects of slurry characteristics on the coating properties are summarised in Table 2.1.

The principles of coating adherence onto Fecralloy® have been meagrely studied in the literature. The only reference to this was in the coating of γ–alumina slurry onto cordierite monoliths (Agrafiotis et al., 1999). The study ascribed the mechanical mechanisms such as the **"**anchoring**"** and interlocking of the γ–alumina particles to the surface irregularities of the ceramic substrate, and to a much lesser extent via chemical and affinity mechanisms.

Considering the importance of monolith catalysts, there are currently several knowledge gaps which need to be filled, such as investigating the coating properties over wider pH and solids concentration ranges, how coating properties are affected by mixing slurries of different psds as well as the principles of coating adherence.

Table 2.1. Summary of previous studies on the effects of slurry characteristics on coating properties.

Study	Slurry characteristics	Coating assessment	Findings
Fei et al. (2003)	aqueous and alcohol based colloidal sols	SEM, FIB	alcohol based sol was more homogeneous on Fecralloy®
Giani et al. (2006)	solids concentration = 20 – 30 wt%	SEM, ultrasonic vibration	coating twice produced double loading but this compromised coating adherence
Jia et al. (2007)	solids concentration = 15 – 45 wt%, pH = 3 – 7, $d_{0.9}$ = 1.68 – 33.39 µm	SEM, ultrasonic vibration, thermal shock	optimal coating loading and adherence at pH = 4 – 6, solids concentration of 35 wt% and $d_{0.9}$ less than 10 µm
Germani et al. (2007)	$d_{0.5}$ = 3 and 28 µm, solids concentration = 26 – 50 wt%	SEM, drop test, ultrasonic vibration	smaller particles showed better adherence
Fornasiero et al. (2008)	PGM based (i.e. Pt and Pd) with and without ceria-zirconia mixed oxides	SEM	high dispersion of PGMs; ceria-zirconia mixed oxides enhanced dispersion

2.2.6 Drying and calcination

The drying and calcination conditions used in the coating method can influence the coating properties, such as in the formation of cracks. Fei et al. (2003) dip-coated Fecralloy® rods in γ–alumina using sol gel preparation, and dried the coatings at room temperature for 1 h, then in an oven at 100 ^{o}C for 2 h before finally calcining in a furnace at 500 ^{o}C for 3 h. They found that thicker coatings were achieved by dip-coating several times, and that drying and calcining each layer separately could avoid cracks caused by large stresses. It was discovered that to achieve an integrated coating without cracks, the critical coating thickness should not be exceeded. The drying and calcination conditions reported in the literature have been in terms of durations (i.e. 100 ^{o}C and 350 – 700 ^{o}C respectively for 1 – 3 h), without any consideration of the profiles adopted (Jia et al., 2007; Cybulski and Moulijn, 2006; Fei et al., 2003; Zhao et al., 2003).

Similarly the heating conditions of coatings have been considered. The heating conditions of coatings in a furnace depend on how heat energy is supplied, e.g. by blowing a stream of hot air or through an encapsulated filament (Ismagilov et al., 2005). The slow drying of coatings has been encouraged as this was viewed to be influential in preventing coating cracks. The fast drying of coatings can lead to high evaporation which quickly thins the coating film, thus causing a detrimental breakage (Giani et al., 2006; Fei et al., 2003). The basis of these has however not been thoroughly studied and well documented.

2.3 CONCLUSIONS

The background literature behind important aspects of slurry coating for emission control applications have been presented in this chapter. Based on the detailed preparation path for coatings, the critical factors which influence γ–alumina coating properties as well as methods for assessing coating quality were discussed.

The suitability of γ–alumina for the role of a catalyst support material was brought about by its unique structure and properties. The iep and the pH at which the particles are well dispersed have been found in previous studies as 7.7 – 7.9 and 3.8 – 4.5 respectively. The stabilisation mechanism has been found to be based on electrostatic repulsion of charged γ–alumina particles.

Different types of mill have been used for mixing and fragmentation of γ–alumina particles in the slurry, but the stirred bead mill has emerged as the most commonly used because of its importance in producing fine and ultra-fine particles. The basic comminution concepts (SN, SE, $E_{m,p}$) were described as the driving forces for the particle fragmentation in the stirred bead mill.

Fecralloy® preoxidation under oxidising conditions at temperatures exceeding 800 ^{o}C has been shown to produce adhering and protective oxide layer which shows compatibility to the γ-alumina coatings. There have been different models developed for representing this important process. However, the techniques for measuring

Fecralloy® surface changes caused by preoxidation have not considered the surface roughness and the topography profile.

Dip-coating was revealed to be the widely used method of coating Fecralloy®, but other methods, such as spraying and suction, have also been used. The important factors which can influence coating properties were revealed as sol type and concentration, slurry solids concentration, pH, psds and the addition of ceria-zirconia oxides and PGMs.

The assessment of coating properties have been based on ultrasonic vibration, SEM, thermal shock, FIB, drop test and profilometer and micrometer measurements. In addressing the knowledge gaps mentioned, the automatic film applicator is used as the coating apparatus in this study. The assessment of coatings will consider both the conventional methods and the new methods which will be developed.

3

PROTOCOLS FOR CHARACTERISING γ–ALUMINA SLURRIES

This chapter focuses on slurry preparation by bead milling to develop experimental protocols for the characterisation of slurries for coating onto Fecralloy® substrates. The relationship between the pH and the zeta potential of particles are determined. The γ–alumina particles are found to be optimally stabilised at a pH of 4. This is followed by the investigation of the fragmentation behaviour of the mill in terms of the number of stress events (SN), stress energy (SE) and the specific energy ($E_{m,p}$). The visualisation of the particles at different stages of milling is done by SEM. This chapter ends with a discussion of the various strategies for achieving the aims of this research.

3.1 INTRODUCTION

The γ–alumina particles which are present in an aqueous suspension need to be sufficiently stabilised with a dispersant, and then fragmented in a stirred bead mill before the commencement of coating. The stabilisation of γ–alumina particles is necessary to prevent the van der Waals forces causing particle aggregation which affects the adherence between the coating and the substrate. The degree of stabilisation is closely related to the zeta potential of particles and the type of dispersant used (Davies and Binner, 2000).

The agitation effect of a bead mill results in the mixing and fragmentation of the γ–alumina particles to reach a particle diameter suitable for coating. At the end of milling it is expected that coating slurries should have particle size distributions (psds) which conform to $d_{0.9} < 15$ μm and $d_{0.1} < 2$ μm. This is the target set by JM as representing the psds of slurries for commercial production of coatings in the industry. The diameters $d_{0.1}$, $d_{0.5}$ and $d_{0.9}$ are based on the 10%, 50% and 90% percentiles of the volume particle distributions. The experimental work in this chapter is aimed at determining the following:

(a) the relationship between the slurry pH and the zeta potential of γ–alumina particles;

(b) how the slurry and milling characteristics affect the psds of the ground particles by considering basic comminution concepts and

(c) the morphology (i.e. shape and size) of the γ–alumina particles at different stages of milling determined by scanning electron microscopy (SEM).

3.2 MATERIALS AND METHODS

3.2.1 Materials

The γ–alumina powder was supplied by Sasol, UK. The particles have a specific surface area of 142 m^2g^{-1} and a $d_{0.9}$ of 43.4 μm. A summary of the properties of the alumina particles is shown in Table 3.1. The slurries were prepared by adding γ–alumina powder in doubly distilled water. An acetic acid solution (1M; Fischer Scientific, UK) was used to adjust pH to a starting value of 4. The γ–alumina concentration in the slurries was 40 wt% and the slurry pH was tested with a pH meter (Mettler-Toledo, UK).

Table 3.1. Properties of γ–alumina powder (data by Sasol, UK).

Typical properties	Values
appearance	white powder
type	calcined alumina
purity (%)	98
odour	none
thermal modifiers (e.g. La^{2+})	none
designated symbol	PURALOX SCFa-140
pore volume (cm^3g^{-1})	0.50
diameter: $d_{0.1}$; $d_{0.5}$; $d_{0.9}$ (μm)	4.6; 20.7; 43.4
loose bulk density (kgm^{-3})	800
surface area 24 h/ 1100 ^oC (m^2g^{-1})	15

3.2.2 Slurry preparation using the bead mill

The slurry particles were then mixed and comminuted inside a stirred bead mill (Union Process, USA) pictured in Figure 3.1. The mill tank (volume = 1.2 litre) was placed vertically and firmly screwed to a metal base. The tank was filled with the slurry and spherical zirconia grinding media of 1 mm or 5 mm diameter.

The contents of the tank were subjected to a sustained mechanical agitation by the rotation of the shaft located inside the tank. The mill had a variable speed of 0 – 1000 rpm, equipped with water jackets for cooling and quick water disconnects for removing the tank.

The operating conditions of the mill are stated below:

(a) milling speed = 500 rpm;

(b) media load (ratio of the volume of grinding media to the volume of the slurry) = 40 vol.%;

(c) media diameter = 1 mm or 5 mm;

(d) milling time = 60 min and

(e) temperature kept between 20 – 22 ^{o}C via a cooling jacket.

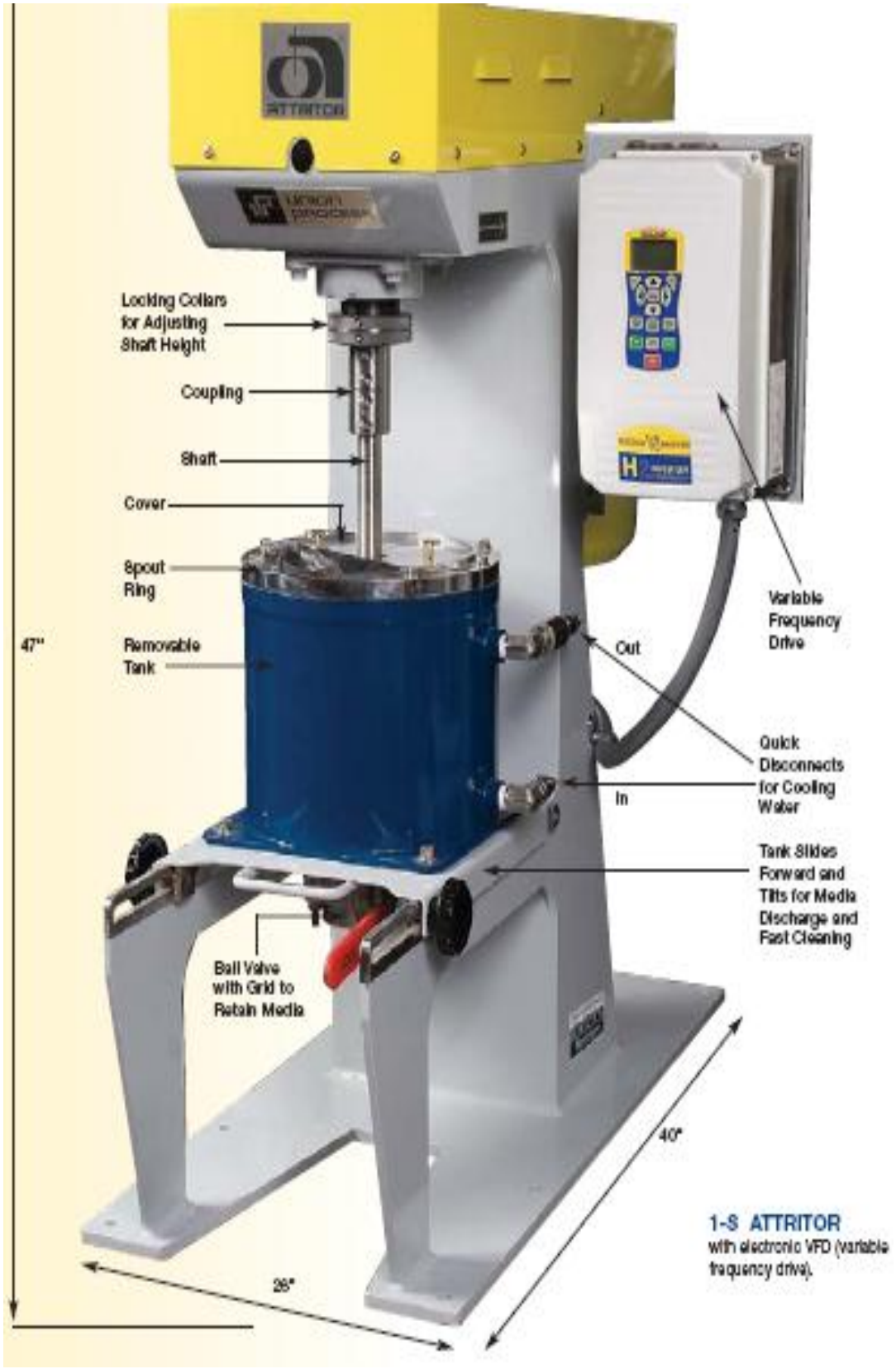

Figure 3.1. A stirred bead mill and its accessories (Union Process, USA).

3.2.3 Particle characterisation

3.2.3.1 Particle sizing

The Mastersizer 2000 (Malvern Instruments, UK) which uses laser diffraction was used for measuring the slurry psds in this study. The attendant benefits of using laser diffraction have been outlined in section 2.2.2.2. A typical layout of the Mastersizer is given below in Figure 3.2.

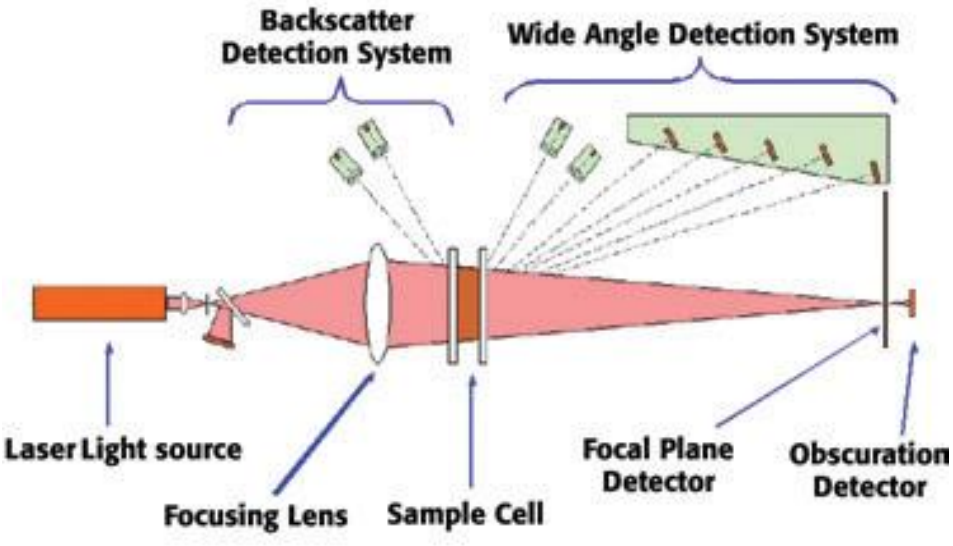

Figure 3.2. A typical layout of the Mastersizer (Kippax, 2005).

A schematic representation of the particle diameters measured by the Mastersizer 2000 is given in Figure 3.3, where $d_{0.1}$, $d_{0.5}$ and $d_{0.9}$ refer to the 10%, 50% and 90% percentile volume diameters respectively.

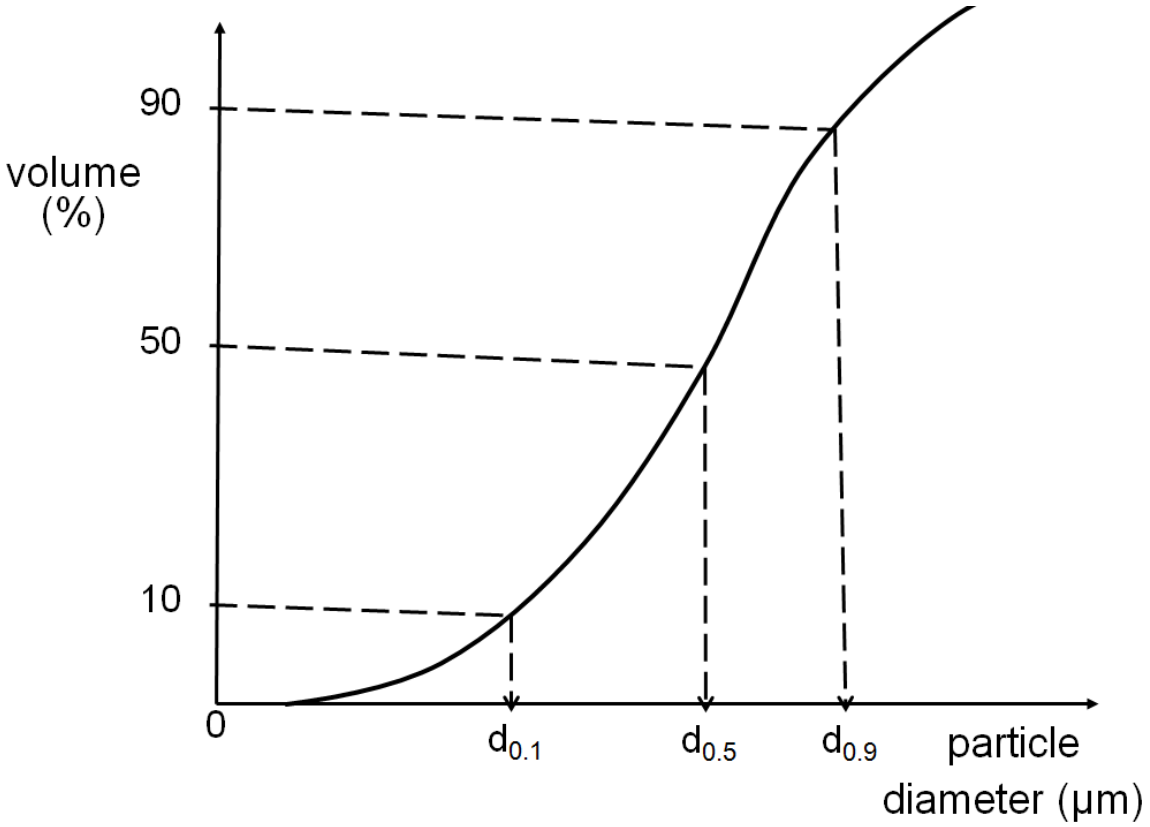

Figure 3.3. Schematic representation of diameters $d_{0.1}$, $d_{0.5}$ and $d_{0.9}$.

3.2.3.2 Acoustosizer and Zetamaster

The relationship between the zeta potential of γ–alumina and slurry pH was determined by electroacoustics and electophoresis using the Acoustosizer (Colloidal dynamics, USA) and Zetamaster (Malvern Instruments, UK) respectively. The aqueous solutions of HCl (1M; Fischer Scientific, UK) and NaOH (1M; Merck Chemicals, UK) were used to alter the slurry pH. The background electrolyte used for the Acoustosizer measurements was KCl solution (10^{-3} M; Fischer Scientific, UK).

The Acoustosizer measurements were recorded for every 1 ml of added HCl or NaOH according to a previous study (Greenwood and Kendall, 2000). As electrophoresis only functions for dilute systems, the slurry was initially diluted to one-twelfths its initial concentration to prevent clogging of the equipment pipes. All the water used was doubly distilled. The slurry was allowed to equilibrate at 25^{o}C before measurements were taken.

3.2.3.3 Milling conditions

Slurries were prepared according to the methods described in sections 3.2.1 & 3.2.2 and then milled at various conditions outlined below:

(a) At 25 – 45 wt% solids concentration, slurries were milled for 60 min using media of 5 mm diameter

(b) At 40 wt% solids concentration, the slurries were milled for 0 – 240 min using media of 5 mm diameter

(c) At 40 wt% solids concentration, the slurries were milled for 0 – 240 min using media of 1 mm or 5 mm diameters.

The psds of the product particles were measured by laser diffraction using the Mastersizer 2000 (Malvern Instruments, UK) as described in section 3.2.3.1.

Four identical sets of psd measurements of standard deviation of 3% were obtained for each of the slurries, and the mean psds were constructed.

3.3 RESULTS AND DISCUSSION

3.3.1 Zeta potential measurements

The relationship between the zeta potential of γ–alumina particles and the slurry pH as measured by the Acoustosizer and Zetamaster is shown in Figure 3.4, while the particles electrokinetic sonic amplitude (ESA) diameter as a function of pH taken by the Acoustosizer is shown in Figure 3.5.

The ESA technique is based on the effect that when an alternating electrical potential was applied to the slurry, it caused the particles to vibrate in a manner that depends on their diameter and on the zeta potential at the frequency of the applied field. When there is a density difference between the particles and the aqueous suspension, this motion would generate an alternating acoustic wave of the same frequency as the applied field. This phenomenon is called the ESA effect and the particle diameter measured is termed the ESA diameter (Sarraf and Herbig, 2008).

These results clearly show the strong dependence of the zeta potential and the ESA diameter of particles on slurry pH. The particles become charged when dispersed in the aqueous slurry, and this results in electrostatic repulsive forces between the particles and counter-ions due to overlap of similarly charged electric double layers. The electrostatic forces, quantified by zeta potential, act opposite to the attractive long-range van der Waals forces. The particles experience the overall effect of the electrostatic and van der Waals forces (Kasprzyk-Hordern, 2004; Davies and Binner, 2000).

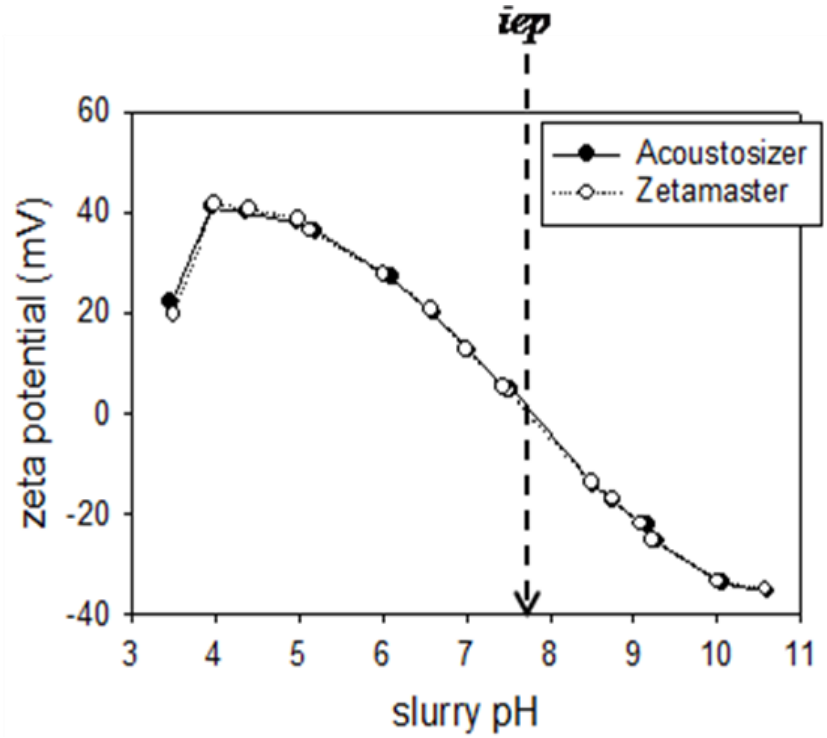

Figure 3.4. Zeta potential of γ–alumina particles as a function of slurry pH.

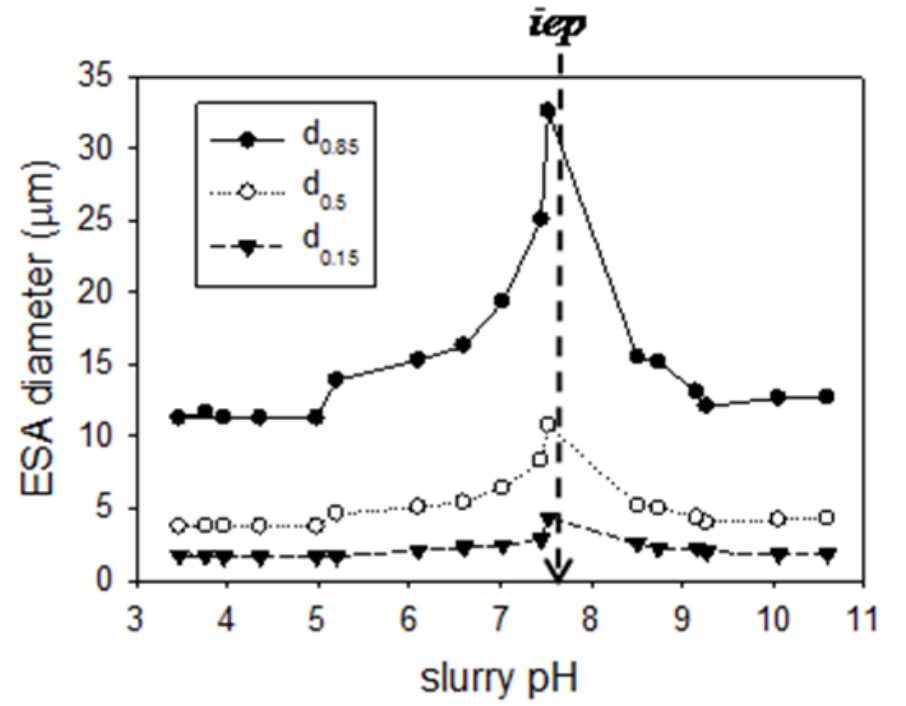

Figure 3.5. ESA diameter of γ–alumina particles as a function of slurry pH.

It is customary to consider slurries having zeta potential greater than $|30|$ mV as sufficiently stabilised (Greenwood, 2003). It is shown in Figure 3.4 that the iep (i.e. pH at which zeta potential equals zero) of the particles is 7.7. This is the pH at which the particles were mostly aggregated as the slurry was characterised by lumps. The natural pH of γ–alumina particles was found to be at 9.1; the zeta potential at this point is -23 mV. This iep and the natural pH values are in good agreement with previous measurements in the literature which were 7.7 – 7.9 and 9.0 – 9.2 respectively (Agrafiotis and Tsetsekou, 2000; Davies and Binner, 2000; Nowack et al., 1996; Tijburg et al., 1991).

As the slurry pH gets close to the iep, the van der Waals attraction forces between particles become dominant, leading to particle aggregation and less stabilisation. At extreme pH of less than 4 however, there exists flocculation in the slurry due to overlap of double layers which causes reduction in the zeta-potential of particles. The ESA measurements in Figure 3.5 followed the same trend showing an increase in particle diameter due to particle aggregation as the slurry pH nears the iep. However, the ESA measurements close to the iep should be treated with caution based on the minimal stabilisation in the slurry (Greenwood, 2003).

The optimal stabilisation of particles was achieved at pH of 4 and this is in accordance with the values in the literature in the range of 3.8 – 4.5 (Agrafiotis and Tsetsekou, 2000; Davies and Binner, 2000; Nowack et al., 1996; Tijburg et al., 1991). This pH value corresponds to a zeta potential of 41 mV. Both the Acoustosizer and the

Zetamaster measurements showed strong correlation throughout the pH interval investigated, confirming the reliability of the data from the two equipments.

3.3.2 Particle size distributions from milling

3.3.2.1 Effect of solids concentration

The diameters $d_{0.1}$, $d_{0.5}$ and $d_{0.9}$ of the slurries of 25 – 45 wt% solids concentration are shown in Table 3.2, while their psds are also shown in Figure 3.6. It is shown from Table 3.2 and from the close positioning of the curves in Figure 3.6, as they show near-complete superimposition, that the psds of the slurries were almost identical after milling. This implies that there was no noticeable effect of solids concentration on the psds of the ground particles as long as the solids concentration remained at 25 – 45 wt%. The psds of all the slurries after milling conformed to the set target of $d_{0.9} < 15$ μm and $d_{0.1} < 2$ μm. The lack of influence of the solids concentration on the slurry psds can be explained by considering the changes to the parameters governing the number of stress events (SN). The increase in the solids concentration produced increasing number of particles in the mill tank (N_P). This means that there was less probability of contact between a particle and the grinding media. However, both the number of media contact (N_C) as well as the probability that a particle is caught and sufficiently stressed at a media contact (P_S) increased with the increase in solids concentration [see SN definition in Equation (2.4) in Chapter 2]. Therefore the overall effect of solids concentration on the ground particles is not clear-cut and, according to Fadhel and

Frances (2001), could also depend on other contributing factors (e.g. the type of material ground).

Table 3.2. Particle diameters for slurries of 25 – 45 wt% concentration after milling for 60 min.

Solids concentration (wt%)	$d_{0.1}$ (μm)	$d_{0.5}$ (μm)	$d_{0.9}$ (μm)
25	1.32	4.19	11.88
30	1.42	4.24	12.01
35	1.45	4.08	11.93
40	1.34	4.36	12.74
45	1.39	4.17	11.71

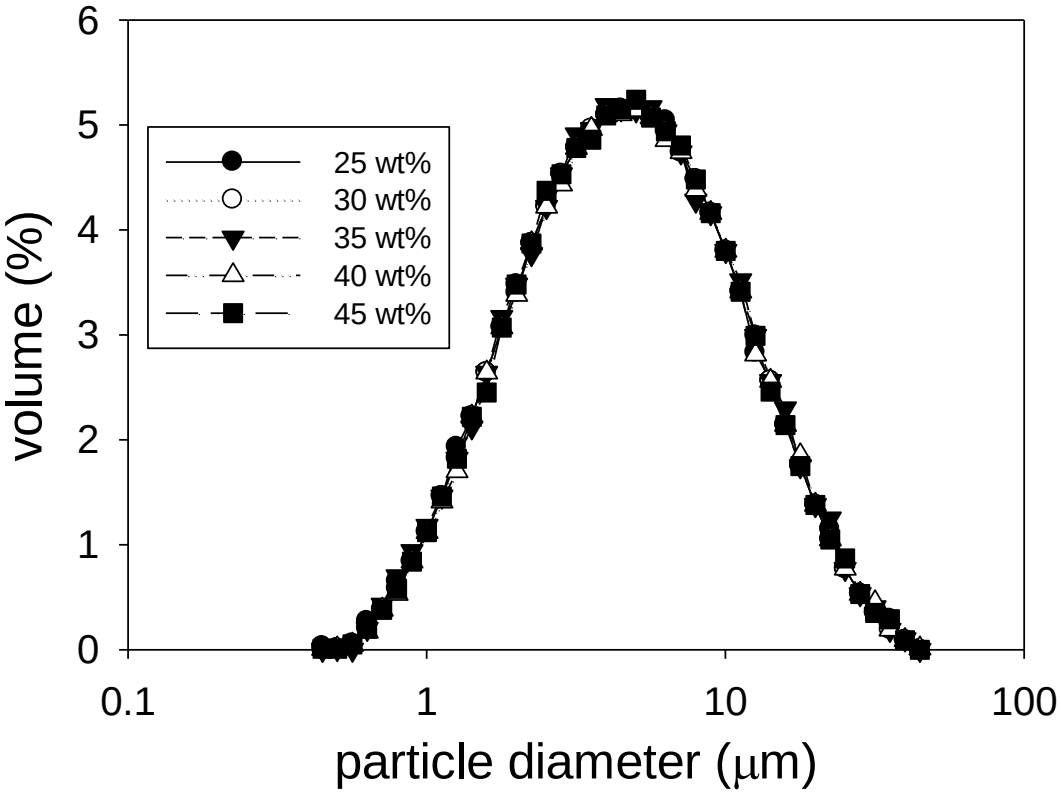

Figure 3.6. Frequency particle size distributions of slurries of 25 – 45 wt% solids concentration milling for 60 min.

3.3.2.2 Effect of milling time

The diameters $d_{0.1}$, $d_{0.5}$ and $d_{0.9}$ of the slurries at 40 wt% solids concentration after milling for 0 – 240 min are shown in Table 3.3, while their psds are shown in Figure 3.7. These results show a general decrease in the particle diameters with the increase in milling time. This behaviour can be explained by considering the relationship between the number of stress events (SN) and the bead milling time (t_m) in Equation 2.5 in Chapter 2. It is clear that SN is directly proportional to the milling time t_m, thus meaning that there was an increase in the number of stress events as milling continued. As a result of this, there is a systematic shift of the psd curves towards the left as smaller particles were being produced. This is highlighted by the presence of bimodal distributions after milling for 10 and 20 min, but these distributions subsequently became unimodal at milling times more than 40 min. It is shown from the results that all the slurries milled for at least 60 min conformed to the set target of $d_{0.9} < 15$ μm and $d_{0.1} < 2$ μm.

Table 3.3. Particle diameters for slurries at 40 wt% concentration after milling for 0 – 240 min.

Bead milling time (min)	$d_{0.1}$ (μm)	$d_{0.5}$ (μm)	$d_{0.9}$ (μm)
0	4.63	20.70	43.43
10	2.64	15.16	33.42
20	1.90	9.56	23.02
40	1.71	6.13	16.47
60	1.34	4.36	12.74
240	1.09	2.76	7.82

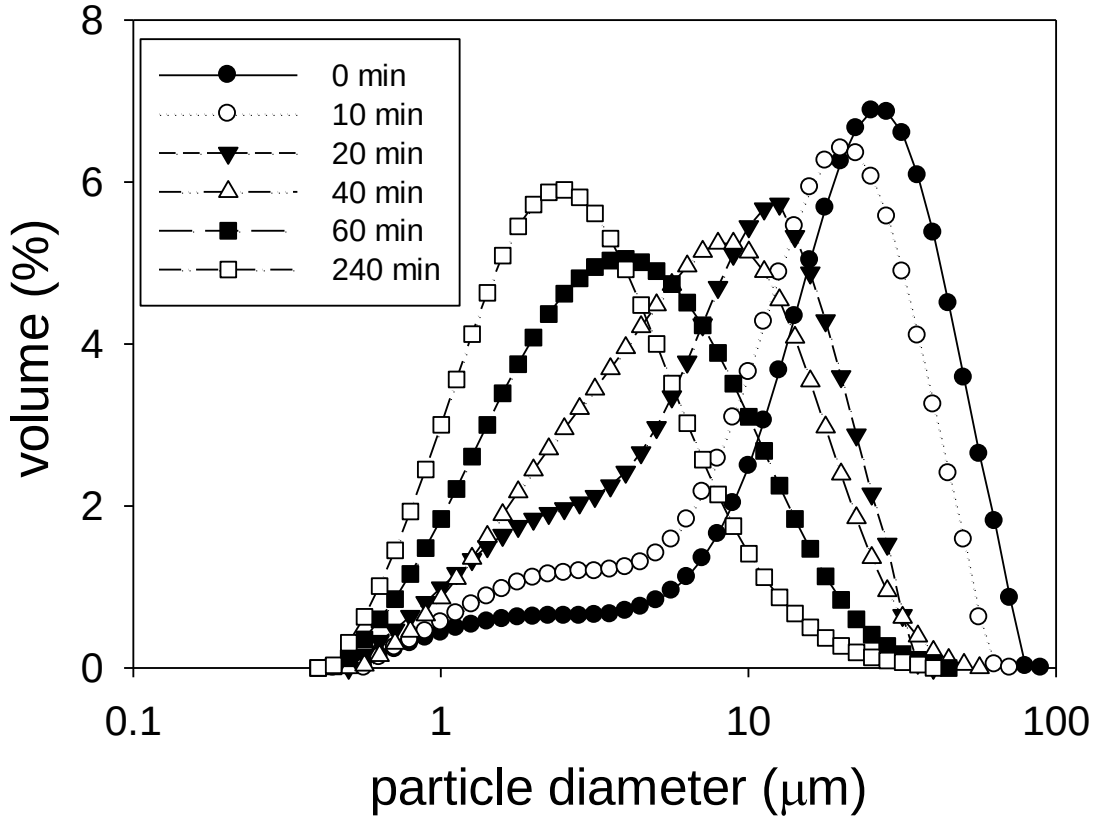

Figure 3.7. Frequency particle size distributions of slurries of 40 wt% solids concentration after milling for 0 – 240 min (5 mm media diameter).

A further understanding of the fragmentation behaviour can be obtained by taking account of the rate of decrease in the particle diameters with the increase in milling time (Figure 3.8). It is shown that large particles have a higher rate of size reduction compared to small particles. This fact is evidenced by the steep slope of $d_{0.9}$ curve compared to those of $d_{0.5}$ and $d_{0.1}$. Similarly, the slope of $d_{0.5}$ curve is steeper than that of $d_{0.1}$. The reason for this development is that large particles were fragmented into smaller ones without regeneration. On the contrary, the smaller particles were being continuously regenerated from the fragments of large particles. The rate of decrease in

the particle diameters as milling progresses is in accordance with similar work which showed an increase in small particles compared to large particles when the milling duration was increased (Blachou et al., 1992).

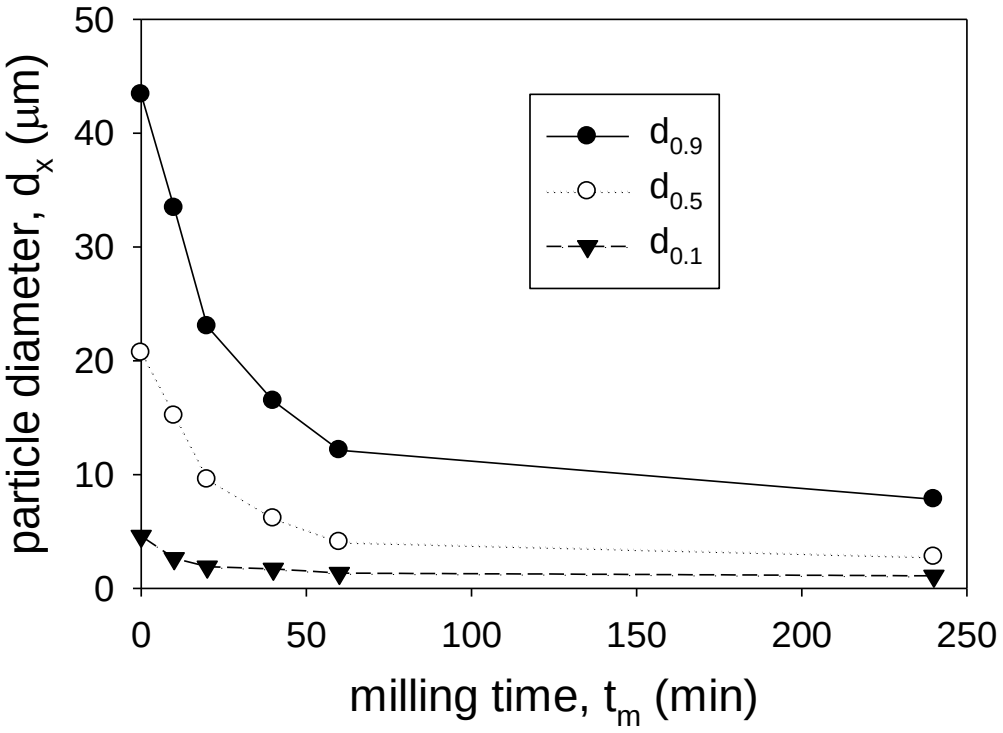

Figure 3.8. Systematic decrease in the slurry particle diameters with the increase in milling time.

3.3.2.3 Effect of grinding media diameter

The slurry psds at the solids concentration of 40 wt% after milling for 0 – 240 min using 1 mm media are shown in Figure 3.9. The corresponding result obtained for the 5 mm media was already shown in Figure 3.7.

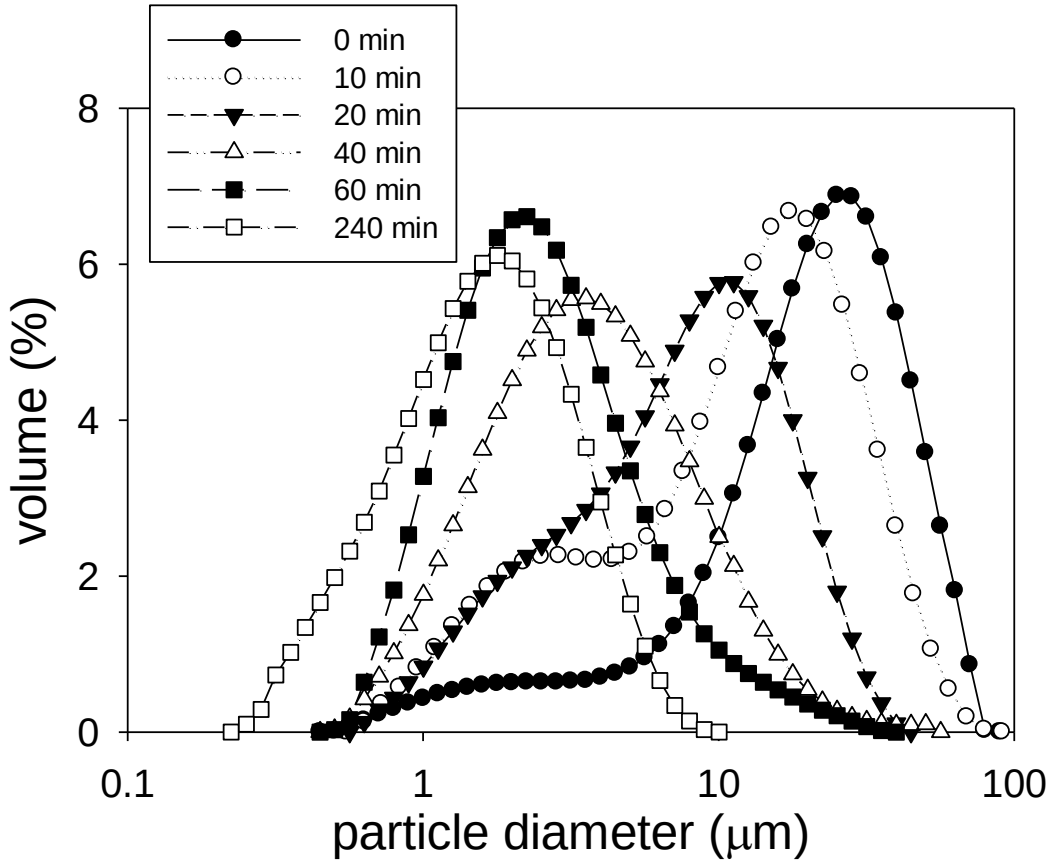

Figure 3.9. Frequency particle size distributions of slurries of 40 wt% solids concentration after milling for 0 – 240 min (1 mm media diameter).

In Figures 3.7 and 3.9 the systematic shift of the psd curves towards the left is a confirmation that smaller particles were being produced in the mill tank. The bimodal distributions obtained in Figure 3.9 at milling times of 10 and 20 min which later became unimodal after further milling shows the transition to formation of finer particles. The particle diameters obtained from both media dimensions are jointly presented in Table 3.4. It is shown from the results that using a 1 mm media diameter resulted in finer particles at equal milling time compared to using a 5mm media diameter. The use of 1 mm media diameter enabled the production of slurry which

conform to the set target of $d_{0.9}$ < 15 μm and $d_{0.1}$ < 2 μm at a reduced time of 40 min, in comparison to the 5 mm media diameter which took 60 min.

Table 3.4. Particle diameters for the slurries at 40 wt% concentration after milling for 0 – 240 min using different media diameters.

milling time (min)	5mm media diameter			1mm media diameter		
	$d_{0.1}$ (μm)	$d_{0.5}$ (μm)	$d_{0.9}$ (μm)	$d_{0.1}$ (μm)	$d_{0.5}$ (μm)	$d_{0.9}$ (μm)
0	4.63	20.70	43.43	4.63	20.70	43.43
10	2.64	15.16	33.42	1.92	11.98	30.03
20	1.90	9.56	23.02	1.79	7.38	17.80
40	1.71	6.13	16.47	1.25	3.39	9.92
60	1.34	4.36	12.74	1.01	2.27	6.35
240	1.09	2.76	7.82	0.45	1.12	3.67

The effect of grinding media diameter on the ground product can be thoroughly appreciated by considering what happens to the key comminution parameters SN, SE and $E_{m,p}$ during the milling process. Given that all other operating parameters are constant except the grinding media diameter d_{GM}, then Equations (2.5) & (2.6) in Chapter 2 reduce to Equations (3.1) & (3.2) respectively:

$$SN \propto \frac{t_m}{d_{GM}^2} \tag{3.1}$$

$$SE \propto SE_{GM} \propto d_{GM}^3 \tag{3.2}$$

Figure 3.10 represents the relationship between particle diameter of the ground products and SN according to Equation (3.1).

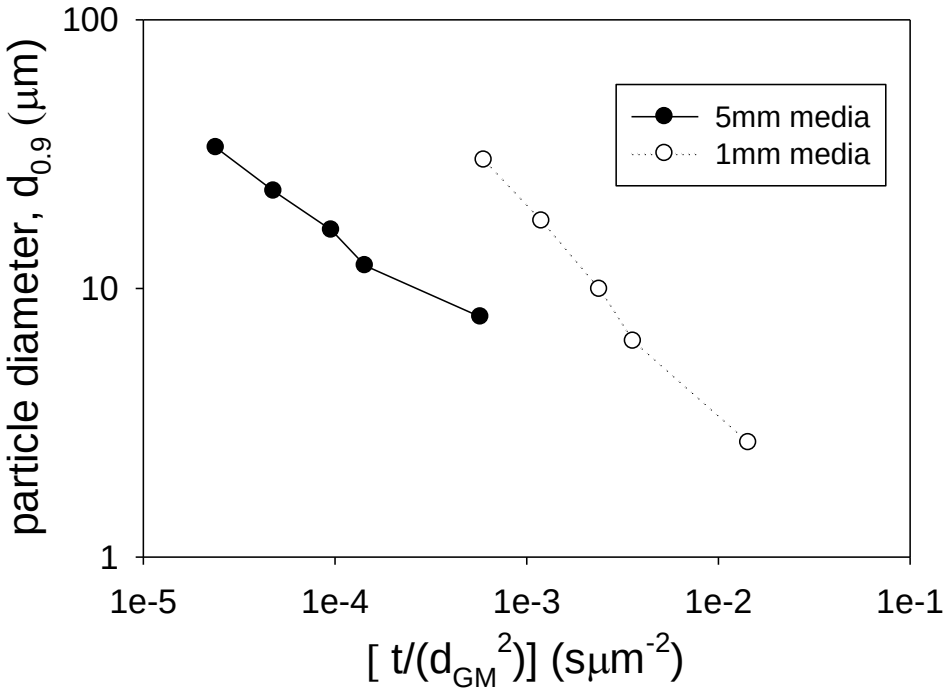

Figure 3.10. Effect of media diameter on SN.

for 1 mm and 5 mm media

$$\frac{SE_5}{SE_1} = \frac{d_{GM5}^3}{d_{GM1}^3} = \frac{5^3}{1^3} = 125\,\text{times} \qquad (3.3)$$

where

SE_1 and d_{GM1} represent the stress energy (J) and diameter (mm) for 1 mm media

SE_5 and d_{GM5} represent the stress energy (J) and diameter (mm) for the 5 mm media

It is shown in Figure 3.10 that the number of stress events SN increased with the decrease in media diameter, while on the other hand Equation (3.3) shows that the stress

energy SE increased with the increase in media diameter. It is known from section 2.2.2.1 that both SN and SE have important influence on the comminution process. Since the use of 1 mm media diameter resulted in smaller particle diameters compared to the 5mm media diameter, there is strong evidence to show that the SN effect appeared dominant on the SE effect in this case.

But the specific energy $E_{m,p}$ is a measure of both SN and SE as indicated in Equation (3.4). Given that all other operation parameters are constant except the media diameter, therefore a ratio of the specific energy to the power number is given by (Fadhel and Frances, 2001):

$$\frac{E_{m,p}}{Po} \propto N^3 t_m \qquad (3.4)$$

This very useful relationship can be used as a basis for describing how efficiently the power drawn by the rotating shaft was translated into $E_{m,p}$ for both media diameters (Fadhel and Frances, 2001).

Figure 3.11 shows clearly that energy was utilised more efficiently in the mill for particle comminution when the 1 mm media diameter was used because smaller particle diameters were produced at the same $\frac{E_{m,p}}{Po}$ input throughout the milling process compared to the 5 mm media. This is a confirmation that 1 mm media had an overall favourable effect on the comminution than the 5 mm media.

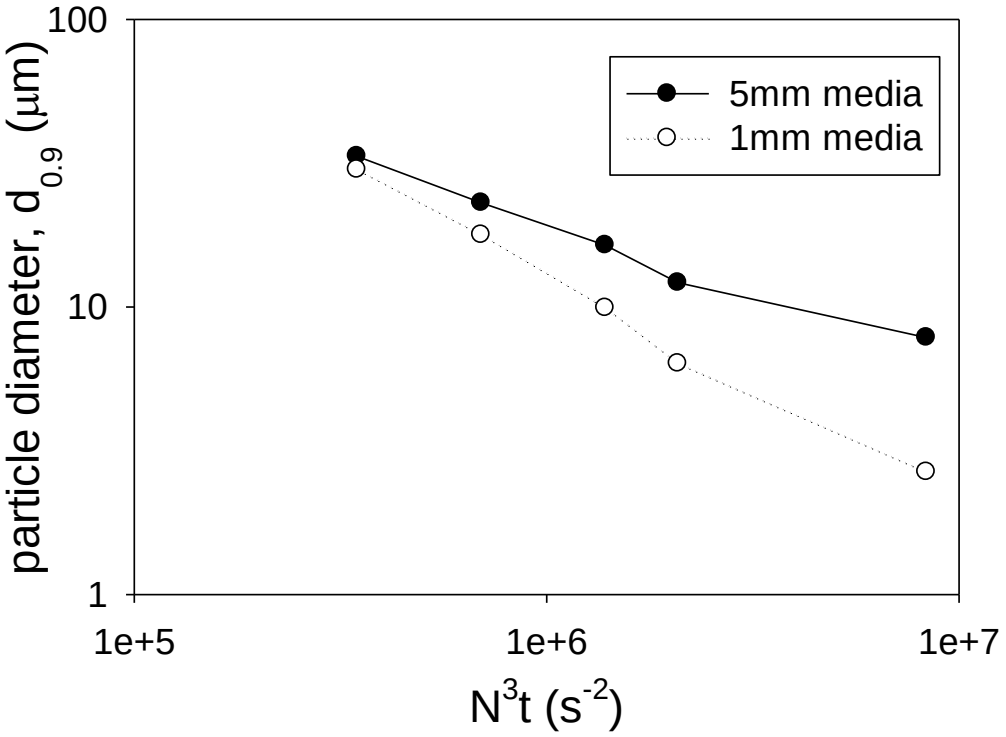

Figure 3.11. Particle diameter $d_{0.9}$ as a function of N^3t.

3.3.3 γ-Alumina morphology

The γ-alumina particles of the following categories were visualised by SEM (Jeol 6060; Oxford Instruments, UK) as shown in Figure 3.12:

(a) as-received particles, i.e. particles not yet milled, and

(b) particles of the slurry obtained after 60 min of milling

It is shown in Figure 3.12 (a) that the as-received γ-alumina particles appear large ($d_{0.9}$ = 43.43 μm), roundly shaped and not fractured.

The particles which have been milled for 60 min in Figure 3.12 (b) are however much smaller ($d_{0.9}$ = 12.74 μm), irregularly shaped and shattered.

The difference in the morphology of γ-alumina particles before and after bead milling is an attestation to the fragmentation brought about by the milling process.

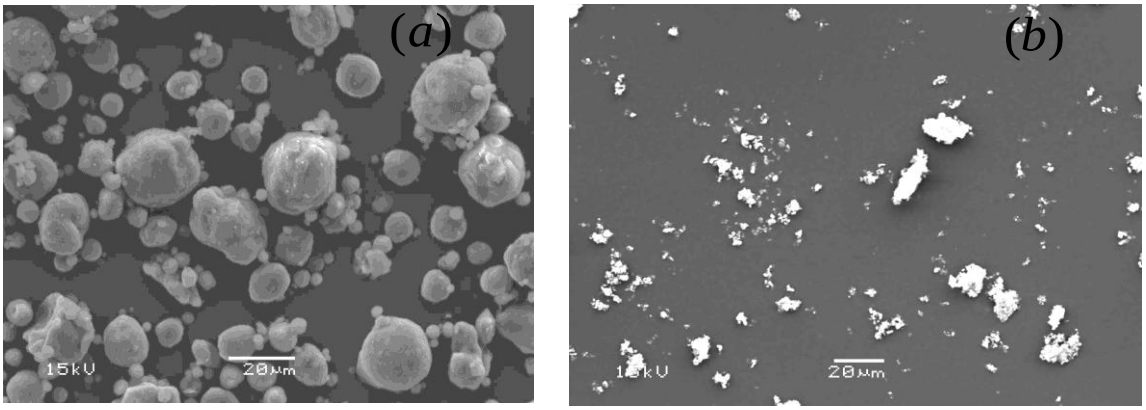

Figure 3.12. SEM images of γ–alumina particles: (a) as-received; and (b) milled for 60 min using media of 5 mm diameter.

3.4 STRATEGIES FOR ACHIEVING RESEARCH AIMS

Having developed protocols for characterising γ–alumina slurries, this section presents an outline of how the research aims listed in section 1.7 (Chapter 1) will be accomplished. A blend of exploratory and engineering techniques will be used to investigate the influential roles of slurry characteristics and the coating process on the final coating quality.

The slurries will be characterised with emphasis on obtaining well dispersed particles at optimal rheological advantage. In addition to the use of SEM and XRD, seasoned efforts will be made in designing a modern method using laser profiling interferometry (LPI) for measuring Fecralloy® surface roughness in two and three dimensional geometries in order to ascertain the optimal preoxidation conditions.

In contrast to the conventional methods, the γ–alumina slurry will be coated onto Fecralloy® using an automatic film applicator equipped with wire-wound bars. Unlike dip-coating (Jia et al., 2007), this method of coating is at a controlled shear rate and, therefore, capable of eliminating coating inconsistencies (Sheen Instruments Manual, 2006). There are currently no known previous studies on the effects of the operating conditions (e.g. coating speed and bar size) of the film applicator on the coating properties. This may be because the film applicator is relatively new for coating Fecralloy®. Therefore, the effects of these operating conditions will be studied with a view to deriving an optimal coating methodology.

The coating properties will be assessed using an ultrasonic vibrator and the SEM. The effects of drying and calcination conditions on the coating properties will also be investigated. This will be followed by the determination of how the slurry characteristics (namely pH and solids concentration) influence the coating properties, while addressing the existing knowledge gap. There will be attempts made to devise a physically derived technique for measuring coating adherence. Finally, the influence of different psds obtained from singly prepared and blended slurries will be studied.

3.5 CONCLUSIONS

The critical effects of the pH on γ–alumina stabilisation have been determined by zeta potential measurements using an Acoustosizer and a Zetamaster. The iep point and the natural pH of γ–alumina were found at 7.7 and 9.1 respectively. The pH which produced optimal stabilisation (i.e. at ζ = 41 mV) was determined as 4. The slurries achieved stabilisation through the electrostatic repulsion of the charged particles.

The basic comminution concepts revealed the key parameters (i.e. SN, SE and $E_{m,p}$) which govern the fragmentation of γ–alumina particles in a bead mill. These parameters were used as tools for describing these experimental investigations that followed:

(a) For slurries at 25 – 45 wt% solids concentration, the ground particles showed no change in their psds because of the neutralizing effect of SN: decrease in N_P, yet increase in N_C and P_S.

(b) For slurries at 40 wt% solids concentration, the ground particles showed a decrease in particle diameters as a function of time due to the increase in SN.

(c) For slurries at 40 wt% solids concentration, the use of 1 mm media diameter resulted into finer particles because the specific energy was used more efficiently in the particle comminution compared to the 5 mm media diameter.

The slurries that conformed to the set target of psds ($d_{0.9}$ < 15 µm and $d_{0.1}$ < 2 µm) were achieved after 40 min of milling using the 1mm diameter media. However, it took 60 min to reach the same target using the 5 mm media diameter.

The differences in SEM images of the particles before and after milling corroborated the fragmentation behaviour that was described by the comminution concepts as the as-received particles changed from round to finer and irregularly shaped fragments.

4

RHEOLOGY OF γ–ALUMINA SLURRIES

This chapter presents the results of experiments to determine the rheology of γ-alumina slurries from the viewpoint of catalyst preparation technology. The parametric effects of slurries (pH, solids concentration, particle size distribution and temperature) are investigated. The results showed the steady shear behaviour of the slurries as shear thinning which was adequately described by the power law model. The slurry had the lowest measured apparent viscosity at the pH of 4 which produced the desired optimal particle stabilisation. The slurry viscosity increased with increase in the solids concentration, fine particles and temperature.

4.1 INTRODUCTION

Now that stabilised γ-alumina slurries of the required particle size distributions have been prepared, the next tier of characterisation that is pertinent to catalyst development is the rheology of the slurries.

Rheology is defined as the science of the deformation and flow of matter. It can also be described as the study of the relationships between stress and strain in a non-rigid substance. The rheology of slurries, though traditionally an academic / technical field, has generated a lot of commercial interest due to its links to quality-determining properties of coatings (Hill and Carrington, 2006; Harris, 1977).

To produce coatings for optimal catalytic performance, it is crucial that the rheological behaviour of γ-alumina slurries should be controlled. This Chapter presents experiments geared to exploring the rheology of γ-alumina slurries from the viewpoint of catalyst preparation technology.

The effects of key slurry characteristics, such as pH, solids concentration, particle size distribution (psd) and temperature are investigated. The findings will be used as a platform for ensuring consistency and assessment of the behaviours of coating slurries.

4.2 RHEOLOGICAL CLASSIFICATION OF SLURRIES

(a) **Newtonian:** These are slurries whose shear stress versus shear rate curve is linear and passes through the origin. The Newton's law of viscosity in Eq. (4.1) is used to describe this behaviour (Harris, 1977).

$$\tau = \mu_{slurry}\,\dot{\gamma} \qquad (4.1)$$

where

τ = shear stress (Pa)

μ_{slurry} = slurry viscosity (referred to as dynamic viscosity for Newtonian fluids) – the constant of proportionality (Pas)

$\dot{\gamma}$ = shear rate (s^{-1})

(b) **non-Newtonian:** These are slurries which do not obey Newton's law of viscosity. They have an apparent viscosity, μ, which may vary with shear rate and time (the apparent viscosity is simply referred to as the viscosity in this thesis). It is defined by Harris (1977):

$$\mu = \frac{\tau}{\dot{\gamma}} \qquad (4.2)$$

The non-Newtonian slurries can be categorised into **time-independent** (e.g. shear thinning, shear thickening and viscoplastic) slurries and **time-dependent** (e.g. thixotropic) slurries.

4.3 EXPERIMENTAL

4.3.1 AR 1000 Rheometer

The rheology of slurries was studied using a stress-controlled AR 1000 rheometer (TA Instruments, UK) equipped with a 40 mm parallel plate geometry (Figure 4.1). The deformation of slurries was measured in the non-destructive region at shear rates not exceeding 1000 s^{-1}. This revealed invaluable information about the microscopic interactions in the slurries, as well as measuring the shear stress / shear rate relationships.

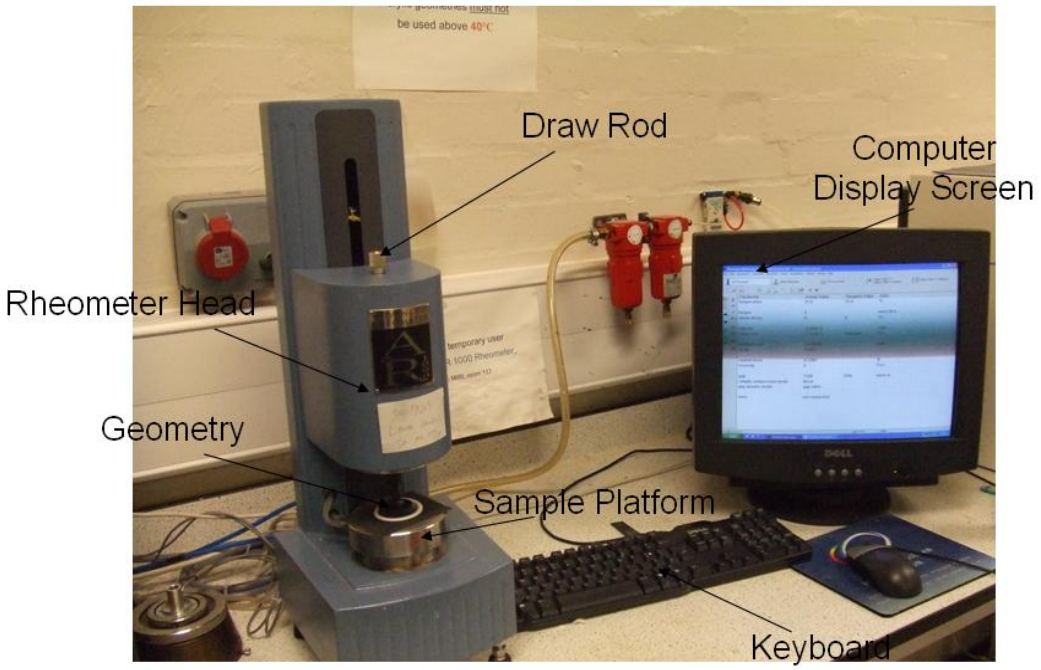

Figure 4.1. AR 1000 rheometer connected to a computer.

4.3.2 Parallel plate Geometry

The 40 mm parallel plate geometry used was made with a stainless steel. The choice of a stainless steel was informed by its structural advantages, notably the low coefficient of thermal expansion as well as the ability to withstand frequent use. The parallel plate geometry was chosen because it allowed the rheological properties of particle-containing slurries to be effectively measured. The gap could be set at a specified distance, thereby obviating problems due to particle size (TA Instruments, UK).

It is widely acknowledged that particle-containing slurries need to have a minimum ratio of gap-to-particle ratio of 10:1. This ratio can be considerably more, typically 20:1, for slurries of solids concentration more than 21 wt % (Barnes, 2000). The control software package of the AR 1000 rheometer enabled rheological measurements to be taken in such a way as to compensate for the stress non-uniformity across the plate diameter. The schematic diagram of the parallel plate is shown in Figure 4.2.

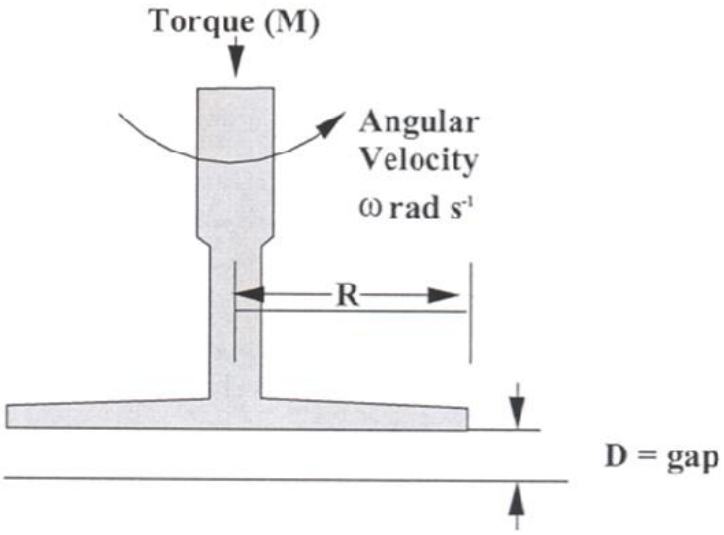

Figure 4.2. Schematic diagram of a parallel plate geometry.

4.3.3 Test for wall slip

The presence of wall slip in slurries will, if not checked, lead to a depletion problem which will inevitably affect the accuracy of the rheological characterisation. Wall slip occurs in two-phase slurries because of the displacement of the dispersed phase away from solid boundaries, leaving a lower viscosity and depleted layer of liquid. This is brought about by steric, hydrodynamic and chemical forces and constraints acting on the disperse phase immediately adjacent to the walls. Wall slip is commonly experienced in slurries containing submicron particles when the concentration is dependent on the slurry viscosity (Barnes, 1995).

To check for wall slip, the shear stress was measured as a function of shear rate under steady state conditions at varying gap values: 400, 500, 600, 700 and 800 μm (Figure 4.3). This was performed on the slurries which were milled for 1 h at a standard pH of 4 according to the procedures explained in sections 3.2.1 & 3.2.2. All slurries were formulated at 40 wt % solids concentration and tested at a temperature of 25 ^{o}C. The slurry sample was placed on the platform of the rheometer, and allowed to relax for 2 mins before rheological tests were done to minimise previous shearing effects. To minimise evaporation during the testing, a trap was used to cover the parallel plate geometry.

It is shown from Figure 4.3 that there exists a variation in the positioning of the steady shear flow curves, thus confirming the presence of wall slip.

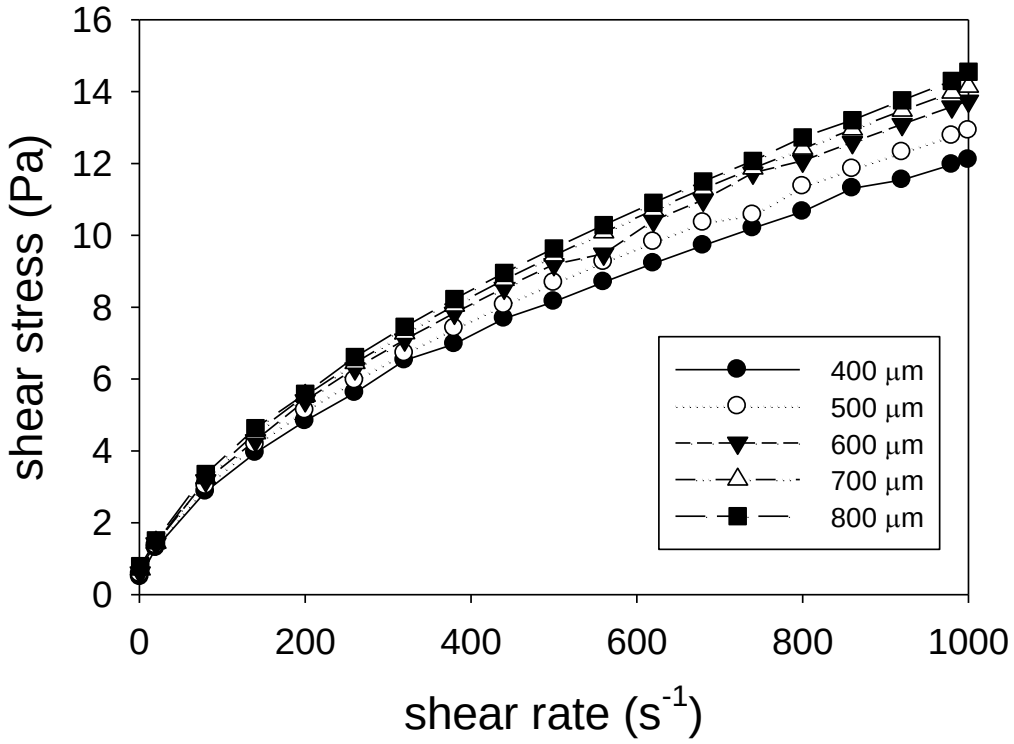

Figure 4.3. Steady shear flow curves for 40 wt% slurries at different gaps without using roughened geometry.

A roughened surface (i.e. P500 water-proof sand paper) was bonded to both plates as demonstrated by previous studies (Barnes, 1995; Magnin and Piau, 1987), and the same tests were repeated. It is confirmed by Figure 4.4 that wall slip has subsequently been eliminated because all the flow curves are nearly superimposed for different gaps. Therefore subsequent measurements were done using the roughened geometry, which has been shown to be capable of eliminating slip effects, therefore providing consistency in rheological measurements. The gap was set at 600 μm, which is 20 times the diameter of the biggest particle in the slurry (i.e. 30 μm).

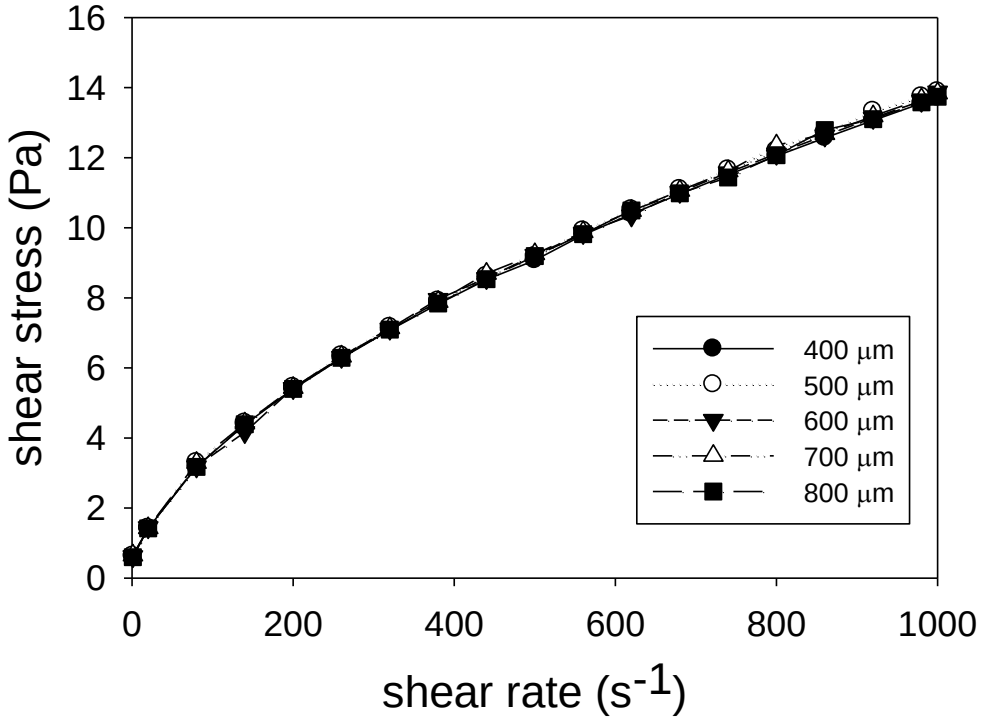

Figure 4.4. Steady shear flow curves for 40 wt% slurries at different gaps with roughened geometry.

4.3.4 Preliminary tests

These tests were designed to investigate the time-dependent and steady shear flow properties of the slurry. The standard slurry characteristics used are the following:

(i) solids concentration = 40 wt%

(ii) slurry pH = 4

(iii) temperature = 25 ^{o}C

(iv) diameter $d_{0.1}$; $d_{0.5}$; $d_{0.9}$ = 1.34; 4.36; 12.74 μm (see definition in section 3.2.3.1)

The two tests are described below:

(a) *Time dependency*: The slurry viscosity as a function of time was investigated for 3 min at different constant shear stresses of 1, 5, 10 and 20 Pa. This procedure was repeated twice after 3 min of relaxation.

(b) *Steady shear flow*: The relationship between the shear stress (and by default the slurry viscosity) and the corresponding shear rate under steady state conditions was investigated.

4.3.5 Parametric characterisation

The rheological effects of key slurry properties (i.e. pH, solids concentration, psd and temperature) were investigated under steady state conditions.

(a) *Effect of pH*: The shear flow of slurries was investigated for pH values of 3, 4, 5, 6, 7, 9 and 10. The pH adjustment was made using solutions of acetic acid for 3 – 7 (acidic and neutral regions) and sodium hydroxide for 9 – 10 (alkaline region). The pH of 8 was left out as the particles were very aggregated at this pH because of the closeness to the iep of 7.7 which was determined in section 3.3.1.

(b) *Effect of solids concentration*: The shear stress was varied under steady state conditions for slurries at solids concentrations of 25 – 45 wt.%.

(c) *Effect of particle size distribution (psd)*: Similar to (b), the shear stress was varied for slurries milled for 10 – 240 min using media of 1 mm or 5 mm diameters (the psds obtained have already been discussed in section 3.3.2.3). The slurries from 5 mm media had diameter $d_{0.9}$ in the range of 7.8 – 33.4 μm, while those from 1 mm media had diameter $d_{0.9}$ in the range of 2.7 – 30.0 μm.

(d) *Effect of temperature*: This test was done at constant shear stress. Having ascertained a constant steady state viscosity for 3 min, the slurry temperature was increased in steps from 4 – 40^{o}C, while the steady state viscosity was measured as a function of temperature.

4.4 RESULTS AND DISCUSSION

4.4.1 Preliminary tests

4.4.1.1 Time dependency

The viscosity-time relationship under unsteady state conditions at constant shear stresses of 1, 5, 10 and 20 Pa is shown in Figure 4.5. The same curves were obtained when the tests were repeated on slurries which have been allowed to relax for 3 min after testing. The transient reduction of viscosity with time at constant shear stress was an indication of the occurrence of a microstructural change in the slurry.

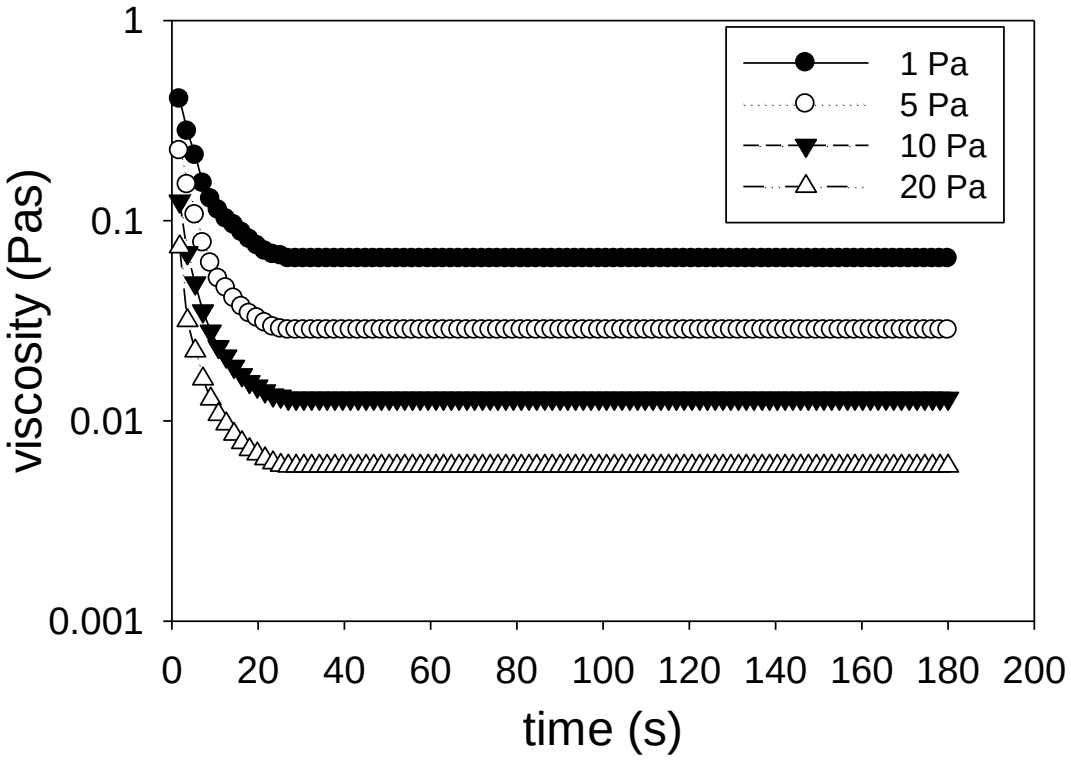

Figure 4.5. Viscosity- time curves at constant shear stress.

This microstructural phenomenon, which is referred to as thixotropy, is commonly associated with most particle-containing slurries. Thixotropy is defined as the decrease in time of viscosity under constant shear stress or shear rate, followed by a gradual recovery when the stress or shear rate is removed (Barnes, 1997; Barnes et al., 1989).

Thixotropy can be advantageous (such as in slurry coating, paints and inks) as it allows coatings and paints to be brushed or spread out upon the substrate (Kuwano et al., 1994; Overdiep, 1986). It can also be disadvantageous (such as in food thickeners, detergents and wastewater sludge) as they may cause creaming of suspended particles (Battistoni et al., 1993; Noik et al., 1993).

In rheological characterisation however, the presence of thixotropic effects in slurries undergoing testing can give inconsistencies in the measurements taken, and this will ultimately lead to inaccurate description of the slurry behavior. Therefore, the tests described in Figure 4.5 would establish whether thixotropy can be removed in subsequent measurements and, if so, how this could be achieved.

It is shown that for all the constant shear stresses examined that the slurry viscosity decreased with time for $t < 25$ s, and remained constant afterwards for $t > 25$ s. This is a confirmation that that time dependency (or thixotropy) could be eliminated in subsequent measurements by shearing at a constant shear stress for $t \approx 25$ s before taking steady shear measurements

4.4.1.2 Steady shear flow

The steady state shear rheology of the slurry between the shear rate region of 0 – 1000 s^{-1} is shown in Figure 4.6.

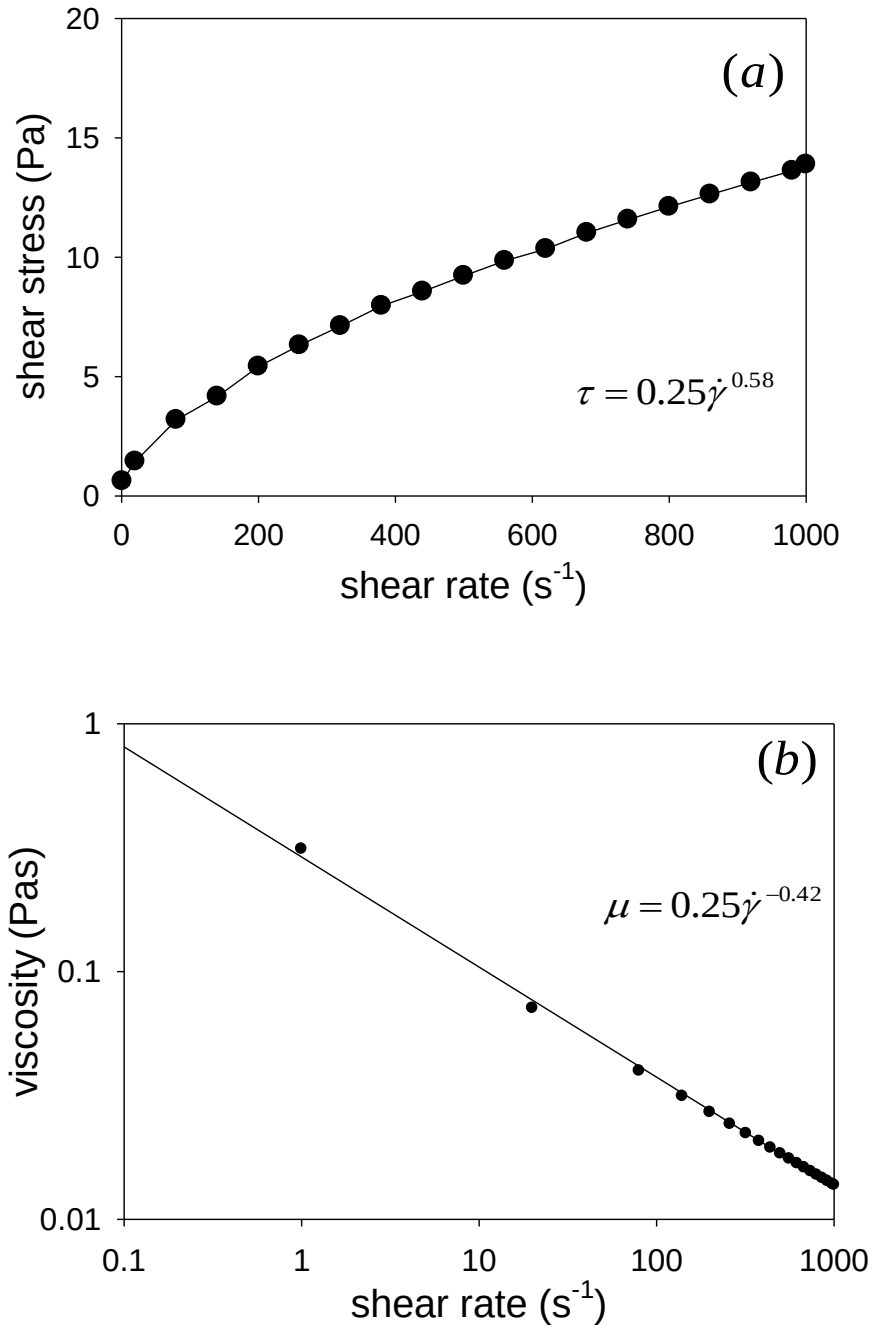

Figure 4.6. Flow curves of 40 wt % slurry at pH of 4 and temperature of 25 ^{o}C : (a) steady shear flow and (b) viscosity.

The behaviour displayed represents a shear-thinning property. This means that the slurry viscosity, which is the gradient of the curve at a given shear rate, decreases with shear rate over the shear rate region investigated. The shear thinning behaviour can be attributed to the particle movement from an initial random arrangement towards the formation of strings. This change in spatial arrangement enables the cooperative movement of particles with fewer restrictions, thereby lowering the viscosity (Chen and Fan, 2002a; Barnes et al., 1989).

The Ostwald de Waele power law model in Equation 4.3 can be used to adequately describe this shear thinning behaviour (Roberts et al., 2001; Harris, 1977).

$$\tau = k\dot{\gamma}^{n} \tag{4.3}$$

where

the consistency index k and flow behaviour index n are empirical curve fitting parameters. The dimensions of k depend upon the value of n, therefore k is not a material property.

The specific equation describing the slurry behaviour is therefore

$$\tau = 0.25\dot{\gamma}^{0.58} \tag{4.4}$$

where

Goodness of fit: r^2 value = 0.99

k = 0.25

n = 0.58

The flow behaviour index n describes whether the slurry is shear thinning or shear thickening. If $n < 1$ the slurry is shear thinning, and if $n > 1$ the slurry is shear thickening. The consistency index k denotes slurry consistency over the shear rate

region investigated.

The shear thinning behaviour of γ–alumina slurries compares favourably with similar studies done by Palmqvist et al. (2006), Vishista et al. (2004) and Anklekar et al. (1998), which studied the rheological behaviour of 5 – 51 wt% slurries.

4.4.2 Parametric characterisation

4.4.2.1 Effect of pH

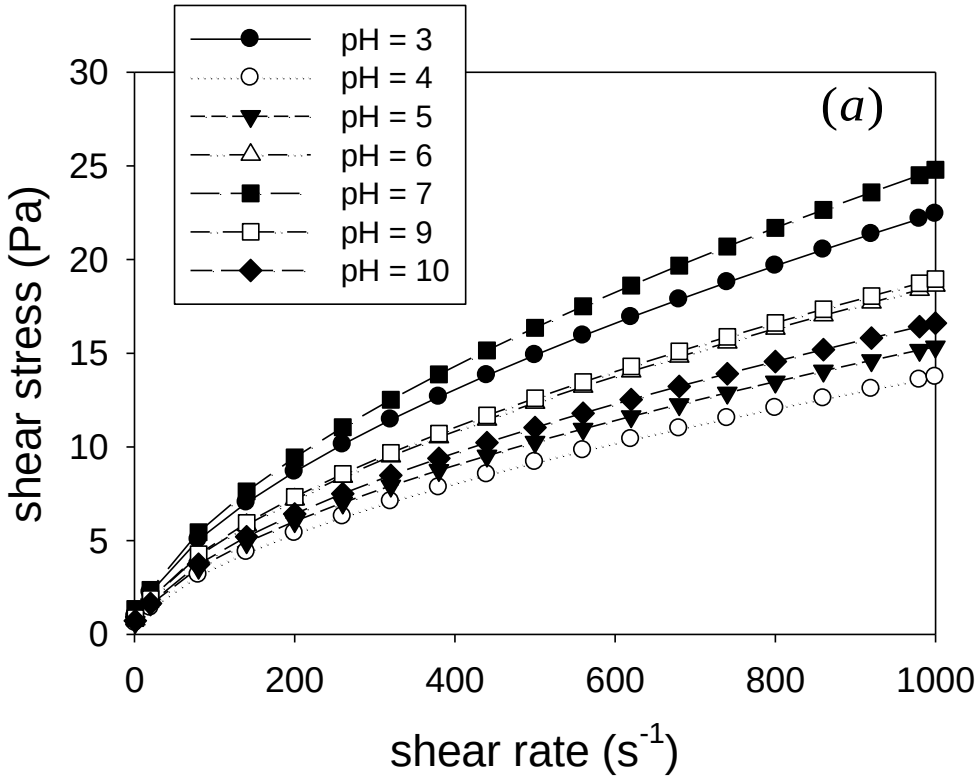

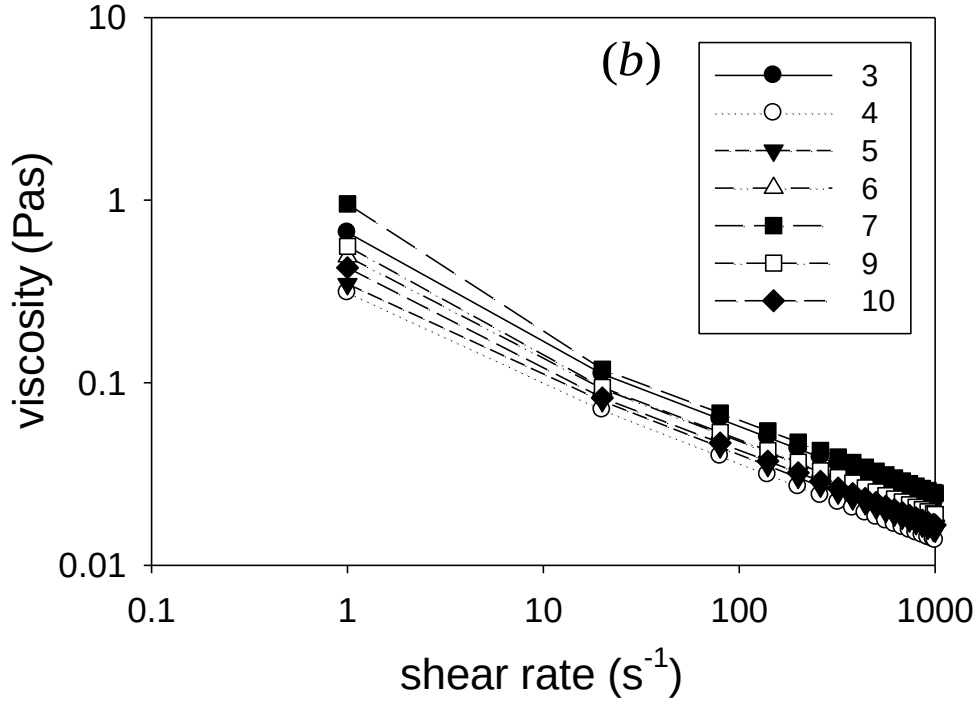

Figure 4.7. Effect of pH on the slurry rheology at 40 wt% solids concentration: (a) steady shear flow and (b) viscosity.

Table 4.1. Key of the power law models at different slurry pH.

Slurry pH	Consistency index k	Flow behaviour index n	Goodness of fit r^2 value
3	0.38	0.59	0.98
4	0.25	0.58	0.99
5	0.28	0.58	0.99
6	0.32	0.59	0.99
7	0.39	0.60	0.98
9	0.32	0.59	0.99
10	0.28	0.59	0.99

Figures 4.7 (a) and (b) show that all the slurries tested at pH range of 3 – 10 exhibited shear thinning behaviour which was adequately described by the power law model and the key parameters are presented in Table 4.1. The steady shear flow curves for the slurry at the pH of 4 are positioned at the bottommost level in Figures 4.7 (a) and (b) which implies that it had the least viscosity at all the shear rate regions examined.

The relationship between the pH and slurry viscosity can be made more visible by considering the viscosity-pH relationship for the slurries at a reference shear rate of 1000 s^{-1} which represents the shear rate used by Johnson Matthey (JM) for coating slurries (Figure 4.8).

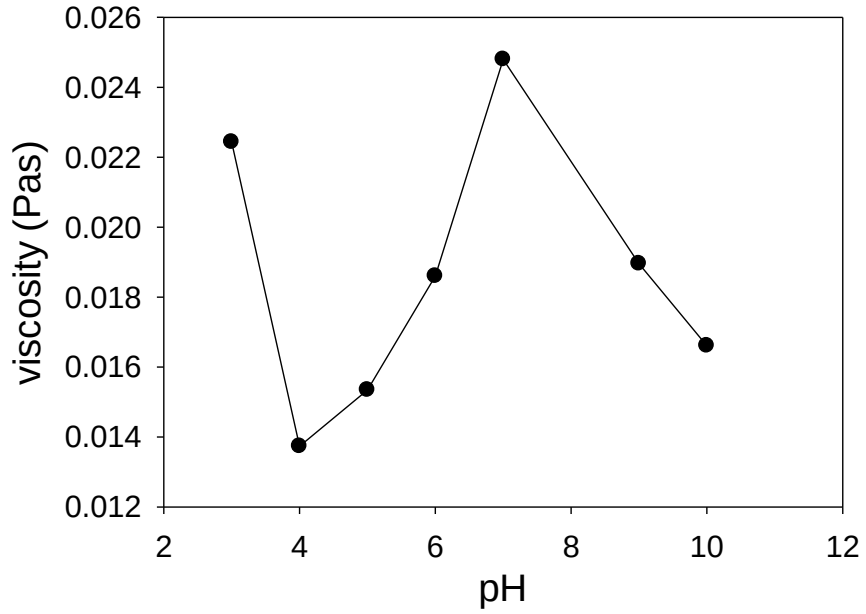

Figure 4.8. Viscosity of 40 wt% slurries as a function of pH at a reference shear rate of 1000 s^{-1}.

The viscosity which was initially at 22.5 mPas at a pH of 3 was reduced to 13.7 mPas, the minimum, at a pH of 4. It is shown that the viscosity then progressively increased to 15.3, 18.5 and 24.8 mPas at pH of 5, 6 and 7 respectively. The viscosity later reduced to around 19.0 and 17.0 mPas at pH of 9 and 10 respectively.

The viscosity-pH relationship consolidates that of the zeta potential and pH which was studied in Chapter 3 and, as such, can be explained in the light of particle stabilisation. The viscosity reduces as the slurry pH moves away from the isoelectric point (iep) of 7.7. The particles were less aggregated away from the iep and there was therefore less resistance to flow. The minimum viscosity was achieved at the pH of 4 which produced the optimal particle stabilisation.

4.4.2.2 Effect of solids concentration

The increase in the slurry solids concentration means that more γ–alumina particles are present in a given mass (or volume) of the aqueous medium. Therefore, thicker slurries were obtained by increasing the solids concentration from 25 – 45 wt% (i.e. 31 – 56 vol.%) because of reduced particle separation. Due to increasing inter-particle interactions with the increase in solids concentration, the particles tend to show more reluctance to flow, which leads to the increase in slurry viscosity (Hoffman, 1992). This is confirmed in Figure 4.9 (a) which shows the steady shear flow curves for the slurries at a solids concentration of 25 – 45 wt%.

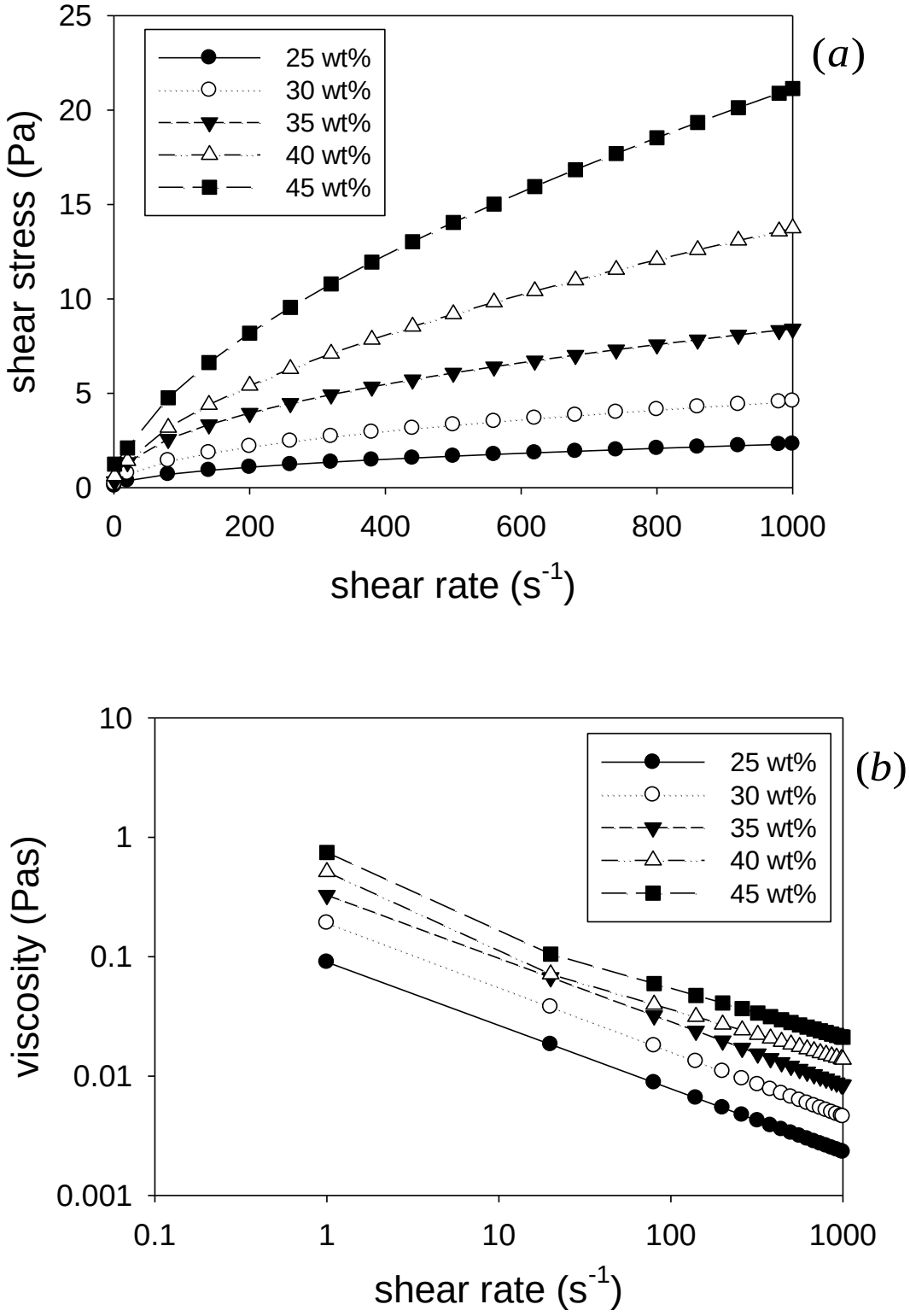

Figure 4.9. Effect of solids concentration on the slurry rheology : (a) steady shear flow and (b) viscosity.

The flow curve of the 25 wt% slurry lies at the bottommost level, while that of the 45 wt% slurry at the topmost level. The flow curves of 30, 35 and 40 wt% slurries are positioned in between those of 25 and 45 wt% in increasing order of solids concentrations and viscosity. Figure 4.9 (a) further shows that all the slurries exhibited shear thinning behaviour which was adequately described by the power law model as listed in Equations (4.5) – (4.9).

25 wt %:	$\tau = 0.04\dot{\gamma}^{0.58}$	(r^2 value = 0.98)	(4.5)
30 wt %:	$\tau = 0.09\dot{\gamma}^{0.57}$	(r^2 value = 0.99)	(4.6)
35 wt %:	$\tau = 0.14\dot{\gamma}^{0.59}$	(r^2 value = 0.99)	(4.7)
40 wt %:	$\tau = 0.25\dot{\gamma}^{0.58}$	(r^2 value = 0.99)	(4.8)
45 wt %:	$\tau = 0.36\dot{\gamma}^{0.59}$	(r^2 value = 0.99)	(4.9)

It is noted that the consistency index k which is proportional to the slurry viscosity increased progressively (0.04, 0.09, 0.14, 0.25 and 0.36) with the increase in solids
The effect of solids concentration is clearly revealed in terms of viscosity in Figure 4.9 (b). The results in Figure 4.9 show good agreement with the findings of Binner and McDermott (2006) and Agrafiotis and Tsetsekou (2000) which also showed that the slurry viscosity increases with an increase in solids concentration.

Figures 4.10 show the modelling of the relationship between the slurry relative viscosity and the solids concentration at a reference shear rate of 1000 s^{-1} using the Kreiger-Dougherty equation given in Chapter 2 – Equation (2.17).

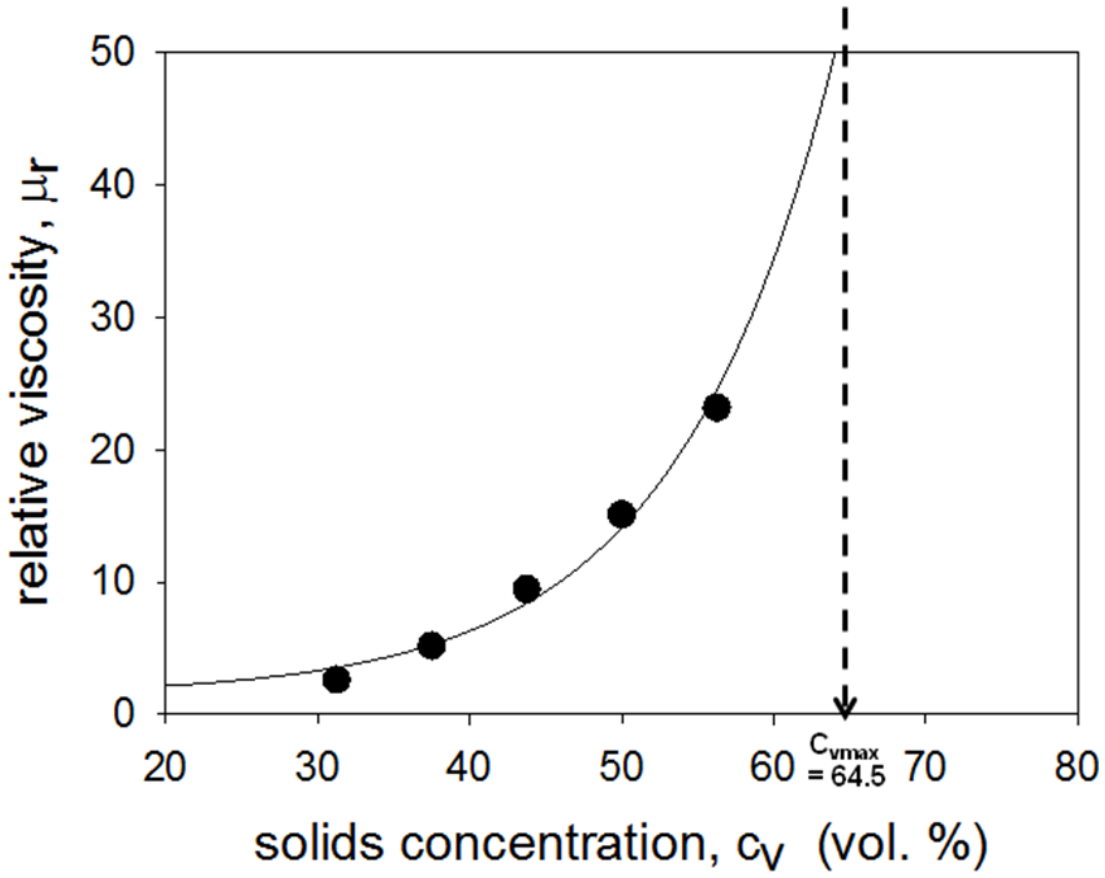

Figure 4.10. Modelling of the effect of solids concentration on viscosity using the Kreiger-Dougherty equation.

The exponential increase in solids concentration from 25 – 45 wt% (i.e. 31 – 56 vol.%) and beyond was properly described by the Kreiger-Dougherty equation with the r^2 value of 0.99. The maximum solids packing $c_{v\max}$ above which the slurry behaves like a rigid solid is determined at the solids concentration when the curve makes a vertical straight line. Therefore $c_{v\max}$ is found to be 64.5 vol% (i.e. 59 wt%) as shown in Figure 4.10.

The increase in slurry viscosity with solids concentration at a reference shear rate of 1000 s^{-1} can also be fitted with Equations (2.18) and (2.20) in Chapter 2.

$$\mu_r = \frac{\mu(c_v)}{\mu^o} = \frac{1}{(1-c_v)^{3.72}} \qquad (r^2 \text{ value} = 0.97) \qquad (4.10)$$

i.e. f = 3.72

Similarly, the characteristic model from the Eilers and Chong equation is

$$\frac{1}{\mu_r^{0.5}-1} = \frac{0.95}{c_v} - 1.57 \qquad (r^2 \text{ value} = 0.98) \qquad (4.11)$$

i.e. C_{EE} = 1.05

$c_{v\max}$ = 64 vol.% (i.e. 58.7 wt%)

The $c_{v\max}$ obtained from the Kreiger-Dougherty equation and the Eilers and Chong equation are nearly identical with a difference of only ±0.5 vol.%, thus confirming the reliability of both models.

4.4.2.3 Effect of particle size distribution

The prolonged milling of γ–alumina slurries lead to fragmented particles as shown in section 3.3.2.2. The fragmentation of particles means that there is a net increase in the number of particles at a constant solids concentration of 40 wt%. As a result of this there is reduced separation between these particles at prolonged milling time. Figure 4.11 (a) and (b) show the steady flow curves of 40 wt% slurries of different psds produced from milling for 10 – 240 min using the media diameters of 5 mm or 1 mm.

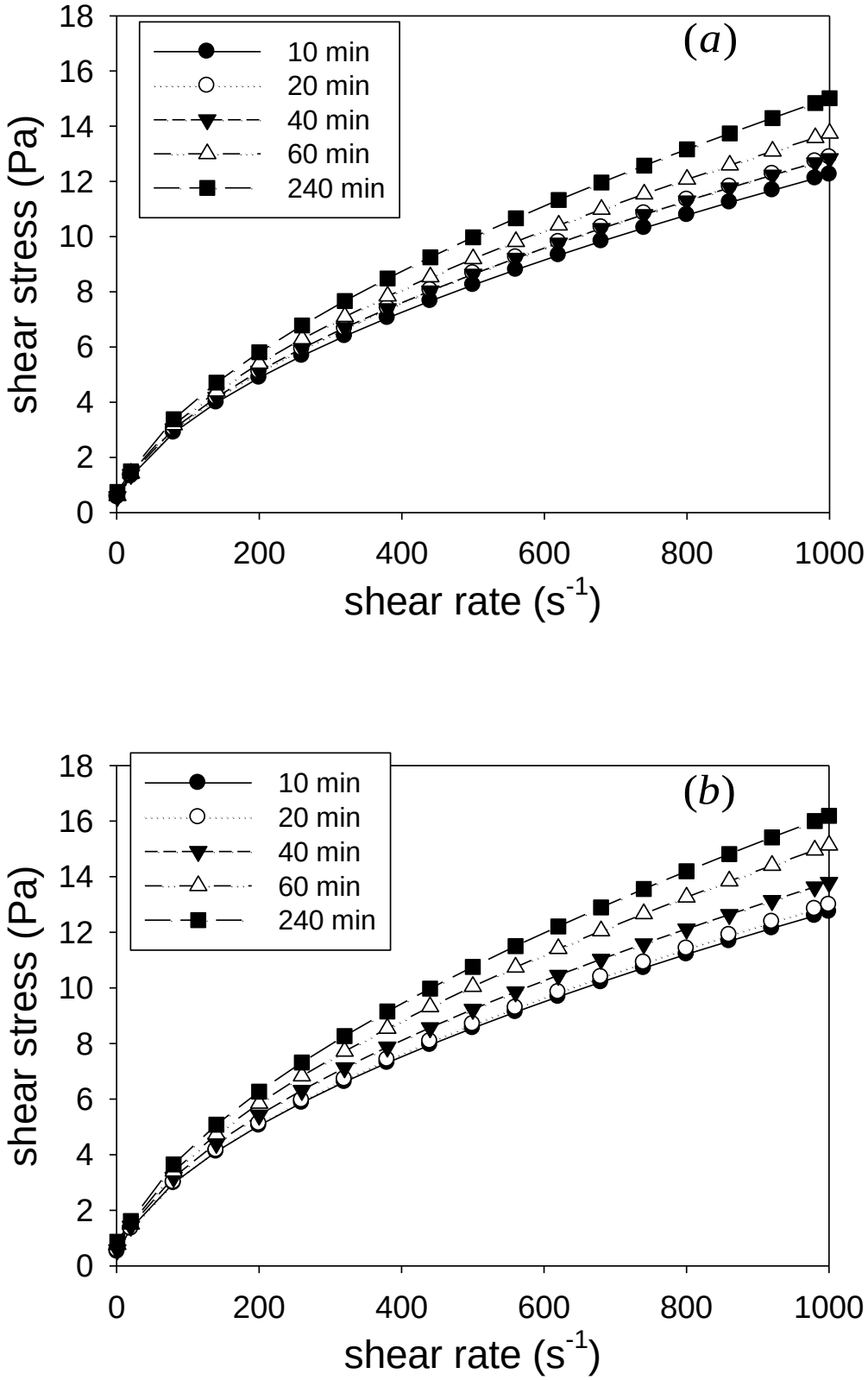

Figure 4.11. Effect of particle size distributions on slurry rheology at 40 wt% solids concentration: steady shear flow curves for slurries milled using (a) 5 mm media diameter and (b) 1 mm media diameter.

It is shown that all the slurries exhibited shear thinning behaviour. The particle diameters produced at the milling times have already been shown in Table 3.4 in section 3.3.2.3. The slurry viscosity as a function of milling time at a reference shear rate of 1000 s^{-1} for both media diameters is shown in Figure 4.12. It is shown that there was a systematic increase in the slurry viscosity as finer particles (i.e. $d_{0.9}$ from 33.42 to 3.67 μm) were produced with the increase in milling time. This is because of an increase in the effective phase volume of the γ–alumina particles as they become finer and are placed closer to one another during shearing (Barnes, 2000; Hoffman, 1992).

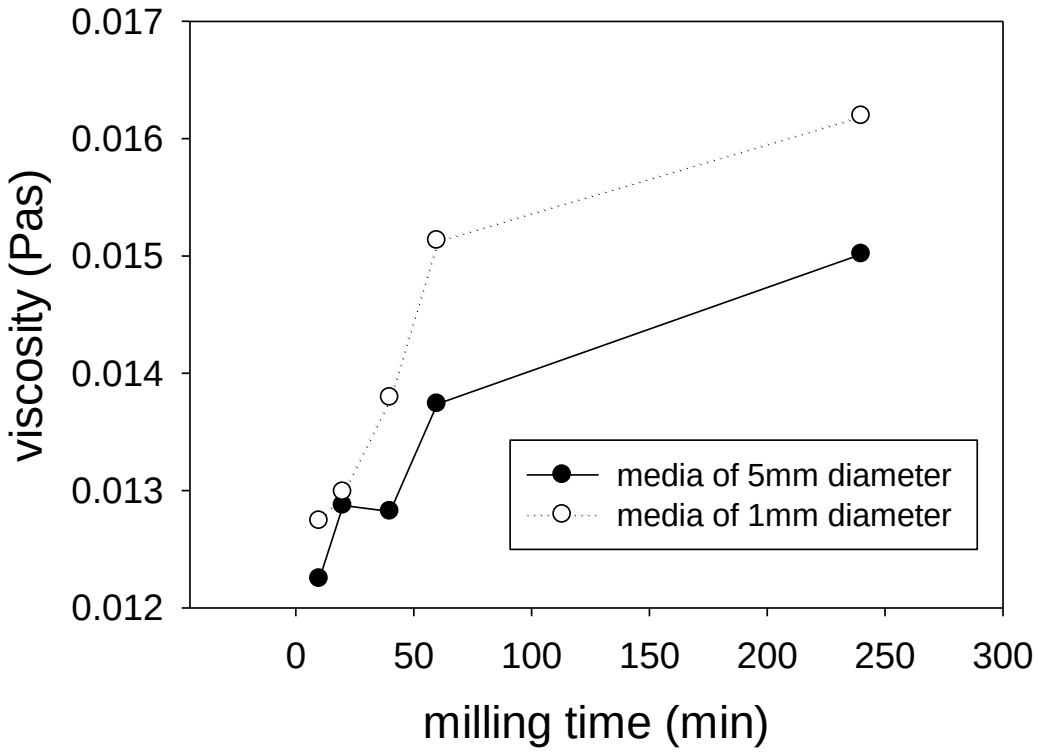

Figure 4.12. Viscosity as a function of milling time at a reference shear rate of 1000 s^{-1} for slurries produced using media of 1 mm or 5 mm diameters.

All the results show good agreement with the findings of Agrafiotis and Tsetsekou (2000) which also showed that the slurry viscosity increases from 45 mPas to 130 mPas

with a decrease in particle diameter $d_{0.9}$ from 6 μm to 2 μm. Though the shear rate at which the viscosity was measured was not specified in Agrafiotis and Tsetsekou (2000), the γ–alumina particles used were dispersed in aqueous ammonium poly-methacrylate at solids concentration of 40 wt%. A similar increase in slurry viscosity with a decrease in particle diameter was obtained by Hill and Carrington (2006) who studied fine and coarse talc of similar diameters $d_{0.5}$ of 5 μm and 19 μm.

4.4.2.4 Effect of temperature

The heat transferred to the slurry under examination via the water bath embedded in the sample platform caused the temperature to increase in steps from 4 – 40 ^{o}C. The thermal energy supplied to the slurry by the heat transfer is changed into kinetic energy of the particles, thereby giving the particles increasing degree of freedom (or velocity) to move about according to the Equation (4.12).

$$k_{ET} = \tfrac{1}{2} m_{al} v_{al}^2 \qquad (4.12)$$

where

k_{ET} = kinetic energy of particles (J)

m_{al} = mass of particles (kg)

v_{al} = particle velocity (m s^{-1})

Figure 4.13 shows the results obtained from the decrease in slurry viscosity with temperature at a solids concentration of 40 wt%. The temperature of the slurry, which had previously attained steady state viscosity at 4 ^{o}C, was increased from 4 – 40 ^{o}C.

The more velocity the particles had at higher temperatures according to Equation (4.12), the less their reluctance to flow, and consequently the reduction in slurry viscosity. In addition, the viscosity of the continuous phase drops as the slurry becomes thinner due to the increase in temperature (Barnes et al., 1989).

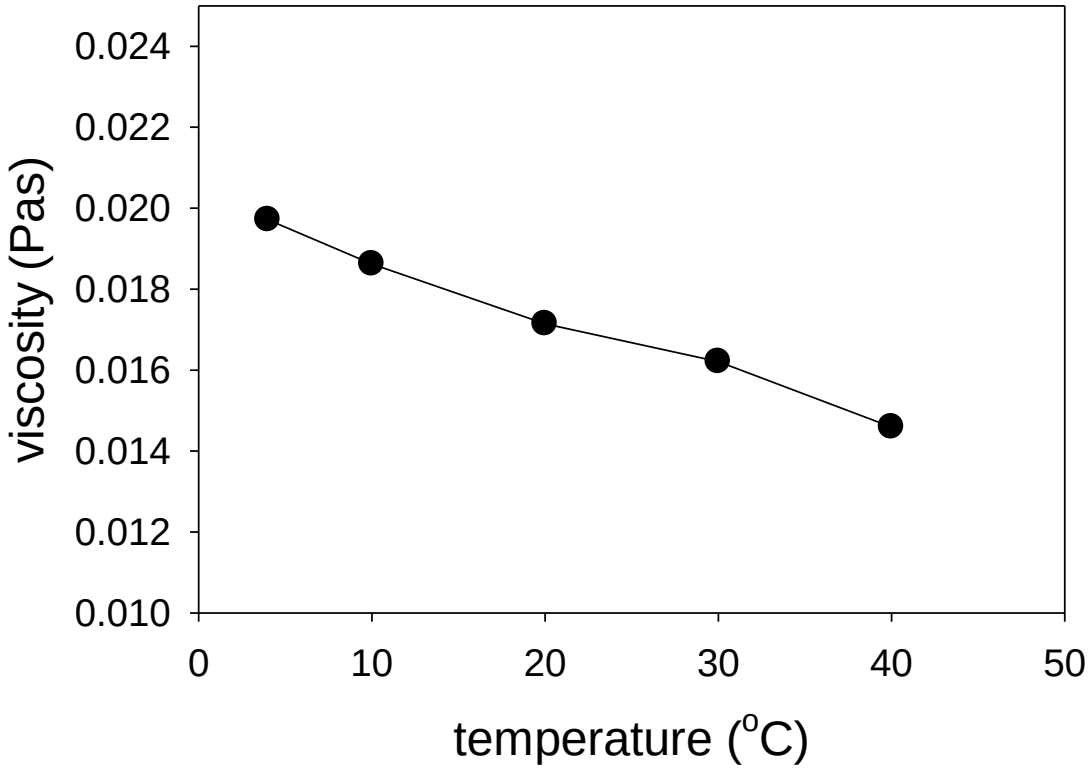

Figure 4.13. Effect of temperature on slurry viscosity at solids concentration of 40 wt%.

4.5 CONCLUSIONS

The rheology of γ–alumina slurries is necessary for proper characterisation and fine-tuning of slurry characteristics. Preliminary tests revealed the thixotropic behaviour of γ–alumina slurries and this could be eliminated by shearing at a constant shear stress for more than 25 s. The steady flow revealed a shear thinning which was adequately described by the power-law model. This behaviour showed a decrease in the slurry viscosity with an increase in shear rate, thus meaning that the particles moved in a cooperative arrangement which produced fewer restrictions.

Furthermore, the parametric characterisation under steady state conditions revealed striking but clear behaviours of the slurry with respect to the pH, solids concentration, particle size distribution and temperature.

The least slurry viscosity was achieved at an optimal pH of 4 because the particles were least aggregated and far away from the i.e.p. of 7.7, therefore having the least reluctance to flow due to electrostatic repulsion.

The increase in solids concentration from 25 to 45 wt % produced thicker slurries (i.e. more inter-particle interactions because of reducing particle separation), the viscosity increased as a result. The maximum solids packing was determined around 59 wt % using the Kreiger-Dougherty and the Eilers and Chong equations.

At a fixed solids concentration of 40 wt%, the reduction in the particle diameters (i.e. $d_{0.9}$ from 33.42 to 3.67 μm) at prolonged milling times resulted into a decrease in particle separation. There was therefore an increase in the effective phase volume of particles and, consequently, an increase in the viscosity.

The slurry viscosity reduced with an increase in temperature from 4 to 40 ^{o}C because of the increase in particle kinetic energy and the associated decrease in the continuous phase viscosity.

5

INFLUENCE OF PREOXIDATION ON FECRALLOY® EFFICACY AS A CATALYST SUPPORT

In this chapter the physiochemical transformations caused by thermal preoxidation of the surface of Fecralloy® coupons are studied to assess their influence on coating adherence. The coupons were preoxidised at 950 ^{o}C for 0, 5, 10 and 30 h and the mass gain was found to fit a hyperbolic model. Measurements were made of surface topography and microstructure using laser profiling interferometry (LPI) and scanning electron microscopy (SEM), with chemical analysis being obtained from X-ray diffraction (XRD). The optimal surface roughness was obtained after 10 h of preoxidation, when the surface contained significant amounts of γ–alumina arranged as randomly oriented whiskers. Upon coating of the treated foil coupons with a γ-alumina slurry, the samples preoxidised for 10 hours gave the best performance in terms of coating loading (7.94 mass %) and adherence (< 10 mass % loss) based on a ultrasonic vibration test.

5.1 INTRODUCTION

Fecralloy® is the integral component from which monolith catalysts are made. Figure 5.1(a) shows the Fecralloy® foil which is fabricated and coated with γ–alumina slurry to produce monolith catalysts of different configurations, such as in Figures 5.1(b) and (c).

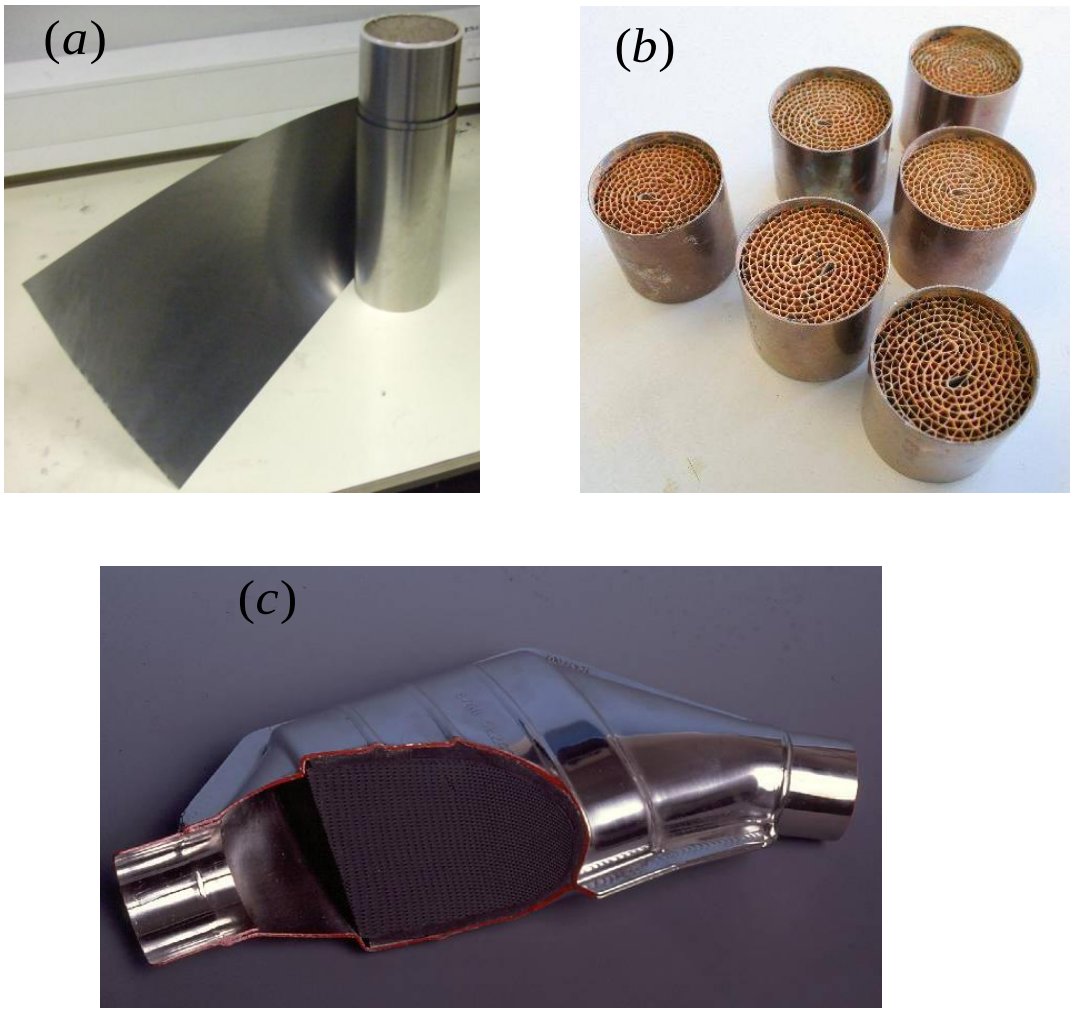

Figure 5.1. Images of Fecralloy® materials: foil not yet configured (a) and tubular monolith catalysts (b) & (c) [pictures: courtesy of Johnson Matthey Plc].

To ensure adherence of the γ–alumina coatings, the Fecralloy® foil needs to be preoxidised, and this changes its surface topography from a rather plain format to a

roughened and layered one. Some studies have assessed the effects of preoxidation on dip-coated foil coupons, by relating the surface microstructure obtained by scanning electron microscopy (SEM) to the coating adherence (e.g. Jia et al., 2007; Zhou et al., 2007; Zhao et al., 2003). However, these comparisons are somewhat qualitative in nature and do not consider a quantitative measure of the surface roughness, nor do they address coating at a controlled shear rate.

This Chapter focuses on a detailed assessment of Fecralloy® surface topography using laser profiling interferometry (LPI) as a function of preoxidation treatment. In addition, SEM and X-ray diffraction techniques are applied to give a comprehensive description of the physiochemical transformations caused by preoxidation. To determine the effect of preoxidation on the coating adherence, the standard γ–alumina slurry prepared and characterised in Chapters 3 and 4 was used. This slurry was deposited onto the Fecralloy® coupons at a controlled shear rate using an automatic film applicator, and the resulting composites were dried and calcined afterwards. The coating loading and adherence were determined to reveal the optimal preoxidation conditions.

5.2 PROPERTIES OF FECRALLOY®

Like most alloys, the properties of the individual constituent elements from which Fecralloy® is produced have direct implications on its overall properties. Fecralloy® is comprised essentially of iron (Fe), chromium (Cr), aluminium (Al) and small quantities of reactive elements, such as yttrium (Y) and manganese (Mn). It is well suited for

catalyst support applications because of its high mechanical strength, thermal conductivity and ductility which make it easy to process. It clearly outperforms cordierite as a monolith material in all these crucial properties (Zhang, 2009; Hickman and Schmidt, 1992a; Hickman and Schmidt, 1992b).

The properties of a typical Fecralloy® are summarised in Table 5.1.

Table 5.1. Physical properties of a typical Fecralloy® based metal monolith used as a catalyst support (Cybulski and Moulijn, 2006).

Property	Values
wall thickness (μm)	40
open facial area (%)	92
specific surface area (m^2g^{-1})	0.005
thermal conductivity ($Js^{-1}m^{-1}K^{-1}$)	16.7
thermal capacity ($Jg^{-1}K$)	1050
density (gcm^{-3})	7.4
thermal expansion (K^{-1})	0 – 15
maximum working temperature (^oC)	1500

5.3 EQUIPMENT

5.3.1 The automatic film applicator

A 1132N automatic film applicator (Sheen Instruments, UK) equipped with wire-wound bars of nominal gaps of 10, 26 and 100 μm is used to coat the Fecralloy® surfaces with γ–alumina slurry (Figure 5.2). The film applicator provides a motorised "draw down" of the wire-wound bars across a substrate at a constant speed. This method of coating Fecralloy® represents a pragmatic shift from the conventional methods described in Chapter 2, and provides tight control of shear rate and bar gap through the coating process. In addition, coating by the film applicator is a laboratory-scale technique which comes with attendant advantages, such as simplicity, accuracy, reproducibility and traverse speed.

The applicator and its components have been designed as a versatile bench top instrument which is suitable for many surface coating industries. Particular attention has been given to the smoothness of travel of the carriage on top of the applicator to prevent any signs of ripple in the deposited coating film. The applicator can be programmed at traverse speeds ranging from 50 to 500 mms^{-1} in increments of 10 mms^{-1} by tuning the front keypad. This clearly dismisses the practice of setting the traverse speed by trial and error, a phenomenon that is synonymous to older versions of film applicators.

Figure 5.2. A 1132N automatic film applicator and its components: (a) coating appliance; (b) view of the wire-wound bar firmly screwed and (c) memory keys for storing coating speeds (Sheen Instruments, UK).

The micro-processor-controlled electronics of the applicator compare the actual traverse speed of the carriage with the selected traverse speed and automatically compensate for any load variations. This ensures an accurate speed control under all operating conditions. During a "draw down" the actual traverse speed of the carriage is indicated on the display screen. The acceleration and deceleration times of the carriage are very

low in order to attain the desired speed as quickly as possible (i.e. low inertia). The commonly used speeds can be stored in 4 memory keys (M1, M2, M3 and M4)

The film applicator has been designed to provide safe operation without the need for additional guarding arrangements. All the gaps between the moving and stationary components have been made as minimal as practicable, thus drastically reducing the risk of injury.

5.3.2 Furnace

An electric chamber furnace manufactured by Lenton furnaces (Hope Valley, UK) is used for preoxidation of Fecralloy® as well as for drying and calcination of the coatings. The furnace could reach a maximum operating temperature of 1200 ^{o}C. The maximum temperature uniformity was brought about by two-side-wall heating elements manufactured from high temperature resistance wire spirals engrafted into cast refractory slabs.

The exhaust chimney fitted to the furnace was connected to the main flue. The insulated door opened upwards and outwards, thus keeping the hot face insulation away from the operator. The power supply is withdrawn from the heating elements by the door control whenever the door is opened to ensure maximum safety. The double skin construction of the furnace is such that natural air convection is allowed to maintain a cool outer case. The furnace has a temperature accuracy of ± 10 ^{o}C.

5.3.3 Laser profiling interferometer (LPI)

The measurement the topography of Fecralloy® surface is aimed at making comparisons about their surface features and knowing the conditions that provide optimal performance for use as catalyst supports. The measurement of surface topography allows for a quantitative (and authoritative) description of the changes emanating from different preoxidation conditions, which hitherto has not been researched.

Surface topography refers to the texture and geometry of surfaces. It examines the deviation between one point (or points) on a surface and another point (or other points) on the same surface. The condition of a surface is defined by its characteristics: texture, roundness, material, hardness and metallurgy (Busch et al., 1998).

The focus of this study is on measuring the primary texture, referred to as roughness, and its topography profile. The roughness defines the surface irregularities and asperities, while the topography profile describes the overall shape of the surface landscape (Smith, 2002). The two-dimensional (2D) and three-dimensional (3D) surface topography of the Fecralloy® are measured using a laser profiling interferometer (Talysurf CCI model, Taylor Hobson, UK).

Though the use of the LPI in the measurement of surface topography of solid materials has been in existence for some years, what is new in this study is the development of the LPI for the surface measurement of Fecralloy®. The schematic layout of the operating unit of the interferometer is shown in Figure 5.3.

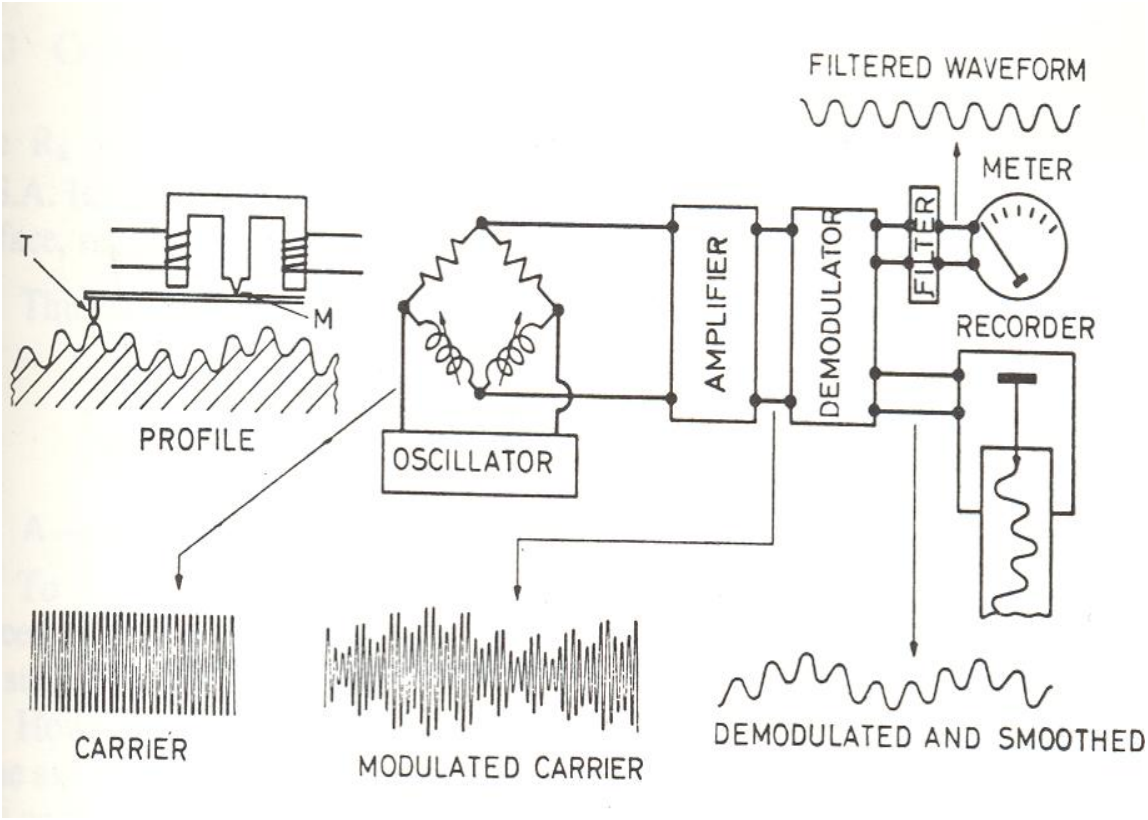

Figure 5.3. A schematic layout of the operating units of LPI – Talysurf model (Galyer and Shotbolt, 1990).

The measuring head comprises the stylus and the shoe (T), which are drawn across the surface under investigation by an electric motor and a gear box. The arm carrying the stylus forms an armature which pivots about the centre piece of a stack of E– shaped stampings. These stampings are around the outer pole pieces of which is a coil carrying an alternating current (a.c.) current. As the armature pivots about the point M, the air gaps are varied, thus modulating the amplitude of the original a.c. current flowing in the coils. This signal is transmitted to an amplifier and this triggers a recorder to produce a permanent digital record of measurements (Galyer and Shotbolt, 1990).

To put the roughness parameters in proper perspective, the inteferometer measuring lengths need to be defined (Smith, 2002):

(a) *Sampling length*: This is the length in the horizontal direction used for indentifying the irregularities that characterise the profile under evaluation. The sampling length L should generally be repetitive in nature as indicated in patterns A and B [Figure 5.4 (a)].

(b) *Evaluation length*: This is the total length in the horizontal direction used for the assessment of the profile under evaluation. As shown in Figure 5.4 (b), this length may include several sampling lengths, which can be up to 5000, depending on the model of the interferometer used.

(c) *Traverse length*: This is the total length of the surface traversed by the stylus in making a measurement. It is expected to be greater than the evaluation length, due to the necessity of allowing run-up and over-travel at each end of the evaluation length [Figure 5.4 (b)]. This is to ensure that any mechanical and electrical transients, together with filter edge effects, are eliminated from measurements.

The Talysurf CCI measured 1000 sampling lengths of 5 μm each, thus, covering a total evaluation length of 5 mm.

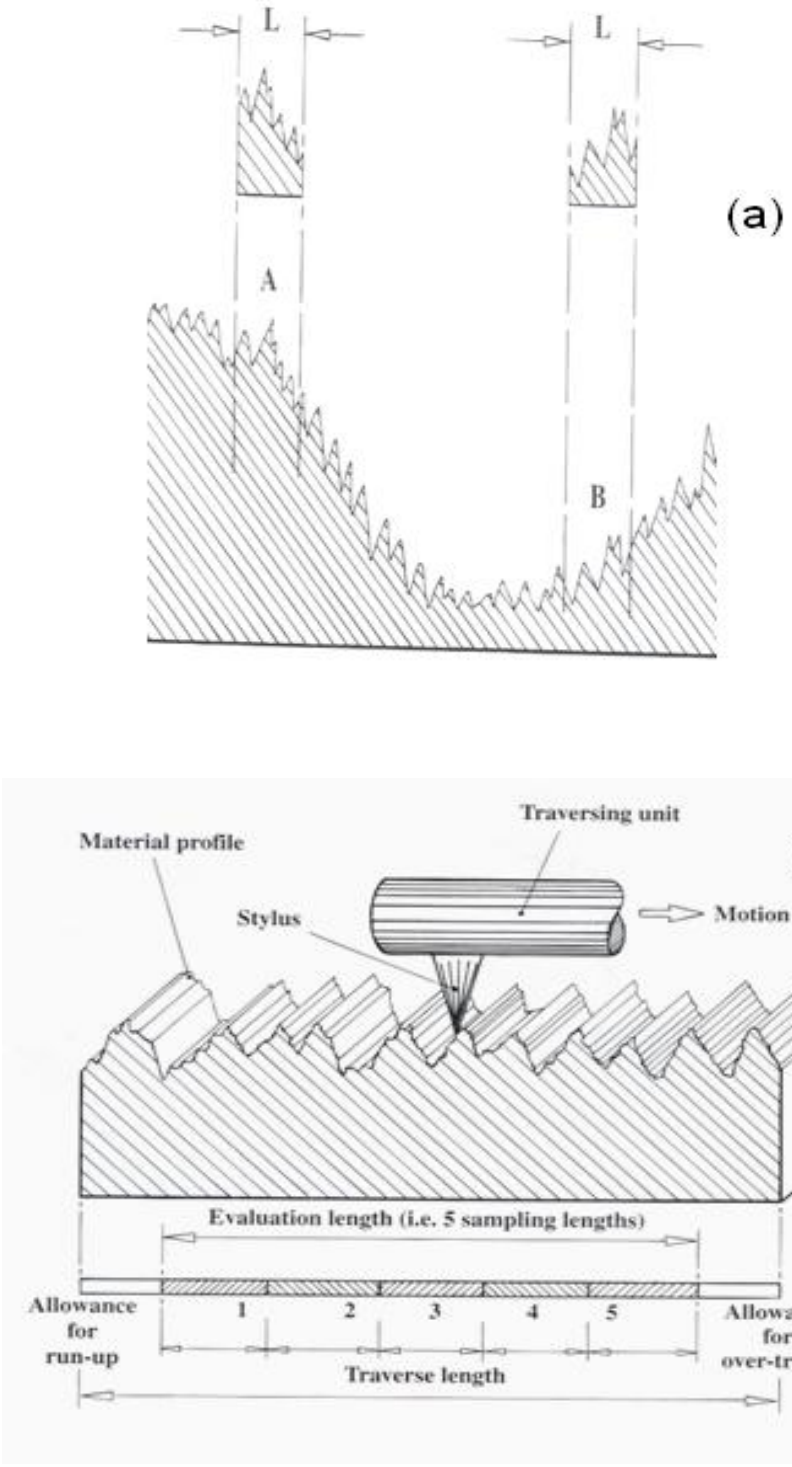

Figure 5.4. A description of basic measuring lengths used for roughness measurements: (a) sampling length and (b) evaluation and traverse length (Smith, 2002).

The definitions of the 2D roughness parameters which were measured are outlined in the following (Benkreira, 2004; Busch et al., 1998)

(a) **Arithmetic average roughness (R_a)**: this is arithmetic average of the absolute values of the deviations from the profile height measured from the centreline along a specified sampling length. This can be calculated by two means: graphical and electrical averaging methods [Figure 5.5 (a)]. The graphical method involves placing a predetermined line over the centreline such that the areas above the line equal the areas below the line. The electrical method, applied by Talysurf CCI, involves automatically averaging the readings. The R_a is given by the relationship:

$$R_a = \frac{y_a + y_b + y_c + \ \ldots \ + y_n}{n} \tag{5.1}$$

(b) **Root-mean-square roughness (R_q)**: this is closely connected to the arithmetic average roughness R_a. It is the square root of the mean of the squares of the distances from the centreline to the profile [Figure 5.5 (a)]. The R_q is given by the relationship:

$$R_q = \sqrt{\frac{y_a^2 + y_b^2 + y_c^2 + \ \ldots \ + y_n^2}{n}} \tag{5.2}$$

(c) **Maximum peak-valley roughness (R_t or R_{max})**: this is a unique measurement in that it determines the distance between lines that contact extreme outer and inner points on the profile [Figure 5.5 (b)].

The 3D roughness parameters (S_a, S_q and S_t) mirror their respective 2D counterparts (R_a, R_q and R_t) and they reveal a wider coverage of the Fecralloy® surface roughness.

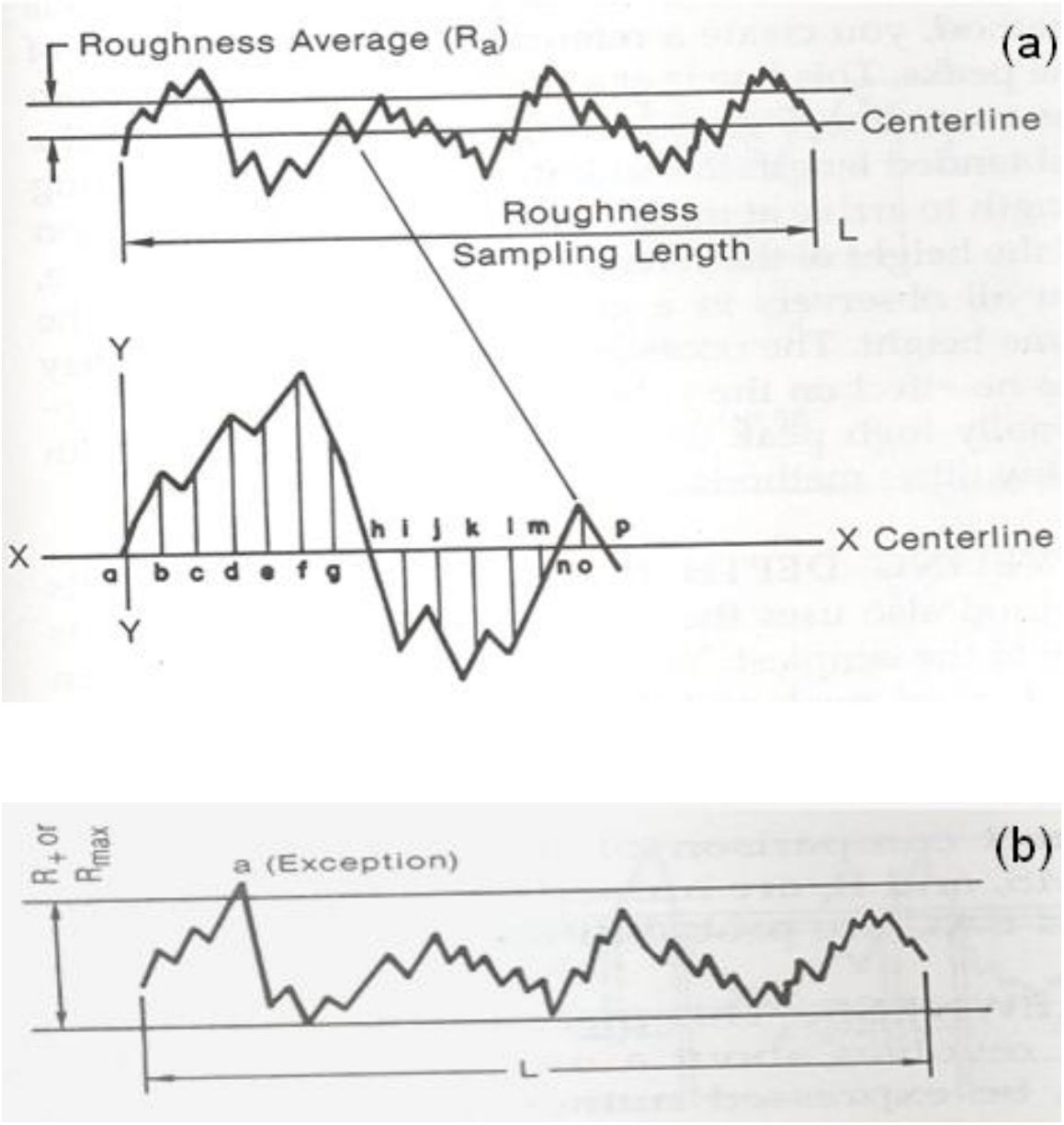

Figure 5.5. Illustration of how roughness parameters are measured: (a) R_a & R_q and (b) R_t or R_{max} (Busch et al., 1998).

5.3.4 Scanning electron microscope (SEM)

The SEM (Jeol 6060; Oxford Instruments, UK) is chosen as the preferred instrument for exploring further the microstructure of the Fecralloy® surface because it provides an in-depth visualisation, brought about by its high resolution and magnification, compared to conventional optical microscopes. The underlying principles of operation of the SEM are simple as shown in Figure 5.6.

The electron gun, situated at the top of the column, emits high-speed electrons. These electrons travel down the column and are squeezed together by lenses to form an electron beam of very small diameter. This electron beam is then focussed such that it collides with the specimen, housed in the specimen chamber, as a diminutive spot. The collisions of the electron beam with the specimen result into the emission of reflective rays, out of which are secondary electrons. The total numbers of electrons counted for several distinct points on the specimen are converted to spots of light on the SEM display screen (called CRT). The shape of the specimen's surface visualised on the CRT is influenced by the yield of the secondary electrons. The specimen image can therefore be adjusted, captured and scrutinised (Smith, 2002; Chescoe and Goodhew, 1990).

Apart from the secondary electrons, the X-rays also form a formidable part of the reflected rays and they can be utilised to yield additional specimen information. The X-rays possess energies that are unique to individual elements. An energy-dispersive spectrometer (EDS) fitted to the SEM is used to detect these energies (Smith, 2002).

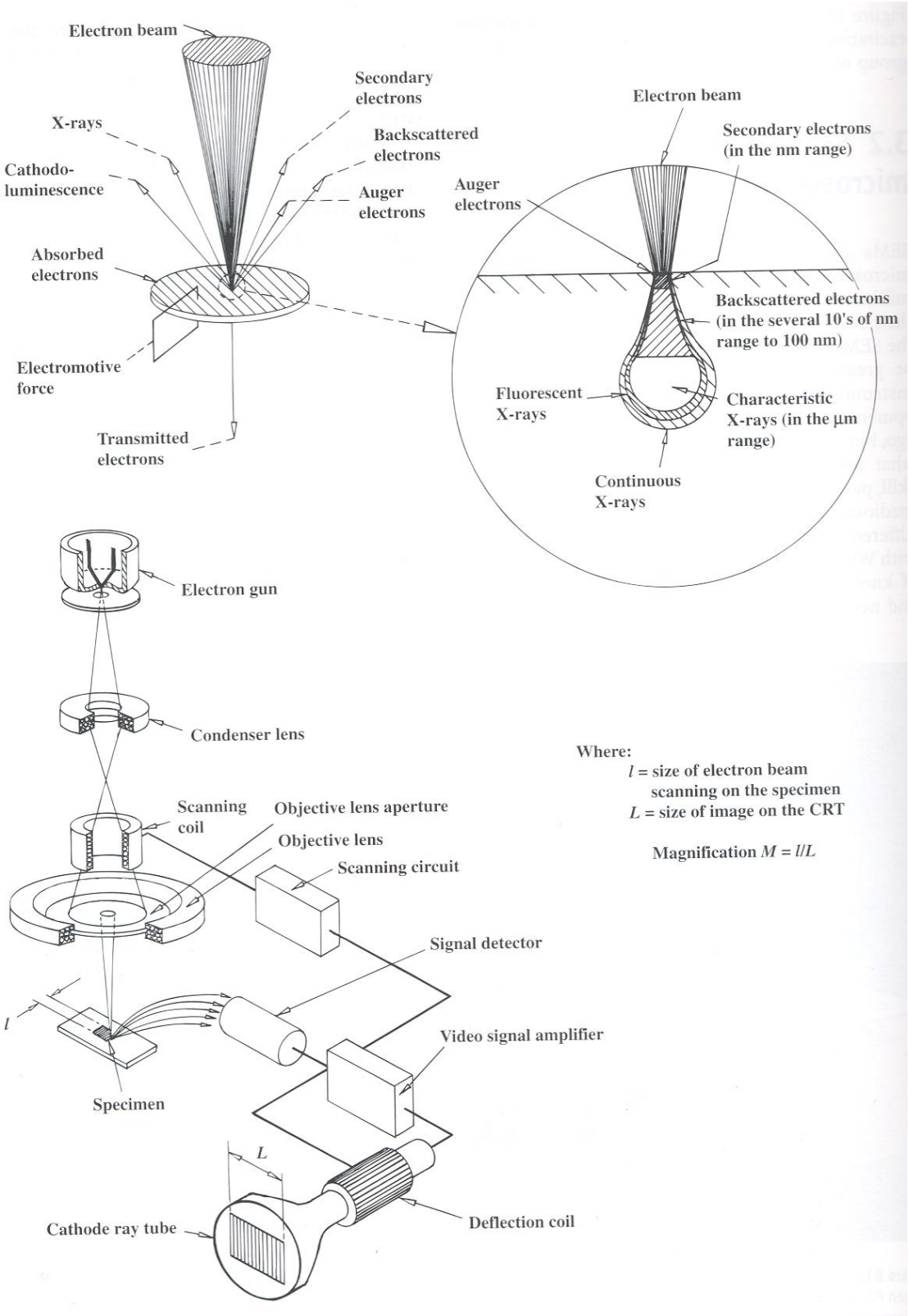

Figure 5.6. The underlying principles of the scanning electron microscope (Courtesy of Jeol, UK).

The X-rays are discovered by applying either a thick- or thin-frame window (typically a Si (Li) detector) for heavier or lighter elements respectively. This semiconductor is positioned at the tip of the detector. The height of the current pulses which are generated by the X-ray illumination is proportional to the energy of the incident X-rays. The sophistication of the EDS systems enables the characterisation of specimen based on the elemental composition in the area under investigation (Smith, 2002).

5.3.5 Diffractometer

An X'Pert Pro diffractometer (Phillips, The Netherlands) is the device used to investigate the chemical composition of the Fecralloy® surface up to a depth of 10 μm by means of X-ray diffraction (XRD). The diffraction of X-rays by the core electrons provides crucial information about the positions of the nuclei in a molecule from which the particular molecule (or complex) can be determined. X-rays have no charges and penetrates molecules because they do not experience any electrostatic repulsion from the core and valence electrons of the molecules. The heavier the molecule is, the more electrons it has, meaning the greater its ability to scatter X-rays. The XRD technique is based on the generation of X-rays by a beam of accelerated electrons striking the Fecralloy® surface and from collisions of electrons with the atoms rapidly decelerating. The energy loss in each deceleration is emitted as a photon of radiation, thus leading to a continuous X-ray spectrum. The XRD technique also helps in revealing the different forms of the crystals present on Fecralloy® surface by analysing the intermolecular and intramolecular distances (Housecroft and Constable, 2002; Bauer, 2000).

5.4 EXPERIMENTAL

5.4.1 Pretreatment and assessment of Fecralloy® foil

Commercially available Fecralloy® foil [Figure 5.7 (a)] of 50 μm thickness with a composition of Fe (72.6 wt%), Cr (22.0 wt%), Al (4.80 wt%), Y (0.30 wt%) and Si (0.30 wt%) (GoodFellow, UK) was used. The foil was cut into 50 × 80 mm coupons shown in Figure 5.7 (b) by a knife. The pretreatment of the coupons involved the following steps (Jia et al., 2007; Wu et al., 2005):

(a) *Degreasing*: ultrasonic cleaning at room temperature in acetone bath for 10 min, and then with distilled water at 80 ^{o}C for 10 min and

(b) *Preoxidation*: oxidation in a furnace (Lenton, UK) at 950 ^{o}C for different durations: 0, 5, 10 and 30 h. The preoxidation temperature profiles are shown in Figure 5.8.

The specific mass gain of the coupons as a function of preoxidation time was determined using a mass balance (Ohaus Corporation, USA).

The surface topography (namely surface roughness and topography profiles) of the coupons was measured by the LPI (Taylor Hobson, UK) described in section 5.3.3.

The surface chemical composition of the coupons was determined by XRD using an X' Pert Pro diffractometer (Phillips, The Netherlands) using a Fe-filtered Co Kα radiation and a power of 45 kV × 30 mA (section 5.3.5).

The surface microstructure of the coupons was assessed by using the Jeol 6060 SEM coupled with EDS (Oxford Instruments, UK) described in section 5.3.4.

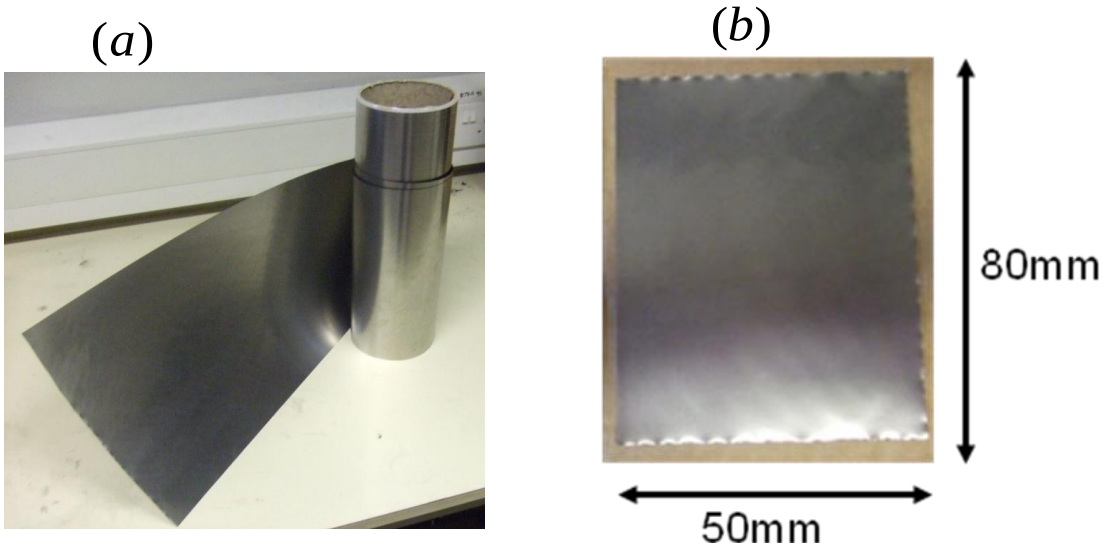

Figure 5.7. Commercially available Fecralloy®: (a) foil and (b) coupon.

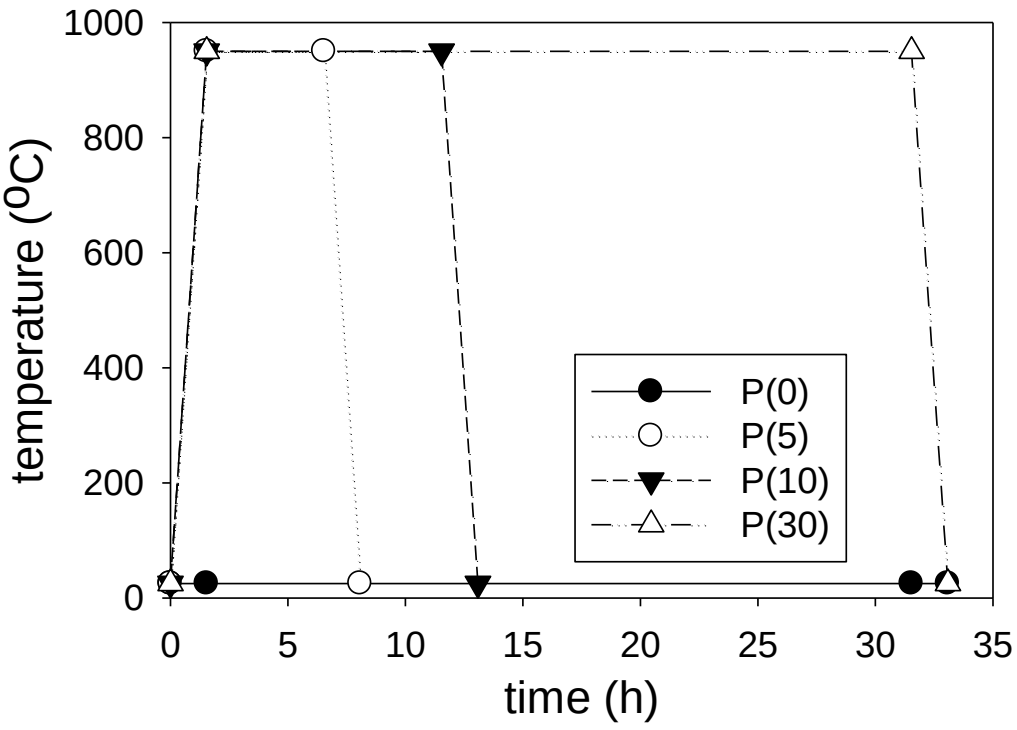

Figure 5.8. Preoxidation temperature profiles of Fecralloy® at 950 °C.

5.4.2 Coating of foils by film applicator

A γ–alumina slurry of $d_{0.5}$ = 4.36 μm and solids concentration of 40 wt% was prepared at a pH of 4 using acetic acid solution (Fischer Scientific, UK) according to the procedure outlined in chapter 3 (sections 3.2.1 & 3.2.2). The slurry was deposited onto the Fecralloy® coupons using the 1132N automatic film applicator (Sheen Instruments, UK) which provided close control of the traverse coating speed.

The procedure for coating the coupons using the film applicator is outlined in the following:

(a) attach the coupon onto the glass plate of the applicator by means of a clip;

(b) firmly screw the wire-wound bar to the carriage of the applicator, ensuring that the bar rests on the coupon;

(c) add slurry on coupon surface at the junction between the coupon and the bar and

(d) program the applicator to use the bar to draw down slurry into thin film across the coupon surface.

The slurry was coated onto the coupons at a traverse speed of 100 mms^{-1} using a bar of 100 μm nominal gap as illustrated in Figure 5.9.

The coated coupons were allowed to partly dry at room temperature, and then oven dried at 110^{o}C for 1 h and finally calcined at 500^{o}C for 1 h (Jia et al., 2007; Truyen et al., 2006). The drying and calcination profile is shown in Figure 5.10.

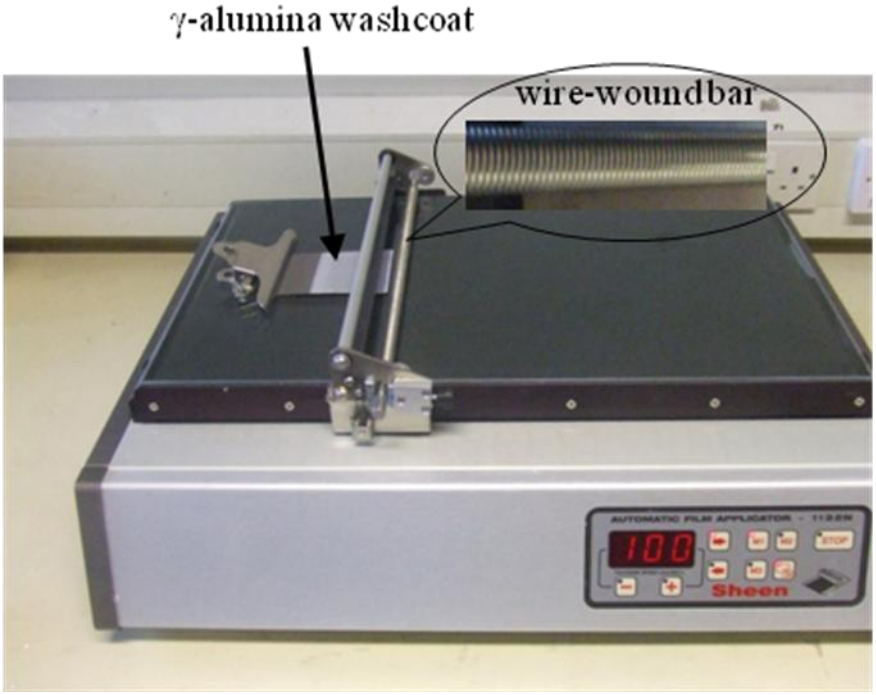

Figure 5.9. An automatic film applicator showing how coating was done.

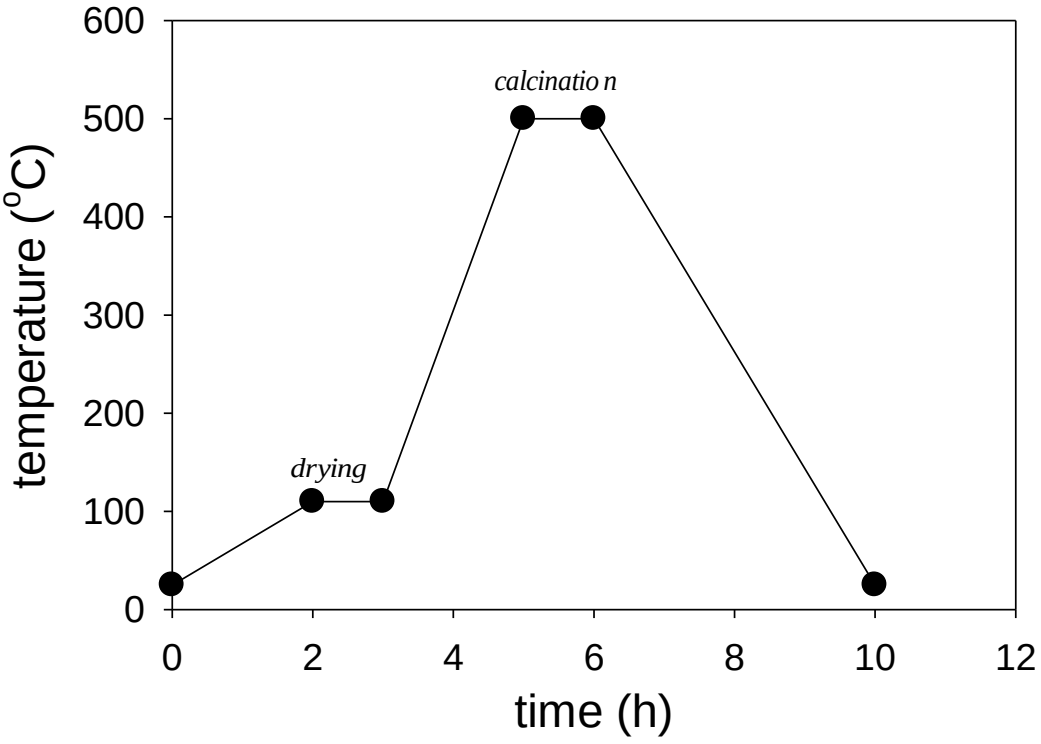

Figure 5.10. Drying and calcination profile of coatings.

5.4.3. Assessment of coating properties

The loading of slurry on Fecralloy® surface was calculated by the percentage mass increase of the coupon after coating according to this expression (Jia et al., 2007):

$$\text{loading} = \left[\frac{(m_c - m_u)}{m_u}\right] \times 100\% \qquad (5.3)$$

where

m_u = mass of foil before coating (kg) and

m_c = mass of foil after coating (kg)

To determine coating adherence, the coated foils were soaked into petroleum ether contained inside a sealed beaker for 30 min, then soaked in an ultrasonic water bath (300 W and 60 Hz) for 1 h and later dried in an oven at 110^{o}C for 2 h (Valentini et al., 2001).

The percentage mass loss was then calculated from Equation (5.4). Thus, the lower the mass loss, the better the coating adherence (Zhou et al., 2007).

$$\text{mass loss} = \left[\frac{(m_c - m_a)}{(m_c - m_u)}\right] \times 100\% \qquad (5.4)$$

where

m_a = mass of foil undergoing ultrasonic vibration (kg)

This was followed by a visual quality assessment of the coatings by the SEM.

5.5 RESULTS AND DISCUSSION

5.5.1 Preoxidation profile

The preoxidation profile shown in Figure 5.11 (a) represents the specific mass gain by foils as a function of preoxidation time. The increase in the specific mass gain of the foil with the increase in preoxidation time was brought about by the continuous formation of an oxide layer on the foil surface. The hyperbolic model [Equation (2.16)] given in section 2.2.4 was simplified in Equation (5.5) and found to adequately describe the preoxidation profile.

It is shown that the rate of oxide formation, which is the gradient of the curve, was highest at the start of preoxidation, and it progressively diminished as preoxidation continued.

$$\overline{\Delta m} = \frac{nt}{z + t} \qquad (r^2 \text{ value} = 0.99) \qquad (5.5)$$

where

constants n and z are 0.27 and 5.0 respectively

The relationship in Equation (5.5) was found to be very similar to the preoxidation profiles obtained from a previous study by Pragnell et al. (2005) at 900 ^{o}C and 925 ^{o}C for 0 – 70 h. The Fecralloy® coupons used in their study were also 50 µm thick and had dimension of 20 mm x 10 mm and the following composition [Cr (22.3 wt%); Al (5.4 wt%); and the remaining 72.3 wt% were mostly Fe and minute quantities of Y].

Figure 5.11 (b) represents the foil coupons P(0), P(5), P(10) and P(30) which have been preoxidised for 0, 5, 10 and 30 h respectively. It is observed that P(0) was very plain, shiny and light-complexioned with no surface oxide layers. P(5) shows that the surface became slighted darkened and spotty after preoxidation for 5 h. As increasing oxide layer was formed on the surface, the darkening and spottiness became more pronounced for P(10) and P(30), the later being the most darkened of all.

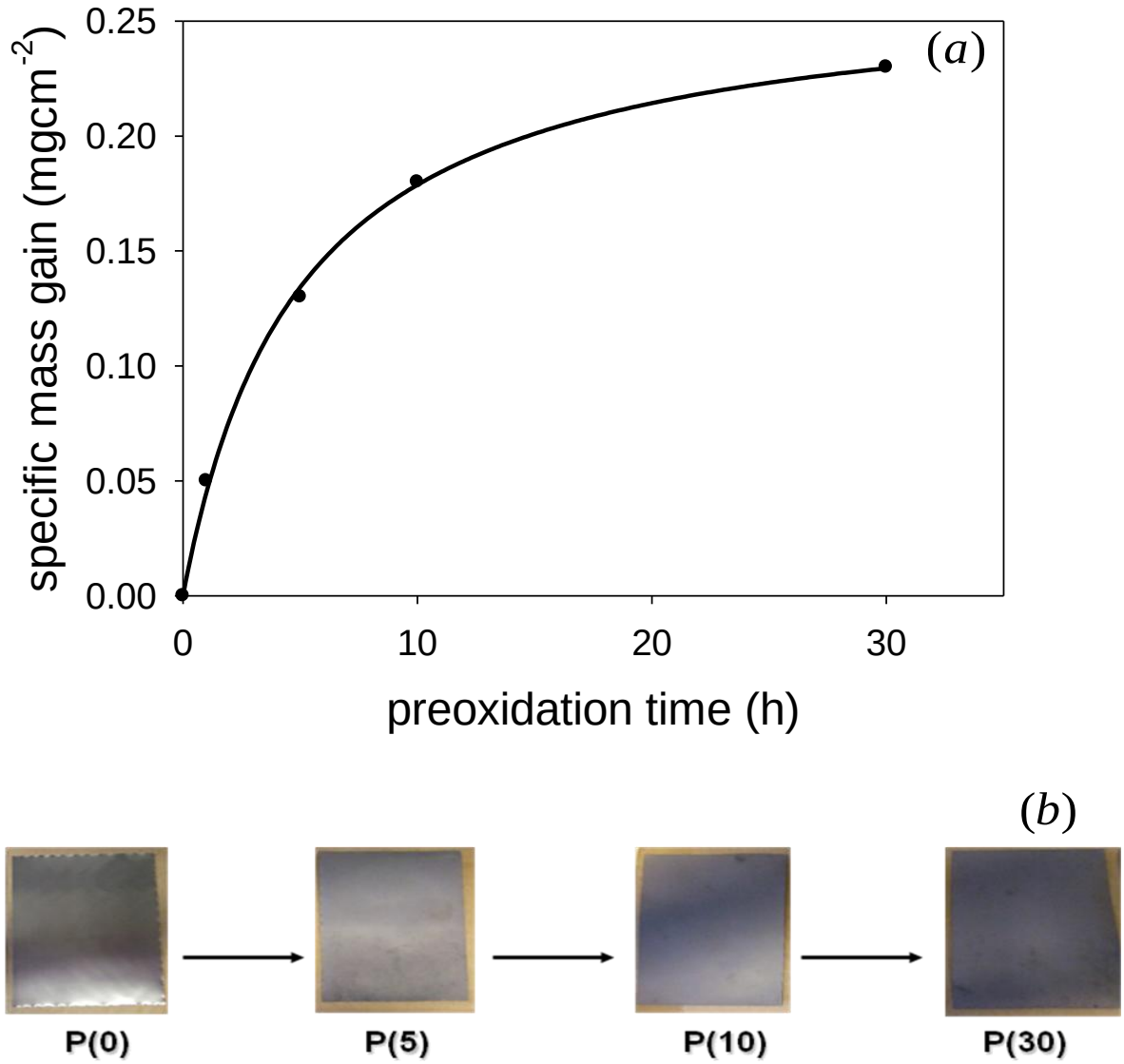

Figure 5.11. Preoxidation profile of Fecralloy® coupons for 0 – 30 h: (a) fitting of curve by hyperbolic model and (b) view of coupons prior to and after preoxidation.

5.5.2 Surface topography of Fecralloy® by LPI

The surface topography of the coupons, represented by the 2D and 3D roughness parameters and the topography profiles (Smith, 2002) measured by the LPI, are shown in Table 5.2 and Figures 5.12 – 5.15.

The roughness parameters for the untreated coupon were very low (e.g. R_a = 0.06 μm and S_a = 0.20 μm) because the surface was untransformed and therefore may be undesirable as a potent catalyst support. In other words, the efficacy for coating adherence on such a surface will be poor.

The roughness parameters increased significantly after 5 h preoxidation at 950 ^oC (i.e. R_a = 0.15 μm and S_a = 0.35 μm). This is a confirmation of the development of surface irregularities and asperities on the Fecralloy® coupon at this period. Coating adherence is promoted by these surface irregularities and asperities, as they act as glues or "sticking points" for coatings.

The roughness parameters peaked at 10 h preoxidation at 950 ^oC (e.g. R_a = 0.31 μm and S_a = 0.83 μm). It is shown that the amounts of potential "sticking points" for coatings have significantly increased, and this will enable the Fecralloy® coupon to be effective for coating adherence.

The roughness parameters however decreased after prolonged preoxidation for 30 h. For this coupon R_a = 0.23 μm and S_a = 0.52 μm, thus meaning that the adherence integrity of the Fecralloy® may be reduced.

Clearly, the Fecralloy® coupon preoxidised at 950 ^oC for 10 h had the roughest surface. This is supported by the topography profiles shown in Figures 5.12 – 5.15 which showed the largest topographical scale for the coupon preoxidised for 10 h. The profiles also exhibit order in their surface structure due to how the material is rolled out when it is made. This is particularly evident in the sample shown in Figure 5.14 which is characterised by deep penetrating grooves.

Table 5.2. Roughness parameters of Fecralloy® coupons preoxidised at 950 ^oC for 0 – 30 h.

Roughness parameters	Type	Definition	Values (μm)			
			0 h	5 h	10 h	30 h
R_a	2D	arithmetic average	0.06	0.15	0.31	0.23
R_q	2D	root-mean-square	0.08	0.17	0.36	0.20
R_t	2D	maximum peak-valley	0.58	1.09	2.46	1.42
S_a	3D	arithmetic average	0.20	0.35	0.83	0.52
S_q	3D	root-mean-square	0.24	0.42	1.01	0.69
S_t	3D	maximum peak-valley	1.76	4.88	9.14	5.27

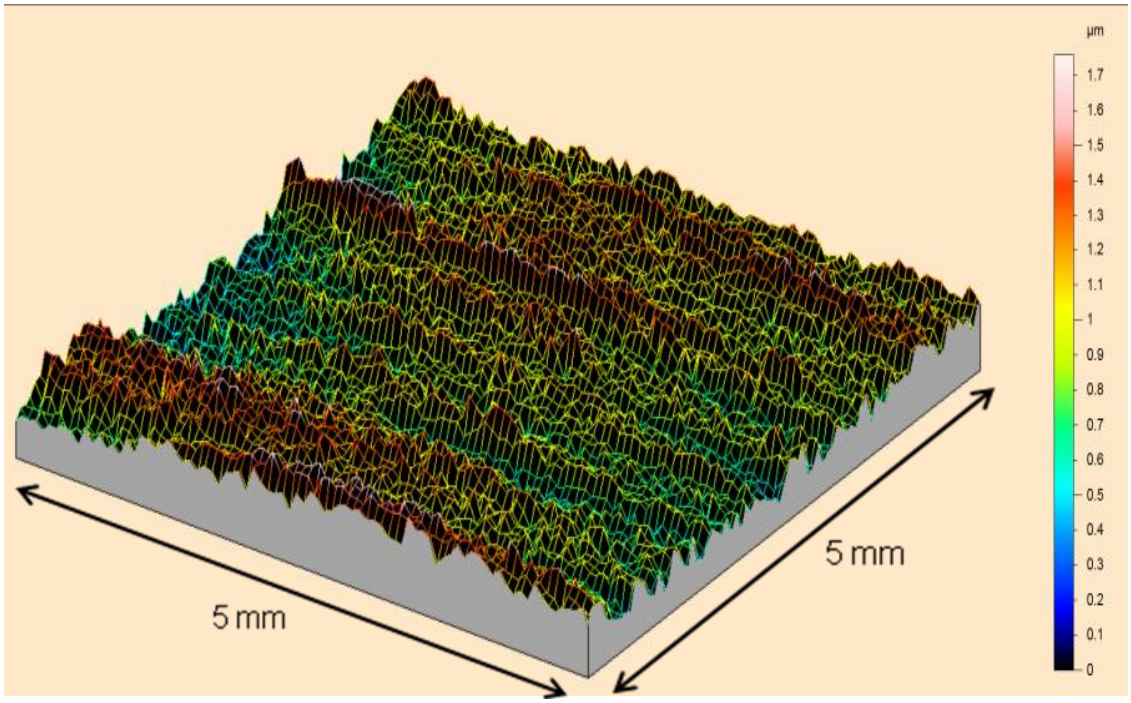

Figure 5.12. Topography profile of Feccralloy® coupon which was not treated.

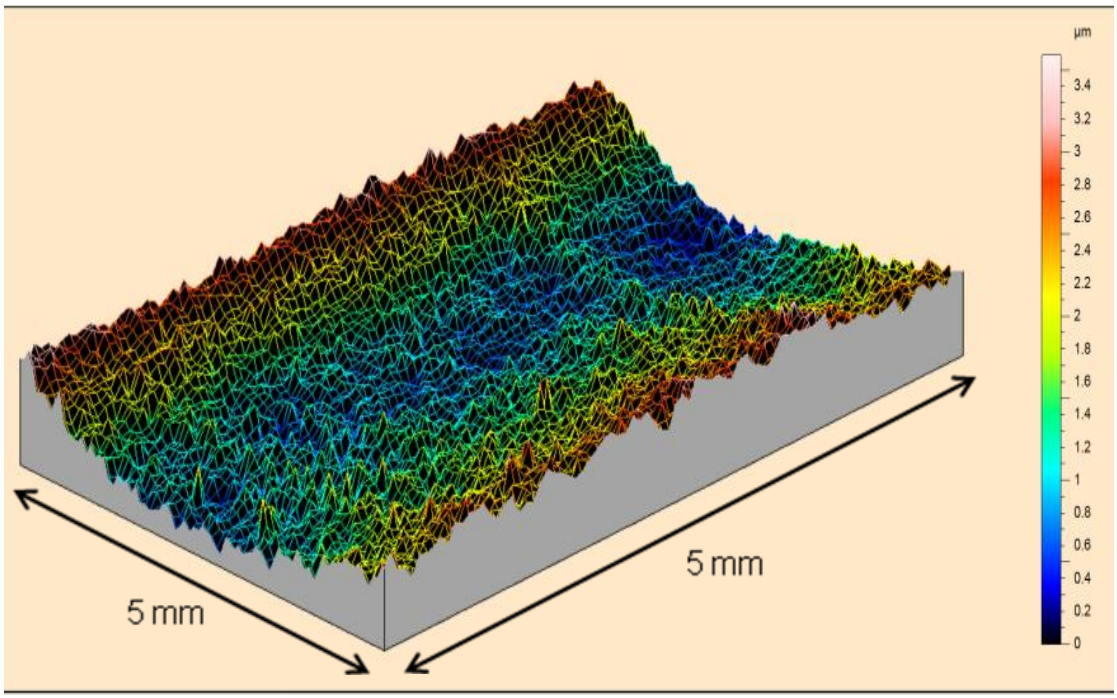

Figure 5.13. Topography profile of Feccralloy® coupon preoxidised at 950 ^{o}C for 5 h.

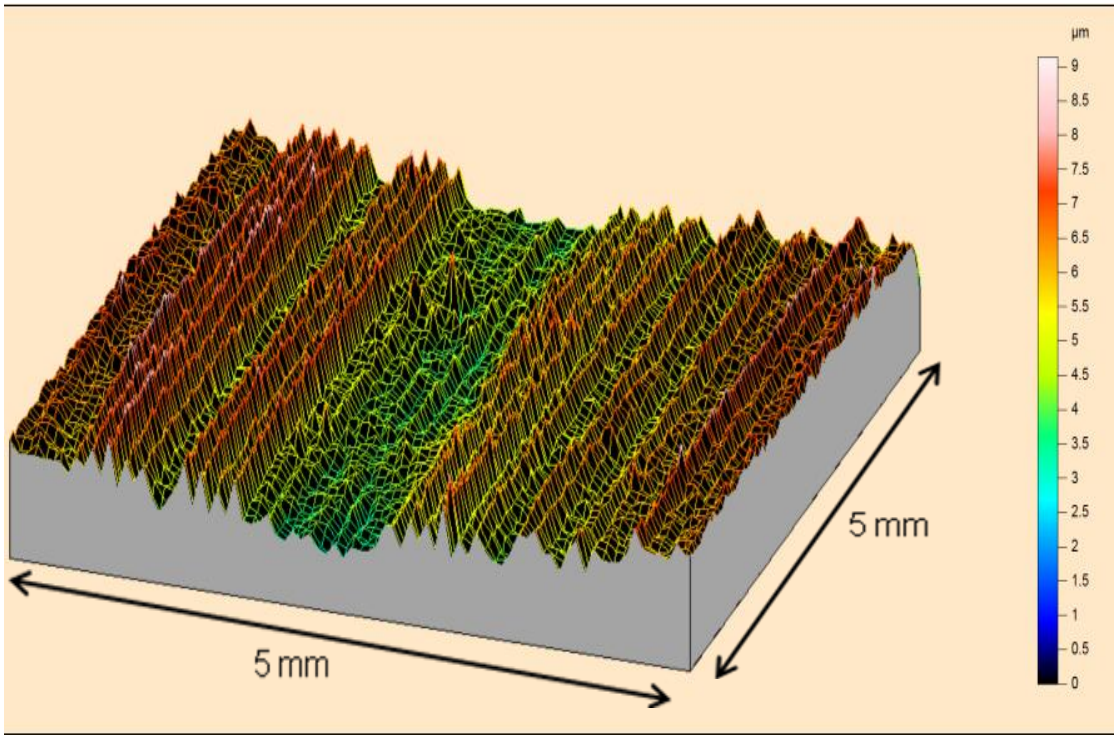

Figure 5.14. Topography profile of Feccralloy® coupon preoxidised at 950 °C for 10 h.

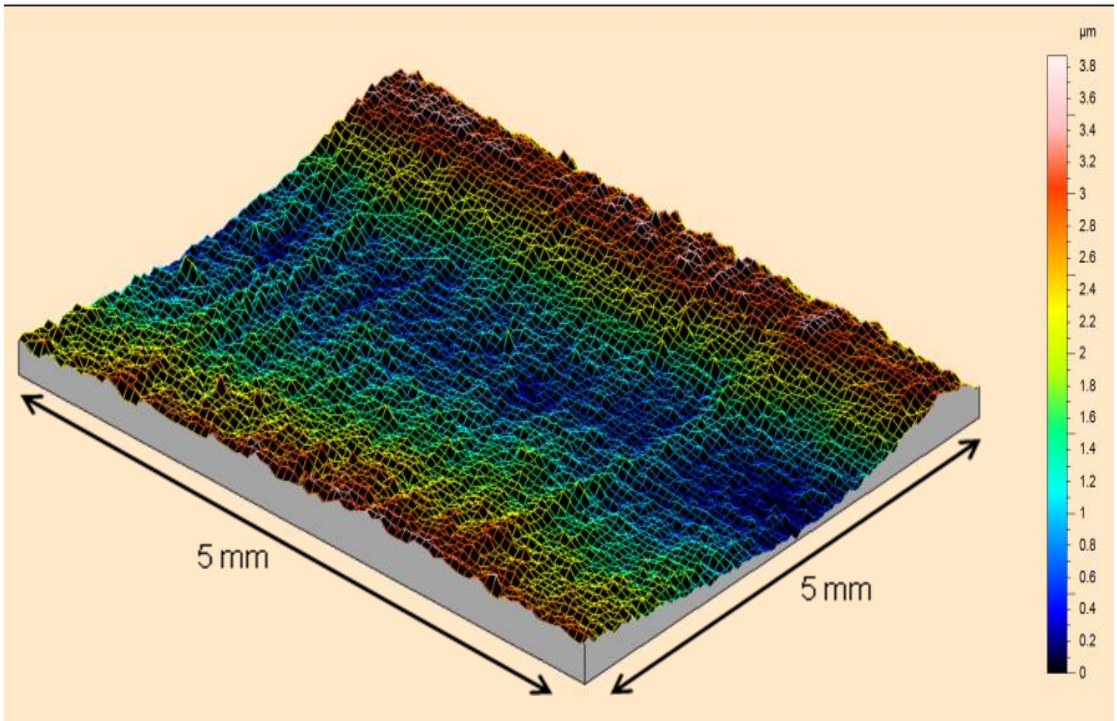

Figure 5.15. Topography profile of Feccralloy® coupon preoxidised at 950 °C for 30 h.

5.5.3 XRD analysis of Fecralloy® surface

The XRD patterns in Figures 5.16 – 5.19 show the surface chemical composition of the coupons preoxidised at 950 ^{o}C for 0 – 30 h. All the coupons at different preoxidation conditions contained some amounts of α–alumina, Fe and Cr on their surfaces. The presence of these items irrespective of the preoxidation conditions was a confirmation of the previous studies by Badini and Laurella (2001) and Tien and Pettit (1972).

The untreated coupon contained Fe(Cr) peak and some α-alumina peaks, which were present in small amounts (Figure 5.16). The coupons were new and not layered at the conditions of non-treatment.

Preoxidation for 5 h produced substantial amounts of θ–alumina and a small amount of α–alumina (Figure 5.17). It is revealed that the most of the θ–alumina formed has not yet been transformed into α–alumina because preoxidation had not sufficiently occurred.

Increased preoxidation to 10 h produced sufficient transformation of θ-alumina into α–alumina, as the peaks of the latter are large and conspicuously visible (Figure 5.18). For these coupons, well formed α–alumina layers were predominantly present on their surface and they represented suitable compatible ingredients for coatings.

Prolonged preoxidation for 30 h however resulted in the formation of α-alumina conglomerates as other alloy elements (i.e. Fe and Cr) were spontaneously oxidized. This is characterised by diminishing peaks of α–alumina (Figure 5.19).

The results are in accordance with the previous studies on this area (e.g. Jia et al., 2007; Nicholls and Quadakkers, 2002) which showed excellent α–alumina composition on coupon surface preoxidised at 950 ^{o}C for 10 h. These studies also reported that the Fecralloy® surface enrichment by aluminium during pretreatment was caused by an elemental transport process.

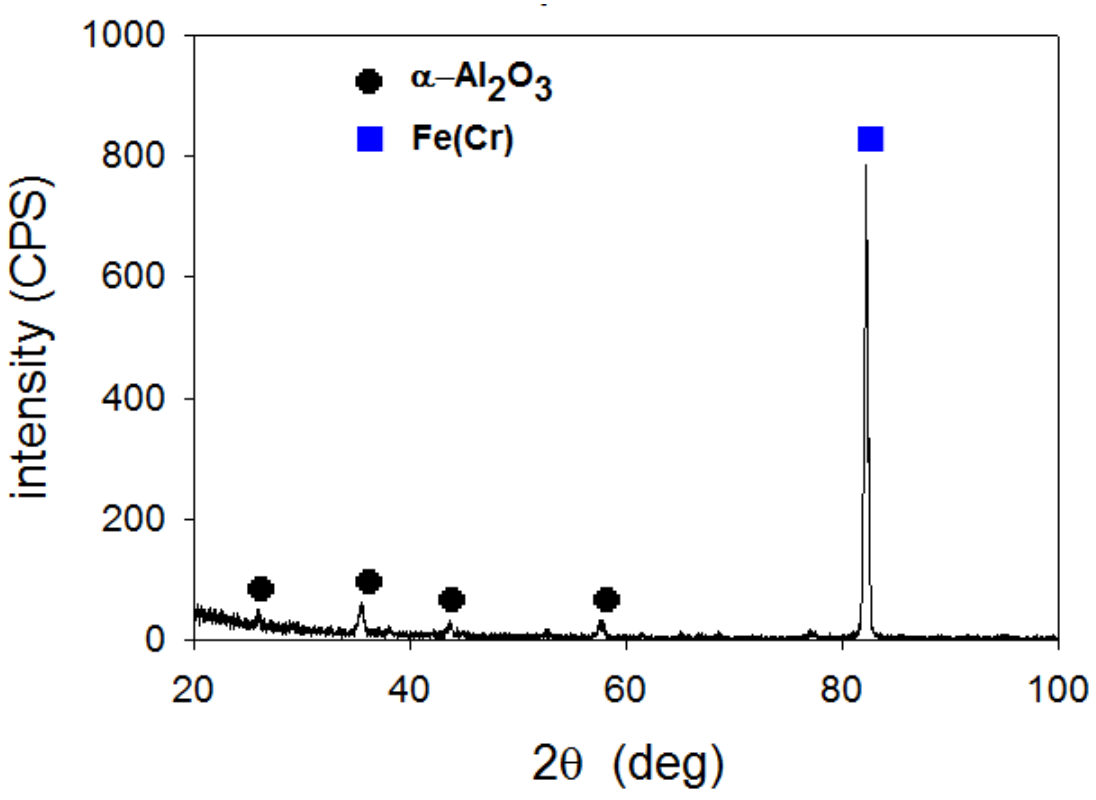

Figure 5.16. XRD patterns of Fecralloy® coupon which was not treated.

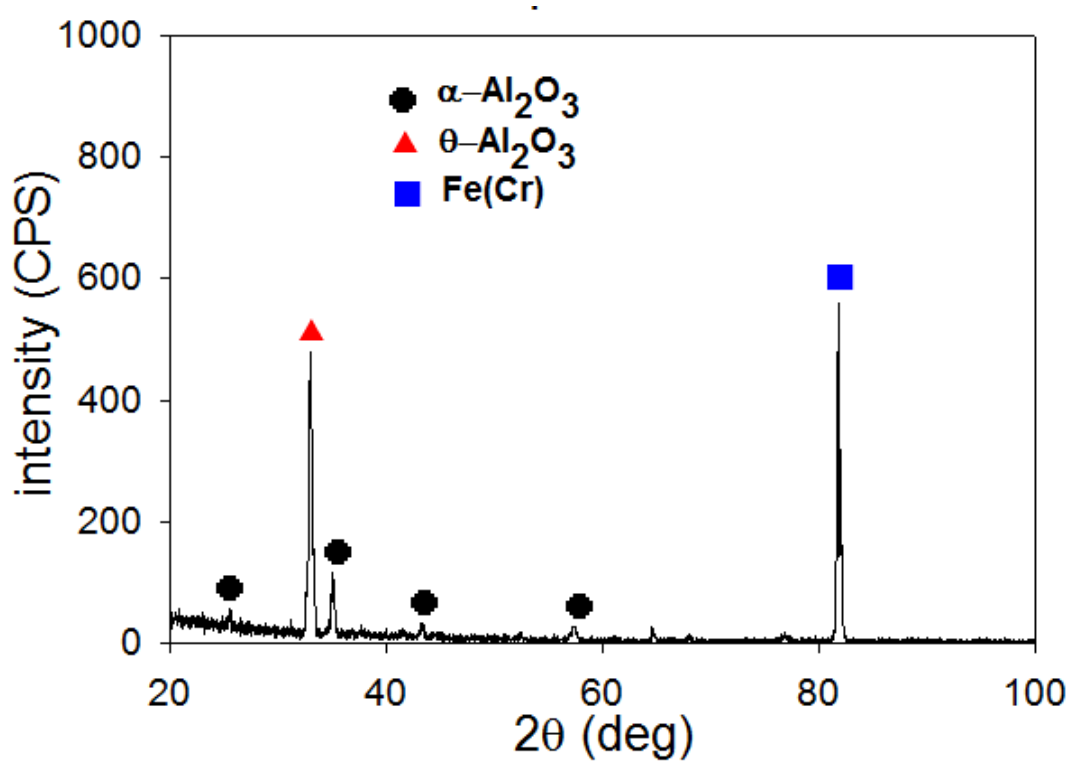

Figure 5.17. XRD patterns of Fecralloy® coupon preoxidised at 950 °C for 5 h.

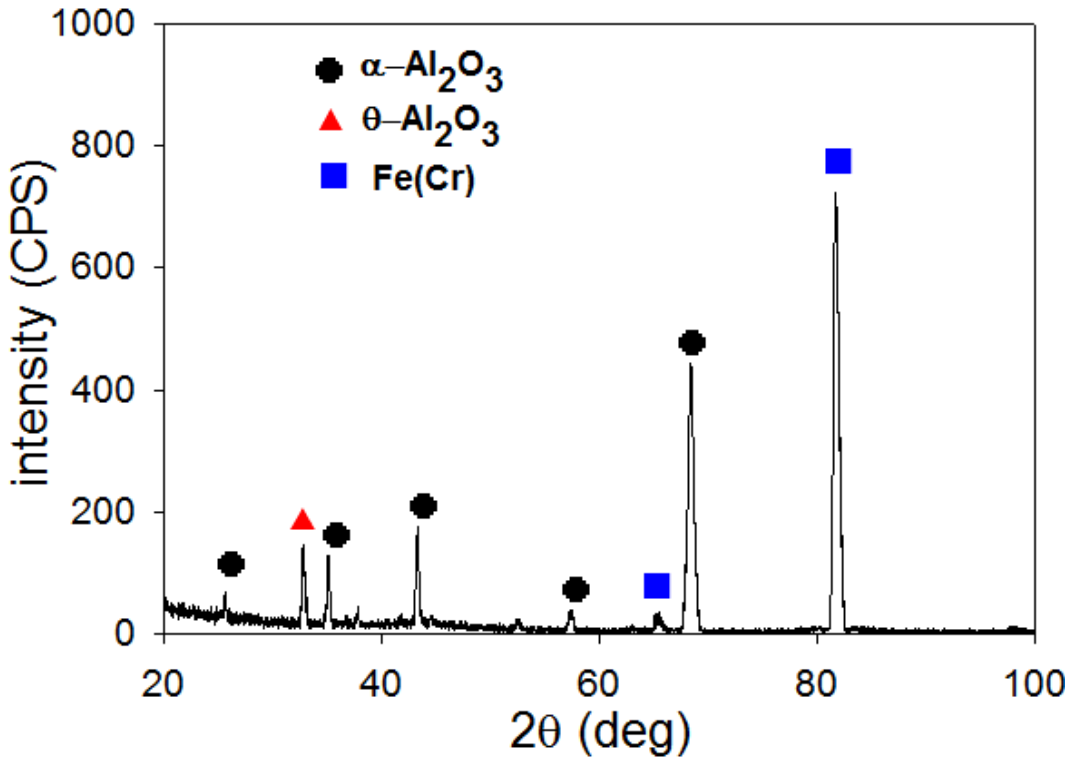

Figure 5.18. XRD patterns of Fecralloy® coupon preoxidised at 950 °C for 10 h.

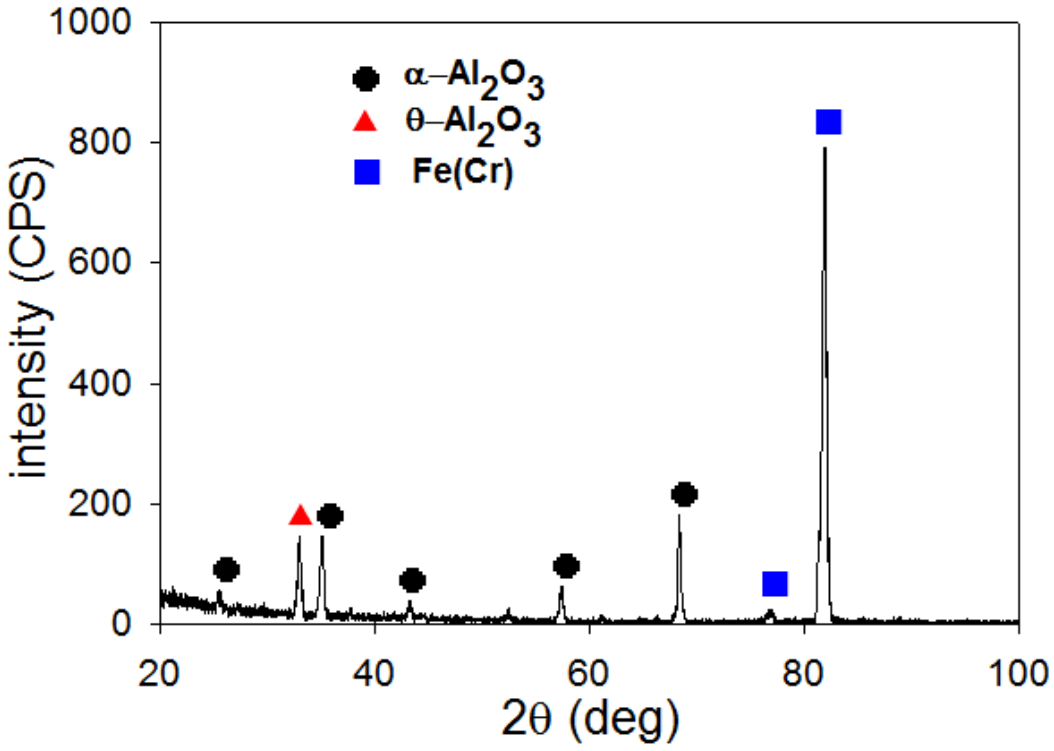

Figure 5.19. XRD patterns of Fecralloy® coupon preoxidised at 950 °C for 30 h.

5.5.4. Fecralloy® surface microstructure by SEM

The SEM micrographs displayed in Figures 5.20 & 5.21 clearly show the distinctions between the surface morphologies of the untreated and pre-oxidised coupons. The untreated coupon [Figures 5.20 & 5.21 (a)] has a plain surface with no significant microstructure while the preoxidised coupons contain α–alumina whiskers [Figures 5.20 & 5.21 (b), (c), (d)].

After 5 h of preoxidation, there exists trace amounts of α-alumina which were irregularly littered across the coupon surface [Figures 5.20 & 5.21 (b)].

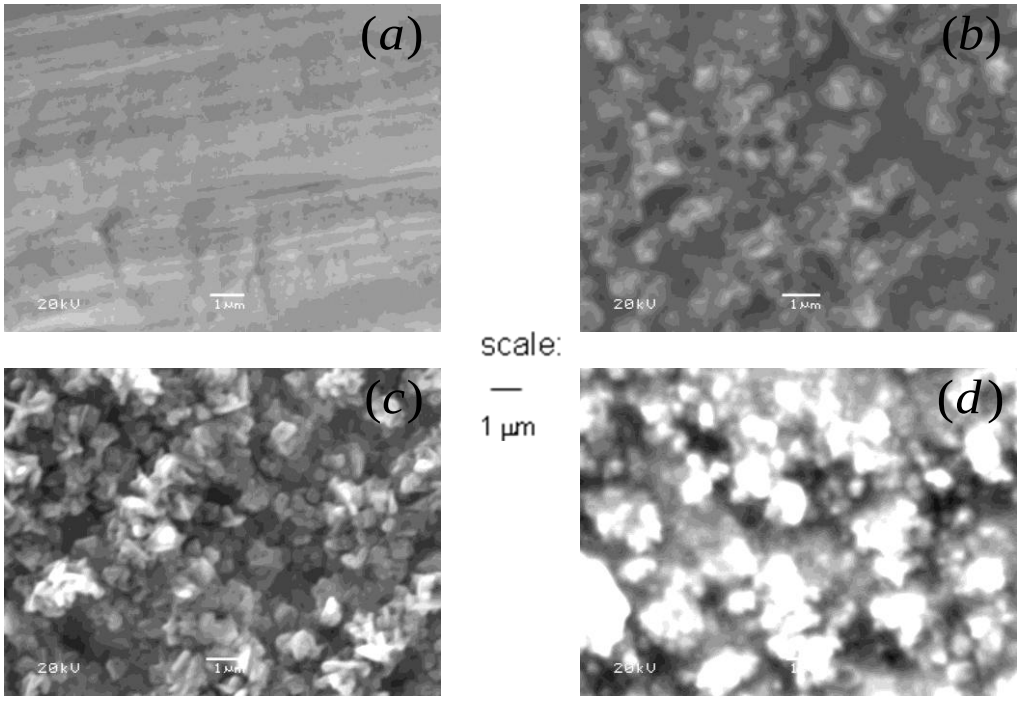

Figure 5.20. SEM micrographs of Fecralloy® coupons preoxidised at 950 °C for: (a) 0; (b) 5; (c) 10 and (d) 30 h (for 1 µm scale).

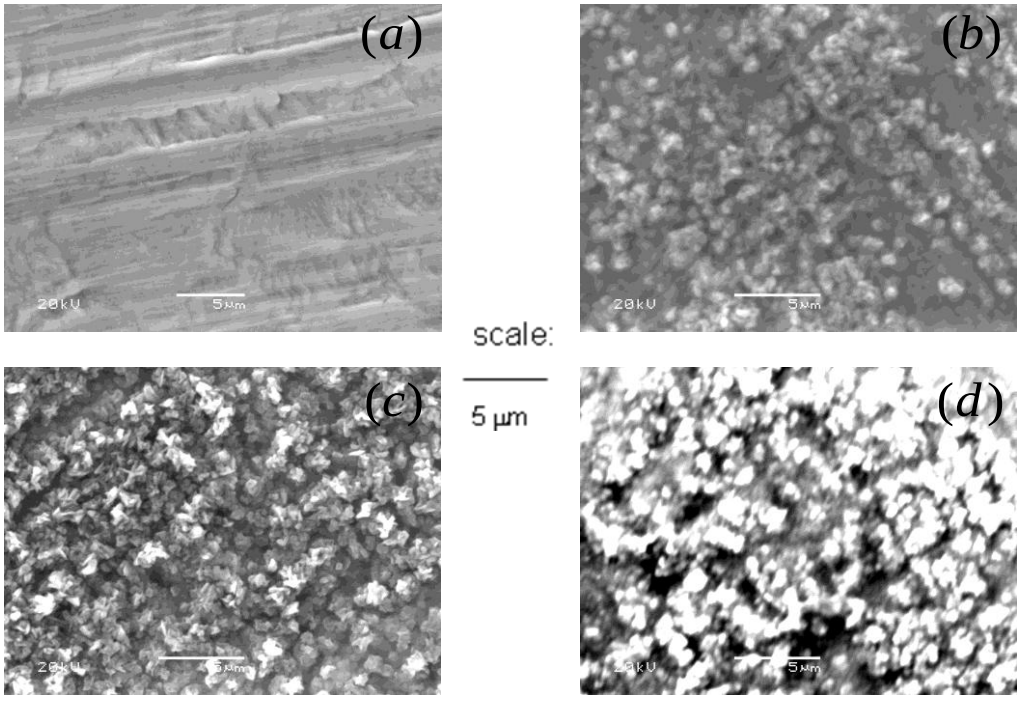

Figure 5.21. SEM micrographs of Fecralloy® coupons preoxidised at 950 °C for: (a) 0; (b) 5; (c) 10 and (d) 30 h (for 5 µm scale).

However, the coupon preoxidised for 10 h was characterised by uniform, full, conspicuous and randomly oriented α-alumina whiskers [Figures 5.20 & 5.21 (c)]. It is shown clearly that at this condition the α-alumina are properly formed and arranged in a manner which positions them for their excellent adhering capabilities (Avila et al., 2005). The attendant effects of preoxidation for up to 30 h was the formation of non-uniform conglomerates of α-alumina [Figures 5.20 & 5.21 (d)].

The results from the EDS which have been incorporated to the SEM revealed the elemental composition of the coupon surface at different preoxidation conditions (Table 5.3). Initially the untreated foil surface had predominately Iron (Fe = 72.4 wt%) and Chromium (Cr = 21.3 wt%) with Aluminium (Al) and Oxygen (O) only 4.8 wt% and 0.7 wt% respectively. The amounts of Fe and Cr fell to 35.5 wt% and 19.0 wt% respectively while the Al and O both increased to 16.1 wt% and 27.4 wt% respectively after 5 h pre-oxidation. At 10 h pre-oxidation Al and O were the majority elements at the coupon surface contained at 34.6 wt% and 37.8 wt% respectively while Fe and Cr both slumped to 19.2 wt% and 7.9 wt% respectively. Prolonged preoxidation resulted in the increase in Fe (32.5 wt%) and Cr (13.5 wt%) at the expense of Al (25.2 wt%) and O (26.7 wt%).

The SEM / EDS results are in accordance with the chemical composition data derived from the XRD analysis, which showed similar pattern in composition changes. All the results show good correlation with the recent findings of Jia et al. (2007) who found optimal surface microstructure and maximum Al (28.5 wt%) and O (36.7 wt%) enrichment after preoxidation at 950 ^{o}C for 10 h.

Table 5.3. Elemental composition of the coupon surfaces by EDS.

Element	Amounts (wt%)			
	Untreated (0 h preoxidation)	5 h preoxidation	10 h preoxidation	30 h preoxidation
Oxygen (O)	0.76	27.40	37.84	26.69
Aluminium (Al)	4.78	16.13	34.56	25.21
Chromium (Cr)	21.33	18.98	7.92	13.54
Iron (Fe)	72.47	36.50	19.19	32.48

5.5.5. Coating loading and adherence

The SEM micrographs of the surface and side views of the coatings are shown in Figures 5.22 & 5.23. It is shown that all the coatings were homogenously distributed on the coupon surface except for the coatings on the untreated coupon. This is because the untreated coupon, unlike the treated coupons, had the least roughness and no wettability, and therefore there was no "grip" on the coatings. The fact that the coatings deposited on the coupons of less than optimal microstructure (i.e. preoxidised for 5 h and 30 h) were homogenous is a confirmation that coating by the automatic film applicator was an effective method of achieving the desired coating distribution. The coatings on the coupon preoxidised for 10 h appeared homogeneous and well supported by the Fecralloy® coupon.

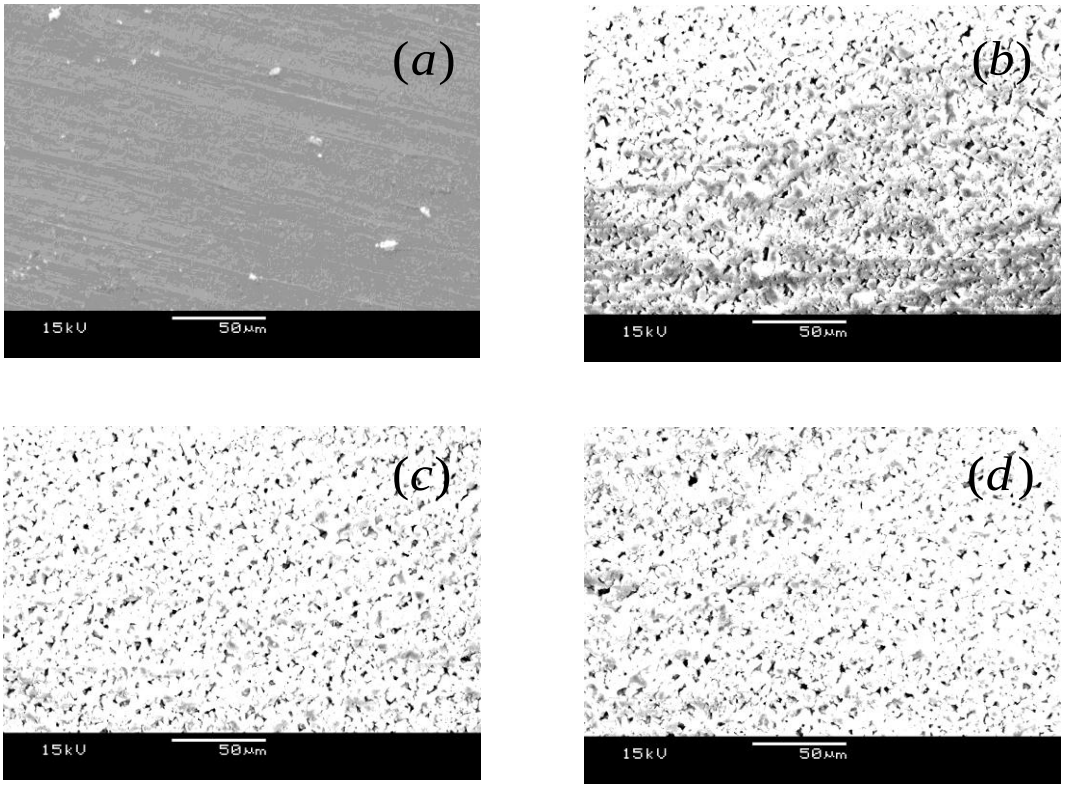

Figure 5.22. SEM micrographs of coatings on Fecralloy® coupons preoxidised at 950 °C for: (a) 0; (b) 5; (c) 10 and (d) 30 h (surface view).

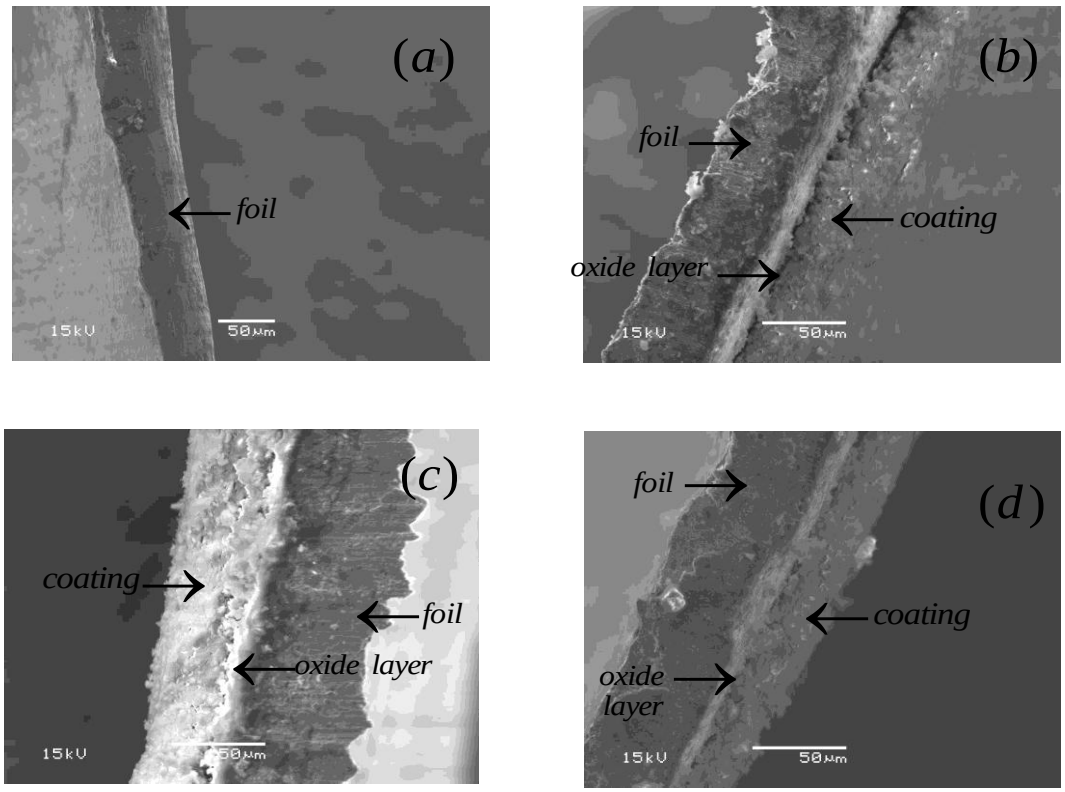

Figure 5.23. SEM micrographs of coatings on Fecralloy® coupons preoxidised at 950 °C for: (a) 0; (b) 5; (c) 10 and (d) 30 h (side view).

The coating loading and mass loss from adhesion test are shown in Table 5.4. These values were obtained by finding the average of 3 measurements, and the standard deviation SD as a percentage of the average was then calculated. Clearly, the duration of preoxidation has a major influence on the capability of the foil to perform well as a catalyst support. The slurry could not really wet the surface of the untreated coupon, hence leading to virtually "no coating loading". The preoxidised coupons however behaved differently as the slurry was wettable to their surfaces, thereby producing the coating loading of 5.19 – 7.94 mass%.

Table 5.4. Coating properties for Fecralloy® coupons preoxidised at 950 ^{o}C for 0 – 30 h.

Preoxidation time (h)	Coating loading (mass %) SD = ±3.1 % of loading	Average film thickness (±2μm)	Mass % loss from adhesion test SD = ±3.5 % of loss
0	0.08	negligible	99.60
5	5.19	27	19.42
10	7.94	38	9.89
30	6.75	33	16.30

The results in Table 5.4 can be properly explained in the light of the Fecralloy® surface characterisation discussed above in sections 5.5.2 – 5.5.4. For the untreated coupon, the coating loading and adherence were unsurprisingly very poor because the foil surface was the least rough. The coupons preoxidised for 5 and 30 h showed improved capabilities which was commensurate with their roughness measurements in section 5.5.2. The optimal coating loading and adherence were obtained from the coupon with

the roughest surface, i.e. the sample preoxidised for 10 h. This is because of the enhanced surface microstructure brought about by the randomly oriented α–alumina whiskers, thereby creating an ideal topography onto which coatings are firmly anchored.

The impingement of the surface roughness on the coating adherence is graphically represented on a bar chart in Figure 5.24 which showed that more coatings were lost by the less rough coupons from the adhesion test. The images of the coatings after the adhesion test are also given in Figure 5.25 which revealed the weakened areas where coatings had been lost. These findings are in accordance with the previous studies by Jia et al. (2007) and Zhao et al. (2003) which found the coupons preoxidised at 950 ^{o}C for 10 h to have the best adherence. The preoxidation of Fecralloy at 950 ^{o}C for 10 h have thereafter been used in recent studies, such as Fornasiero et al. (2008) and Shen et al. (2006).

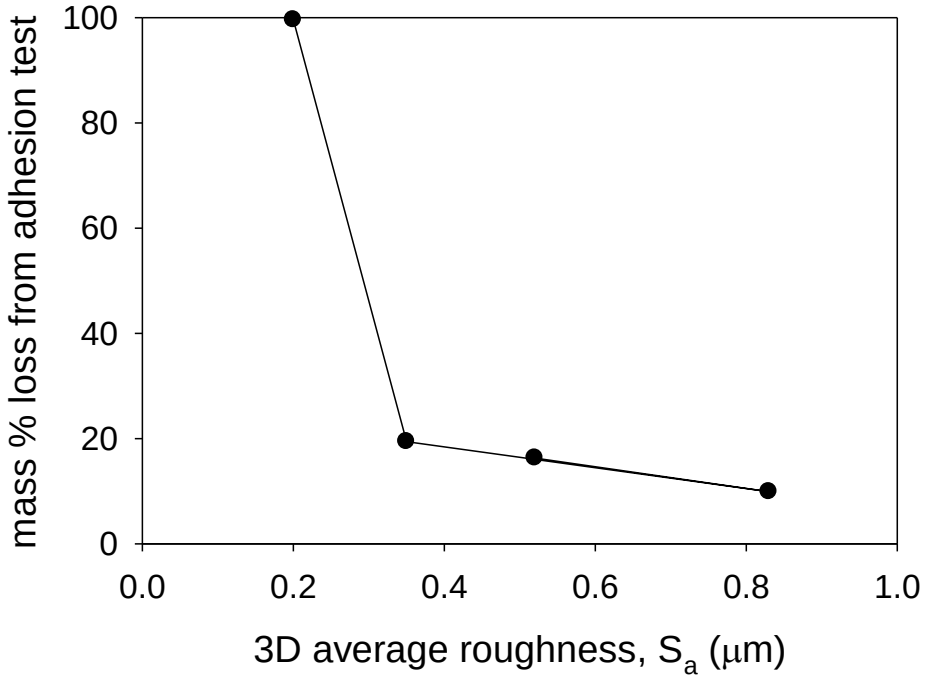

Figure 5.24. Mass % loss from adhesion test versus Fecralloy® surface roughness.

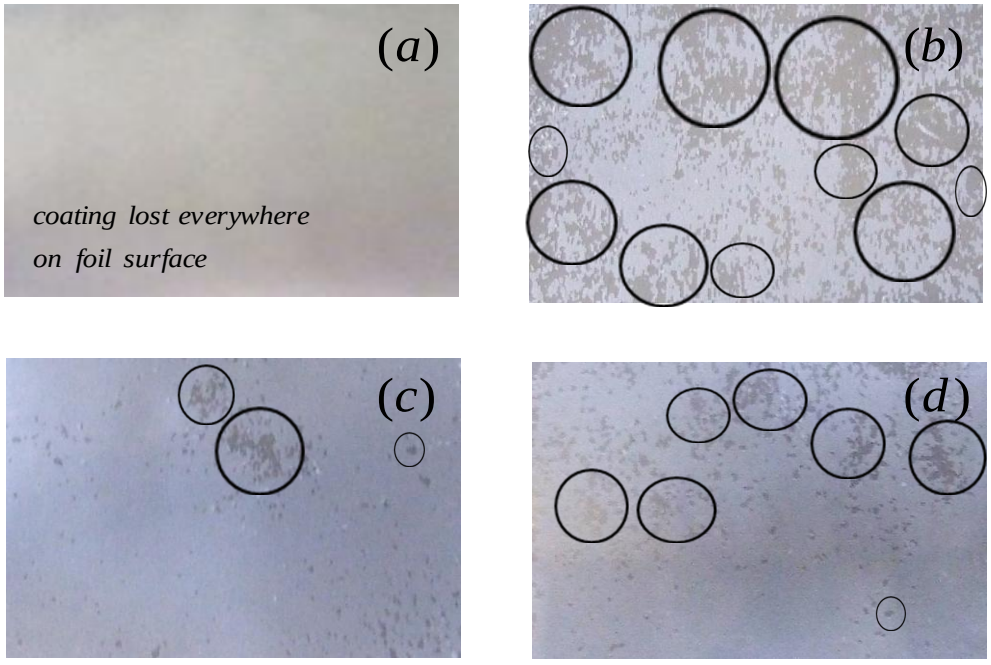

Figure 5.25. Coatings on Fecralloy® coupons after adhesion test: (a) 0; (b) 5; (c) 10 and (d) 30 h (circles indicating some areas of coating loss).

5.6 CONCLUSIONS

Fecralloy® foils are materials from which metallic monolith catalysts are made. The preoxidation conditions have been shown to be central to achieving a high degree of performance of Fecralloy® as a catalyst support, in terms of loading and adherence of the applied γ–alumina coating. A simplified hyperbolic model provided a good fit for specific mass gain by the coupons as a function of preoxidation time from 0 – 30 h.

The surface topography (namely roughness and profile) of Fecralloy® coupons determined by the LPI revealed that preoxidation at 950 ^{o}C for 10 h produced the roughest surface (R_a = 0.15 μm and S_a = 0.35 μm). The SEM / EDS and XRD results

also showed that the optimal surface microstructure was achieved at these preoxidation conditions, thus confirming the consistency of these techniques.

Upon coating the preoxidised Fecralloy® coupons with γ–alumina slurry using the automatic film applicator, the optimal coating loading (7.9 mass %) and adherence (9.9 mass % loss) were obtained from coupons preoxidised at 950 ^{o}C for 10 h, as these conditions produced the optimal surface topography and microstructure. These coupon surfaces were also typified by conspicuous and randomly-oriented α–alumina whiskers which promote coating adherence.

Whereas the untreated coupons exhibited no significant microstructure and wettability, the coating loading and adherence were extremely poor. The coupons preoxidised at 950 ^{o}C for 5 h and 30 h showed average surface topography, with their surface microstructure below par, such that their coating loading (< 6.8 mass %) and adherence (> 16.2 mass %) were comparably worse than the optimal.

The automatic film applicator was also shown to be an appropriate coating instrument which enabled the production of homogeneous and well adhered coatings.

6

COATING METHODOLOGY AND FACTORS INFLUENCING COATING PROPERTIES

In this chapter the optimal methodology for coating Fecralloy® using the automatic film applicator was determined by investigating the effects of the drying profile, calcination, coating speed and bar gap on the coating properties. It is shown that the drying profile (15, 25, 40 and 85 ^{o}C/min) produced no effect on the coating properties, and that calcination resulted into the sintering and redistribution of coatings. The coating speed (50, 100, 250 and 500 mms^{-1}) had no effects on coating properties, while the increase in the bar gap (10, 25 and 100 µm) produced an increase in the coating loading with a slight impingement on coating adherence. The effects of the slurry pH (3 – 10) on coating properties showed that the optimal loading (7.94 mass%) and adherence (9.89 mass%) were achieved at a pH of 4. The increase in slurry solids concentration (25 – 45 wt%) produced an increase in the coating loading, but the loss from adhesion test was less than 10 mass% for solids concentrations not exceeding 40 wt%.

6.1 INTRODUCTION

The aim of this project is acquire knowledge which enables the production of high quality coatings for best autocatalytic performance. It is known from Chapter 2 that the coating quality is influenced by several critical factors, among which are the coating methodology and the slurry characteristics. The coating methodology in this study refers to the essential coating process parameters (i.e. drying and calcination) and the film applicator operating conditions (i.e. coating speed and bar gap).

Fei et al. (2003) found that the large stresses which occurred on Fecralloy® rods at excessive coating thickness could result into cracks, and concluded that a critical coating thickness should not be exceeded to avoid cracks. The effects of drying and calcination on the coating properties have, however, not been thoroughly studied in the literature, particularly the drying profiles and the mechanical interactions caused by calcination. Furthermore, there is no detailed understanding of how the film applicator coating speed and bar gap influence the coating properties.

Jia et al. (2007) in their pioneering study found the effects of γ–alumina slurry characteristics (pH = 3.5 – 6.5; solids concentration = 15 – 45 wt%) on dip-coated Fecralloy® coatings. The coating process was repeated several times in their study to achieve the desired loadings. Though they showed that well adhered coatings were produced from slurries at solids concentration not exceeding 35 wt% and pH in the range of 4 – 6, there were notably inconsistencies in the coating loadings achieved.

This could be due to the coating technique used. Also, the pH range investigated in their study was somewhat limited.

To derive the optimal coating methodology in this study, experiments will be performed to investigate drying and calcination conditions as well as the coating speed and bar gap on the film application. The methodology derived from these investigations will then be used as the standard procedure for producing coatings in the subsequent experimental work to ensure consistency.

This is followed by experimental studies on how slurries of different characteristics (namely pH and solids concentration) interact on the Fecralloy® surface to produce coatings. The techniques for assessing coatings are based on the quantitative mass increase, SEM and ultrasonic vibration.

6.2 DERIVATION OF OPTIMAL COATING METHODOLOGY

6.2.1 Experimental

The Fecralloy® coupons described in section 5.4.1 were coated with γ–alumina slurry at a pH of 4 and solids concentration of 40 wt% using the automatic film applicator according to the procedure outlined in section 5.4.2. The coatings were allowed to partly dry at room temperature.

The coating properties (loading, adherence and visualisation) were assessed according the methods explained in section 5.4.3 for the following cases:

(a) Coatings heated at different rates of 15, 25, 40 and 85 ^{o}C/h to 110 ^{o}C. The samples were then calcined for 1 h at 500 ^{o}C. These coatings were named according to their heating rates (i.e. F_{15}, F_{25}, F_{40} and F_{85})

(b) Coatings dried at 110 ^{o}C for 1 h at 85 ^{o}C/h; one was not calcined ($F_{uncalcined}$) and the other was calcined at 500 ^{o}C for 1 h ($F_{calcined}$).

(c) Coatings ($F^{(10)}$, $F^{(26)}$ and $F^{(100)}$) produced using different wire-wound bar gaps (10, 26 and 100 μm) of the film applicator. They were all dried and calcined afterwards at 110 ^{o}C for 1 h and at 500 ^{o}C for 1 h respectively.

(d) Coatings (F_{S100}, F_{S250} and F_{S500}) produced at different coating traverse speed (100, 250 and 500 mms^{-1}) of the film applicator. They were all dried and calcined afterwards at 110 ^{o}C for 1 h and at 500 ^{o}C for 1 h respectively.

All the coatings were cooled at 85 ^{o}C/h to 25 ^{o}C.

6.2.2 Results and discussion

6.2.2.1 Effect of drying profile

Figure 6.1 represents the drying profiles of coatings heated at 15 – 85 ^{o}C/h to 110 ^{o}C and calcined at the same conditions at 500 ^{o}C for 1 h. The heating rates did not exceed 85 ^{o}C/ h so as to prevent an excessive build up of thermal stress in the Fecralloy® which could lead to structural damage (Trimm, 1995). The coating loading, thickness and adherence for the drying profiles are given in Table 6.1. These values were obtained by finding the average of 4 measurements, and the standard deviation SD as a percentage of the average was then calculated.

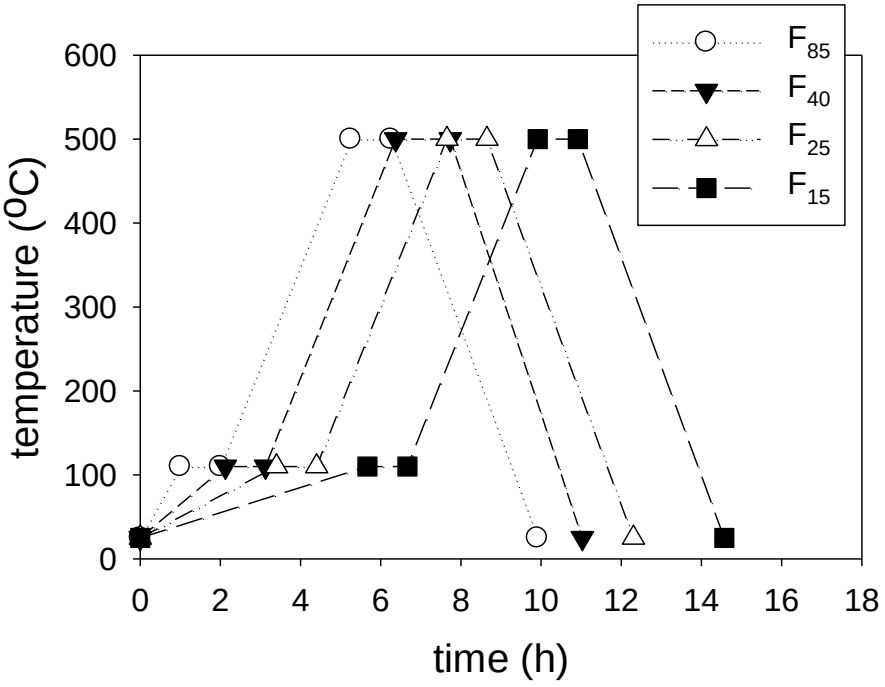

Figure 6.1. Drying profiles for coatings F_{15} – F_{85}.

Table 6.1. Properties of coatings dried at 15 – 85 ^{o}C/h for 1 h.

Heat up (^{o}C/h)	Coating loading (mass %) SD = ±1.7 % of loading	Average film thickness (±2µm)	Mass % loss from adhesion test SD = ±2.5 % of loss
85	7.94	38	9.89
40	7.81	39	10.23
25	8.05	37	9.61
15	7.76	38	9.82

Table 6.1 shows that there is no clear difference in the coating loading and adherence of F_{15} – F_{85}. The coatings showed good adherence capabilities of only 9.6 – 10.2 mass% loss from ultrasonic vibration. The SEM images of surfaces and sides of the coatings are shown in Figures 6.2 & 6.3.

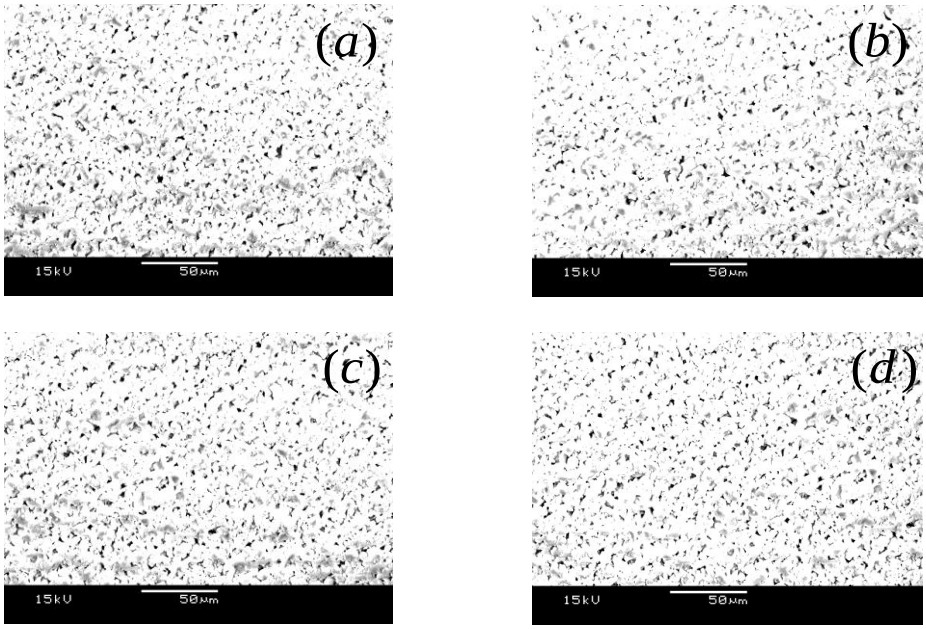

Figure 6.2. SEM surface images of coatings dried at different rates (a) F_{15} ; (b) F_{25} ; (c) F_{40} and (d) F_{85}.

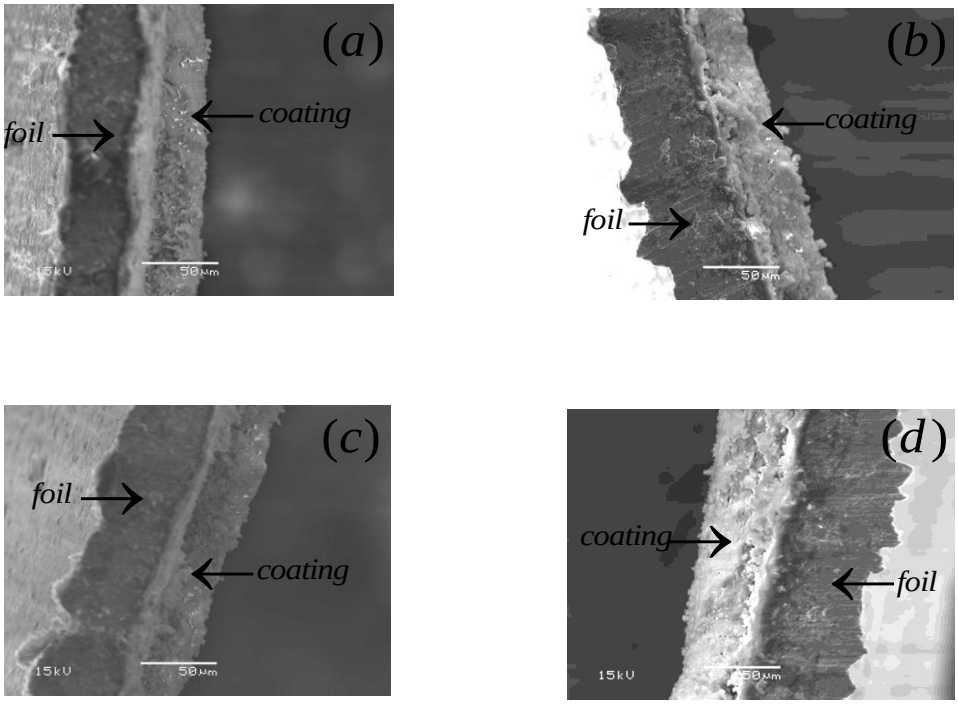

Figure 6.3. SEM side images of coatings dried at different rates (a) F_{15} ; (b) F_{25} ; (c) F_{40} and (d) F_{85}.

The SEM images in Figures 6.2 and 6.3 show homogeneous coatings with no cracks present in them. The absence of cracks in the coatings is a confirmation that the stresses developed in the coatings during drying were not large enough to generate shrinkages which could result into cracks (Fei et al., 2003; Thevenin et al., 2001). In addition to this, the critical coating thickness was not exceeded, thus leading to well-integrated coatings exhibiting good adherence. It can therefore be concluded that drying coatings at different heating rates between 15 – 85 ^{o}C/h had no effect on the coating adherence.

6.2.2.2 Effect of calcination

The SEM images of surfaces and sides of the uncalcined ($F_{uncalcined}$) and calcined ($F_{calcined}$) coatings are shown in Figures 6.4 and 6.5 respectively. Figure 6.4 shows that there are contrasting surface characteristics between $F_{uncalcined}$ and $F_{calcined}$. Whilst $F_{uncalcined}$ [Figure 6.4(a)] is shown to be inhomogeneous and incoherently packaged on the Fecralloy® surface, $F_{calcined}$ [Figure 6.4(b)] on the other hand is homogeneous and well packaged. These differences highlight the effects of calcination, which are sintering and redistribution of γ–alumina particles on the Fecralloy® surface (Pinna, 1998; Flynn and Wanke, 1974a; Flynn and Wanke, 1974b) .

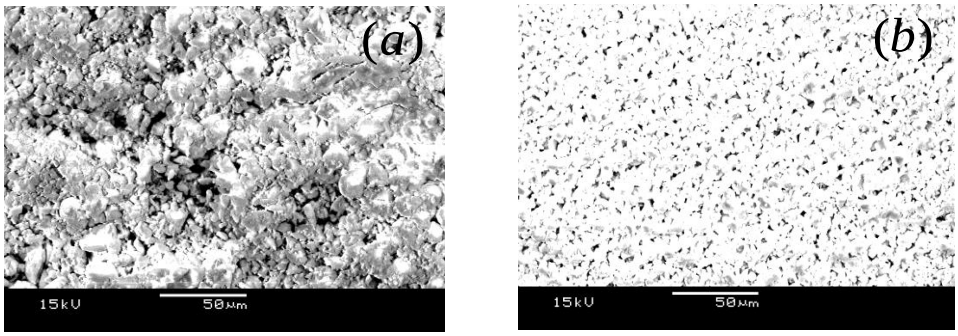

Figure 6.4. SEM surface images of coatings (a) $F_{uncalcined}$ and (b) $F_{calcined}$.

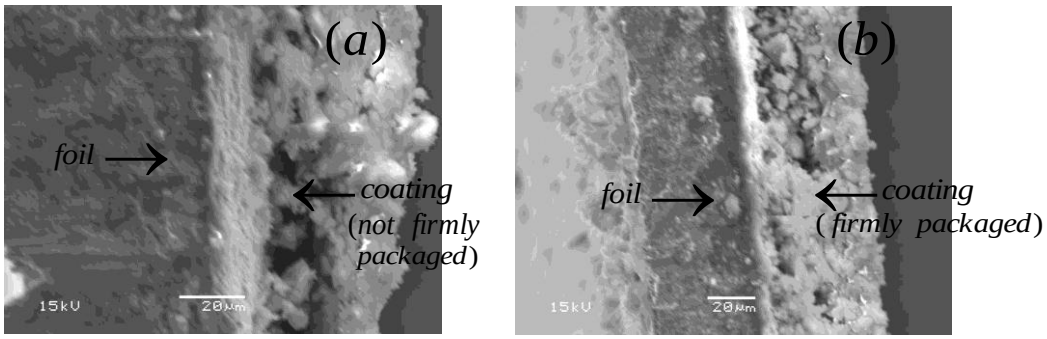

Figure 6.5. SEM side images of coatings (a) $F_{uncalcined}$ and (b) $F_{calcined}$.

Sintering is the bonding of a mass of powder at increased temperature to form small necks which then grow causing the powder to densify. At the microscopic level, the atomic rate of diffusion of the particles is very high at the calcination temperature of 500^{o}C, they therefore diffuse from the grain boundaries and deposit in the available pores (Ashby and Jones, 1998). There is consequently greater interactions of the particles as smaller particles are displaced to vacant spaces which are yet to be filled on the Fecralloy® surface. Calcination also serves the purpose of decomposing precursors to oxides, for coatings produced from metal precursors, as well as for the removal of extraneous binders (Pinna, 1998).

The SEM images of sides of the coatings in Figure 6.5 also show that, unlike $F_{calcined}$, gaps were present in the coating layer of $F_{uncalcined}$ and this is a confirmation that the coating was not firmly packaged. The coating properties are shown in Table 6.2. The values were averaged over 5 measurements with a standard deviation within 2.1 % for both coating loading and the mass % from adhesion test. Whilst there was no real difference in the coating loading, there was a much higher coating loss (i.e. 31.4 mass %) from the adhesion test. This is because there was no sintering and redistribution in $F_{uncalcined}$; therefore, there was no strong anchorage of the coating on Fecralloy® surface.

Table 6.2. Coating properties of $F_{uncalcined}$ and $F_{calcined}$.

Coating type	Coating loading (mass %)	Average film thickness (±2μm)	Mass % loss from adhesion test
$F_{uncalcined}$	8.21	40	31.37
$F_{calcined}$	7.94	38	9.89

6.2.2.3 Effect of bar gap

The wire-wound bars of different nominal gaps (10, 26 and 100 µm) mounted on the film applicator for coating the Fecralloy® coupons are shown in Figure 6.6. The coatings produced from these bars are shown in Figure 6.7, while the coating properties are given in Table 6.3.

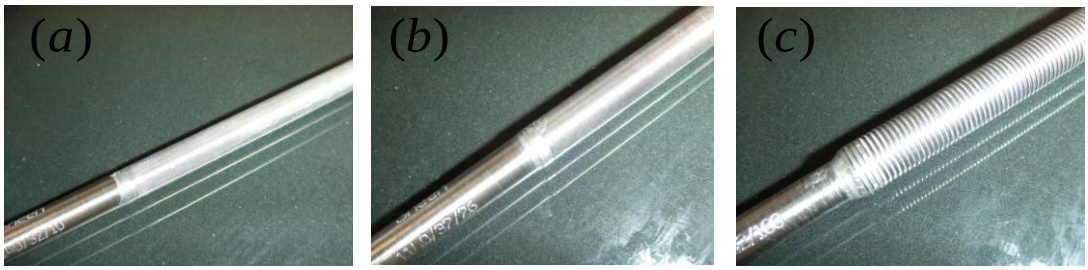

Figure 6.6. Wire-wound bars of different nominal gaps mounted on the film applicator to produce coatings: (a) 10 µm; (b) 26 µm and (c) 100 µm.

Table 6.3. Properties of coatings produced using bars of different nominal gaps.

Coating type	Coating loading (mass %) SD = ±1.9 % of loading	Average film thickness (±2µm)	Mass % loss from adhesion test SD = ±2.4 % of loss
$F^{(10)}$	1.18	8	6.57
$F^{(26)}$	2.79	15	8.26
$F^{(100)}$	7.94	38	9.89

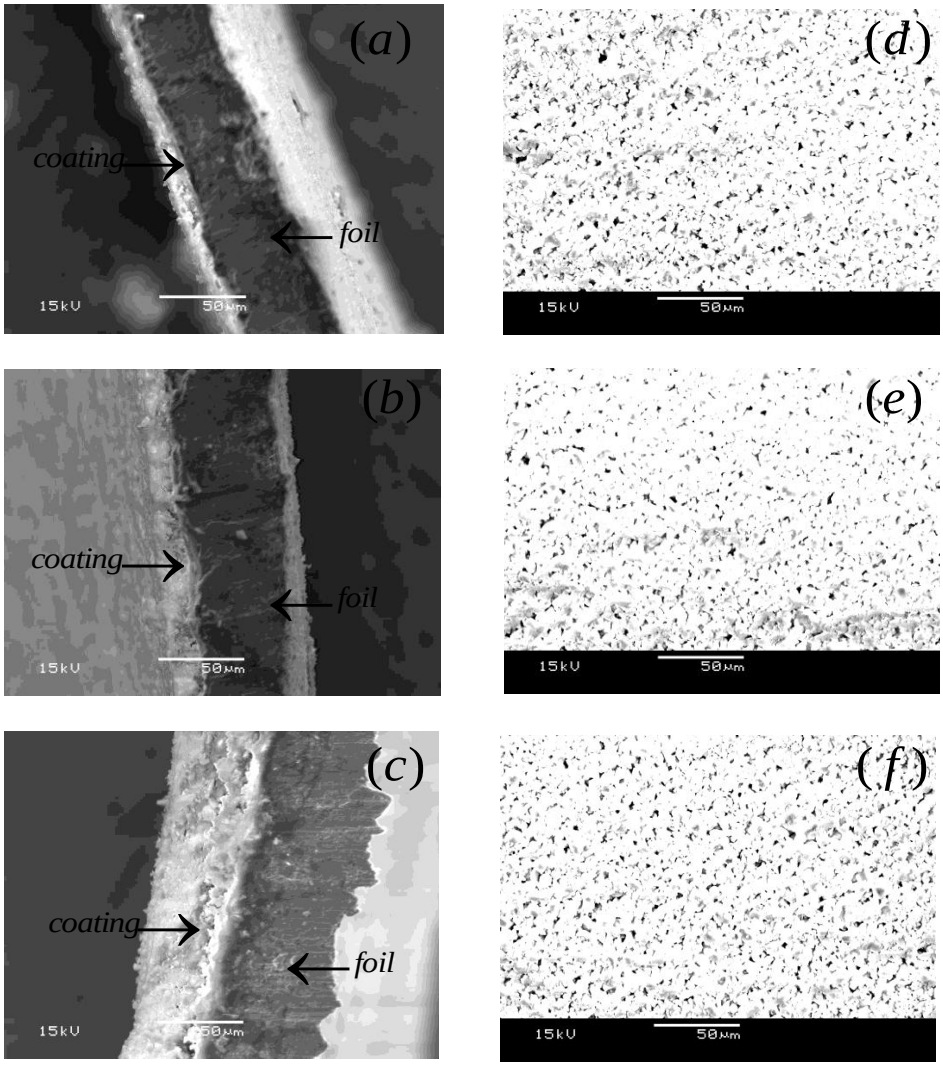

Figure 6.7. SEM side and surface images of coatings produced using bars of different gaps: (i) $F^{(10)}$ (a, d) (ii) $F^{(26)}$ (b, e) and (iii) $F^{(100)}$ (c, f).

It is shown in Figure 6.7 (d – f) that all the coatings are homogeneously distributed on the Fecralloy®. Figure 6.7 (a – c) shows that the coating thickness increased with increasing bar gap. This is because the mass of washcoat deposited (i.e. coating loading) on the Fecralloy® during coating increased when the bar gap was widened from 10 µm to 26 µm and finally to 100 µm (Table 6.3). This means that at increased coating loading there would be more active species absorped onto the γ–alumina on the Fecralloy® if the coating slurry contained PGMs [see Equation (1.4) in Chapter 1].

There was however a slight impingement on the coating adherence as the mass % loss from ultrasonic vibration increased with the increasing bar gap. The values were averaged over 5 measurements with standard deviation SD within 1.9 % and 2.4 % for the coating loading and the mass % loss respectively.

It is noteworthy that the mass % loss from adhesion test was less than 10 mass % for all the coatings assessed, which in comparison with tests of similar procedure (e.g. Jia et al., 2007; Shen et al., 2006; Valentini et al., 2001), was a good coating adherence. In these previous studies the coating loss of more than 12 mass% was mostly considered as poor in terms of adherence.

6.2.2.4 Effect of coating speed

Figure 6.8 shows the coatings produced using the film applicator at a fixed bar gap of 100 µm, but at different coating speeds of 100, 250 and 500 mms^{-1}. The coating loading and adherence results are given in Table 6.4. The values were averaged over 4 measurements with a standard deviation within 2.1 % and 3.0 % for the coating loading and the mass % loss respectively. The shear rate at which the slurry was drawn across the Fecralloy® increased with increasing coating speed of 100, 250 and 500 mms^{-1}, therefore corresponding to 1000, 2500 and 5000 s^{-1} respectively. The results show that there was no difference in the coating loading and adherence, and the SEM images show homogeneous distribution of coatings.

Table 6.4. Properties of coatings produced using different coating speeds.

Coating type	Coating loading (mass %) SD = ±2.1 % of loading	Average film thickness (±2 µm)	Mass % loss from adhesion test SD = ±3.0 % of loss
F_{S100}	7.94	38	9.89
F_{S250}	8.15	39	9.80
F_{S500}	7.83	38	9.49

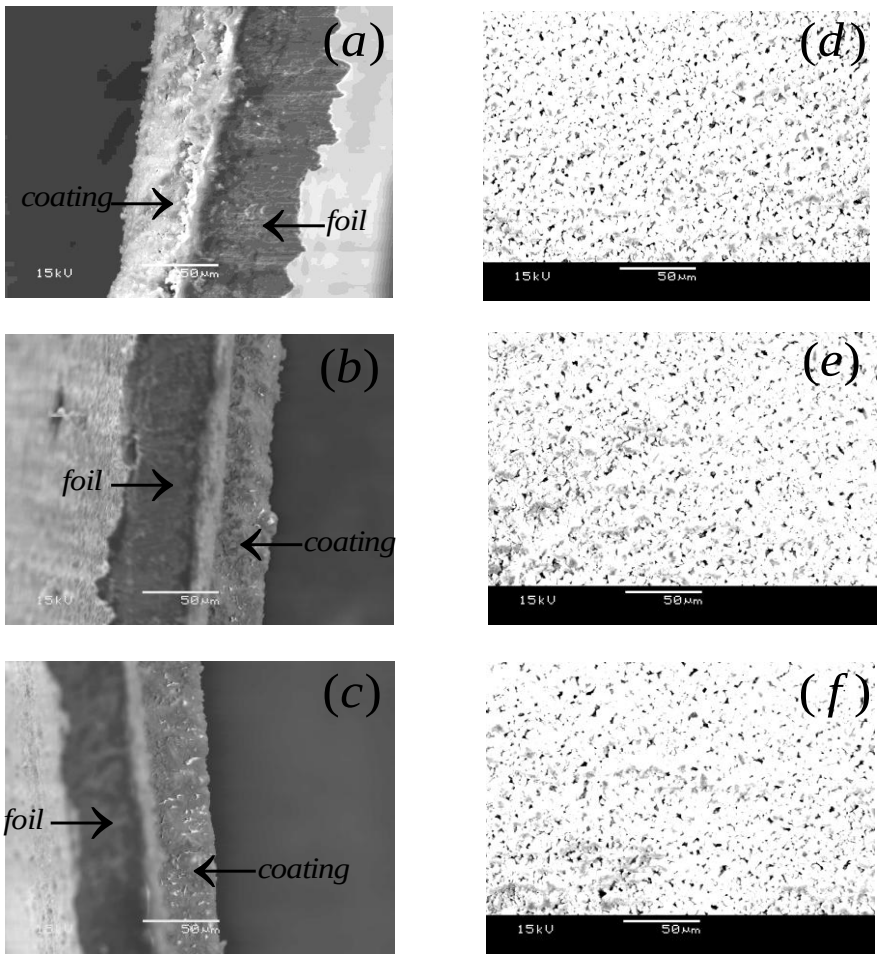

Figure 6.8. SEM side and surface images of coatings produced using different coating speeds: (i) F_{S100} (a, d), (ii) F_{S250} (b, e), and (iii) F_{S500} (c, f).

6.2.2.5 Outline of coating methodology

From the results showing how the coating process parameters and the operating conditions of the film applicator influence the coating properties, the following statements for the coatings investigated can be made:

(i) Drying of coatings at heating rates between 15 – 85 ^{o}C/h produced crack-free coatings and had little effect on the coating properties. This is because the stresses developed during drying were not large enough to generate shrinkages which lead to cracks.

(ii) Calcination of coatings at 500 ^{o}C for 1 h brought about homogeneity, sintering and redistribution of coatings, which resulted into strong coating adherence.

(iii) Increase in the bar gap produced greater coating loading and thickness but had minimal impingement on coating adherence. The loss of coating from ultrasonic vibration was less than 10 mass% for the bar gaps of 10, 26 and 100 μm.

(iv) Though the shear rate (1000, 2500 and 5000 s^{-1}) of drawdown increased due to increasing coating speed (100, 250 and 500 mms^{-1}), this caused no effect on coating properties.

For consistency and to produce coatings for optimal catalytic performance, the methodology for coating using the film applicator is summarised below:

(i) Drying at 110 ^{o}C for 1h at the rate of 85 ^{o}C/h which makes the drying process relatively fast (compared to 15, 25 and 40 ^{o}C/h), and therefore reduces production time.

(ii) Calcination to be performed at 500 ^{o}C for 1 h as this is critical to coating adherence.

(iii) Bar gap at 100 µm which produces high coating loading with minimal reduction in coating adherence.

(iv) Coating speed at 100 mms^{-1} (i.e. shear rate of 1000 s^{-1}) which is in accordance with the shear rate used for rheological characterisation in Chapter 4.

6.3 FACTORS INFLUENCING COATING PROPERTIES

6.3.1 Experimental

The effects of slurry pH and solids concentration on the coating properties are determined in this investigation. The Fecralloy® coupons described in section 5.4.1 were coated with γ–alumina slurry using the film applicator according to the procedure

outlined in section 5.4.2. The coating methodology adopted has been previously outlined in section 6.2.2.5.

The coating properties (loading, adhesion and SEM visualisation) were assessed according the methods explained in section 5.4.3. The following are the various slurry characteristics used for producing coatings:

(a) Slurries at fixed solids concentration of 40 wt% and at pH of 3, 4, 5, 6, 7, 9 and 10. The slurry pH was adjusted using solutions of acetic acid and sodium hydroxide as described in section 4.3.5 (a) in Chapter 4.

(b) Slurries at a fixed pH of 4 and at solids concentrations of 25, 30, 35, 40 and 45 wt%.

6.3.2 Results and discussion

6.3.2.1 Effect of pH

The surface and side images of coatings produced using slurry pH of 3 – 10 are shown in Figures 6.9. The coating loading and adherence measurements are given in Table 6.5. The values were averaged over 5 measurements with standard deviation within 2.1 % and 3.7 % for the coating loading and the mass % loss respectively. The coatings

were not properly adhered onto the Fecralloy® at a slurry pH of 3 and 7 with the adhesion loss of 15.4 and 20.2 mass % respectively because the γ–alumina particles were very sparingly dispersed in the slurry at this pH values due to very low zeta potential of particles (section 3.3.1).

Table 6.5. Properties of coatings produced at different slurry pH values.

Slurry pH	Coating loading (mass %) SD = ±2.1 % of loading	Average film thickness (±2μm)	Mass % loss from adhesion test SD = ±3.7 % of loss
3	6.27	22	15.35
4	7.94	35	9.89
5	8.21	36	11.17
6	8.37	36	11.93
7	6.05	21	20.18
9	7.48	33	13.69
10	7.99	34	12.02

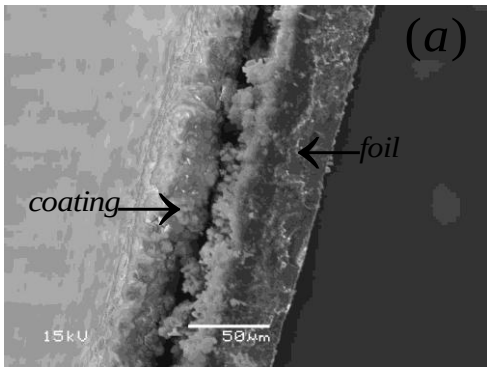

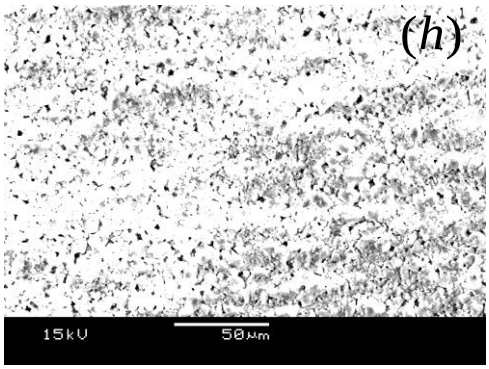

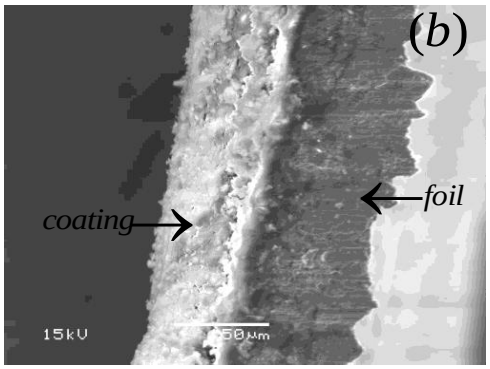
(b)
coating
foil
15kV
50µm

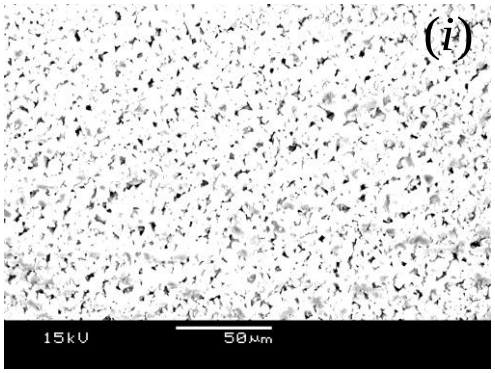
(i)
15kV
50µm

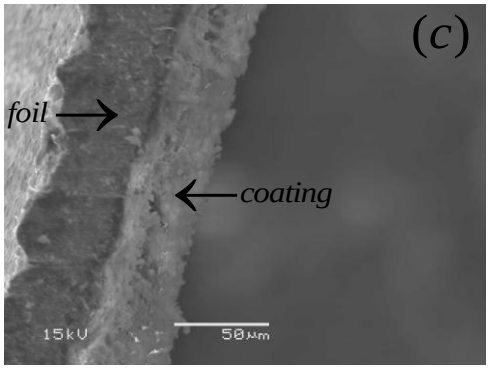
(c)
foil
coating
15kV
50µm

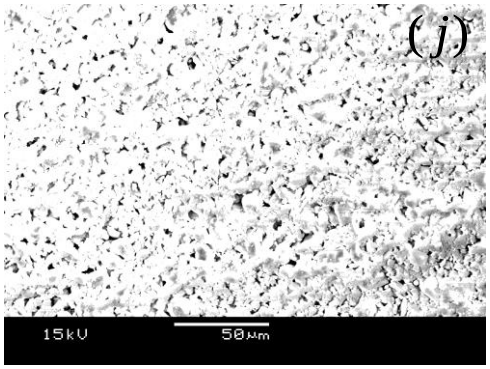
(j)
15kV
50µm

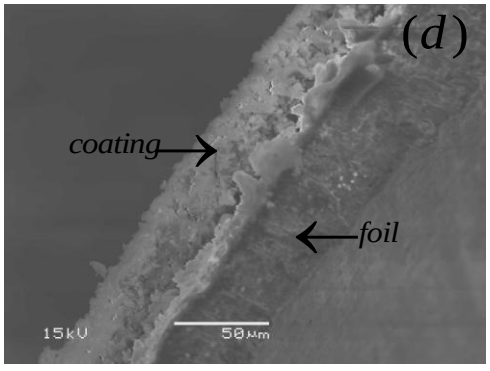
(d)
coating
foil
15kV
50µm

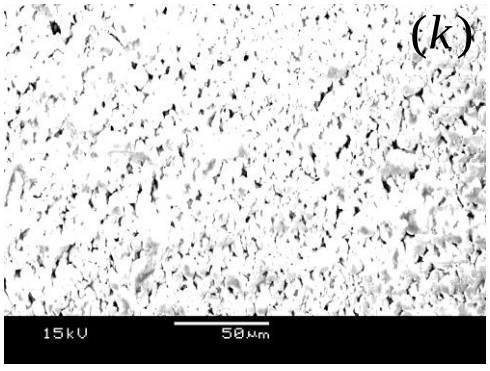
(k)
15kV
50µm

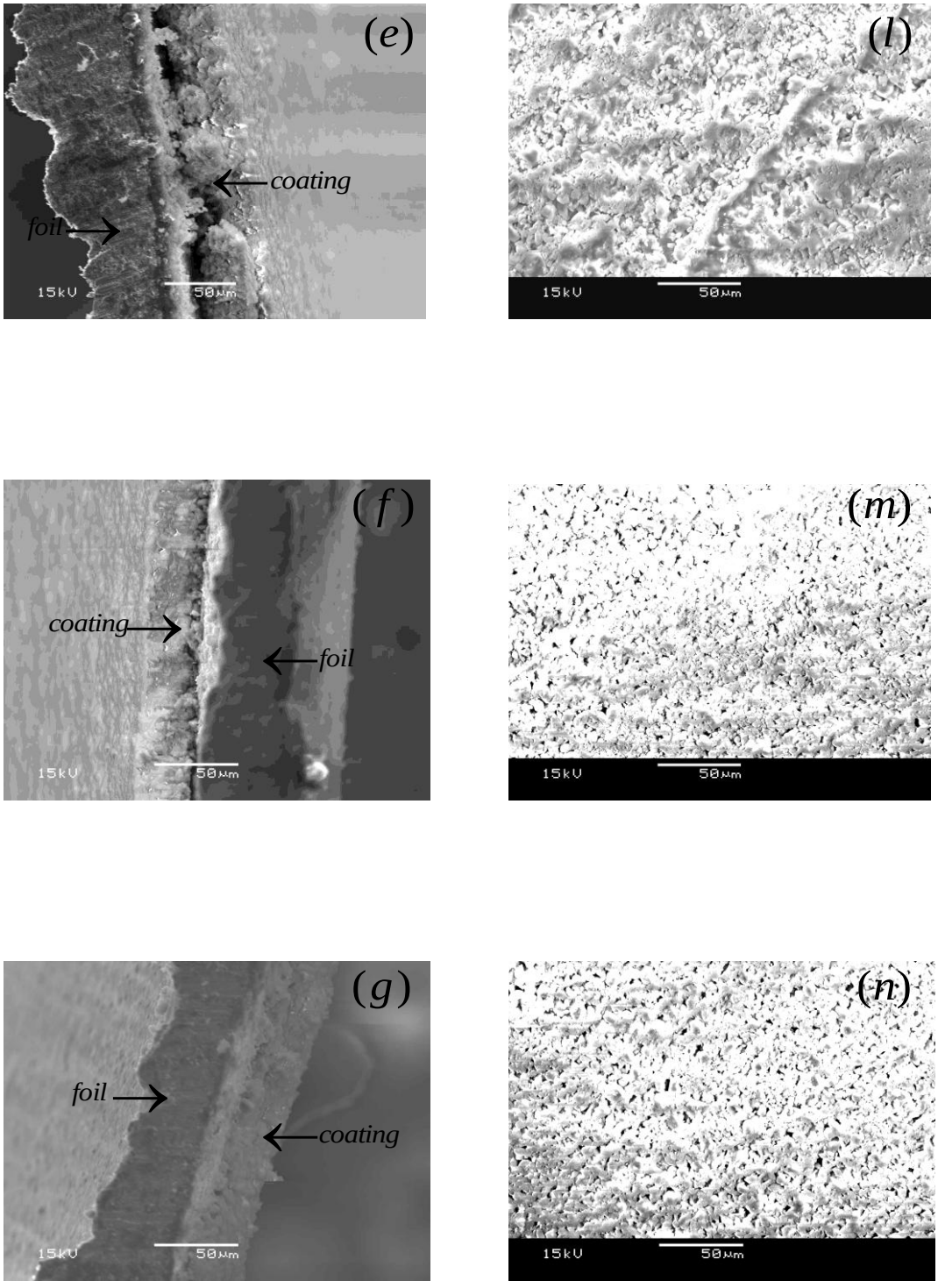

Figure 6.9. SEM side and surface images of coatings produced from slurries of different pH values: (i) 3 (a, h); (ii) 4 (b, i); (iii) 5 (c, f); (iv) 6 (d, k); (v) 7 (e, l); (vi) 9 (f, m) and (vii) 10 (g, n).

The coating images show particle aggregates and less homogeneity occurring, and this is not surprising as it was discovered in Chapter 3 that particle stabilisation at the pH values of 3 and 7 is minimal. The coating adherence at the pH values of 5, 6, 9 and 10 fared better at 11.2 – 13.7 mass % loss because of the increased particle stabilisation as the pH values are further away from the iep determined at 7.7.

The pH of 4 gave the best coating adherence of 9.89 mass % as the particles were well dispersed at this pH and could move and fill the asperities on the Fecralloy® surface. The results are in line with the rheological results in section 4.4.2.1 which showed that the slurry had the minimum viscosity at a pH of 4 when the particles are adequately dispersed. Though not on a par with the pH of 4, the coating adherence at the pH values of 5, 6 and 10 decreased to around 12 mass% loss.

Figure 6.10 shows the relationship between the coating adherence [Figure 6.10 (a)] from the slurries and the corresponding zeta potential measurements [Figure 6.10 (b)]. The mass% loss of coatings from ultrasonic vibration depends on some factors, such as coating loading, duration of test and vibration frequency (Sun et al., 2007; Zhou et al., 2007). Based on previous studies of similar test procedures, it is found that coating losses exceeding 12 mass% are usually equated to poor adherence. Similarly, the coating adherence is considered as good for mass% losses below 12 mass% (Jia et al., 2007; Shen et al., 2006). In Figure 6.10 (a), line A represents the 12 mass % loss above which coatings are poorly adhered, and below which coating adherence is considered to be good. By convention the region between lines B and C in Figure 6.10 (b) denotes

poor stabilisation at which the zeta potential of particles is less than $|30|$ mV (Greenwood, 2003).

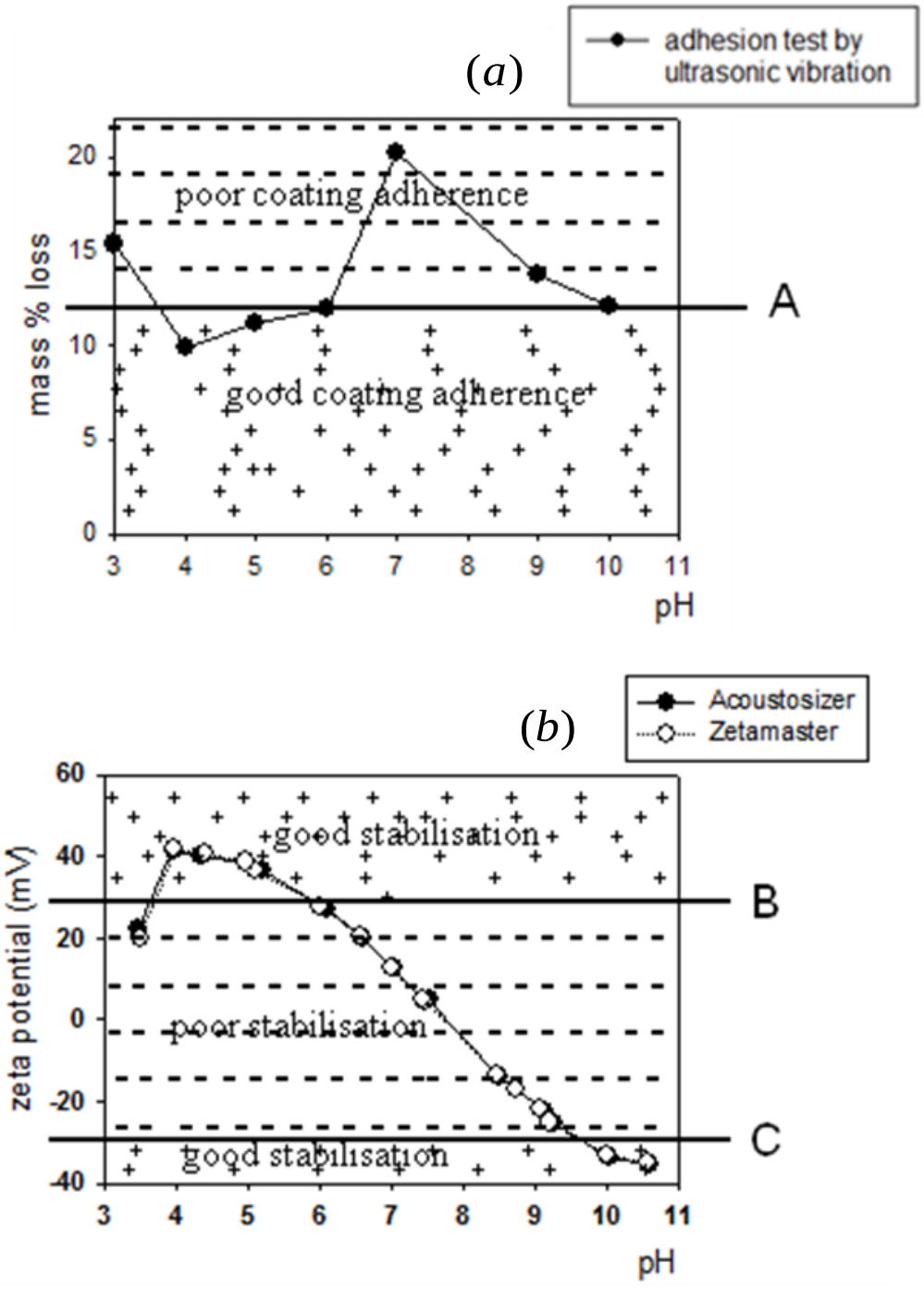

Figure 6.10. Relationship between coating adherence and particle stabilisation.

It is shown in Figure 6.10 (a) that the mass% from ultrasonic vibration for coatings at pH of 4, 5, 6 and 10 are in the region of good coating adherence which in turn corresponds to good particle stabilisation in Figure 6.10 (b). The coating adherence are in good agreement with the work done by Jia et al (2007) which concluded that the slurry pH should be between 4 – 6 to give the minimal mass % from ultrasonic adhesion test.

6.3.2.2 Effect of solids concentration

The coating properties are given in Table 6.6 and the coating SEM images are shown in Figure 6.11. The values were averaged over 5 measurements with standard deviation within 2.2 % and 3.5 % for the coating loading and the mass % loss respectively. The increase of the slurry solids concentration leads to more particles being attached onto the Fecralloy® surface per unit area. It is shown that the coating loading and thickness increased with the increasing solids concentration. The coating adherence was on the other hand diminished as more particles were anchored onto a finite Fecralloy® surface area with increasing solids concentration, therefore the particles least anchored were probable of being removed by ultrasonic adhesion tests.

The coatings from slurries of concentrations not more than 40 wt% are homogeneous and they resulted in the loss of less than 10 mass %. The increase in the slurry solids concentration beyond 40 wt% resulted into lack of homogeneity, the development of cracks and very poor coating adherence (loss of 17 mass %).

Table 6.6. Properties of coatings produced at different solids concentrations

Solids concentration (wt %)	Coating loading (mass %) SD = ±2.2 % of loading	Average film thickness (±2μm)	Mass % loss from adhesion test SD = ±3.5 % of loss
25	3.94	13	4.05
30	5.18	19	5.97
35	6.33	26	7.72
40	7.94	38	9.89
45	10.91	48	17.06

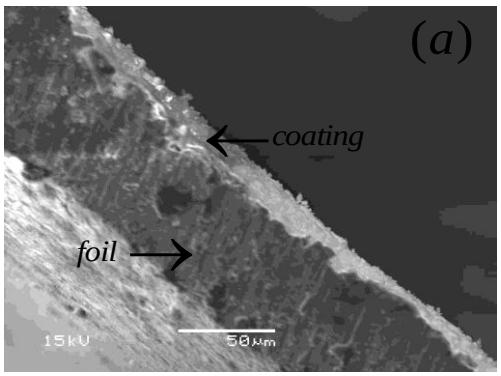

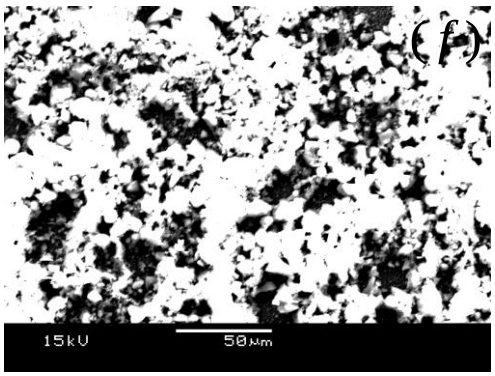

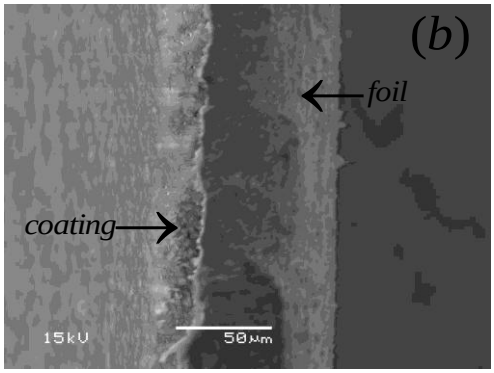

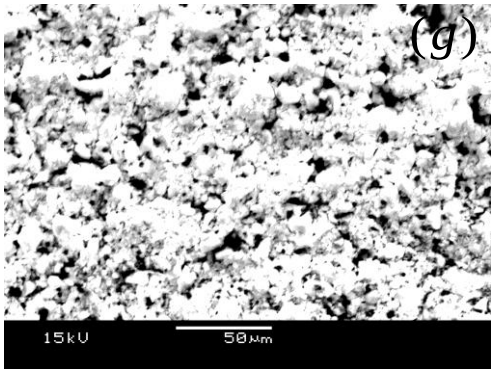

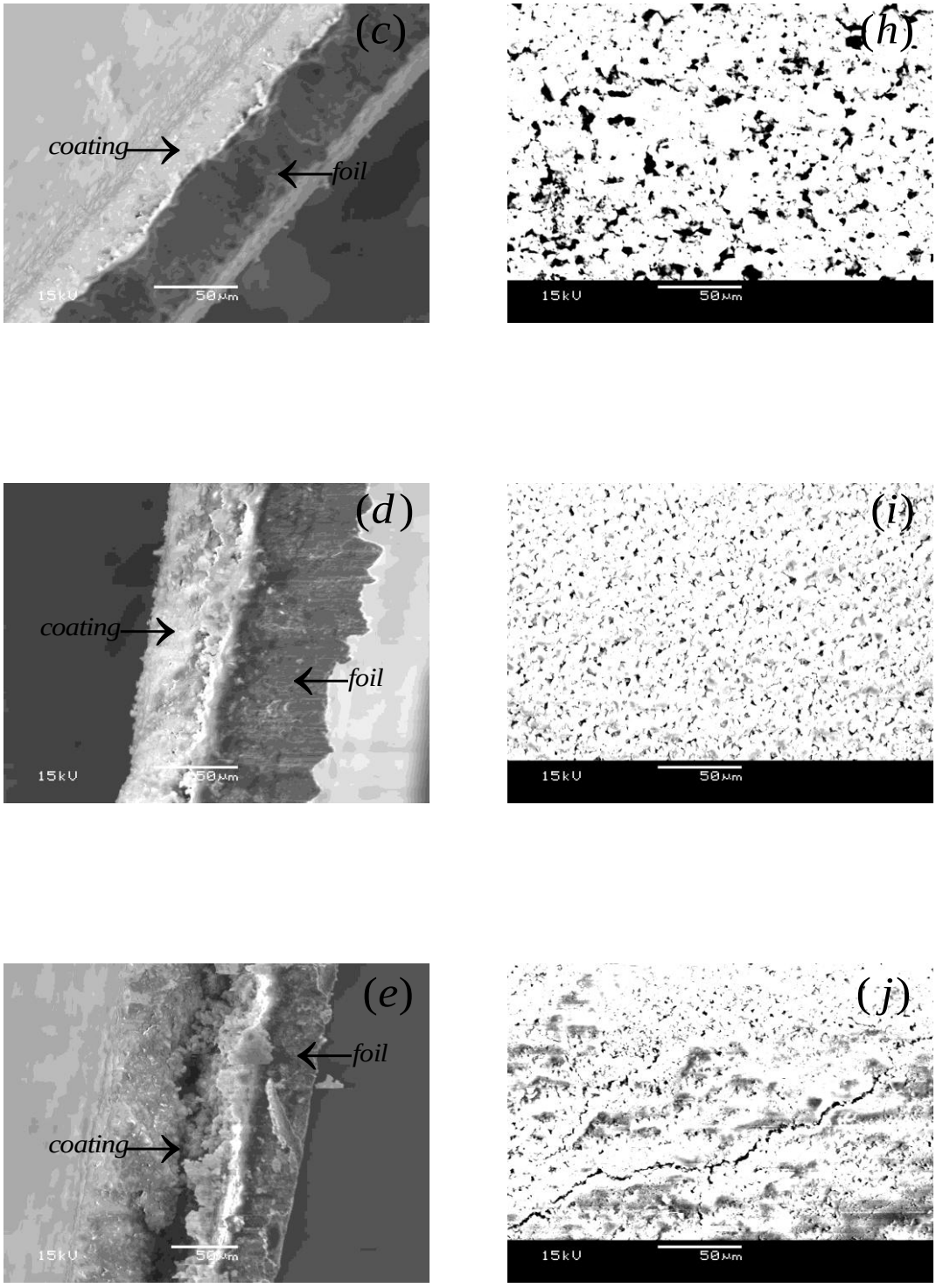

Figure 6.11. SEM side and surface images of coatings produced at different solids concentrations: (i) 25 wt% (a, f), (ii) 30 wt% (b, g), (iii) 35 wt% (c, h), (iv) 40 wt% (d, i), and (v) 45 wt% (e, j).

It is shown in Chapter 4 (section 4.4.2.2) that the slurry viscosity increased from 2.31 to 21.14 mPas with the increase in solids concentration at the reference shear rate of 1000 s^{-1}. But the poor coating adherence and crack formation at solids concentration of 45 wt% goes beyond viscosity effects, it means that a critical coating thickness had been exceeded which made the coating liable to cracks (Chiu et al., 1993). These cracks were induced by large stresses during drying which results into high shrinkage gradients (Zhou et al., 2007; Fei et al., 2003). These cracks were also present in coatings heated at rates less than 15 ^{o}C/h, and the coating adherence remained poor at this concentration. Therefore, the cracks in the coatings at 45 wt% solids concentration accompanied by the poorly anchored particles onto the Fecralloy® caused the poor coating adherence.

It is shown from the results that cracks, formed when the critical coating thickness is exceeded, are inextricably linked to poor coating adherence as the mass% loss from ultrasonic vibration greatly increased at 45 wt% solids concentration. Hence, the critical coating thickness from the slurries investigated is considered as between 36 and 48 μm.

These results are also in accordance with the study by Jia et. al (2007) which dip-coated Fecralloy® coupons twice and found that coatings produced from slurry of solids concentration 15 – 35 wt% resulted in good adherence of no more than 1.26 mass% loss from thermal shock test. Though their study did not consider slurries at solids concentration of 40 wt%, the coatings obtained at 45 wt% were also characterised by cracks.

In a similar study by Zhou et al. (2007) which dip-coated Fecralloy® coupons several times using the slurry solids concentration of 21.6 wt%, it was found that 26.0, 27.6 and 55.6 mass% losses from ultrasonic vibration were obtained at coating loading of 10, 20 and 30 mass% respectively. The critical coating thickness was determined at 50 μm in their study, though a sol layer was deposited on the Fecralloy® as an intermediary between the γ–alumina washcoat. Their results, like the present study, also showed decreasing coating adherence with the increase in coating loading, and that cracks were formed on the poorly adhered coatings.

6.4 CONCLUSIONS

An optimal methodology for coating γ–alumina slurry on Fecralloy® coupons was derived in terms of drying and calcination conditions as well as the bar gap and coating speed of the automatic film applicator. For the coatings calcined but dried at different heating rates of 15 – 85 ^{o}C/h, no cracks were formed because the stresses developed in them during drying were not large enough to generate shrinkages which could result into cracks. These coatings therefore showed similar loading and adherence properties.

The effects of calcination at 500 ^{o}C for 1 h was far reaching as it brought about homogeneity, sintering and redistribution of coatings, which resulted into strong coating adherence. The ultrasonic adhesion test showed that 9.89 mass% loss from the calcined coatings compared to the 31.37 mass% for the uncalcined coatings.

The increase in the bar gap (10, 26, 100 μm) produced greater coating loading and thickness, and this had minimal consequences on the coating adherence. It was shown that the loss of coating from ultrasonic vibration test was less than 10 mass % for each of the bar gaps.

The shear rate increased (1000, 2500, 5000 s^{-1}) when the coating speed was increased (100, 250, 500 mms^{-1}), but this caused no effect on the coating loading and adherence. The coating methodology derived from the tests for subsequent experiments is summarised in the following: (a) drying at 110 ^{o}C for 1h at the rate of 85 $^{o}C/h$; (b) calcinations at 500 ^{o}C for 1 h; (c) bar gap at 100 μm and (d) coating speed at 100 mms^{-1}

It was concluded from the investigations done on slurries at pH values of 3 – 10 that the best coating properties were achieved at pH of 4. This pH produced the optimal stabilisation as a result of which particles could move freely into the asperities on the Fecralloy® surface which ultimately resulted into an optimal coating adherence of 9.89 mass% loss. The coatings from slurries of solids concentrations not more than 40 wt% were homogeneous and they resulted in adhesion loss of less than 10 mass %. The cracks formation as well as the poorly anchored particles on the coatings at 45 wt% concentration brought about an adhesion loss of 17 mass%.

7

USE OF ELECTROMECHANICAL TESTING SYSTEM FOR MEASURING THE ADHERENCE OF COATINGS OF VARIOUS PARTICLE SIZE DISTRIBUTIONS

This chapter focuses on the measurement of the adherence of coatings of various particle size distributions by a newly devised dual compression-tension technique using an electromechanical testing system. This method is based on the measurement of the work of adhesion between the coating and the substrate. It involves compressing the coating with a probe at a fixed load, and then removing the probe together with the coating at right angles to the substrate surface at a withdrawal speed of 10 mm/min. The coatings made from singly prepared and blended slurries are tested to determine ways of improving the coating adherence. It is found that for coatings made from the singly prepared slurries of 40 wt% solids concentration, the finest particles ($d_{0.9}$ of 12.14 μm) showed the best adherence with an ultimate strength of 0.59 MPa and 85 – 90 mass% coating removal. At 45 wt% solids concentration, the coatings from blended slurries had poor adherence as well as cracks (break stress of 0.09 MPa and > 85 wt% contact area removal).

7.1 INTRODUCTION

The adherence of coatings onto the Fecralloy® is fundamental to the longevity and effectiveness of the monolith catalyst. As there are mechanical and thermal stresses inside the exhaust system of automobiles, the coating adherence needs to be sufficient to resist these stresses (Cybulski and Moulijn, 2006). There is urgent need to devise new methods for measuring the coating adherence because none of the conventional methods (e.g. ultrasonic vibration, drop test) described in section 2.2.5.1 give a physical measure of the adhesive or cohesive properties of coatings. A physically derived method is ascertained when the measured coating variables are based on fundamental scientific quantities, such as tensile stress, displacement and compression load (Xu and Li, 2007).

Jia et al. (2007) and Germani (2007) have studied how the coating adherence is influenced by the particle size distributions (psds) of γ–alumina slurries, and their findings showed a strong relationship. Jia et al. (2007) studied the adherence of coatings of particle diameter $d_{0.9}$ of 1.68 – 33.39 μm on Fecralloy® coupons using ultrasonic vibration. They found that the mass loss was below 2.0 % for coatings of $d_{0.9}$ less than 10 μm, whereas more than 19.8 mass% was determined for coatings of $d_{0.9}$ beyond 15.23 μm. This is because finer particles were firmly anchored onto the rough surface of the Fecralloy®. Furthermore, Germani et al. (2007) used both ultrasonic vibration and drop tests for measuring the adherence of coatings of $d_{0.5}$ of 3 and 28 μm on stainless steel platelets, and they also concluded that finer particles produced better coating adherence. However, these studies neither revealed the shapes of the psds used nor considered how blends of different psds might improve coating adherence.

Modified psds can be generated by mixing two or more slurries of different psds at specified volume proportions. This results in better solids packing as the small particles are able to fit into the pores between the large particles (Figure 7.1), therefore improving the flow properties and leading to an increase in the maximum solids fraction (Zaman and Dutcher, 2006; Greenwood et al., 1997; Peters et al., 1996). Greenwood et al (1997) found that the particle diameter ratio of 6.37 at a volume ratio of 75:25 (large to small particles) resulted into an ideal packing which produced slurries of low viscosity for polystyrene lattices up 55 wt% solids concentration.

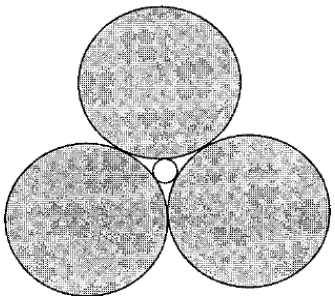

$$\frac{d_l}{d_s} = 6.37$$

Figure 7.1. A two-dimensional illustration showing the particle diameter ratio which produced an ideal packing for polystyrene lattices (Greenwood et. al, 1997).

Johnson Matthey (JM) is particularly interested in improving coating adherence by using modified psds obtained from blended γ–alumina slurries. This has the potential of increasing catalytic performance for a minimum platinum group metal (PGM) loading. There are presently no previous studies in the open literature which have focussed on using blended γ–alumina slurries for improving coating properties. The few studies in this area have been based on blends of polystyrene and polymethyl methacrylate (Qin and Zaman, 2003; Greenwood et al., 1998; Greenwood et al., 1997; Hoffman, 1992), latex systems (Peters et al., 1996), and silica particles (Zaman and Dutcher, 2006).

The use of the electromechanical testing system (ETS) for testing of materials (e.g. metals, ceramics and polymers coatings) has been in existence for many years but its application in the assessment of catalyst coatings has not been explored (Mukhopadhyay et al., 2009; Fereshteh-Saniee et al., 2008; Peters et al., 1996). This may be because no one has endeavoured to or, if otherwise, the findings have not been published. The newly devised dual compression-tension ETS technique offers a scientifically governed means of measuring the coating adherence.

This Chapter focuses on the ways by which coating adherence can be improved using different psds obtained from singly prepared and blended slurries, and the advantages associated with using the ETS for assessing coatings. The ETS technique is the main method for assessing coatings, while ultrasonic vibration is used as a subordinate. The empirical characterisations of slurries (psds and rheology) are also determined prior to coating of slurries onto the Fecralloy® coupons using the film applicator.

7.2 EQUIPMENT

7.2.1 Electromechanical testing system (ETS)

The ETS (Instron, UK) acts under a set of programming instructions to perform tension, compression or bending analysis of the coatings. The ETS used is a dual column 5860 series model (Figure 7.2) of load capacity of 2 kN. This model is controlled by the standard Bluehill® 2 software.

The dual column layout offers better stiffness compared to the single column models.

Features of the system used are (Instron Materials Testing Catalog, 2009):

- measurement of force and extension to within ± 0.4 %.
- speed range from 0.005 to 2500 mm/min.
- multiple force transducers for extensional and compression measurements.

Figure 7.2. Instron 5860 series model (Instron, UK).

7.2.2 Bead mills

The stirred bead mill (Union Process, USA) was described in section 3.2.2. The next set of mills are capable of producing slurries of fine particles at shorter times because they have been designed for milling at higher milling speed compared to the stirred bead mill.

7.2.2.1 Eiger mini mill

The Eiger mini mill (Eiger Machinery, USA) is widely used for the preparation of slurries in the laboratory (Figure 7.3). It consists of an in-built pump and pre-disperser and has a variable speed agitator between 0 – 2000 rpm.

Figure 7.3. Eiger mini mill (Courtesy : Johnson Matthey, Sonning Common, UK).

It is therefore capable of producing sub micron particles in shorter time compared to the stirred bead mill which has maximum speed of 1000 rpm. The zirconia grinding media used had 1 mm diameter. The mill is designed with intrinsically safe electrical control as well as quick release latches which allowed easy removal of components.

7.2.2.2 Netzsch mill

The LABSTAR mill (Netzsch, Germany) is a multi-functional laboratory machine used for preparing nanoparticle slurries through superfine grinding (Figure 7.4). These slurries were difficult to achieve by other mills previously described. Due to the horizontal position of the chamber, the shaft gives an even activation of the grinding media over the whole chamber. The shaft speed can be adjusted between 0 – 5000 rpm. The grinding media used were zirconia spheres of 0.4 mm or 0.6 mm diameter.

Figure 7.4. LABSTAR Netzsch Mill (Courtesy : Johnson Matthey, Sonning Common, UK).

7.3 EXPERIMENTAL

7.3.1 Preparation of slurries and coatings

The following γ–alumina slurries were prepared at a fixed pH of 4 (adjusted using acetic acid).

(a) ***Singly prepared slurries (S_{S10} – S_{S240})***: Based on single particle size distribution, they were prepared in separate batch processes using the stirred bead mill (Union Process, USA) at a solids concentration of 40 wt %. They were prepared at milling times between 10 – 240 min as outlined in Table 7.1.

(b) ***Blended slurries***: Prepared at the Johnson Matthey Technology Centre, Sonning Common (UK). Different milling times were used in either of the mills described above or a combination of mills. The desired diameter ratio for them was 6.37 in line with the value obtained by Greenwood et al. (1997). This is to find out if this ratio could produce coatings of improved quality. These slurries were then mixed by a shear blender at volume ratios (small to large particles) of 100:0, 75:25, 50:50, 25:75 and 0:100 (Robbins et al., 2007).

They are divided into 2 groups based on their solids concentration.

(i) **Slurries S_{LG} and S_{SM}** prepared in both Eiger and Netzsch mills at a solids concentration of 40 wt %. The milling conditions of the slurries are given in Table 7.1.

(ii) **Slurries S_{LX} and S_{SX}** were prepared in the stirred bead mill (Union Process, USA) at a solids concentration of 45 wt% for 40 min and 24 h respectively.

The milling conditions of these slurries are given in Table 7.1

Table 7.1. Milling conditions for the singly prepared and blended slurries.

Slurry category	Slurry name	Milling conditions
singly prepared (40 wt%)	S_{S10}, S_{S20}, S_{S40}, S_{S60}, S_{S240}	Stirred bead mill: speed = 500 rpm, media diameter = 5 mm, media load = 40 vol%, milling time = 10, 20, 40, 60 and 240 min.
blended (40 wt%)	S_{LG}	Netzsch mill: pump speed = 170 rpm, agitator speed = 3000 rpm, media = 0.6 mm diameter, milling time = 10.22 min. *(Feed from Eiger mill: media = 1mm diameter, agitator speed = 450 rpm, milling time = 6.5 min).*
	S_{SM}	Netzsch mill: pump speed = 170 rpm, agitator speed = 3000 rpm, media = 0.4 mm diameter, milling time = 87.85 min. *(Feed from Eiger mill: media = 1mm diameter, agitator speed = 450 rpm, milling time = 18.2 min).*
blended (45 wt%)	S_{LX}	Stirred bead mill: speed = 500 rpm, media diameter = 1 mm, media load = 40 vol%, milling time = 40 min.
	S_{SX}	Stirred bead mill: speed = 500 rpm, media diameter = 1 mm, media load = 40 vol%, milling time = 24 h.

The psds and the steady shear rheology of the slurries described in (a) and (b) above were measured using the Mastersizer 2000 (Malvern Instruments, UK) and the AR 1000 rheometer (TA Instruments, UK) respectively.

The Fecralloy® coupons described in section 5.4.1 were coated with these slurries using the automatic film applicator according to the procedure outlined in section 5.4.2. The coatings were allowed to partly dry at room temperature. They were then dried and calcined in a furnace (Lenton, UK) at 110 ^{o}C for 1 h and 500 ^{o}C for 1 h respectively (Jia et al., 2007; Truyen et al., 2006).

7.3.2 Preliminary work on coating adherence using micromanipulation

A micromanipulation technique was first tested for measuring the coating adherence from the slurries S_{S60} and produced according to section 7.3.1 (a). The apparatus [Figure 7.5 (a)] comprises of a T-shaped probe which was connected to a force transducer mounted on a three dimensional micromanipulator (MicroInstruments, UK). The probe lies perpendicular to the coating, and it removes the coating from the Fecralloy® surface as it is being pulled [Figure 7.5 (b)].

It is shown that a constant force was obtained initially (region A), but the force increased as probe scratches the coating along the horizontal direction (region B). The oscillation of the curve (region C) is attributed to the interactions between the coating and the substrate as the probe moved across the surface until the coating has been

removed (region D) (Hooper et al., 2006; Liu et al., 2002). But the inability to distinguish between the removal of the coating and the scratching of the metal prompted the use of the ETS which is specially designed for dual tensile-compression operations.

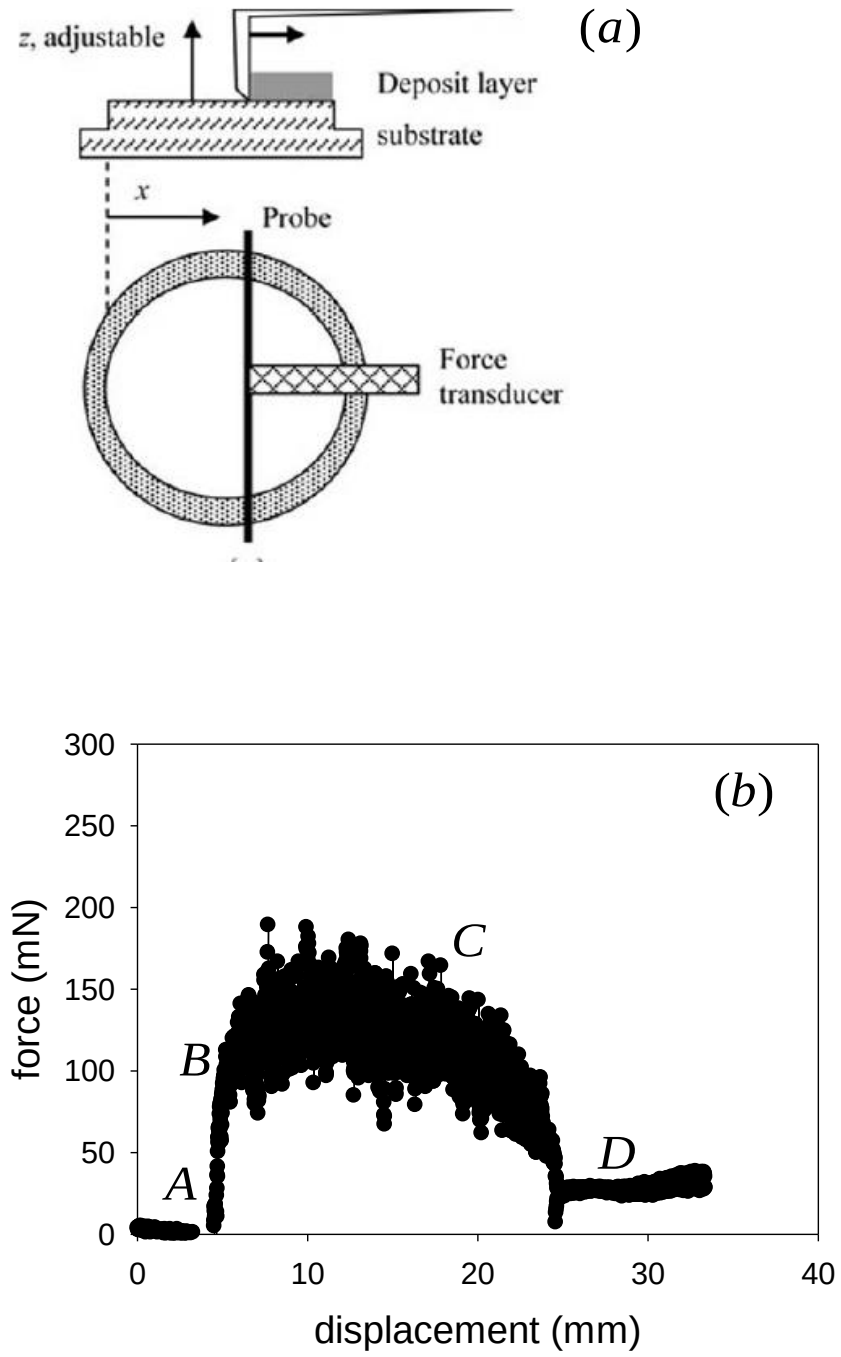

Figure 7.5. The removal of coating by micromanipulation: (a) schematic representation of apparatus (Hooper et al., 2006) and (b) sequence of the coating removal.

7.3.3 ETS methodology for assessing coating adherence

The ETS was the first instrument produced by Instron in 1946 and is still the most widely used instrument made by the company. Also referred to as a universal tester, it is used in many industries where characterisation of material properties is required (Instron Materials Testing Catalog, 2009).

The ETS dual compression-tension technique enables the measurement of the force as a function of displacement, and thus the work required to disrupt the coating. The ETS is composed of a dual column which houses a load cell of 1 kN. A computer connected to the ETS produces a graphical display of the measurements taken.

The adjoining tools described below were developed for the ETS tests.

(a) *Metal probe*: This is a stainless steel tube which is connected to the ETS load cell for compression and removal of the coating [Figure 7.6 (a)]. The height and diameter are 8 cm and 1 cm respectively, therefore makes a contact area of 0.79×10^{-4} m^2 with the coating.

(b) *Annular supports*: These are specially fabricated threaded rings made from stainless steel [Figure 7.6 (b)]. They have inner and outer diameters of the 2.1 cm and 4.4 cm respectively. They are used for holding the coatings securely and firmly onto the ETS sample platform.

(c) *Carbon tapes*: These are double sided adhesive circular tapes (TAAB Laboratories Equipment, UK) of thickness of 0.0125 cm and diameter of 2.5 cm [Figure 7.6 (c)]. They are cut into smaller dimensions to fit the circular end of the probe.

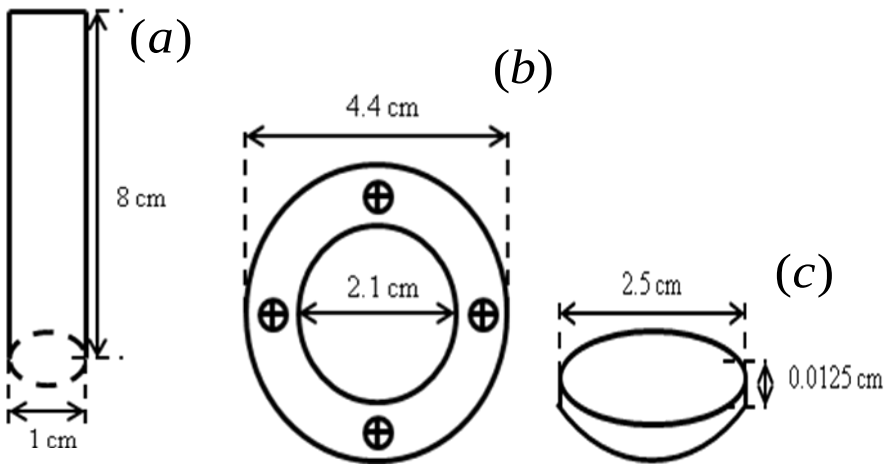

Figure 7.6. Schematic representation of the adjoining tools: (a) metal probe; (b) annular support and (c) carbon tape.

The procedures for the ETS tests are described below.

(i) The coating is firmly screwed onto the platform base of the ETS using the annular support [Figure 7.7(a)].

(ii) The metal probe joined with a carbon tape is mounted onto the ETS, and then lowered to make contact with the coating.

(iii) The displacement rate of the probe is programmed into the instrument using a test profiler such that the coating is compressed at a specified load [Figure 7.7(b)].

(iv) The probe is then lifted up at a given withdrawal speed of 10 mm/min, which ultimately pulls off the coating. The coating remaining on the substrate is shown in Figure 7.7 (c), while the probe with the detached coating is shown in Figure 7.7 (d).

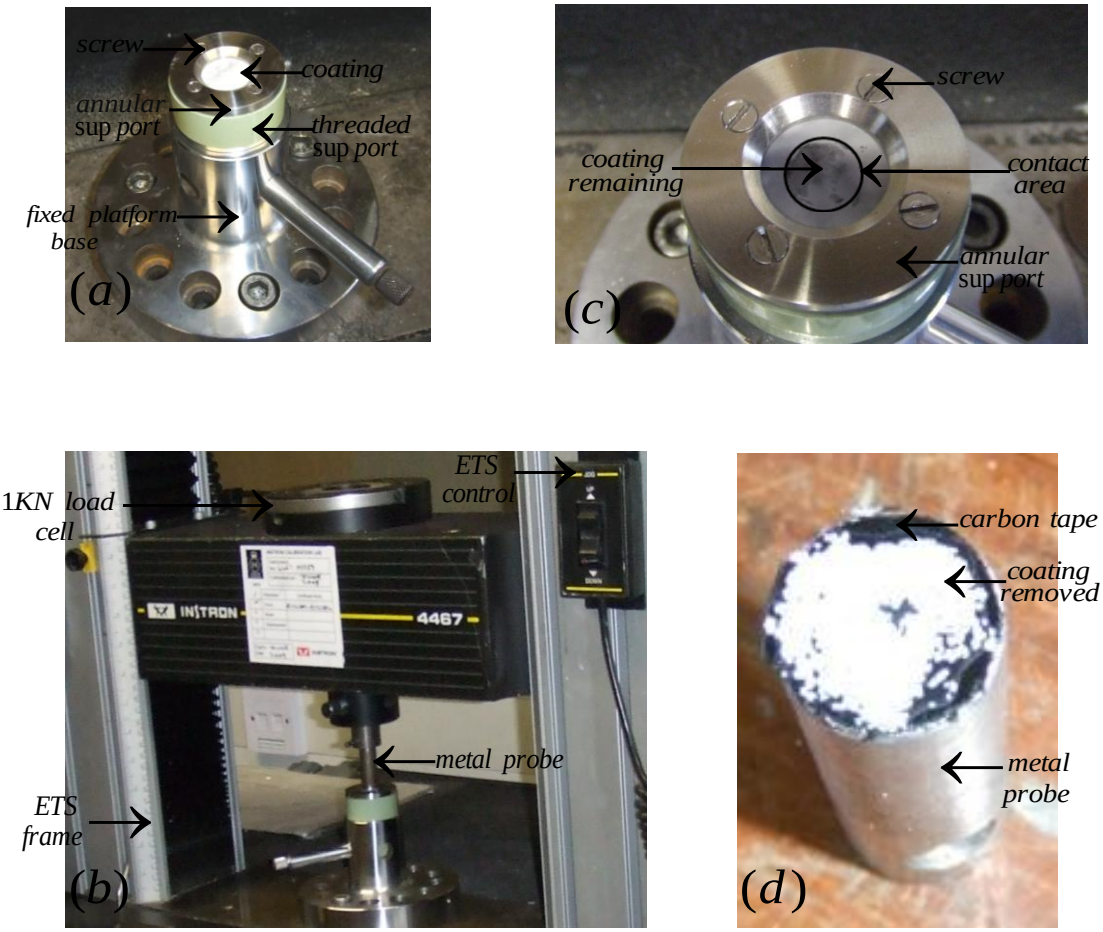

Figure 7.7. Pictures showing how coating adherence is being measured by ETS: (a) coating firmly screwed; (b) coating compressed by probe; (c) coating remaining after test and (d) probe showing coating removed.

The measurements are divided into 2 stages. The first is decompression which records the force and displacement of the probe from the point of compression until the instant the compression is withdrawn and the probe moves into tension. The tension stage measures the force on the probe throughout coating detachment until the probe is completely removed from the coating. The measurements are then converted into graphs of stress versus displacement by the test profiler software installed on the computer.

A typical profile obtained from the ETS is represented in Figure 7.8. This shows a drop in the applied compression stress as the probe is being lifted up. The point of zero is the equilibrium, i.e. the instance when no force is acting on the probe. The stress increases thereafter as the probe is being lifted up, thus representing the start of tension. The moment of complete rupture (or removal) of the coating is referred to as the breaking point and the corresponding stress at this point is called the ultimate strength (Pavlina and Van Tyne, 2008). The stress goes to zero after the breaking point as the probe is finally released from tension. The ultimate strength is a very important parameter for quantifying the adherence strength of the coating. The amount of coating removed, which is dependent on the contact area of the probe, is the mass % difference in the coatings on the substrate before and after the test.

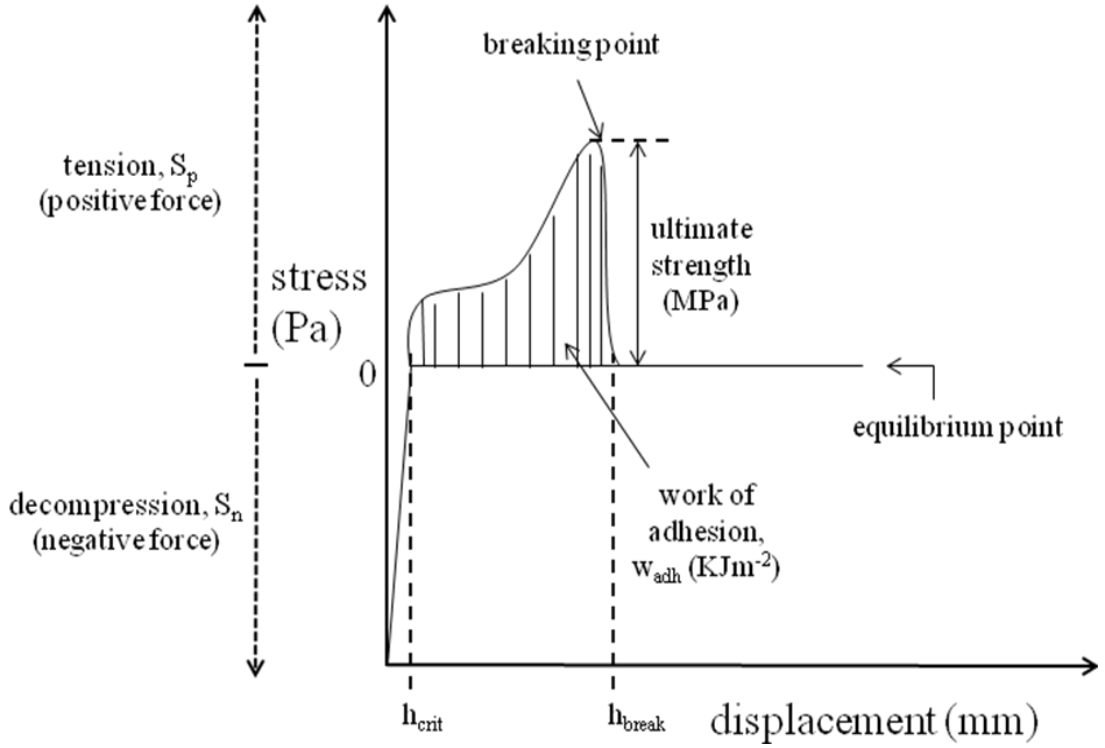

Figure 7.8. ETS profile showing fundamental parameters measured.

The portion of the graph above the zero line (i.e. shaded area) is referred to as the work of adhesion, which is defined as the energy per unit area required to remove the coating from the substrate as shown in Equation (8.1) (Wei and Hutchinson, 1998). This was calculated by Simpson's rule using Matlab® (The MathWorks, USA).

$$w_{adh} = \int_{h_{crit}}^{h_{break}} S_p .dh \quad = \int_{h_{crit}}^{h_{break}} \frac{F_p}{A} .dh \quad = \frac{1}{A} \int_{h_{crit}}^{h_{break}} F_p .dh \tag{8.1}$$

where

$w_{adh} =$ work of adhesion (kJm^{-2})

$S_p =$ stress on coating due to tension (MPa)

$F_p =$ force on coating due to tension (kN)

$h_{crit} =$ displacement at stabilisation stress (mm)

$h_{break} =$ displacement at breaking point (mm)

$A =$ contact area (mm^2)

Tests were performed on coatings derived from section 7.3.1 (a) at different compression loads of 100, 200 and 300 N to determine the effects of the compression load on the coating adherence. This will also reveal the right compression to use for subsequent tests. The coatings obtained from the slurries described in section 7.3.1 were then assessed using the methodology described.

For comparison, the coating adherence was also assessed by ultrasonic vibration, while other coating properties (i.e. loading and SEM visualisation) were assessed according the methods explained in section 5.4.3.

7.4 RESULTS AND DISCUSSION

7.4.1 Coatings from singly prepared slurries

7.4.1.1 Particle size distributions and rheology

The particle size distributions – frequency curves and characteristic diameters ($d_{0.1}$, $d_{0.5}$ and $d_{0.9}$) – of the singly prepared slurries produced using the 5 mm media have already been given in Chapter 3 – Figure 3.7 and Table 3.3. The key data from these distributions are outlined in Table 7.2, as well as the slurry apparent viscosity at a reference shear rate of 1000 s^{-1} at which the coating was applied.

Table 7.2. Particle diameters and rheological data for singly prepared slurries at 40 wt% produced using 5 mm media.

Slurry type	Bead milling time (min)	$d_{0.1}$ (µm)	$d_{0.5}$ (µm)	$d_{0.9}$ (µm)	Viscosity at reference shear rate of 1000 s^{-1} (mPas)
S_{S10}	10	2.64	15.16	33.42	12.2
S_{S20}	20	1.90	9.56	23.02	12.8
S_{S40}	40	1.71	6.13	16.47	12.9
S_{S60}	60	1.34	4.36	12.74	13.7
S_{S240}	240	1.09	2.76	7.82	15.0

The results showed a systematic decrease in the particle diameters with the increase in milling time from 10 to 240 min as large particles were fragmented into smaller

irregularly shaped particles. As explained in section 4.4.2.3, the increase in slurry viscosity with the decrease in particle diameter is explained by the increase in the effective phase volume of the particles as they become finer and are placed closer to one another (Barnes, 2000; Hoffman, 1992).

7.4.1.2 ETS tests at different compression loads

These tests were performed using coatings produced from slurries S_{S60} in Table 7.2. The ETS profiles obtained at different compression loads of 100, 200 and 300 N are shown in Figure 7.9. The plots show a drop in the stress at A due to the decompression occurring as the probe was being pulled upwards. After reaching an equilibrium point of zero the stress began to increase at tension, thus leading to an offset at B and this feature is exhibited for all the compression forces. The offset, which varies between 0.27 – 0.32 MPa, is analogous to the coating yield strength and is considered as the stress required for disruption of the cohesive forces in the coatings at the onset of detachment (Ashby and Jones, 1996).

The stress levelled slightly thereafter, followed by a notable increase in the stress until the ultimate strength was attained at C. This region represents the breaking point when the coatings were detached from the substrate. It is shown that the same ultimate strength of 0.59 MPa was achieved for all the compression forces. Following coating detachment, the stress reached equilibrium at D due to the upward free movement of the probe. The ETS results are summarised in Table 7.3.

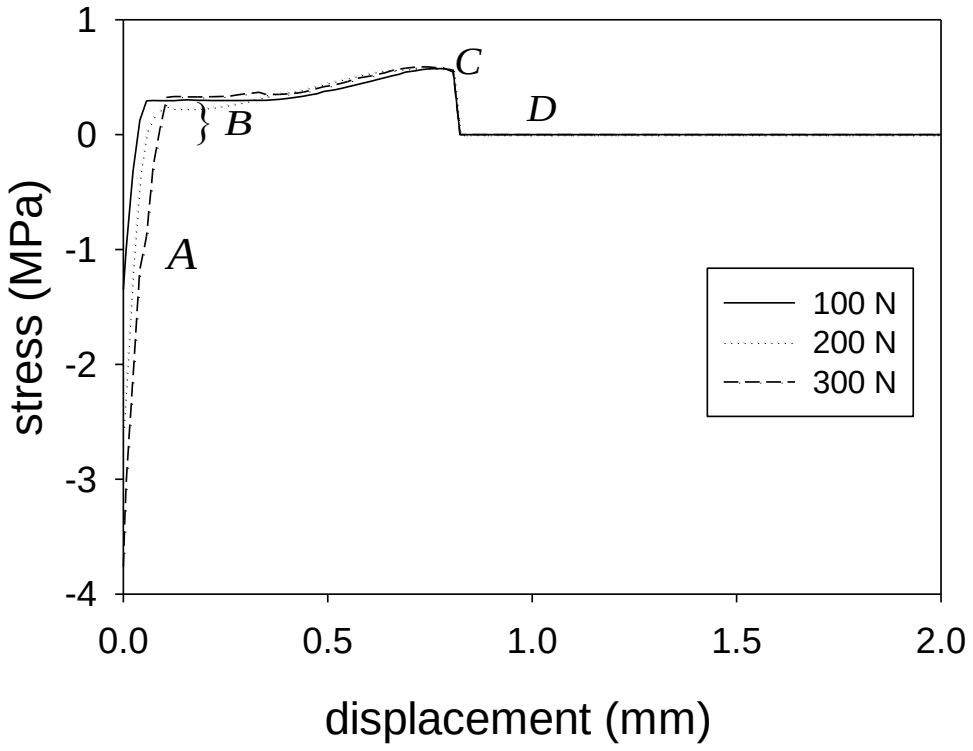

Figure 7.9. Tensile stress versus displacement at different compression loads.

Table 7.3. ETS results at different compression loads.

Compression force (N)	Offset B (MPa)	Ultimate strength C (MPa)	Amount removed (mass % contact area)	Work of adhesion (kJm^{-2})
100	0.29	0.59	86 – 90	0.34
200	0.27	0.59	85 – 90	0.33
300	0.32	0.59	85 – 89	0.33

These inferences can therefore be made from the ETS tests at compression loads of 100 to 300 N:

(a) the plots followed the same profile pattern which shows the consistency of the ETS measurements;

(b) the cohesive forces in the coatings brought about the offset exhibited under tension;

(c) the ultimate strength for the removal of coatings was the same for all the compression loads, thus meaning that the ultimate strength is independent on the compression load in the range of 100 – 300 N and

(d) the work of adhesion and the amount of coatings removed were calculated as between 0.33 – 0.34 kJm^{-2} and 85 – 90 mass % respectively.

The compression load will therefore be fixed at 200 N for subsequent tests for consistency.

7.4.1.3 Main ETS tests

The coatings used in these tests were produced from slurries S_{S10}, S_{S40} and S_{S60} described in Table 7.2. These coatings were compressed at fixed load of 200 N by the probe, and the tests were conducted according to the methodology described in section 7.3.3. Figure 7.10 shows the graph of stress as a function of displacement for all the coatings assessed.

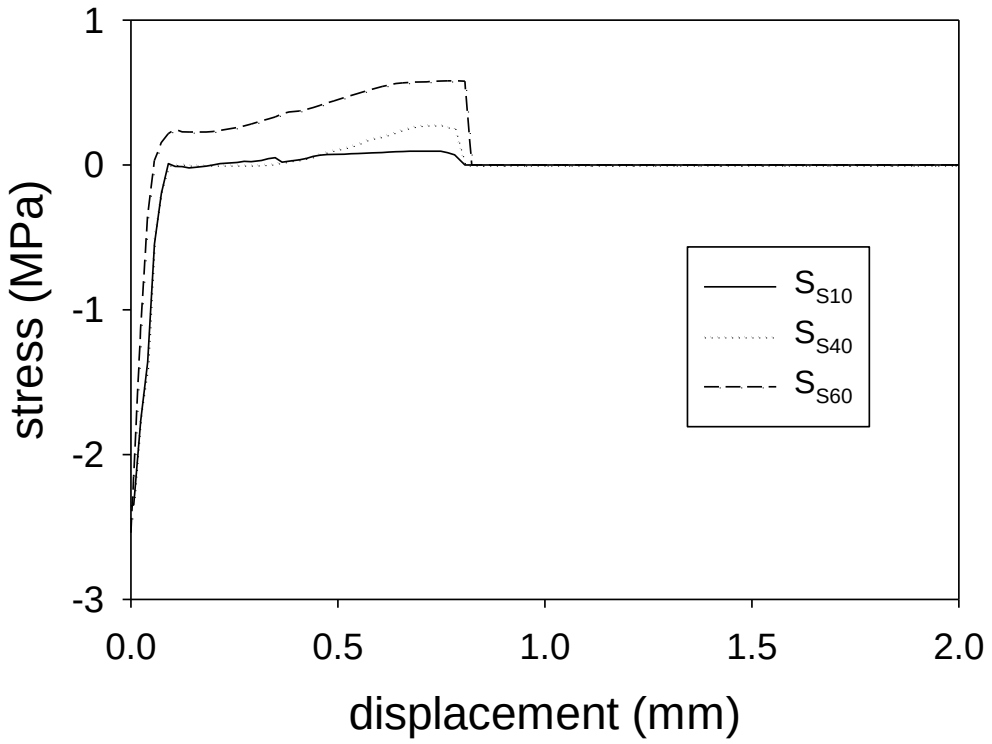

Figure 7.10. ETS profiles for coatings from slurries S_{S10}, S_{S40} and S_{S60}.

All the three plots shown in Figure 7.10 have similar profiles: decompression until the stress was zero at equilibrium, followed by increased stress at tension until the ultimate strength was attained at coating removal, and finally the attainment of equilibrium. It is shown that the ultimate strength, which is the determinant of the adherence quality, is dependent on the particle diameter of coatings. The highest ultimate stress of 0.59 MPa, inferring best adherence, was achieved by the coatings from slurry S_{S60} ($d_{0.9}$ of 12.74 µm), followed by 0.29 MPa for S_{S40} ($d_{0.9}$ of 16.47 µm), and then the least ultimate strength of 0.10 MPa corresponded to S_{S10} ($d_{0.9}$ of 33.42 µm).

Similarly, the ultimate strength and the work of adhesion both followed the same trend as they all increased with finer coating particles. Furthermore, the coating amounts removed were dependent on the particle diameter $d_{0.9}$ as presented in the detailed results shown in Table 7.4.

Table 7.4. ETS results for coatings from $S_{S10} - S_{S60}$.

Slurry type	Diameter $d_{0.9}$ (μm)	Ultimate strength (MPa)	Amount removed (mass % contact area)	Work of adhesion (kJm^{-2})
S_{S10}	33.42	0.10	> 97	0.03
S_{S40}	16.47	0.29	88 - 93	0.07
S_{S60}	12.74	0.59	85 - 90	0.33

In addition to requiring the lowest ultimate strength of 0.10 MPa, the coatings from large particles were almost totally removed (> 97 mass %) from the measurement contact area. The finest coatings, on the other hand, had the least removal (85 – 90 mass %) at the highest ultimate strength of 0.59 MPa (coating pictures shown in Figure 7.11). This is an evidence of a cohesive failure (i.e. internal coating fractures) for fine particles rather than adhesive failure (i.e. coating peeling off the surface) for large particles.

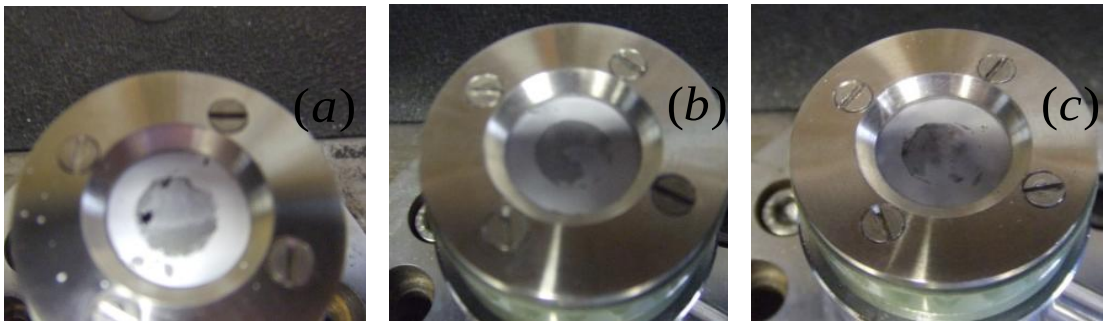

Figure 7.11. Coating pictures after ETS tests showing amounts removed: (a) S_{S10}; (b) S_{S40} and (c) S_{S60}.

This implies that at the least stress applied, large particulate coatings were more susceptible to removal from the substrate because of their poor adherence. The measurements by ultrasonic vibration given in Table 7.5 also show the same pattern, i.e. low mass % coating loss by finer particles. The SEM coating images (Figure 7.12) show that at the same solids concentration of 40 wt%, there was reduction in the coating thickness with the decrease in particles diameter.

Table 7.5. Coating properties by ultrasonic vibration for $S_{S10} - S_{S240}$.

Slurry type	$d_{0.9}$ (µm)	Coating loading (mass %) SD = ±2.5 % of loading	Average film thickness (±2 µm)	Mass % loss from adhesion test SD = ±3.3 % of loss
S_{S10}	33.42	7.4	53	37.3
S_{S20}	23.02	7.5	44	28.0
S_{S40}	16.47	8.1	40	15.5
S_{S60}	12.74	8.0	38	9.9
S_{S240}	7.82	7.8	37	8.0

It is therefore established from all the results that finer particles exhibit better coating adherence as evidenced by their ultimate strength. For finer particles of $d_{0.9}$ not exceeding 12.74 µm, the ultimate strength of at least 0.59 MPa and less than 10 mass % coating loss from ultrasonic vibration were achieved. This is because finer particles can, unlike their large counterparts, properly penetrate and anchor onto the rough asperities on the Fecralloy® surface, therefore leading to good coating adherence.

These findings are in agreement with the work done by Jia et al. (2007), who, having investigated coatings of $d_{0.9}$ of 1.68 – 33.39 µm, found the adherence of coatings of $d_{0.9}$ more than 15.23 µm to be poor, i.e. 19.80 mass% loss from ultrasonic vibration.

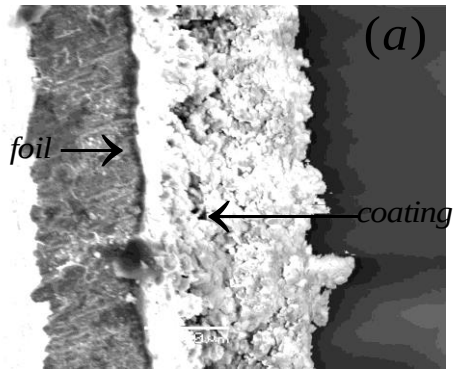

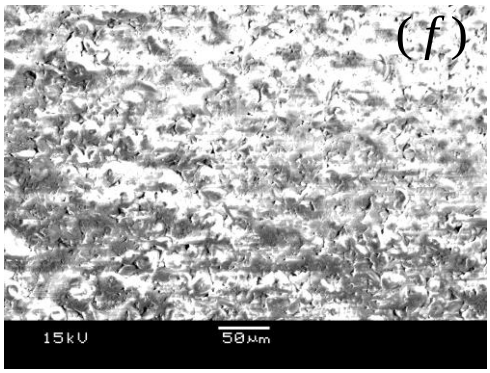

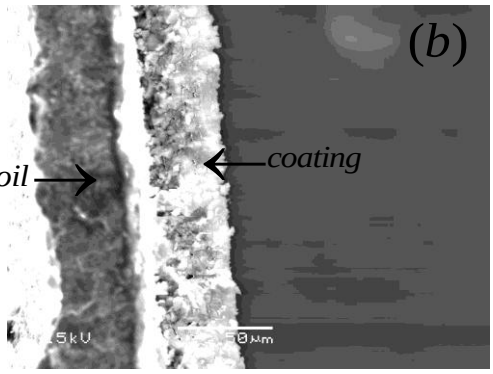

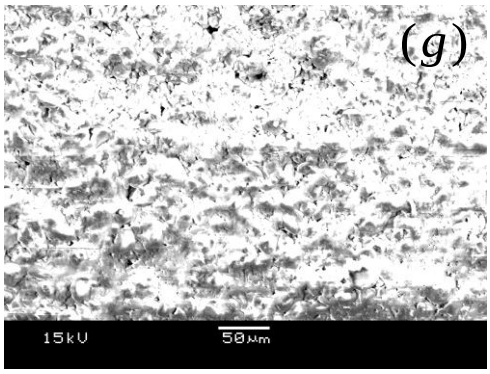

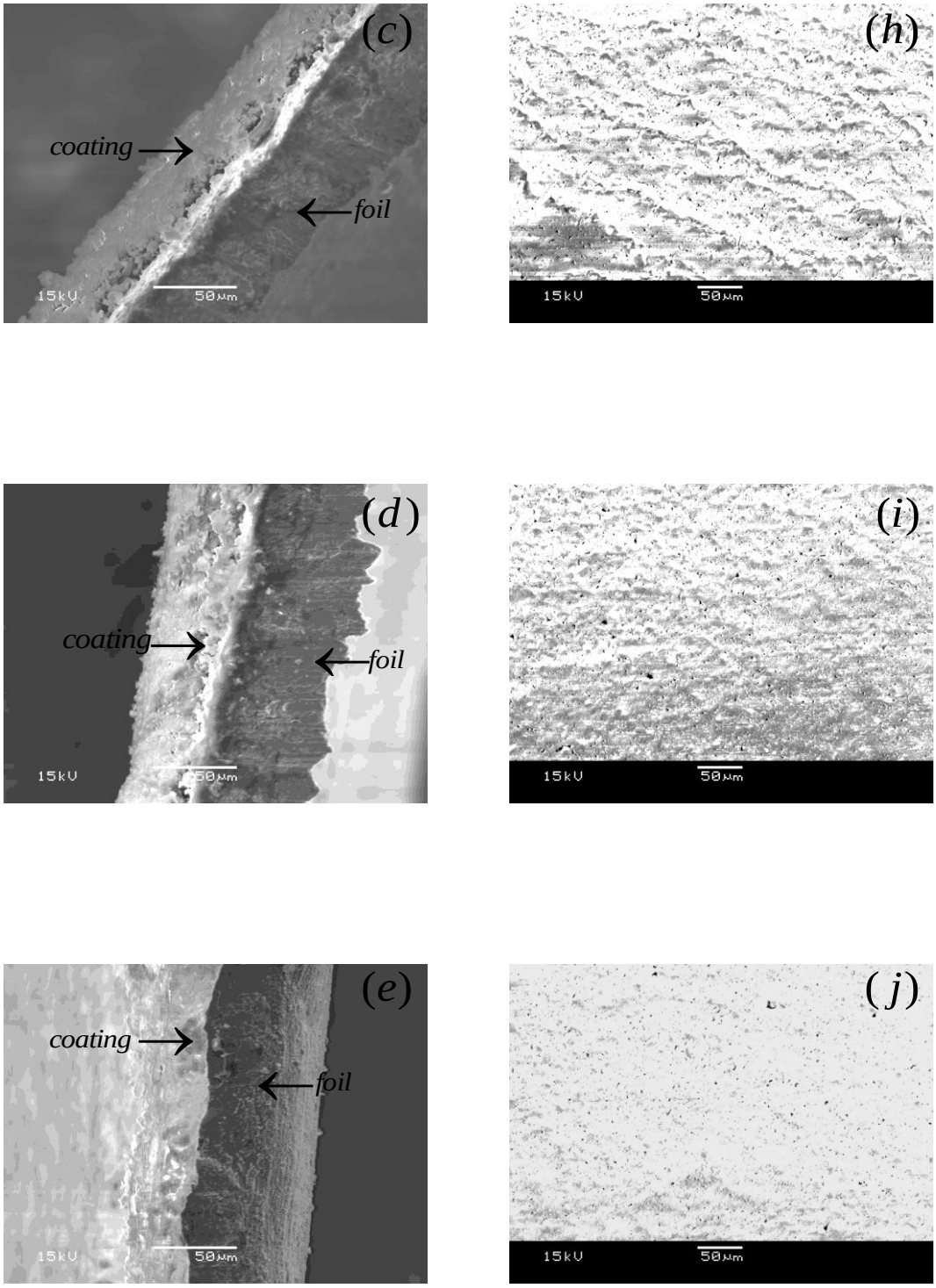

Figure 7.12. SEM side and surface images of coatings from slurries: (i) S_{S10} (a, f); (ii) S_{S20} (b,g); (iii) S_{S40} (c, h); (iv) S_{S60} (d, i) and (v) S_{S240} (e,j).

7.4.2 Coatings from blended slurries

7.4.2.1 Blends at 40 wt% concentration

7.4.2.1.1 Particle size distributions

The psds – frequency curves and characteristic diameters ($d_{0.1}$, $d_{0.5}$ and $d_{0.9}$) – of the slurries S_{SM} and S_{LG} as well as their blends are given in Figure 7.13 and Table 7.6. All these slurries were prepared by a combination of the Eiger and Netzsch mills to reach the desired psds. Slurries S_{SM} and S_{LG} had particle diameter $d_{0.9}$ of 0.440 µm and 2.501 µm respectively, therefore leading to a ratio of 5.68 which is close to 6.37 derived by Greenwood et al. (1997). As expected S_{SM} contained finer particles than S_{LG} because S_{SM} was milled for a longer time using 0.4 mm media diameter in comparison with the 0.6 mm media diameter for S_{LG}. Figure 7.13 shows a systematic decrease (i.e. shift to the right) in the particle diameters with the addition of larger proportions of S_{LG} to S_{SM}. The hypothesis before the slurry preparation was to find the psd $d_{0.1}$, $d_{0.5}$ and $d_{0.9}$ of the blends at diameters proportional to the volume ratios of particles in S_{SM} and S_{LG}.

Table 7.6. Characteristic diameters of slurries S_{LG} and S_{SM} and their blends.

Slurry type	$d_{0.1}$ (µm)	$d_{0.5}$ (µm)	$d_{0.9}$ (µm)	Description of curve
large (S_{LG})	0.695	1.284	2.501	unimodal
S_{SM}: S_{LG} (25:75)	0.610	1.268	2.336	slightly skewed to the left
S_{SM}: S_{LG} (50:50)	0.473	1.196	1.920	more skewed to the left
S_{SM}: S_{LG} (75:25)	0.286	1.087	1.760	bimodal
small (S_{SM})	0.102	0.192	0.440	bimodal

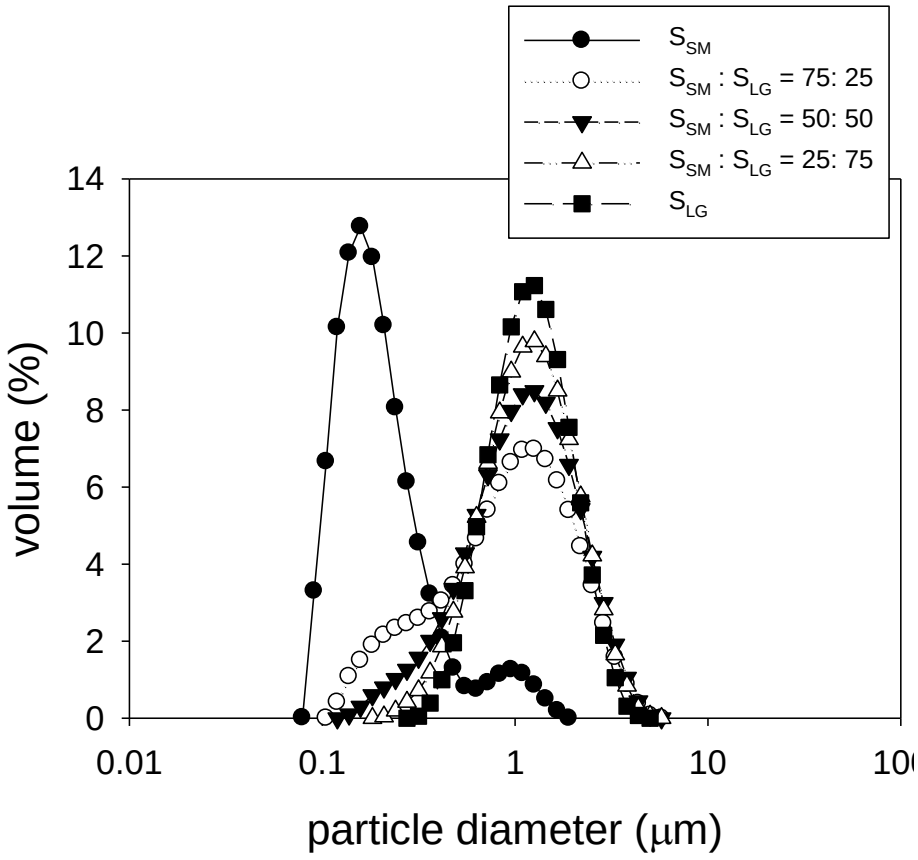

Figure 7.13. Particle size distributions for slurries S_{LG} and S_{SM} and their blends.

However, Table 7.6 and Figure 7.13 show that the particle diameters of the blends are closer to those of S_{LG}, and this may be due to the void packing in the blends. The largest shift occurred between S_{SM} and the blend of 25 vol% S_{LG} + 75 vol% S_{SM}, and these slurries have bimodal psds arising from increasing proportions of large particles.

7.4.2.1.2 Rheology

The steady shear flow curves of the mixed slurries are given in Figure 7.14. Though all the curves are shear-thinning, described by the power law model, the slurries containing finer particles show increased viscosity due to an increase in the effective phase volume.

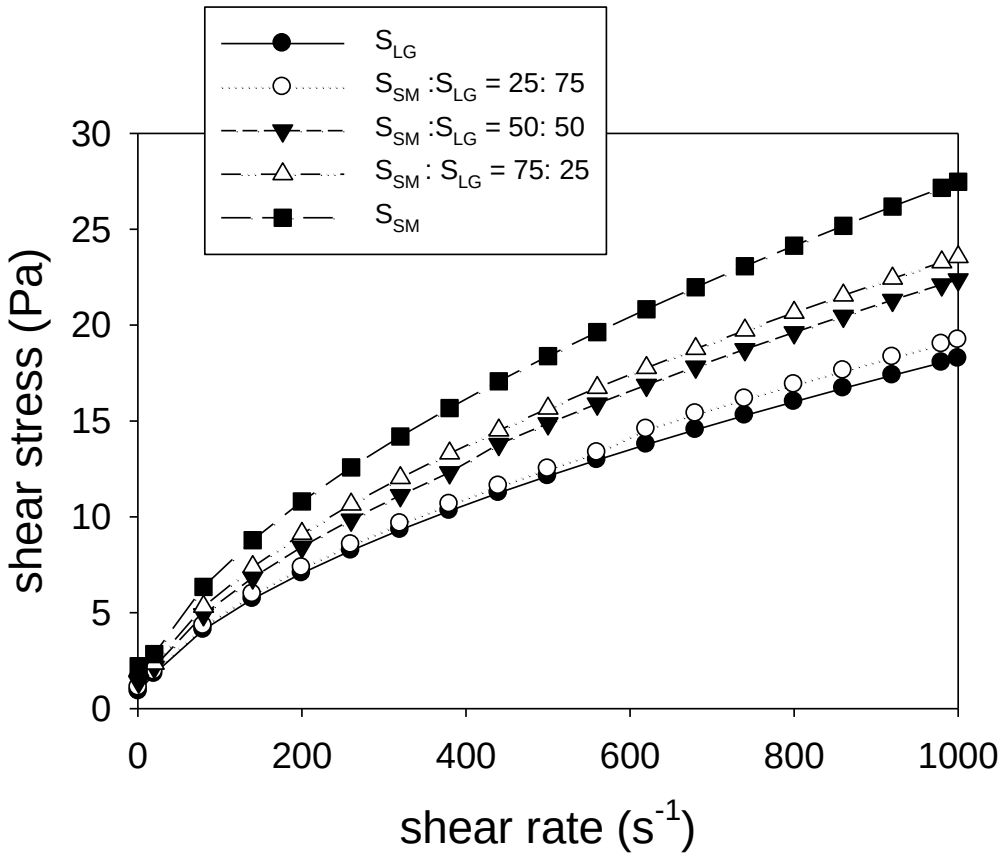

Figure 7.14. Steady shear curves for slurries S_{LG} and S_{SM} and their blends.

Table 7.7. Shear rheology of slurries S_{LG} and S_{SM} and their blends.

Slurry type	Consistency index k	Flow behaviour index n	Goodness of fit r^2 value	Viscosity at reference shear rate of 1000 s^{-1} (mPas)
large (S_{LG})	0.31	0.59	0.99	18.25
S_{SM}: S_{LG} (25:75)	0.34	0.58	0.99	19.23
S_{SM}: S_{LG} (50:50)	0.38	0.59	0.99	22.38
S_{SM}: S_{LG} (75:25)	0.40	0.59	0.98	23.55
small (S_{SM})	0.50	0.58	0.99	27.48

The reduced viscosity of the blends in relation to S_{SM} (Table 7.7) is explained by the close particle packing as smaller particles fit into the interstices created by the larger ones. Therefore the flow curves of the blends lie in between S_{SM} and S_{LG} (Greenwood et al., 1997; Probstein et al., 1994).

7.4.2.1.3 ETS tests

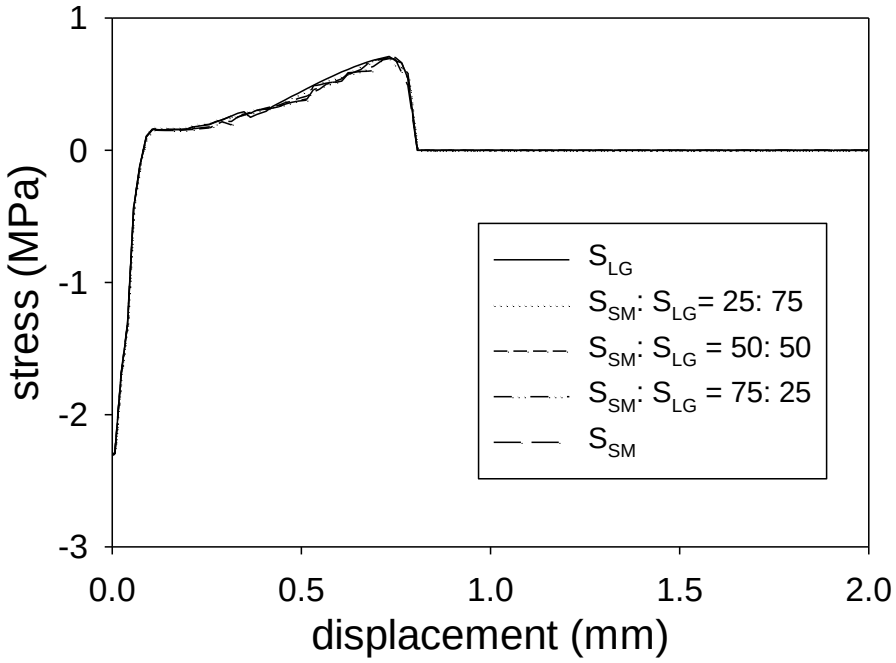

Figure 7.15. ETS profiles for coatings from S_{LG} and S_{SM} and their blends.

Figure 7.15 shows the ETS profiles of the coatings described in sections 7.4.2.1.1 & 7.4.2.1.2 based on the methodology outlined in section 7.3.2. It is shown that all the coatings from the blended slurries at 40 wt% solids concentration have relatively similar adherence parameters: ultimate strength of 0.73 – 0.74 MPa, work of adhesion of 0.41 kJm^{-2} and the coating removed of 84 – 90 mass % contact area. The detailed ETS

results are presented in Table 7.8, while the pictures of the coatings after the tests are shown in Figure 7.16. Though the coatings had particle distributions based on the volume ratios of their blends, the coating adherence measured by the ETS and the mass % loss from ultrasonic vibration (Table 7.9) showed no difference.

Table 7.8. ETS results for coatings from S_{LG} and S_{SM} and their blends.

Slurry type	$d_{0.9}$ (µm)	Ultimate strength (MPa)	Amount removed (mass % contact area)	Work of adhesion (kJm^{-2})
large (S_{LG})	2.501	0.73	86 – 90	0.41
S_{SM}: S_{LG} (25:75)	2.336	0.74	85 – 88	0.41
S_{SM}: S_{LG} (50:50)	1.920	0.74	85 – 88	0.41
S_{SM}: S_{LG} (75:25)	1.760	0.73	85 – 89	0.41
small (S_{SM})	0.440	0.74	84 – 87	0.41

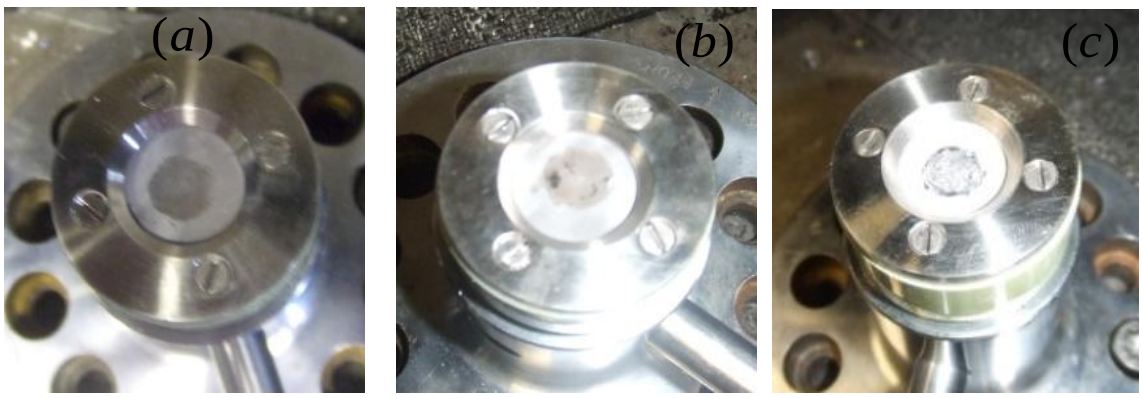

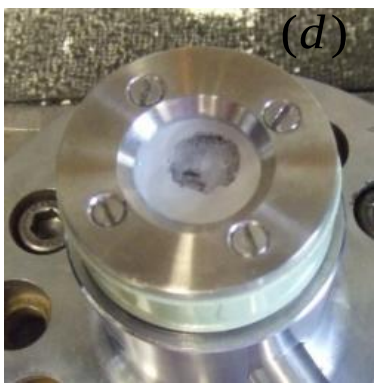

Figure 7.16. Coating pictures after ETS tests showing amounts removed: (a) S_{LG} ; (b) S_{SM}: S_{LG} (25:75); (c) S_{SM}: S_{LG} (50:50); (d) S_{SM}: S_{LG} (75:25) and (e) S_{SM}.

Table 7.9. Coating properties by ultrasonic vibration for S_{LG} and S_{SM} and their blends.

Slurry type	$d_{0.9}$ (µm)	Coating loading (mass %) SD = ±2.0 % of loading	Average film thickness (±2 µm)	Mass % loss from adhesion test SD = ±3.1 % of loss
large (S_{LG})	2.501	8.2	38	9.8
S_{SM}: S_{LG} (25:75)	2.336	7.5	36	10.2
S_{SM}: S_{LG} (50:50)	1.920	7.7	37	9.7
S_{SM}: S_{LG} (75:25)	1.760	8.0	37	8.6
small (S_{SM})	0.440	8.5	36	9.1

The SEM micrographs (Figure 7.17) show that all the coatings were homogeneous and free of cracks. These coatings have good adherence based on their high ultimate strength of 0.73 – 0.74 MPa and less than 9 mass % loss from ultrasonic vibration, thus

showing better performance than the coatings from singly prepared slurries, but there is insensitivity to the proportions in the blends.

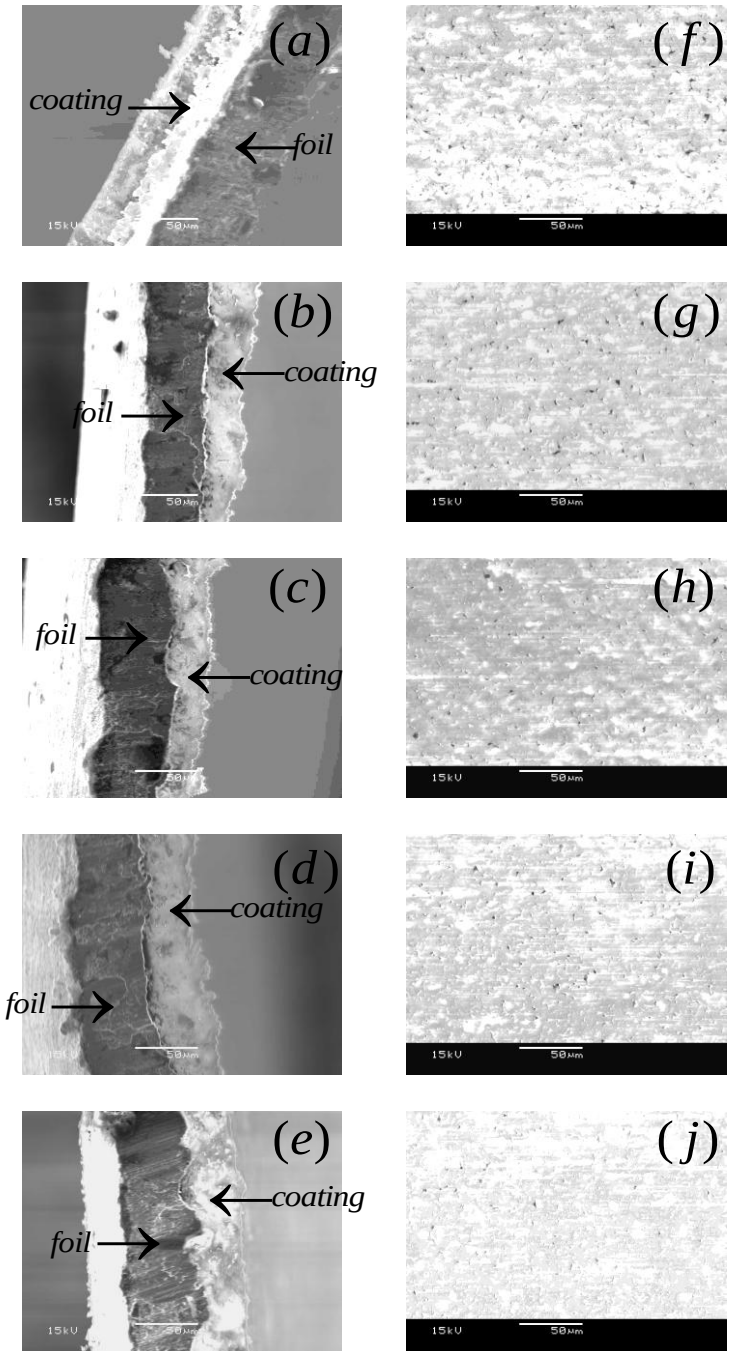

Figure 7.17. SEM side and surface images of S_{LG} and S_{SM} coatings and their blends: $d_{0.9}$ of (i) 2.501 µm (a, f); (ii) 2.336 µm (b,g); (iii) 1.920 µm (c, h); (iv) 1.760 µm (d, i) and (v) 0.440 µm (e,j).

7.4.2.2 Blends at 45 wt% concentration

7.4.2.2.1 Particle size distributions

The psds – frequency curves and characteristic diameters ($d_{0.1}$, $d_{0.5}$ and $d_{0.9}$) – of the slurries S_{SX} and S_{LX} as well as their blends are given in Figure 7.18 and Table 7.10. All these slurries were prepared using the stirred bead mill (Union Process, Ohio) to reach the desired psds. Slurries S_{SX} and S_{LX} had particle diameter $d_{0.9}$ of 2.153 µm and 10.338 µm respectively, therefore leading to a ratio of 4.80 which is comparable to the 5.68 used for the blends at 40 wt% solids concentration. This is to establish if closer particle packing would lead to good coating adherence at the increased solids concentration of 45 wt%. It is shown that S_{SX} contained finer particles than S_{LX} because S_{SX} was milled for longer time of 24 h compared to 40 min for S_{LX}.

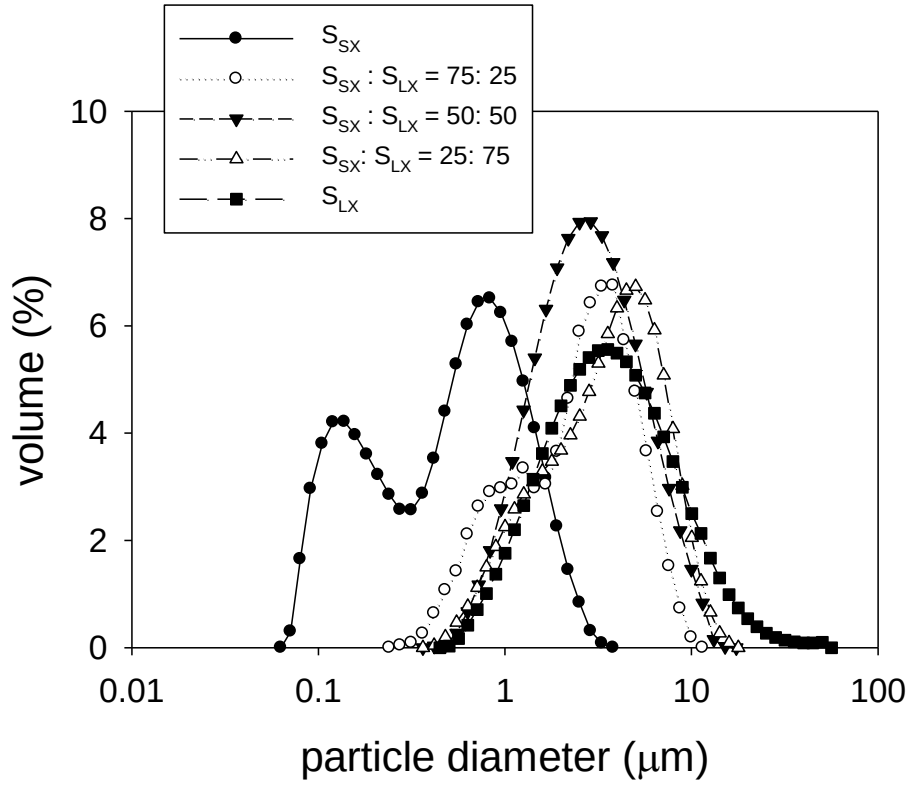

Figure 7.18. Particle size distributions for slurries S_{LX} and S_{SX} and their blends.

Table 7.10. Characteristic diameters of slurries S_{LX} and S_{SX} and their blends.

Slurry type	$d_{0.1}$ (µm)	$d_{0.5}$ (µm)	$d_{0.9}$ (µm)	Description of curve
Large (S_{LX})	1.207	3.418	10.338	unimodal
S_{SX}: S_{LX} (25:75)	1.166	3.179	8.905	slightly skewed to the left
S_{SX}: S_{LX} (50:50)	1.139	2.941	6.879	more skewed to the left
S_{SX}: S_{LX} (75:25)	1.008	2.745	5.788	bimodal
Small (S_{SX})	0.163	0.575	2.153	bimodal

Figure 7.18 is similar to Figure 7.13 in that it shows a systematic decrease (i.e. shift to the right) in the particle diameters with the addition of larger proportions of S_{LX} to S_{SX}. The particle diameters of the blends show similar characteristics to those in Table 7.6 in that they are closer to the large particles of S_{LX}. The largest shift occurred between S_{SX} and the blend of 25 vol% S_{LX} + 75 vol% S_{SX}, and these slurries are shown as having bimodal psds.

7.4.2.2.2 Rheology

The steady shear flow curves of the mixed slurries are given in Figure 7.19. It is shown that all the slurries exhibit shear-thinning behaviour which is adequately described by the power law model (Table 7.11). The blends have reduced viscosity because of their close particle packing as smaller particles fit into the interstices created by the larger ones. Therefore the flow curves of the blends lie in between S_{SX} and S_{EX} (Greenwood et al., 1997; Probstein et al., 1994).

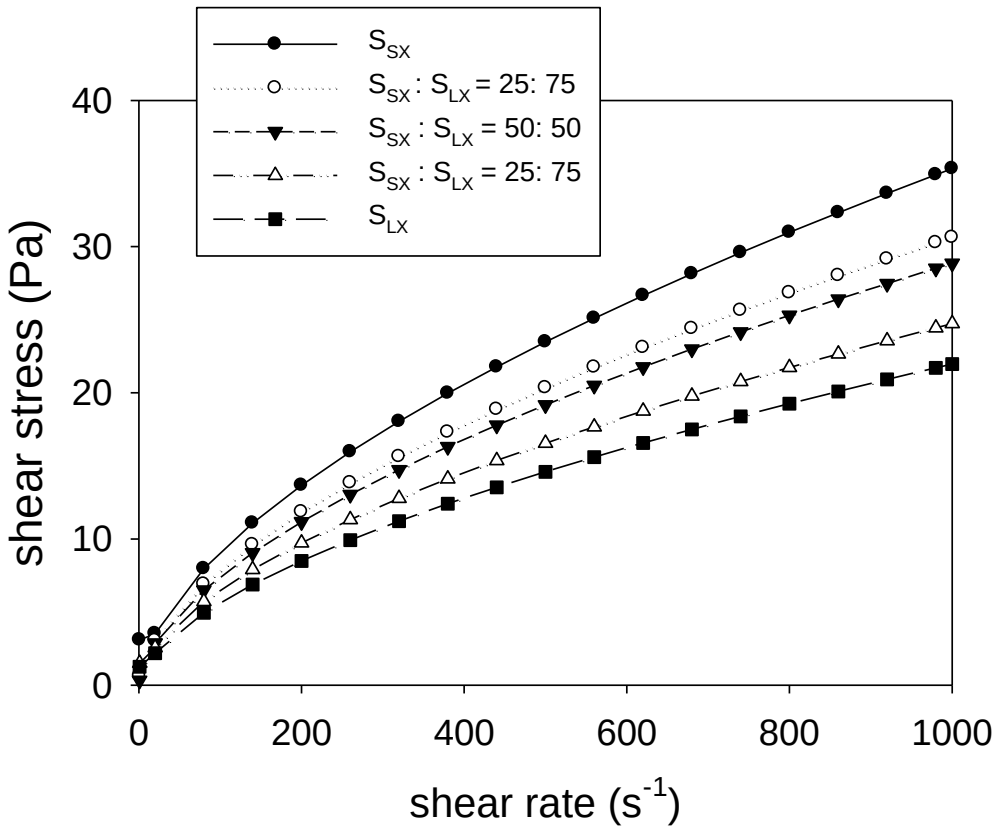

Figure 7.19. Steady shear curves for slurries S_{LX} and S_{SX} and their blends.

Table 7.11. Shear rheology of slurries S_{LX} and S_{SX} and their blends.

Slurry type	Consistency index k	Flow behaviour index n	Goodness of fit r^2 value	Viscosity at reference shear rate of 1000 s^{-1} (mPas)
large (S_{LX})	0.40	0.58	0.98	21.96
S_{SX}: S_{LX} (25:75)	0.45	0.58	0.99	24.73
S_{SX}: S_{LX} (50:50)	0.48	0.59	0.98	28.85
S_{SX}: S_{LX} (75:25)	0.56	0.58	0.99	30.62
small (S_{SX})	0.60	0.59	0.99	35.33

7.4.2.2.3 ETS tests

Figure 7.20 shows the graph of the stress versus displacement on the coatings described in sections 7.4.2.2.1 & 7.4.2.2.2 based on the ETS methodology outlined in section 7.3.2. It is shown that all the coatings from the blended slurries at 45 wt% solids concentration have poor coating adherence: ultimate strength (0.09 MPa), work of adhesion (0.03 kJm^{-2}) and the coating amounts removed (> 95 mass % contact area).

The detailed ETS results are presented in Table 7.12, while the pictures of the coatings after the tests are shown in Figure 7.21. It is shown that for all the coatings there was more than 95 mass % removal from the contact area at a relatively low ultimate strength of 0.09 MPa.

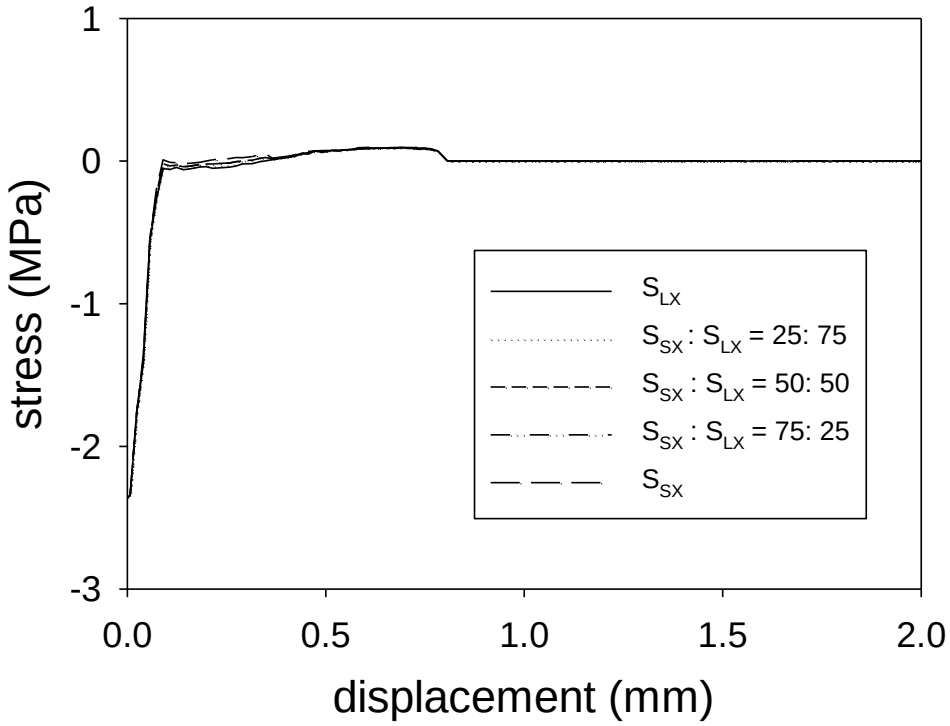

Figure 7.20. ETS profiles for coatings from S_{LX} and S_{SX} and their blends.

Table 7.12. ETS results for coatings from S_{LX} and S_{SX} and their blends.

Slurry type	$d_{0.9}$ (µm)	Ultimate strength (MPa)	Amount removed (mass % contact area)	Work of adhesion (kJm^{-2})
large (S_{LX})	10.338	0.09	> 95	0.03
S_{SX}: S_{LX} (25:75)	8.905	0.09	> 95	0.03
S_{SX}: S_{LX} (50:50)	6.879	0.09	> 95	0.03
S_{SX}: S_{LX} (75:25)	5.788	0.09	> 95	0.03
small (S_{SX})	2.153	0.09	> 95	0.03

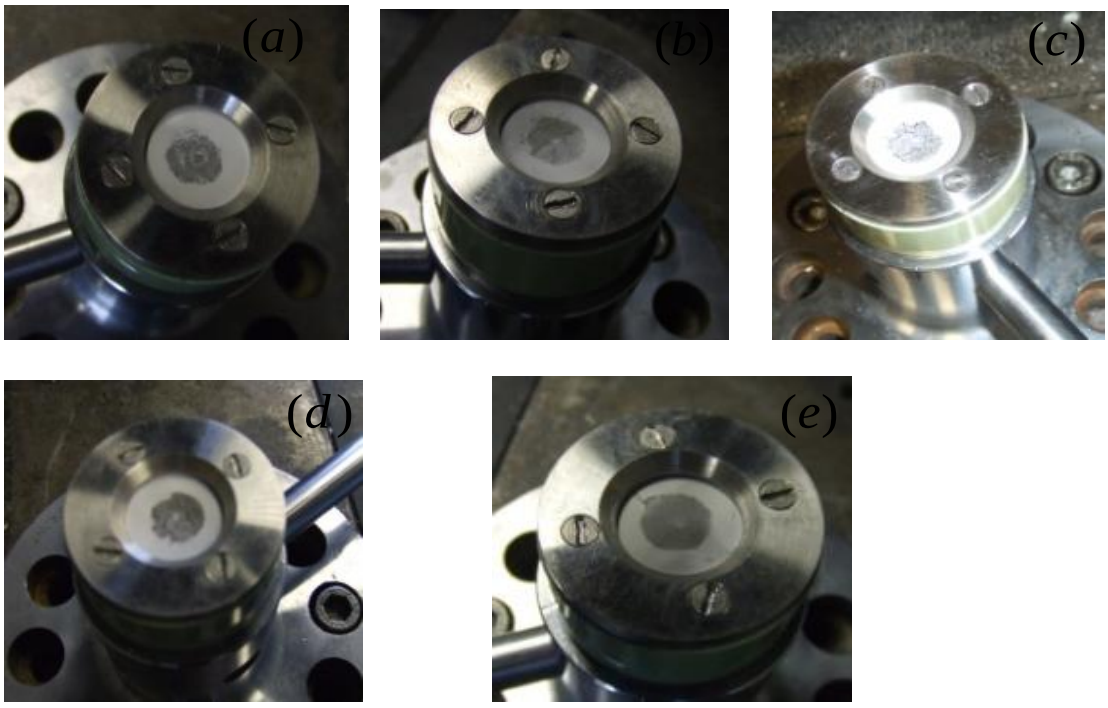

Figure 7.21. Coating pictures after ETS showing amounts removed: (a) S_{LX} ; (b) S_{SX}: S_{LX} (25:75); (c) S_{SX}: S_{LX} (50:50); (d) S_{SX}: S_{LX} (75:25) and (e) S_{SX}.

The measurements by ultrasonic vibration given in Table 7.13 also show large mass % loss for all the blends at 45 wt% solids concentration meaning that they had poor adherence. In support of this, the SEM micrographs (Figure 7.22) show the presence of cracks in the coatings, particularly ones containing greater percentage of large particles (S_{LX}). The presence of cracks is a confirmation that the coatings were not firmly anchored onto the substrate as the critical thickness had been exceeded (see section 6.3.2.2).

Table 7.13. Coating properties by ultrasonic vibration for S_{LX} and S_{SX} and their blends.

Slurry type	$d_{0.9}$ (µm)	Coating loading (mass %) SD = ±2.6 % of loading	Average film thickness (±2 µm)	Mass % loss from adhesion test SD = ±3.9 % of loss
large (S_{LX})	10.338	10.8	52	19.9
S_{SX}: S_{LX} (25:75)	8.905	11.5	49	18.8
S_{SX}: S_{LX} (50:50)	6.879	12.1	47	17.5
S_{SX}: S_{LX} (75:25)	5.788	10.3	47	18.7
small (S_{SX})	2.153	11.0	46	17.2

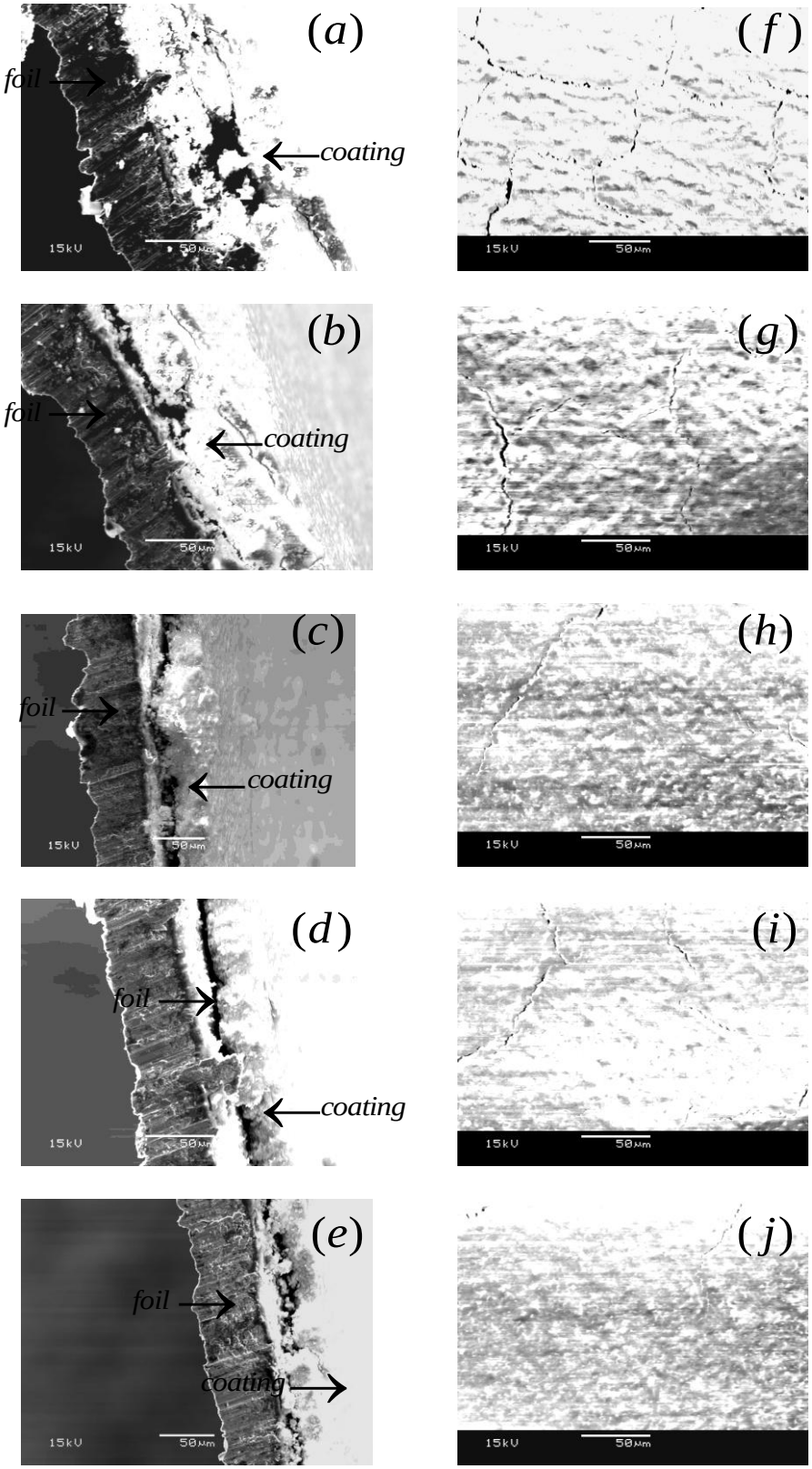

Figure 7.22. SEM side and surface images of S_{LX} and S_{SX} coatings and their mixtures: $d_{0.9}$ of (i) 10.338 µm (a, f); (ii) 8.905 µm (b,g); (iii) 6.879 µm (c, h); (iv) 5.788 µm (d, i) and (v) 2.153 µm (e,j).

There is therefore poor adherence for the coatings from the blends at 45 wt% concentration as evidenced by the low ultimate strength (0.09 MPa) and large losses (17 – 20 mass %) from the ETS and ultrasonic vibration tests respectively. The coating adherence losses from ultrasonic vibration are similar to those obtained from singly prepared slurries at the same concentration in Chapter 6 (section 6.3.2.2). The coating adherence was insensitive to close packing of particles at 45 wt% solids concentration, and there was therefore poor coating adherence in all the coatings investigated.

7.5 CONCLUSIONS

In this Chapter a quantitative technique based on the ETS was described for the measurement of adherence of coatings of different particle size distributions. The ETS methodology is summarised in the following: a probe connected to the ETS initially compresses the coating at a specified load, and is subsequently lifted upwards at a withdrawal speed of 10 mm/min, and as a result pulling off alongside the coating. The stress on the probe is then measured as a function of displacement. The adherence parameters identified were ultimate strength (the adherence strength of coating), work of adhesion (the energy per unit area required for coating removal) and the amount of coating removed from the substrate. It was shown that the use of initial compression loads from 100 to 300 N had no effect on the coating adherence.

For coatings produced from the singly prepared slurries at 40 wt% solids concentration, the finest particles ($d_{0.9}$ of 12.14 μm) produced the best coating adherence at an ultimate

strength of 0.59 MPa and 85 – 90 mass % removal. The finest particles also had the least mass % loss from ultrasonic vibration test. The coating pictures after the ETS test showed that finer particle coatings exhibited cohesive failure arising from internal coating fractures rather than the adhesive failure exhibited by large particle coatings.

The coatings at 40 wt% solids concentration from blended slurries showed better adherence (i.e. ultimate strength of 0.73 – 0.74 MPa) than the singly prepared slurries, but were insensitive to the volume proportions in the blends. The SEM micrographs showed that these coatings were homogeneous and not comprised of cracks.

The coatings at 45 wt% solids concentration from blended slurries had poor adherence. The ETS test showed a low ultimate strength of 0.09 MPa and more than 95 wt% removal, while the loss from ultrasonic vibration was more than 17 mass %. The SEM micrographs confirmed the presence of cracks in these coatings because the critical coating thickness had been exceeded. It was therefore shown from the results that the psds obtained from blended slurries produced no improvement in the coating adherence at increased solids concentration of 45 wt%.

8

CONCLUSIONS

8.1 OVERVIEW OF FINDINGS

Monolith catalysts fitted into automobiles are central to reducing emissions. With globalisation and the rapid increase in the use of motor vehicles, there is increasing need for new technological advancements in monolith catalyst production. The work described in this thesis has focussed on doing this by determining how to produce high quality γ–alumina coatings on Fecralloy® using the automatic film applicator. The links between the slurry characteristics and the coating process to the final coating quality have been determined.

The film applicator equipped with wire-wound bars was established as consistent technique of coating γ–alumina slurries onto Fecralloy® coupons because the deposition was performed under controlled shear rate. The psds of the ground slurries were found to be governed by the basic comminution parameters of the bead mill, such as number of stress events (SN), stress energy (SE) and specific energy ($E_{m,p}$). Acoustosizer and

Zetamaster measurements found that the particles in this slurry were optimally stabilised at a pH of 4 which corresponded to a zeta potential of +41 mV. The isoelectric point (iep) of the particles was found at a pH of 7.8 while the natural pH was found at 9.1. The stabilisation mechanism was based on electrostatic repulsion of charged particles, and this resulted in an increase in the zeta potential of particles. The steady shear flow experiments showed that the slurries exhibited shear thinning behaviour which was adequately described by the power-law model.

The main findings of this research are presented in the following:

8.1.1 Influence of Fecralloy® preoxidation

This study has shown that Fecralloy® preoxidation by thermal treatment under oxidising conditions is very crucial to producing good coating adherence. An aluminium-rich oxide layer is formed on Fecralloy® surface during preoxidation and this provides protection against high temperature oxidation, thereby prolonging the component life. The specific mass of the oxide layer as a function of preoxidation time from 0 – 30 h was properly described by a simplified hyperbolic model.

In a pioneering investigation, the LPI was used in exploring the surface topography (a combination of surface roughness and topography profile) of the Fecralloy® coupons. From the coupons preoxidised at 950 ^{o}C for 0 – 30 h, the LPI confirmed that the roughest surface (R_a = 0.15 μm and S_a = 0.35 μm) and dip penetrating configurations

were formed on the coupons preoxidised at 950 ^{o}C for 10 h. At these conditions the SEM showed the formation of conspicuous and randomly oriented α–alumina whiskers on the surface, while the EDS revealed largest composition of elemental surface Al. Similarly, the EDS analyses performed on the coupons showed a peak of the α–alumina composition at the surface at 950 ^{o}C for 10 h.

Upon coating the preoxidised Fecralloy® coupons with γ–alumina slurry using the film applicator, the optimal coating loading (7.9 mass %) and ultrasonic vibration adherence (9.9 mass % loss) were obtained from coupons preoxidised at 950 ^{o}C for 10 h, as these conditions produced the optimal surface topography and microstructure. In previous studies (e.g. Jia et al., 2007; Shen et al., 2006; Valentini et al., 2001), the coating loss of less than 12 mass% from ultrasonic vibration was mostly considered as good in terms of adherence.

On the other hand the untreated coupons, which exhibited no significant microstructure and wettability, had extremely poor coating loading and adherence. The coupons preoxidised at 950 ^{o}C for 5 h and 30 h showed average surface topography and microstructure such that their coating loading (< 6.8 mass %) and adherence (> 16.2 mass %) were comparably worse than the optimal.

As coating adherence is critical to the longevity and catalytic function in the exhaust system (Cybulski and Moulijn, 2006), Fecralloy® preoxidation at 950 ^{o}C for 10 h will ensure good coating adherence and reduce PGMs loss to the barest minimum.

8.1.2 Optimal coating methodology

The use of the film applicator in coating Fecralloy® coupons in this research represented a pragmatic shift from the conventional methods, such as dip coating and spraying. The film applicator and its components have been designed as a versatile bench top instrument which is suitable for producing surface coatings at controlled shear rate, thus leading to consistency in the coating properties**.**

The optimal methodology for coating γ–alumina slurry on the coupons was derived in terms of drying and calcination conditions as well as the bar gap and coating speed of the film applicator. For the coatings calcined but dried at different rates of 15 – 85 ^{o}C/h, no cracks were formed because the stresses developed in them during drying were not large enough to generate shrinkages which are the causative indices of cracks. These coatings therefore showed similar loading and adherence properties. As a result of this, a faster drying rate of 85 ^{o}C which reduced the production time was chosen as the optimal.

The effects of calcination at 500 ^{o}C for 1 h was far reaching as it brought about homogeneity, sintering and redistribution of coatings, which resulted into strong coating adherence. It was evident from the SEM images that the sintering of the calcined coatings caused densification of the γ–alumina particles as they were firmly layered on the substrate. The ultrasonic adhesion test showed 9.89 mass% loss from the calcined coatings compared to the 31.37 mass% for the uncalcined coatings.

The increase in the bar gap (10, 26, 100 μm) produced greater coating loading and thickness, and this had minimal consequences on the coating adherence. Since greater concentration of PGMs could be obtained at high coating loadings, the bar gap of 100 μm was chosen as the optimal. The shear rate increased (1000, 2500, 5000 s^{-1}) when the coating speed was increased (100, 250, 500 mm s^{-1}), but had no effect on the coating loading and adherence.

The coating methodology derived from the tests were then outlined as:

(a) drying at 110 ^{o}C for 1 h at the rate of 85 ^{o}C/h;

(b) calcination at 500 ^{o}C for 1 h;

(c) bar gap at 100 μm and

(d) coating speed at 100 mm s^{-1}

8.1.3 Effects of slurry characteristics on coating properties

The control of slurry characteristics (i.e. pH and solids concentration) would not only result in well dispersed slurries at optimal rheological advantage, but most importantly produce coatings of the desired properties. The viscosity, an important rheological parameter, was found to be related to the slurry pH and solids concentration. Steady flow tests showed that at a fixed solids concentration of 40 wt%, the pH of 4 produced the minimum viscosity (i.e. 13.7 mPas at a reference shear rate of 1000 s^{-1}) as the particles were optimally stabilised at a zeta potential of +41 mV. The slurry viscosity increased as the particles came close to the iep of 7.8 because of the reduced

electrostatic repulsion of particles. Similarly, the increase in solids concentration from 25 – 45 wt% produced increased viscosity as particle spacing decreased with more particles per unit volume, therefore leading to increased inter-particle interactions.

A general viscosity based approach to describing the effects of slurry characteristics on the coating properties should be avoided as good coating properties was achieved from slurries at increased viscosity, in the case of finer particles. Therefore the context (i.e. pH, solids concentration, psds and other defining features such as stabilisation conditions) at which the slurry viscosity was measured are more critical. For the slurries at pH of 3 – 11, the ultrasonic vibration showed that the optimal coating adherence of 9.89 mass% loss was found at the pH of 4, while the adherence losses at pH of 5 and 6 were similarly good at below 12 mass%. The coating adherence loss at the remaining pH values were comparably poor at 12.02 – 20.18 mass% because the particles were not properly stabilised and aggregates were being formed.

In the case of slurries of $d_{0.9}$ of 12.14 μm and solids concentration not exceeding 40 wt%, the ultrasonic vibration test showed that the coating adherence was less than 10 mass% loss, while the adherence at 45 wt% was around 17 mass% loss. Though the slurry viscosity increased from 25 – 45 wt%, the coating adherence at 45 wt% was relatively poor as cracks were present because the critical coating thickness had been exceeded, and the loosely anchored coatings were susceptible to losses.

8.1.4 Use of electromechanical testing system for assessing coating adherence

As conventional methods for assessing coating adherence only produce relative data which are not physically derived, this research looked inwards at addressing this issue by the dual compression-tension technique using the electromechanical testing system (ETS). This is because the adherence parameters (such as ultimate strength, work of adhesion) measured by the ETS can be related to the stresses inside the exhaust system of automobiles. The ETS technique involves compressing a metal probe on the coating at a specified load, and then removing together with the coating at a withdrawal speed of 10 mm/min. The adherence profile of the test is generated by a computer which was connected to the ETS. The adherence of the detached coating was quantified by the ultimate strength obtained from the profile.

The tests showed that the use of compression load from 100 to 300 N had no effect on the coating adherence. For the coatings made from singly prepared slurries of 40 wt% solids concentration produced by milling at different times, the ultimate strengths achieved varied with the particle diameters. The finest particles of $d_{0.9}$ of 12.14 μm produced the best coating adherence at an ultimate strength of 0.59 MPa and 85 – 90 mass % removal. The finest particles also had the least mass % loss from ultrasonic vibration test.

Though they showed better adherence than the singly prepared slurries, the coatings made from blended slurries of 40 wt% solids concentration had no change in coating adherence (i.e. ultimate strength of 0.73 – 0.74 MPa) as they were insensitive to the

different volume proportions in the blends. The SEM micrographs showed that these coatings were homogeneous and not comprised of cracks at this concentration.

However the coatings made from blended slurries of 45 wt% solids concentrations had poor adherence. The ETS tests showed a low break stress of 0.09 MPa and more than 95 wt% removal, while the loss from ultrasonic vibration was more than 17 mass %. The SEM micrographs confirmed the presence of cracks in these coatings because the critical coating thickness had been exceeded. It was therefore shown from the results that at increased solids concentration of 45 wt%, the blends of different psds produced no improvement in coating adherence.

8.2 RECOMMENDATIONS AND FUTURE OUTLOOK

This research has addressed vital issues relating to the production of γ–alumina coatings of desired quality on Fecralloy® using the film applicator, and therefore recommends the following:

(a) Fecralloy® preoxidation to be done at 950 ^{o}C for 10 h;
(b) drying at 110 ^{o}C for 1 h at the rate of 85 ^{o}C/h while calcination at 500 ^{o}C for 1 h;
(c) bar gap of the film applicator to be at 100 μm;
(d) coating slurries should be optimally stabilised at a pH of 4;
(e) the solids concentration should be controlled and not exceed 40 wt% and
(f) the particles should be prepared such that the diameter $d_{0.9}$ should be around 12 μm.

However there are some important areas in the coating of Fecralloy® yet to be fully explored. One of them is the multiple coating (i.e. multiple layer deposition) on Fecralloy® using the film applicator and the implications. This may be of paramount importance in instances where the coating loading and thickness achieved from the first deposition fall short. Some studies have suggested, though very vaguely, that the coating layer of the first deposit adheres more onto the substrate than that layer of the second deposit, and this effect is repeated as more deposits are added (Zhou et al., 2007; Agrafiotis and Tsetsekou, 2000). The mechanisms which govern multiple coating adherence behaviour are not well understood, and the LPI technique could be used for this investigation.

Another area of interest is the use of the film applicator to coat ceramic substrates which have been specially made for this purpose. The findings from this can be compared to those from Fecralloy® coupons. Though some studies have suggested that γ–alumina coatings have better adherence onto ceramic substrates than metallic ones (Avila et al., 2005), but some other studies have also suggested similar coating adherence for both substrates as long as the Fecralloy® is properly preoxidised (Cybulski and Moulijn, 2006). Investigations in this area are expected to be considerable in the future with technological advancements in the pursuit of improved substrates.

With the introduction of more stringent legislations to tackle emissions, there will be a need to devise more physically derived techniques, in addition to the ETS, for measuring coating adherence. These techniques can be based on the simulation of the

automotive exhaust systems and the use of robotics to standardise testing procedures for the catalyst industry.

REFERENCES

1. Acres, G. J. K. and Harrison, B., 2004, The development of catalysts for emission control from motor vehicles: early research at Johnson Matthey, *Topics in Catalysis*, 28 (1-4), 3-11.

2. Agashe, K. B. and Regalbuto, J. R., 1997, A revised physical theory for adsorption of metal complexes at oxide surfaces, *Journal of Colloid and Interface Science*, 185 (1), 174-189.

3. Agrafiotis, C. and Tsetsekou, A., 2000, The effect of processing parameters on the properties of γ-alumina washcoats deposited on ceramic honeycombs, *Journal of Materials Science*, 35 (4), 951-960.

4. Agrafiotis, C., Tsetsekou, A. and Ekonomakou, A., 1999, The effect of particle size on the adhesion properties of oxide washcoats on cordierite honeycombs, *Journal of Materials Science Letters*, 18 (17), 1421-1424.

5. Agrafiotis, C., Tsetsekou, A. and Leon, I., 2000, Effect of slurry rheological properties on the coating of ceramic honeycombs with yttria-stabilized-zirconia washcoats, *Journal of the American Ceramic Society*, 83 (5), 1033-1038.

6. Anklekar, R. M., Borkar, S. A., Bhattacharjee, S., Page, C. H. and Chatterjee, A. K., 1998, Rheology of concentrated alumina suspension to improve the milling output in production of high purity alumina powder, *Colloids and Surfaces A-Physicochemical and Engineering Aspects*, 133 (1-2), 41-47.

7. Ashby, M. F. and Jones, D. R. H., 1996, The yield strength, tensile strength, hardness and ductility, in *Engineering Materials 1*, 2nd edn, Butterworth-Heinemann, Oxford, 77-92.

8. Ashby, M. F. and Jones, D. R. H., 1998, Production, forming and joining of ceramics, in *Engineering materials 2: an introduction to microstructures, processing and design*, 2nd edn, Butterworth-Heinemann, Oxford, 194-215.

9. Avila, P., Montes, M. and Miro, E. E., 2005, Monolithic reactors for environmental applications - a review on preparation technologies, *Chemical Engineering Journal*, 109 (1-3), 11-36.

10. Badini, C. and Laurella, F., 2001, Oxidation of FeCrAl alloy: influence of temperature and atmosphere on scale growth rate and mechanism, *Surface & Coatings Technology*, 135 (2-3), 291-298.

11. Bandosz, T. J., Lin, C. and Ritter, J. A., 1998, Porosity and surface acidity of SiO_2-Al_2O_3 xerogels, *Journal of Colloid and Interface Science*, 198 (2), 347-353.

12. Barnes, H. A., 1995, A review of the slip (wall depletion) of polymer-solutions, emulsions and particle suspensions in viscometers - its cause, character, and cure, *Journal of Non-Newtonian Fluid Mechanics*, 56 (3), 221-251.

13. Barnes, H. A., 1997, Thixotropy - a review, *Journal of Non-Newtonian Fluid Mechanics*, 70 (1-2), 1-33.

14. Barnes, H. A., 2000, Measuring the viscosity of large-particle (and flocculated) suspensions - a note on the necessary gap size of rotational viscometers, *Journal of Non-Newtonian Fluid Mechanics*, 94 (2-3), 213-217.

15. Barnes, H. A., Hutton, J. F. and Walters, K., 1989, *An introduction to rheology* Elsevier, Amsterdam.

16. Battistoni, P., Fava, G., Stanzini, C., Cecchi, F. and Bassetti, A., 1993, Feed characteristics and digester operative conditions as parameters affecting the rheology of digested municipal solid-wastes, *Water Science and Technology*, 27 (2), 37-45.

17. Bauer, C. L., 2000, *Development and application of X-ray diffraction techniques for understanding molecular solids*, PhD Thesis, University of Birmingham, Birmingham.

18. Becker, M., Kwade, A. and Schwedes, J., 2001, Stress intensity in stirred media mills and its effect on specific energy requirement, *International Journal of Mineral Processing*, 61, 189-208.

19. Benkreira, H., 2004, The effect of substrate roughness on air entrainment in dip coating, *Chemical Engineering Science*, 59 (13), 2745-2751.

20. Benkreira, H., 2007, Coating and polymer processing, *International Polymer Processing*, 22 (1), 3-8.

21. Bennett, M. J., Nicholls, J. R., Simms, N. J., Naumenko, D., Quadakkers, W. J., Kochubey, V., Fordham, R., Bachorczyk, R., Goossens, D., Hattendorf, H., Smith, A. B. and Britton, D., 2005, Lifetime extension of FeCrAlRe alloys in air: Potential roles of an enhanced Al-reservoir and surface pre-treatment, *Materials and Corrosion*, 56 (12), 854-866.

22. Binner, J. G. P. and McDermott, A. M., 2006, Rheological characterisation of ammonium polyacrylate dispersed, concentrated alumina suspensions, *Ceramics International*, 32 (7), 803-810.

23. Binner, J. G. P. and Santacruz, I., 2006, Rheological characterisation of electrosterically dispersed alumina suspensions during in situ coagulation, *Journal of the American Ceramic Society*, 89 (3), 863-868.

24. Blachou, V., Goula, D. and Philippopoulos, C., 1992, Wet milling of alumina and preparation of slurries for monolithic structures impregnation, *Industrial & Engineering Chemistry Research*, 31 (1), 364-369.

25. Braaten, A., Groshek, J. and Smith, P., 1998, Film applicators - the past, the present, the future - highlights some of the factors driving today's film coating processes, *Pulp & Paper-Canada*, 99 (10), 48-52.

26. Brown, G. E., Henrich, V. E., Casey, W. H., Clark, D. L., Eggleston, C., Felmy, A., Goodman, D. W., Gratzel, M., Maciel, G., McCarthy, M. I., Nealson, K. H., Sverjensky, D. A., Toney, M. F. and Zachara, J. M., 1999, Metal oxide surfaces and their interactions with aqueous solutions and microbial organisms, *Chemical Reviews*, 99 (1), 77-174.

27. Bruck, R., 2002, Development status of metal substrate catalysts, in *Materials aspects in automotive catalytic converters*, Bode, H. edn, Wiley-VCH Weinheim, 19.

28. Bruck, R., Diringer, J., Martin, U. and Maus, W., 1995, Flow improved efficiency by new cell structures in metallic substrates, *SAE paper 950788*.

29. Brunelle, J. P., 1978, Preparation of catalysts by metallic complex adsorption on mineral oxides, *Pure and Applied Chemistry*, 50 (9-10), 1211-1229.

30. Burgos, N., Paulis, M. A. and Montes, M., 2003, Preparation of Al_2O_3/Al monoliths by anodisation of aluminium as structured catalytic supports, *Journal of Materials Chemistry*, 13 (6), 1458-1467.

31. Busch, T., Harlow, R. and Thompson, R. L., 1998, Surface measurements, in *Fundamentals of dimensional metrology*, 3rd edn, Delmar Publishers, New York, 499-524.

32. Chapman, L. R., 1982, *Enhanced oxide whiskers growth on peeled Al-containing stainless steel foils*, US Patent 4,331,631.

33. Chen, J. Y. and Fan, Z., 2002a, Modelling of rheological behaviour of semisolid metal slurries - Part 2 - Steady state behaviour, *Materials Science and Technology*, 18 (3), 243-249.

34. Chen, J. Y. and Fan, Z., 2002b, Modelling of rheological behaviour of semisolid metal slurries - Part 3 - Transient state behaviour, *Materials Science and Technology*, 18 (3), 250-257.

35. Chescoe, D. and Goodhew, P. J., 1990, How and why electron microscopes work, in *The operation of transmission and scanning electron microscopes*, Oxford University Press, New York, 1-24.

36. Chiu, R. C., Garino, T. J. and Cima, M. J., 1993, Drying of granular ceramic films 1. Effects of processing variables on cracking behaviour, *Journal of the American Ceramic Society*, 76 (9), 2257-2264.

37. Collins, N. R. and Twigg, M. V., 2007, Three-way catalyst emissions control technologies for spark-ignition engines - recent trends and future developments, *Topics in Catalysis*, 42-43, 323-332.

38. Cowen, H. C. and Webster, S. J., 1974, *Corrosion of steels in CO_2* Thomas Telford Ltd, London.

39. Cristiani, C., Valentini, M., Merazzi, M., Neglia, S. and Forzatti, P., 2005, Effect of ageing time on chemical and rheological evolution in γ-Al_2O_3 slurries for dip-coating, *Catalysis Today*, 105 (3-4), 492-498.

40. Cybulski, A. and Moulijn, J. A., 1994, Modelling of heat transfer in metallic monoliths consisting of sinusoidal cells, *Chemical Engineering Science*, 49 (1), 19-27.

41. Cybulski, A. and Moulijn, J. A., 2006, *Structured catalysis and reactors*, 2nd edn, Taylor & Francis, London.

42. Daghetti, A., Lodi, G. and Trasatti, S., 1983, Interfacial properties of oxides used as anodes in the electrochemical technology, *Materials Chemistry and Physics*, 8 (1), 1-90.

43. Davies, J. and Binner, J. G. P., 2000, The role of ammonium polyacrylate in dispersing concentrated alumina suspensions, *Journal of the European Ceramic Society*, 20 (10), 1539-1553.

44. Debye, P., 1933, A method for the determination of the mass of electrolytic ions, *Journal of Chemical Physics*, 1 (1), 13-16.

45. Deng, W., Bodart, P., Pruski, M. and Shanks, B. H., 2002, Characterization of mesoporous alumina molecular sieves synthesized by nonionic templating, *Microporous and Mesoporous Materials*, 52 (3), 169-177.

46. Dressler, M., Nofz, M. and Gemeinert, M., 2006, Rheology, UV-vis transparency and particle size distribution, *Journal of Sol-Gel Science and Technology*, 38, 261-269.

47. Edirisinghe, M. J., Shaw, H. M. and Tomkins, K. L., 1992, Flow behavior of ceramic injection-molding suspensions, *Ceramics International*, 18 (3), 193-200.

48. Edvinsson, R. K., Holmgren, A. M. and Irandoust, S., 1995, Liquid-phase hydrogenation of acetylene in a monolithic catalyst reactor, *Industrial & Engineering Chemistry Research*, 34 (1), 94-100.

49. Evans, H. E., Donaldson, A. T. and Gilmour, T. C., 1999, Mechanisms of breakaway oxidation and application to a chromia-forming steel, *Oxidation of Metals*, 52 (5-6), 379-402.

50. Fadhel, H. B. and Frances, C., 2001, Wet batch grinding of alumina hydrate in a stirred bead mill, *Powder Technology*, 119 (2-3), 257-268.

51. Fei, W., Kuiry, S. C., Sohn, Y. and Seal, S., 2003, Sol gel alumina coating on Fe-Cr-Al-Y fibre media for catalytic converters, *Surface Engineering*, 19 (3), 189-194.

52. Fereshteh-Saniee, F., Alavi-Nia, A. and Atrian-Afyani, A., 2008, An experimental investigation on the deep drawing process of steel-brass bimetal sheets, *Steel Research International*, 1, 63-70.

53. Flynn, P. C. and Wanke, S. E., 1974a, A model of supported metal catalyst sintering 1. Development of model, *Journal of Catalysis*, 34, 390-399.

54. Flynn, P. C. and Wanke, S. E., 1974b, A model of supported metal catalyst sntering 2. Application of model, *Journal of Catalysis*, 34, 400-410.

55. Fornasiero, P., Montini, T., Graziani, M., Zilio, S. and Succi, M., 2008, Development of functionalized Fe-Al-Cr alloy fibers as innovative catalytic oxidation devices, *Catalysis Today*, 137 (2-4), 475-482.

56. Fukuda, K., Takao, K., Hoshi, T. and Furukimi, O., 2002, Improved high temperature oxidation resistance of REM added F-20%Cr-5%Al alloy by pre-annealing treatment, in *Materials aspects in automotive catalytic converters*, H. Bode, ed., Wiley-VCH, Weinheim, 59.

57. Galyer, J. F. W. and Shotbolt, C. R., 1990, Measurement of surface texture and roundness, in *Metrology for engineers*, 5th edn, Cassell, London, 184-206.

58. Germani, G., Stefanescu, A., Schuurman, Y. and van Veen, A. C., 2007, Preparation and characterization of porous alumina-based catalyst coatings in microchannels, *Chemical Engineering Science*, 62 (18-20), 5084-5091.

59. Giani, L., Cristiani, C., Groppi, G. and Tronconi, E., 2006, Washcoating method for Pd/γ-Al_2O_3 deposition on metallic foams, *Applied Catalysis B-Environmental*, 62 (1-2), 121-131.

60. Gonzalez-Pena, V., Diaz, I., Marquez-Alvarez, C., Sastre, E. and Perez-Pariente, J., 2001, Thermally stable mesoporous alumina synthesized with non-ionic surfactants in the presence of amines, *Microporous and Mesoporous Materials*, 44, 203-210.

61. Greenwood, R., 2003, Review of the measurement of zeta potentials in concentrated aqueous suspensions using electroacoustics, *Advances in Colloid and Interface Science*, 106, 55-81.

62. Greenwood, R. and Kendall, K., 2000, Effect of ionic strength on the adsorption of cationic polyelectrolytes onto alumina studied using electroacoustic measurements, *Powder Technology*, 113 (1-2), 148-157.

63. Greenwood, R., Luckman, P. F. and Gregory, T., 1997, The effect of diameter ratio and volume ratio on the viscosity of bimodal suspensions of polymer lattices, *Journal of Colloid and Interface Science*, 191 (1), 11-21.

64. Greenwood, R., Luckman, P. F. and Gregory, T., 1998, Minimising the viscosity of concentrated dispersions by using bimodal particle size distributions, *Colloids and Surfaces A-Physicochemical and Engineering Aspects*, 144 (1-3), 139-147.

65. Haagen-Smit, A. J., Bradley, C. E. and Fox, M. M., 1953, *Industrial & Engineering Chemistry Research*, 45, 2086.

66. Haagen-Smit, A. J. and Fox, M. M., 1954, *Journal of Air Pollution Control Association*, 4 (105), 136.

67. Hao, X., Spieker, W. A. and Regalbuto, J. R., 2003, A further simplification of the revised physical adsorption (RPA) model, *Journal of Colloid and Interface Science*, 267 (2), 259-264.

68. Harris, J., 1977, Rheology, in *Rheology and non-Newtonian flow*, Longman Group, London, 1-23.

69. Held, W., Rohlfs, M. W., Swars, H., Bruck, R. and Kaiser, F. W., 1994, Improved cell design for increased catalytic conversion efficiency, *SAE paper 940932*.

70. Hickman, D. A. and Schmidt, L. D., 1992a, Synthesis gas-formation by direct oxidation of methane over Pt monoliths, *Journal of Catalysis*, 138 (1), 267-282.

71. Hickman, D. A. and Schmidt, L. D., 1992b, The role of boundary-layer mass-transfer in partial oxidation selectivity, *Journal of Catalysis*, 136 (2), 300-308.

72. Hill, A. and Carrington, S., 2006, Understanding the links between rheology and particle parameters, *American Laboratory*, 38 (21), 22-25.

73. Hoffman, R. L., 1992, Factors affecting the viscosity of unimodal and multimodal colloidal dispersions, *Journal of Rheology*, 36 (5), 947-965.

74. Hooper, R. J., Liu, W., Fryer, P. J., Patterson, W. R., Wilson, D. I. and Zhang, Z., 2006, Comparative studies of fluid dynamic gauging and a

micromanipulation probe for strength measurements, *Food and Bioproducts Processing*, 84 (C4), 353-358.

75. Housecroft, C. E. and Constable, E. C., 2002, *An introduction to organic, inorganic and physical chemistry*, 2nd edn, Pearson Education Limited, Essex.

76. Hunter, R. J., 1998, Recent developments in the electroacoustic characterisation of colloidal suspensions and emulsions, *Colloids and Surfaces A-Physicochemical and Engineering Aspects*, 141 (1), 37-66.

77. Incropera, F. P. and DeWitt, D. P., 2002, Introduction, in *Fundamentals of heat and mass transfer*, 5th edn, John Wiley & Sons, New York, 1-3.

78. Instron Materials Testing Catalog, 2009, Instron Ltd, Massachusetts.

79. Ionescu, A., Allouche, A., Aycard, J. P., Rajzmann, M. and Hutschka, F., 2002, Study of γ-alumina surface reactivity: Adsorption of water and hydrogen sulfide on octahedral aluminum sites, *Journal of Physical Chemistry B*, 106 (36), 9359-9366.

80. Ismagilov, Z. R., Yashnik, S. A., Matveev, A. A., Koptyug, I. V. and Moulijn, J. A., 2005, Characteristics of drying and active component distribution in alumina monoliths using (HL)-H-1-NMR imaging, *Catalysis Today*, 105 (3-4), 484-491.

81. Janickle, M. T., Kestenbaum, H., Hagendorf, U., Schuth, F., Fichtner, M. and Schubet, K., 2000, The controlled oxidation of hydrogen from an explosive mixture of gases using a microstructured reactor/heat exchanger and Pt/Al_2O_3 catalyst, *Journal of Catalysis*, 191 (2), 282-293.

82. Jia, L. W., Shen, M. Q. and Wang, J., 2007, Preparation and characterization of dip-coated γ-alumina based ceramic materials on FeCrAl foils, *Surface & Coatings Technology*, 201 (16-17), 7159-7165.

83. Jobson, E., 2004, Future challenges in automotive emmision control, *Topics in Catalysis*, 28 (1-4), 191-199.

84. Johnson Matthey Annual Report & Accounts, 2009, Johnson Matthey Plc, London.

85. Kasprzyk-Hordern, B., 2004, Chemistry of alumina, reactions in aqueous solution and its application in water treatment, *Advances in Colloid and Interface Science*, 110 (1-2), 19-48.

86. Kestenbaum, H., de Oliveira, A. L., Schmidt, W., Schuth, F., Ehrfeld, W., Gebauer, K., Lowe, H., Richter, T., Lebiedz, D., Untiedt, I. and Zuchner, H., 2002, Silver-catalysed oxidation of ethylene to ethylene oxide in a microreaction system, *Industrial & Engineering Chemistry Research*, 41 (4), 710-719.

87. Kippax, P., 2005, *Measuring particle size using modern laser diffraction techniques*, Malvern Instruments Ltd, Worcestershire.

88. Koopal, L. K., 1996, Mineral hydroxides: from homogeneous to heterogeneous modelling, *Electrochimica Acta*, 41 (14), 2293-2305.

89. Kuwano, K., Yamazaki, Y., Otsubo, S., Hasegawa, S. and Nagasawa, M., 1994, Effects of thixotropic agents on the viscoelastic properties of paints for automobiles, *Kobunshi Ronbunshu*, 51 (2), 93-98.

90. Kwade, A., 1999, Wet comminution in stirred media mills - research and its practical application, *Powder Technology*, 105 (1-3), 14-20.

91. Kwade, A., 2003, A stressing model for the description and optimization of grinding processes, *Chemical Engineering & Technology*, 26 (2), 199-205.

92. Kwade, A., 2004, Mill selection and process optimization using a physical grinding model, *International Journal of Mineral Processing*, 74 S93-S101.

93. Kwade, A., Blecher, L. and Schwedes, J., 1996, Motion and stress intensity of grinding beads in a stirred media mill .2. Stress intensity and its effect on comminution, *Powder Technology*, 86 (1), 69-76.

94. Kwade, A. and Schwedes, J., 2002, Breaking characteristics of different materials and their effect on stress intensity and stress number in stirred media mills, *Powder Technology*, 122 (2-3), 109-121.

95. La Parola, V., Deganello, G., Scire, S. and Venezia, A. M., 2003, Effect of the Al/Si atomic ratio on surface and structural properties of sol-gel prepared aluminosilicates, *Journal of Solid State Chemistry*, 174 (2), 482-488.

96. Lippens, B. C. and Steggerda, J. J., 1970, *Physical and chemical aspects of adsorbents and catalysts* Academic Press, London.

97. Liu, W., Christian, G. K., Zhang, Z. and Fryer, P. J., 2002, Development and use of a micromanipulation technique for measuring the force required to disrupt and remove fouling deposits, *Food and Bioproducts Processing*, 80 (C4), 286-291.

98. Määthänen, M. and Lylykangas, R., 1990, Mechanical strength of a metallic catalytic converter made of precoated foil, *SAE paper 900505*.

99. Macedo, M. I. F., Osawa, C. C. and Bertran, C. A., 2004, Sol-gel synthesis of transparent alumina gel and pure gamma alumina by urea hydrolysis of aluminum nitrate, *Journal of Sol-Gel Science and Technology*, 30 (3), 135-140.

100. Magnin, A. and Piau, J. M., 1987, Shear rheometry of fluids with a yield stress, *Journal of Non-Newtonian Fluid Mechanics*, 23, 91-106.

101. Meille, V., 2006, Review on methods to deposit catalysts on structured surfaces, *Applied Catalysis A-General*, 315, 1-17.

102. Meille, V., Pallier, S., Bustamante, G., Roumanie, M. and Reymond, J., 2005, Deposition of γ–Al_2O_3 layers on structured supports for the design of new catalytic reactors, *Applied Catalysis A-General*, 286, 232-238.

103. Morterra, C. and Magnacca, G., 1996, A case study: Surface chemistry and surface structure of catalytic aluminas, as studied by vibrational spectroscopy of adsorbed species, *Catalysis Today*, 27 (3-4), 497-532.

104. Mukhopadhyay, P., Biswas, S. and Chokshi, A. H., 2009, Deformation characterization of superplastic AA7475 alloy, *Transactions of the Indian Institute of Metals*, 62 (2), 149-152.

105. Nicholls, J. R. and Quadakkers, W. J., 2002, Materials issues relevant to the development of future metal foil automotive catalytic converters, in *Materials aspects in automotive catalytic converters*, H. Bode, ed., Wiley-VCH, Weinheim, 31.

106. Nievergeld, A. J., 1998, *Automotive exhaust gas conversion: reaction kinetics, reactor modelling and control*, PhD Thesis, University of Technology, Eindhoven.

107. Noik, C., Monot, F., Ballerini, D. and Lecourtier, J., 1993, Characterization of xanthan protein complexes obtained with various fermentation conditions, *Acs Symposium Series*, 532, 253-265.

108. Nowack, B., Lutzenkirchen, T., Behra, P. and Sigg, L., 1996, Modeling the adsorption of metal-EDTA complexes onto oxides, *Environmental Science & Technology*, 30 (7), 2397-2405.

109. Omura, N., Hotta, Y., Sato, K., Kinemuchi, Y., Kume, S. and Watari, K., 2005, Characterisation of Al_2O_3 slurries prepared by wet jet milling, *Journal of Ceramic Society of Japan*, 113 (7), 491-494.

110. Onishi, A., 2007, The impact of CO_2 emissions on the world economy policy simulations of FUGI global model, *Journal of Policy Modeling*, 29 (6), 797-819.

111. Onozaki, K., 2009, Population is a critical factor for global carbondioxide increase, *Journal of Health Science*, 55 (1), 125-127.

112. Overdiep, W. S., 1986, The effect of a reduced solvent content of solvent-borne solution paints on film formation, *Progress in Organic Coatings*, 14 (1), 1-21.

113. Pachauri, R., Ravindranath, N., Bosch, P., Bernstein, L. and Metz, B., 2007, *Climate change 2007: Synthesis report*, United Nations, NewYork.

114. Paglia, G., Buckley, C. E., Rohl, A. L., Hart, R. D., Winter, K., Studer, A. J., Hunter, B. A. and Hanna, J. V., 2004a, Boehmite derived γ-alumina system. 1. Structural evolution with temperature, with the identification and structural determination of a new transition phase, γ'-alumina, *Chemistry of Materials*, 16 (2), 220-236.

115. Paglia, G., Buckley, C. E., Udovic, T. J., Rohl, A. L., Jones, F., Maitland, C. F. and Connolly, J., 2004b, Boehmite-derived gamma-alumina system. 2. Consideration of hydrogen and surface effects, *Chemistry of Materials*, 16 (10), 1914-1923.

116. Palmqvist, L., Lyckfeldt, O., Carlstrom, E., Davoust, P., Kauppi, A. and Holmberg, K., 2006, Dispersion mechanisms in aqueous alumina suspensions at high solids loadings, *Colloids and Surfaces A-Physicochemical and Engineering Aspects*, 274 (1-3), 100-109.

117. Pavlina, E. J. and Van Tyne, C. J., 2008, Correlation of yield strength and tensile strength with hardness of steel, *Journal of Materials Engineering and Performance*, 17 (6), 888-893.

118. Pecharroman, C., Sobrados, I., Iglesias, J. E., Gonzalez-Carreno, T. and Sanz, J., 1999, Thermal evolution of transitional aluminas followed by NMR and IR spectroscopies, *Journal of Physical Chemistry B*, 103 (30), 6160-6170.

119. Perez, P., Haanappel, V. A. C. and Stroosnijder, M. F., 2001, Formation of an alumina layer on a FeCrAl alloy by thermal oxidation for potential medical implant applications, *Surface & Coatings Technology*, 139 (2-3), 207-215.

120. Perry, R. H., Green, D. W. and Maloney, J. O., 1997, Liquid-solid operation and equipment, in *Perry's chemical engineers' handbook*, 7th edn, McGraw-Hill, New York, 12-18.

121. Peters, A. C., Overbeek, G. C., Buckmann, A. J. P., Padget, J. C. and Annable, T., 1996, Bimodal dispersions in coating applications, *Progress in Organic Coatings*, 29 (1), 183-194.

122. Pinna, F., 1998, Supported metal catalysts preparation, *Catalysis Today*, 41 (1-3), 129-137.

123. Pint, B. A., Garrattreed, A. J. and Hobbs, L. W., 1995, The reactive element effect in commercial ods Fecral alloys, *Materials at High Temperatures*, 13 (1), 3-16.

124. Pragnell, W. M., Evans, H. E., Naumenko, D. and Quadakkers, W. J., 2005, Aluminium depletion in FeCrAlY steel during transitional alumina formation, *Materials at High Temperatures*, 22 (3-4), 561-566.

125. Pratt, A. S. and Cairns, J. A., 1977, Noble metal catalysts on metallic substrates, *Platinum Metals Review*, 21, 74-83.

126. Probstein, R. F., Sengun, M. Z. and Tseng, T. C., 1994, Bimodal model of concentrated suspension viscosity for distributed particle sizes, *Journal of Rheology*, 38 (4), 811-829.

127. Qin, K. D. and Zaman, A. A., 2003, Viscosity of concentrated colloidal suspensions: comparison of bidisperse models, *Journal of Colloid and Interface Science*, 266 (2), 461-467.

128. Rawle, A., 2002, The importance of particle sizing for the coatings industry. Part 1: particle size measurement, *Advances in Colour Science and Technology*, 5 (1), 1-12.

129. Rawle, A., 2003, *Basic principles of particle size analysis*, Malvern Instruments Ltd, Worcestershire.

130. Reymond, J. P., 2001, Structured supports for noble catalytic metals: stainless steel fabrics and foils, and carbon fabrics, *Catalysis Today*, 69 (1-4), 343-349.

131. Richardson, J. T., Peng, Y. and Remue, D., 2000, Properties of ceramic foam catalyst supports, *Applied Catalysis A-General*, 204 (1), 19-32.

132. Robbins, P. T., Bridson, R. H., Chen, Y., Westerman, D., Gillham, C. R., Roche, T. C. and Seville, J. P. K., 2007, The effects of high shear blending on α-lactose monohydrate, *International Journal on Pharmaceutics*, 339 (1-2), 84-90.

133. Roberts, G. P., Barnes, H. A. and Carew, P., 2001, Modelling the flow behaviour of very shear-thinning liquids, *Chemical Engineering Science*, 56 (19), 5617-5623.

134. Rogers, G. and Mayhew, Y., 1992, Fundamental Concepts, in *Engineering thermodynamics: work and heat transfer*, 4th edn, Longman Group, Harlow, 7-13.

135. Roth, T., Kloos, K. and Broszeit, E., 1987, Structure, internal stresses, adhesion and wear resistance of sputtered alumina coatings, *Thin Solid Films*, 153, 123-133.

136. Sakurai, K., Shimoji, K., Yoshinaga, T., & Watanabe, K., 1998, *Electrically heated catalytic converter for an engine*, US Patent 5,744,104.

137. Sarraf, H. and Herbig, R., 2008, Electrokinetic sonic amplitude measurement of concentrated alumina suspensions: effect of electrosteric stabilisation, *Journal of Ceramic Society of Japan*, 116 (9), 928-934.

138. Schimpf, S., Lucas, M., Mohr, C., Rodemerck, U., Bruckner, A., Radnik, J., Hofmeister, H. and Claus, P., 2002, Supported gold nanoparticles: in-depth catalyst characterisation and application in hydrogenation and oxidation reactions, *Catalysis Today*, 72 (1-2), 63-78.

139. Schuessler, M., Portscher, M. and Limbeck, U., 2003, Monolithic integrated fuel processor for the conversion of liquid methanol, *Catalysis Today*, 79 (1-4), 511-520.

140. Schwarz, J. A., Contescu, C. and Contescu, A., 1995, Methods for preparation of catalytic materials, *Chemical Reviews*, 95 (3), 477-510.

141. Shaw, D. J., 1992, *Introduction to colloid and surface chemistry*, 4th edn, Butterworth-Heinemann, Oxford.

142. Sheen Instruments Manual, 2006, *1132N automatic film applicator*, Sheen Instruments Ltd, Kingston.

143. Shen, M. Q., Jia, L. W., Zhou, W. L., Wang, J. and Huang, Y., 2006, Influence of $Ce_{0.68}Zr_{0.32}O_2$ solid solution on depositing γ-alumina washcoat on FeCrAl foils, *Bulletin of Materials Science*, 29 (1), 73-76.

144. Shi, J. L. and Zhang, J. D., 2000, Compaction and sintering behavior of bimodal alumina powder suspensions by pressure filtration, *Journal of the American Ceramic Society*, 83 (4), 737-742.

145. Sidwell, R. W., Zhu, H. Y., Kibler, B. A., Kee, R. J. and Wickham, D. T., 2003, Experimental investigation of the activity and thermal stability of hexaaluminate catalysts for lean methan-air combustion, *Applied Catalysis A-General*, 255 (2), 279-288.

146. Smith, G. T., 2002, *Industrial metrology* Springer, London.

147. Spieker, W. A. and Regalbuto, J. R., 2001, A fundamental model of platinum impregnation onto alumina, *Chemical Engineering Science*, 56 (11), 3491-3504.

148. Starov, V., Zhdanov, V., Meireles, M. and Molle, C., 2002, Viscosity of concentrated suspensions: influence of cluster formation, *Advances in Colloid and Interface Science*, 96 (1-3), 279-293.

149. Stott, F. H., Wood, G. C. and Stringer, J., 1995, The influence of alloying elements on the development and maintenance of protective scales, *Oxidation of Metals*, 44 (1-2), 113-145.

150. Sun, H., Quan, X., Chen, S., Zhao, H. M. and Zhao, Y. Z., 2007, Preparation of well-adhered γ-Al_2O_3 washcoat on metallic wire mesh monoliths by electrophoretic deposition, *Applied Surface Science*, 253 (6), 3303-3310.

151. Tatlock, G. J., Al-Badairy, H., Bennett, M. J., Newton, R., Nicholls, J. R. and Galerie, A., 2005, Air oxidation of commercial FeCrAlRE alloy foils between 800 and 950 ^{o}C, *Materials Science and Technology*, 21 (8), 893-900.

152. Thevenin, P. O., Ersson, A. G., Kušar, H. M. J., Penon, P. G. and Järås, S. G., 2001, Deactivation of high temperature combustion catalysts, *Applied Catalysis A-General*, 212, 189-197.

153. Tien, J. K. and Pettit, F. S., 1972, Mechanism of oxide adherence on Fe-25Cr-4Al (y Or Sc) alloys, *Metallurgical Transactions*, 3 (6), 1587.

154. Tijburg, I. I. M., Geus, J. W. and Zandbergen, H. W., 1991, Application of lanthanum to pseudo-boehmite and γ-Al_2O_3, *Journal of Materials Science*, 26 (23), 6479-6486.

155. Tikhov, S. F., Fenelonov, V. B., Zaikovskii, V. I., Potapova, Y. V. and Sadykov, V. A., 1999, The three-dimensional microporous structure of alumina synthesized through the aluminum hydrothermal oxidation route, *Microporous and Mesoporous Materials*, 33 (1-3), 137-142.

156. Tolpygo, V. K., 1999, The morphology of thermally grown α-Al_2O_3 scales on Fe-Cr-Al alloys, *Oxidation of Metals*, 51 (5-6), 449-477.

157. Trimm, D. L., 1995, Material selection and design of high temperature catalytic combustion units, *Catalysis Today*, 26 (3-4), 231-238.

158. Trueba, M. and Trasatti, S. P., 2005, γ-Alumina as a support for catalysts: a review of fundamental aspects, *European Journal of Inorganic Chemistry*, 17, 3393-3403.

159. Truyen, D., Courty, M., Alphonse, P. and Ansart, F., 2006, Catalytic coatings on stainless steel prepared by sol-gel route, *Thin Solid Films*, 495, 257-261.

160. Twigg, M. V., 2006, Roles of catalytic oxidation in control of vehicle exhaust emissions, *Catalysis Today*, 117 (4), 407-418.

161. Twigg, M. V., 2007, Progress and future challenges in controlling automotive exhaust gas emissions, *Applied Catalysis B-Environmental*, 70 (1-4), 2-15.

162. U.S Atomic Energy Commission Report, 1966, *Embrittlement-resistant iron-aluminium-yttrium alloys*, UK Patent 1,045,993.

163. Valentini, M., Cristiani, G., Levi, M., Tronconi, E. and Forzatti, P., 2001, The deposition of γ-Al_2O_3 layers on ceramic and metallic supports for the preparation of structured catalysts, *Catalysis Today*, 69 (1-4), 307-314.

164. Vishista, K. and Gnanam, F. D., 2004, Role of deflocculants on the rheological properties of boehmite sol, *Materials Letters*, 58 (10), 1576-1581.

165. Voyutsky, S., 1978, Electrical properties of colloidal systems, in *Colloid Chemistry*, Mir Publishers, Moscow, 183.

166. Wefers, K., 1990, *Alumina chemicals: science and technology handbook* The American Ceramic Society, Westerville, Ohio, 13.

167. Wei, Y. and Hutchinson, J. W., 1998, Interface strength, work of adhesion and plasticity in the peel test, *International Journal of Fracture*, 93 315-333.

168. Williams, J. L., 2001, Monolith structures, materials, properties and uses, *Catalysis Today*, 69 (1-4), 3-9.

169. Wloch, E., Lukaszczyk, A., Zurek, Z. and Sulikowski, B., 2006, Synthesis of ferrierite coatings on the FeCrAl substrate, *Catalysis Today*, 114 (2-3), 231-236.

170. Wu, X. D., Weng, D., Xu, L. H. and Li, H. D., 2001, Structure and performance of γ-alumina washcoat deposited by plasma spraying, *Surface & Coatings Technology*, 145 (1-3), 226-232.

171. Wu, X. D., Weng, D., Zhao, S. and Chen, W., 2005, Influence of an aluminized intermediate layer on the adhesion of a γ-Al_2O_3 washcoat on FeCrAl, *Surface & Coatings Technology*, 190 (2-3), 434-439.

172. Wyckoff, R. W. G., 1968, *Miscellaneous inorganic compounds, silicates and basic structural information*, 2nd edn, Interscience Publishers, New York.

173. Xu, C. and Li, S., 2007, Research on peeling properties of galvannealed coatings, *Proceedings of the ASME International Conference on Manufacturing Science and Engineering*, 887-890.

174. Xu, J. H. and Koelling, K. W., 2005, Temperature dependence of rheological behavior of a metallic automotive waterborne basecoat, *Progress in Organic Coatings*, 53 (3), 169-176.

175. Yang, Y. P. and Sigmund, W. M., 2002, Expanded percolation theory model for the temperature induced forming (TIF) of alumina aqueous suspensions, *Journal of the European Ceramic Society*, 22 (11), 1791-1799.

176. Yang, Y. P. and Sigmund, W. M., 2003, A new approach to prepare highly loaded aqueous alumina suspensions with temperature sensitive rheological properties, *Journal of the European Ceramic Society*, 23 (2), 253-261.

177. Zaman, A. A. and Dutcher, C. S., 2006, Viscosity of electrostatically stabilized dispersions of monodispersed, bimodal, and trimodal silica particles , *Journal of the American Ceramic Society*, 89 (2), 422-430.

178. Zhao, S., Zhang, J. Z., Weng, D. and Wu, X. D., 2003, A method to form well-adhered γ-Al_2O_3 layers on FeCrAl metallic supports, *Surface & Coatings Technology*, 167 (1), 97-105.

179. Zhou, J., Jia, J. S., Zhang, H. U., Yuan, Z. S. and Wang, S. D., 2007, The influence of preparative parameters on the adhesion of alumina washcoats deposited on metallic supports, *Applied Surface Science*, 253 (23), 9099-9104.